Anderson localization with cold atoms : dynamics in disorder and prospects from chaos

Tony Prat

THÈSE DE DOCTORAT
DE L'UNIVERSITÉ PIERRE ET MARIE CURIE

Spécialité : Physique

École doctorale : « Physique en Île-de-France »

réalisée

au Laboratoire Kastler Brossel

présentée par

Tony Prat

pour obtenir le grade de :

DOCTEUR DE L'UNIVERSITÉ PIERRE ET MARIE CURIE

Sujet de la thèse :

Localisation d'Anderson avec des atomes froids: dynamique dans le désordre et perspectives avec des modèles chaotiques

soutenue le 25 septembre 2017

devant le jury composé de :

M.	Denis Basko	Rapporteur
M.	Nicolas Cherroret	Invité
M^{me}	Leticia F. Cugliandolo	Présidente du jury
M.	Dominique Delande	Directeur de thèse
M.	Vincent Josse	Examinateur
M.	Peter Schlagheck	Rapporteur
M^{me}	Patrizia Vignolo	Examinatrice

Remerciements

Ces trois années de thèse furent à la fois plaisantes et enrichissantes, je le dois à de nombreuses personnes que je souhaiterais remercier ici.

Je voudrais d'abord remercier Denis Basko et Peter Schlagheck pour avoir accepté le rôle de rapporteur. Je les remercie aussi, ainsi que les autres membres du jury, Leticia Cugliandolo, Vincent Josse et Patrizia Vignolo, pour leurs questions pertinentes lors de la soutenance.

J'ai eu la chance d'être encadré pendant ces trois années par deux directeurs de thèse investis. La thèse doit beaucoup à la passion de Dominique et la rigueur de Nicolas. Je leur suis infiniment reconnaissant pour leurs conseils, nos nombreuses discussions et plus généralement pour l'ambiance qu'ils ont su créer au sein du groupe.

J'ai passé trois excellentes années au LKB, pour cela je remercie en particulier mes co-bureaux successifs qui ont toujours illuminé le bureau 206. Merci Panayotis, Sanjib, Michael, Pierre-Elie, Thibault et Tamara. Je remercie aussi tous ceux avec qui j'ai partagé mes déjeuners, en particulier les membres de l'équipe Casimir, les métrologistes et Pierre-François.

Je remercie Lucile d'avoir accepté le rôle de marraine, et de l'avoir pleinement assumé (de la meilleure manière, en m'invitant régulièrement au restaurant).

Je suis aussi reconnaissant à Laetitia, Romain, Thierry, Monique et Nora pour leur bienveillance et leur efficacité ; avec le recul je suis surpris de la facilité avec laquelle tous les aspects administratifs ont été traités. Merci aussi aux personnes qui se sont succédées au service info et à Bintou et Annick.

Merci aussi à ceux que j'ai eu la chance de rencontrer pendant la thèse, Clément, Félix, Thimothée, Thomas, Irénée, Charlie, Nicola, Malo, Henry, Jan. Ainsi qu'à ceux que j'ai eu plaisir à retrouver ici ou là, Thibault, Félix, Loïc, et tous les collègues d'Orsay.

Enfin, je souhaiterais remercier mes amis et ma famille. Merci
aux amis de Charlotte, à Séverine pour les meilleurs brunchs que j'ai connu, et aux amis de pharmas et Idriss avec qui on a toujours plaisir à partager un verre (ou deux).
aux amis d'Orsay, et affiliés, pour toutes ces soirées, tous ces bons moments,
à Laure, Maël, Margot, JB, Corine et Pierre, pour votre hospitalité sans fin, c'est toujours un plaisir de séjourner à Auzeville (et ailleurs),
aux amis de toujours, que j'ai toujours une grande joie à retrouver, pour votre amitié indéfectible,
à la famille, pour votre générosité, pour votre soutien, et pour ce que vous êtes,
à Charlotte, d'être là, dans la sérénité comme dans l'appréhension, pour tout le bonheur que tu m'as apporté, et que tu continues à me procurer.

Resumé

Dans cette thèse, nous étudions théoriquement différents effets liés à la localisation d'Anderson. Nous nous concentrons sur le contexte des atomes froids, dans lesquels sont simulés des potentiels désordonnés ou des systèmes chaotiques. Ce résumé long en français suit la structure de la thèse en sept chapitres.

Après une introduction à la localisation d'Anderson, présentant à la fois des aspects théoriques et expérimentaux et constituant le chapitre 1, nous présentons une théorie approchée de la distribution d'énergie des nuages atomiques dans les potentiels speckles. Cette étude est menée en deux étapes. La première est présentée dans le chapitre 2, où nous considérons les propriétés statistiques des potentiels optiques de type speckle, en particulier celles des minima d'intensité. Dans le chapitre 3, nous présentons la deuxième partie de l'étude, une méthode de calcul de la fonction spectrale et de la densité d'états, valable dans la limite de désordre fort. En utilisant les résultats obtenus au chapitre 2, nous appliquons cette méthode au cas unidimensionnel.

Dans le chapitre 4, nous caractérisons le mouvement du centre de masse de paquets d'ondes lancés avec une vitesse finie dans un potentiel aléatoire. Cette étude dévoile une manifestation nouvelle et inattendue de la localisation d'Anderson : après un mouvement initial balistique, le centre de masse du paquet présente une rétro-réflexion et revient lentement à sa position initiale. Nous avons nommé ce phénomène l'effet de boomerang quantique. Le cœur du chapitre 4 consiste en une description analytique de l'effet de boomerang quantique en une dimension.

Dans le chapitre 5, les interactions atome-atome sont introduites dans les simulations numériques, au niveau champ moyen (Gross-Pitaevskii). Leur effet sur le phénomène de boomerang quantique est étudié. L'effet des interactions est aussi étudié dans l'étalement en énergie d'ondes planes évoluant dans des potentiels aléatoires tridimensionnels. Enfin, nous discutons la façon dont les interactions affectent le pic de rétro-diffusion cohérente, et, en particulier, nous trouvons, de façon inattendue, une construction incomplète du pique aux temps courts.

Dans le chapitre 6, nous prenons une direction différente et considérons un modèle déterministe (quoique chaotique), le kick rotor. Nous montrons que des modèles de kicks rotors offrent des perspectives intéressantes pour l'étude de localisation d'Anderson. D'une part, avec de fortes motivations expérimentales et théoriques, nous présentons des éléments probants en faveur d'un kick rotor sans spin dans l'ensemble symplectique. D'autre part, le réexamen de kicks rotors modulés quasi-périodiquement, communément étudiés, révèle des résultats intrigants.

Enfin, le chapitre 7 résume nos résultats et donne quelques perspectives pour de futurs travaux.

Introduction

La thèse commence par une introduction à la physique de la localisation d'Anderson. La localisation d'Anderson a été prédite en 1958 par Anderson. Depuis, le sujet a été l'objet de nombreux travaux. Ceci furent aussi bien théoriques qu'expérimentaux. Le sujet est aussi intéressant du point de vue mathématique, des preuves mathématiques de la localisation ont pu être obtenues. Il sera vain d'essayer de rendre compte de tous ces développement dans une thèse.

Concernant les aspects théoriques, nous avons donc choisi de présenter dans les grandes lignes deux théories populaires de la localisation. La première, la théorie auto-cohérente de Vollhard et Wölfle, est une théorie microscopique de la localisation. L'idée est de décomposer la distribution de densité à un point $\boldsymbol{r}$ et à un temps t comme une somme interférentielle de chemins. Parmi ces différents chemins, seuls deux classes sont prises en compte. Le choix de ces deux classes étant basé sur des arguments physiques. La première classe rassemble tous les termes non-interférentiels, c'est le Diffuson, le processus associé est un processus de marche aléatoire, bien décrit par une équation de diffusion aux temps longs et sur des échelles de distance suffisamment grandes. La deuxième classe, appelée Cooperon, correspond à ce qui est communément appelé la localisation faible. Cette contribution interférentielle est en effet responsable d'une réduction du transport associé au Diffuson. La localisation d'Anderson survient quand le Cooperon devient important. C'est le cas en basse dimensions ($d \leq 2$) et à désordre fort en haute dimensions. La théorie auto-cohérente permet de traiter le premier cas, sous une hypothèse de champ moyen. Cette hypothèse empêche la description du cas tridimensionnel, où la présence d'un point critique, s'accompagnant de fluctuations importantes, est incompatible avec le champ moyen. Nous montrons aussi certaines limites de cette théorie en une dimension, par la comparaison avec une théorie exacte, la théorie de Berezinskii. On observe en particulier des déviations à la théorie auto-cohérente dans les ailes de la distribution de densité. Là encore, ces déviations sont associées à des fluctuations importantes, qui violent l'hypothèse de champ moyen.

La théorie d'échelle de la localisation propose une approche différente. Adoptant un point de vue macroscopique, cette dernière consiste à étudier comment la conductance g d'un échantillon varie avec sa longueur. Cette étude est menée à travers une fonction Gell-Mann-Low β, qui encode la variation du logarithme de la conductance avec le logarithme de la taille du système. Cette théorie se base sur deux hypothèses. La première est que la fonction β considérée ne dépend que de la conductance elle-même (d'où le nom de *théorie d'échelle à un paramètre*). La deuxième hypothèse est la continuité et la régularité de la fonction β. La connaissance des régimes asymptotiques (à grand et petit g) clôt le raisonnement. En effet, comment nous le montrons dans la thèse, le comportement qualitatif de la fonction β se déduit directement de ces trois éléments (un seul paramètre pertinent, régularité de la fonction β et connaissance des régimes asymptotiques).

De ce comportement qualitatif, on peut tirer deux informations d'importance : la théorie d'échelle à un paramètre prédit que la localisation prévaut en basse dimensions ($d \leq 2$) et qu'une transition entre localisation et diffusion est attendue en haute dimensions ($d > 2$). En particulier, la possibilité d'une transition en deux dimensions a longtemps était débattue, la prédiction de la théorie d'échelle à un paramètre, en faveur de la localisation de tous les états, est aujourd'hui communément acceptée.

Après ces discussions théoriques, nous donnons dans la thèse un bref compte rendu des nombreux travaux expérimentaux associés à la localisation d'Anderson. Au départ, le sujet s'est développé autour d'expériences de matière condensée. Ces expériences ont donné lieu à de nombreux développements, mais la richesse de la physique de la matière condensée constitue une difficulté quant à l'observation directe de la localisation d'Anderson. En particulier, les interactions électron-électron ou le couplage électron-phonon rendent l'observation de la localisation d'Anderson « pure » très difficile.

Par la suite, de nombreuses expériences ont été réalisées dans le but d'observer la localisation d'Anderson dans des contextes différents. En effet, la localisation d'Anderson est avant tout un phénomène d'interférences, il peut donc être observé à priori avec tout type d'ondes. Ces expériences ont permis l'observation de la localisation d'ondes très variées, parmi lesquelles les micro-ondes, les ondes élastiques, la lumière et les ondes sonores.

Plus récemment, la localisation d'Anderson d'ondes de matière a été observée avec des atomes froids. Les plateformes expérimentales d'atomes froids offrent des possibilités très intéressantes pour l'étude de la localisation. D'une part, ces plateformes offrent un haut niveau de contrôle. En parti-

culier, les interactions inter-atomiques peuvent être maitrisées, et il est possible d'atteindre un faible couplage atome-environnement. D'autre part, les expériences utilisant le couplage lumière-matière permettent l'observation des atomes au sein même du milieu désordonné et de suivre leur évolution.

Ces possibilités clés ont donné lieu à un renouvellement de l'intérêt porté à la localisation d'Anderson. En effet, ces possibilités offrent d'intéressantes perspectives expérimentales et théoriques. Par exemple, les expériences d'atomes froids basés sur un protocole de trempe impose de prendre en compte la distribution d'énergie des atomes (au lieu de considérer uniquement l'énergie de Fermi).

L'introduction se termine par une discussion de l'effet des interactions sur la localisation d'Anderson. Deux grandes lignes de recherche sont distinguées. En premier lieu est discuté l'effet des interactions au niveau champ moyen, où de nombreux scénarios ont été étudiés. Ce point de vue, adopté par la suite dans le chapitre 5 de la thèse, est contrasté par une courte discussion sur la localisation à N corps. Cette thématique de recherche explore la possibilité d'étendre la localisation d'Anderson à des problèmes à N corps, pour lesquels la localisation est prédite dans l'espace de Fock.

Propriétés statistiques des potentiels speckles

Le deuxième chapitre de la thèse concerne les propriétés statistiques des potentiels speckles. Le chapitre commence par une introduction à la physique des atomes froids.

Dans les expériences d'atomes froids, on utilise l'interaction entre les atomes et un rayonnement lumineux monochromatique pour induire un potentiel effectif. En pratique, sous certaines conditions, la dynamique des atomes plongés dans le rayonnement peut être décrite par une dynamique hamiltonienne, dans laquelle le potentiel extérieur est proportionnel à l'intensité lumineuse. Dans une première section de ce chapitre, nous montrons comment l'on dérive cette évolution hamiltonienne.

La dynamique des atomes plongés dans le rayonnement est bien décrite par une approximation semi-classique où les atomes sont traités quantiquement et le champ électrique composant le rayonnement est traité classiquement. Sous l'approximation d'un atome à deux niveaux, l'hamiltonien de l'atome est alors composé de trois termes. Le premier est associé à l'énergie cinétique de l'atome, le deuxième à l'interaction dipolaire entre l'atome et le rayonnement et le troisième est consacré à l'état interne de l'atome. A partir de cet Hamiltonien, on peut calculer l'équation d'évolution de l'opérateur densité. Sous l'hypothèse d'un faible nombre d'atomes excités, l'équation pour la projection de l'opérateur densité sur l'état interne fondamental est fermée. Il suffit alors d'intégrer le mouvement sur les micro-oscillations du centre de masse de l'atome pour obtenir qu'en effet, la dynamique de l'atome à deux niveaux se réduit à une dynamique hamiltonienne, et on trouve que le potentiel extérieur est proportionnel à l'intensité lumineuse.

A partir de ces résultats, on se rend compte que créer un potentiel désordonné se réduit à générer un profil d'intensité lumineuse désordonné. Celui ci est généralement obtenu expérimentalement en transmettant un laser à travers une plaque rugueuse. Dans la thèse, nous discutons cette possibilité. Nous introduisons le schéma expérimental correspondant et décrivons le profil d'intensité ainsi obtenu. Cette dernière étape consiste en l'expression du champ complexe en un point donné comme la superposition du champ diffusé par chaque morceau de la plaque rugueuse (principe de Huygens-Fresnel). Il s'en suit, par le théorème de la limite centrale, que le champ complexe a une statistique gaussienne, dont on déduit la statistique du potentiel résultant comme étant exponentielle. On considère ensuite les corrélations spatiales du potentiel résultant. Celles ci se trouvent liés à la transformée de Fourier de la distribution d'intensité au sein de la plaque rugueuse. Les corrélations peuvent ainsi être contrôlées par l'application de masques sur la plaque rugueuse.

Dans une troisième partie du chapitre, nous considérons des propriétés plus spécifiques des potentiels speckles, celles des minima d'intensité. Plus précisément, nous nous intéressons à la distribution jointe de la profondeur et de la courbure des dits minima d'intensité. Le calcul de la distribution jointe se fait, en suivant Goodman, par l'introduction du champ complexe, dont le potentiel est le module carré. Comme nous l'avons vu, ce champ complexe est gaussien. A partir de ce champ complexe et de ses dérivées, elles aussi gaussienne, on obtient la distribution recherchée par changement de variable. Cette distribution a trois propriétés remarquables, importantes pour la suite de la thèse. Premièrement elles présentent une très faible probabilité de trouver un minima dont la courbure est faible. Cette dernière a au contraire tendance à prendre une valeur typique, donnée dans la thèse en terme des propriétés du potentiel. La dernière propriété remarquable est la présence de la plupart des minima à basses énergies.

Fonction spectrale et densité d'états semi-classiques dans les potentiels speckles

Dans ce chapitre, on s'intéresse aux propriétés spectrales des atomes dans les potentiels de type speckle. Ces propriétés sont très importantes dans le contexte des expériences d'atomes froids. En effet, la procédure de trempe, généralement utilisée dans ce type d'expérience, peuple toute une distribution d'énergie. Les quantités physiques (libre parcours moyen, longueur de localisation, ...) dépendant de l'énergie, la dynamique totale résulte de la superposition des composantes d'énergie du paquet d'ondes.

Dans une première partie de ce chapitre, nous considérons la limite de désordre faible, où des calculs perturbatifs sont possibles. On choisit pour mener à bien ces calculs d'introduire le formalisme des fonctions de Green. A cet effet, on introduit d'abord formellement la fonction de Green, puis son développement perturbatif associé. Nous introduisons ensuite le concept de self-énergie, d'abord comme une simplification du développement perturbatif de la fonction de Green. Nous discutons ensuite son sens physique : la partie réelle déplace l'énergie alors que la partie imaginaire donne un temps de vie. Par la suite, nous discutons le sens à donner à la terminologie "désordre faible", en particulier dans le cas des potentiels de type speckle. Finalement, nous introduisons la fonction spectrale, la distribution d'énergie moyenne des ondes planes dans le potentiel désordonné.

Dans une deuxième partie du chapitre, nous motivons l'étude de la fonction spectrale. Sa connaissance est en effet primordiale pour décrire la distribution d'énergie de paquets d'ondes arbitraires. Et la distribution d'énergie joue un rôle très important. Nous donnons quelques exemples pour lesquels la distribution d'énergie joue un rôle crucial.

Dans un premier temps, nous considérons une situation réalisée expérimentalement, où un paquet d'ondes initialement étroit évolue dans un potentiel speckle unidimensionnel. Ce speckle a une caractéristique intrigante : à faible désordre, le coefficient de diffusion est fortement énergie-dépendent, présentant des changements brusques lorsque l'énergie dépasse des valeurs spécifiques. L'évolution totale, intégrée sur toute les composantes d'énergies du paquet d'ondes, peut donc différer de l'évolution d'une composante énergétique individuelle. En effet, à grande distance, la localisation exponentielle (habituellement attendue) est transformée en une localisation algébrique.

À l'inverse, un paquet d'ondes composé uniquement d'atomes diffusifs peut apparaître proche de localisé en raison de la fonction spectrale. En effet, même si pour une énergie donnée, le noyau est diffusif, l'évolution totale peut apparaître sous-diffusive en raison de la dépendance énergétique spécifique du coefficient de diffusion. L'évolution totale dans ce cas ressemble à la situation où une seule composante d'énergie avec un noyau sous-diffusif est en jeu, imitant ainsi l'apparition de la localisation d'Anderson.

La connaissance précise de la distribution d'énergie est également nécessaire pour la caractérisation de la transition d'Anderson en trois dimensions. En effet, dans ce cas, les composantes d'énergie se répartissent des deux côtés du seuil de mobilité, la dynamique complète est alors une superposition de comportements localisés et diffusifs. La connaissance de la distribution d'énergie est nécessaire pour extraire des quantités physiquement pertinentes (par exemple la position du seuil de mobilité).

La troisième partie du chapitre est consacrée à la limite de désordre fort. Comme on le montre dans la thèse, cette limite est bien décrite par des approximations semi-classiques. Nous commençons par la limite classique, en négligeant la non-commutativité de $\boldsymbol{p}$ et $\boldsymbol{r}$. Nous comparons le résultat ainsi obtenu à des simulations numériques exactes pour trois distributions de potentiel différentes : la distribution gaussienne, la distribution speckle rouge et la distribution speckle bleu. On trouve que pour la distribution gaussienne, la fonction spectrale est bien décrite par sa limite classique. Le cas d'une distribution speckle est plus délicat, en particulier proche de sa discontinuité où la limite classique est complètement fausse.

Pour aller plus loin, on propose une expansion en puissance de $\hbar$ de l'opérateur d'évolution, à partir de laquelle on déduit des corrections systématiques à la limite classique de la fonction spectrale. Cette méthode présente deux étapes principales, dans une premier temps une expansion en commutateur de l'opérateur d'évolution est présentée. A partir de cette expansion, la moyenne sur le désordre est calculée par une expansion en cumulant. Cette dernière s'appuie sur la représentation du potentiel speckle comme le module carré d'un champ complexe, ainsi d'un théorème de Leonov et Shiryaev, qui permet de mener à bien le calcul. Cette technique nous permet de calculer une correction au premier ordre non nul en $\hbar$ de la fonction spectrale. Cette correction affine la description de la fonction spectrale dans le cas du potentiel gaussien et des potentiels speckle loin de leur discontinuité. La problème proche de la discontinuité des potentiels speckles demeure.

Pour calculer la fonction spectrale des potentiels speckles proche de leur discontinuité, nous développons une nouvelle approche semi-classique, cette fois ci basée sur une approximation de phase stationnaire. Il apparait qu'à l'approximation de phase stationnaire et aux énergies d'intérêts (pour lesquelles l'approche précédente ne suffit pas), il est possible d'approximer le potentiel speckle par des oscillateurs harmoniques (inversés) isolés. En utilisant les propriétés statistiques des potentiels speckles calculées dans le chapitre 2, on arrive à une très bonne description de la fonction spectrale proche des discontinuités des potentiels speckles.

En connectant les deux méthodes, une description satisfaisante de l'ensemble du spectre énergétique est possible. Notre description semi-classique fournit en outre une interprétation physique de caractéristiques intrigantes de la fonction spectrale. En particulier, pour le potentiel speckle bleu, nous avons montré que le pique de la fonction spectrale à faible énergie est essentiellement associé à l'état fondamental d'un atome dans un puits de potentiel, alors que la bosse secondaire est associée aux états excités. Nous avons également souligné qu'en dépit de leur symétrie, speckle rouge et bleu ont des caractéristiques remarquablement différentes dans le régime semi-classique, venant de la nature des trajectoires classiques impliquées aux énergie proche de zéro : pour le potentiel bleu, ces trajectoires classiques se trouvent dans des puits potentiels profonds, alors que pour le potentiel rouge, elles sont au voisinage du sommet de puits inversés.

Ce travail a donné lieu à une publication dans Physical Review A.

Une suite logique de ce travail serait de considérer le cas tridimensionnel, impliqué dans des questions importantes liées à la localisation d'Anderson. Cette tâche semble cependant difficile, en raison de l'existence de courbes le long desquelles le potentiel est nul, rendant l'application de la méthode développée dans cette thèse moins évidente.

Effet de boomerang quantique

Dans ce chapitre, on s'intéresse à une situation proche de l'expérience réalisée en 2008 à Palaiseau. Dans cette expérience, un paquet d'ondes étroit est lâché dans un potentiel désordonné et l'évolution de son profil de densité est enregistrée au cours du temps. Nous proposons de reproduire la même expérience, en donnant en plus une vitesse initiale. Dans la thèse, nous donnons une description analytique et numérique complète du mouvement du centre de masse du paquet d'ondes en une dimension.

Dans un premier temps, on considère une approche classique du problème. Celle-ci utilise le théorème d'Ehrenfest pour relier le centre de masse à la vitesse moyenne. La dynamique de la vitesse moyenne est ensuite décrite par deux équations de Boltzmann couplées. La solution de ces équations prédit un mouvement du centre de masse relativement simple : après un mouvement balistique, le centre de masse sature au libre parcours moyen. Ceci s'interprète très simplement par l'isotropisation de la distribution de vitesse aux temps courts. Une fois la distribution de vitesse isotrope, il n'y a plus de mouvement du centre de masse, celui reste à un libre parcours moyen, qu'il a parcouru avant que la distribution de vitesse ne devienne isotrope.

Nous présentons dans un deuxième temps une approche numérique permettant de simuler efficacement ce problème. Cette méthode utilise les polynômes de Chebyshev pour obtenir une représentation de l'opérateur d'évolution bien appropriée à une implémentation numérique. Nous donnons quelques détails sur cette méthode et sur son implémentation. Elle est ensuite utilisée pour simuler le mouvement du paquet d'ondes initialement doté d'une vitesse initiale. On trouve que, au lieu de saturer au libre parcours moyen comme attendu, le centre de masse, après son mouvement balistique, retourne lentement à l'origine. Nous appelons cet effet l'effet de Boomerang quantique.

Dans un troisième temps, nous apportons une preuve simple de l'effet de Boomerang quantique, utilisant une expansion en modes du paquet d'ondes. Cette démonstration donne la forme finale du paquet d'ondes, parfaitement symétrique par rapport à l'origine. En étudiant numériquement la dynamique du paquet d'ondes, on observe que celui-ci subit en effet une symétrisation gauche-droite au cours du temps. Plutôt qu'à un mouvement rigide et global du paquet d'ondes, l'effet de Boomerang quantique est en fait associé à cette symétrisation.

Pour aller plus loin, et calculer le centre de masse aux temps finis, nous utilisons une technique diagrammatique. Cette technique, exacte dans la limite de désordre faible, a été introduite par Berezinskii en 1973. Dans un premier temps, nous relions le centre de masse au produit de deux fonctions de Green, ce qui nous permet d'utiliser la technique de Berezinskii pour calculer le centre de masse.

La technique de Berezinskii est basée sur une expansion perturbative du produit des deux fonctions de Green, qui est ensuite resommée, permettant ainsi une description non perturbative. L'expansion perturbative est exprimée en termes de diagrammes, eux même constitués de vertex reliés par des lignes. Pour effectuer la resommation de ses diagrammes, un point clé est la possibilité, en une dimension, d'inclure les facteurs associés aux lignes dans les vertex. Un diagramme est ainsi le produit des facteurs associés à ses vertex. Les lignes se réduisent à des contraintes dans le choix des vertex. A partir de cette représentation en termes de vertex, il est possible de calculer les diagrammes en étudiant comment ceci changent lorsque le point initial et le point final sont déplacés. On déduit de ce raisonnement des équations pour le centre de masse.

Ces équations demeurent compliquées, leur solution générale n'est pas connue. Une possibilité est alors de les résoudre aux temps longs, ce qui simplifie la tache et rend possible l'obtention du retour asymptotique du paquet d'ondes à l'origine. Ce résultat est en très bon accord avec nos simulations

numériques aux temps longs. Pour aller plus loin, et décrire le centre de masse à tout temps, nous avons développé une nouvelle méthode de résolution des équations de Berezinskii. En effet, nous avons montré qu'il est possible de résoudre ces équations sous la forme d'une expansion de Taylor. Cette dernière peut être calculée de façon systématique à l'aide d'un ordinateur. En calculant les 100 premiers termes de l'expansion de Taylor, on se rend vite compte que la série correspondante à un rayon de convergence fini (que nous estimons à quatre temps de diffusion). Il est cependant possible de dépasser cette limite par une resommation de Padé. Cette dernière offre une excellente description du centre masse à tout temps, même quand l'approximant de Padé est d'ordre relativement bas.

La méthode de Berezinskii développée dans ce chapitre est en principe limitée au cas d'un potentiel gaussien non corrélé. Nous argumentons dans la thèse que le centre de masse suit la même courbe pour des potentiels non-gaussien et corrélés. Ses arguments sont confirmés par des simulations numériques qui montrent que le centre de masse est indépendant de la distribution du potentiel.

Pour finir, nous montrons qu'une relation simple relie le centre de masse et la largeur du paquet d'ondes. Cette relation se trouve être à la base de notre calcul du mouvement du centre de masse.

Ces travaux ont donné lieu à la rédaction d'une lettre soumise à Physical Review Letters.

Le raisonnement présenté dans la thèse et expliquant l'effet de boomerang quantique en termes de modes localisés réels s'applique en dimension quelconque. L'effet de boomerang quantique est donc attendu également en dimensions supérieures, à condition que la dynamique soit localisée. Ceci offre des perspectives intéressantes pour de futurs travaux. Par exemple, en prolongement de travaux récents sur le pique de rétro-diffusion, il serait très intéressant d'effectuer une analyse numérique fine de l'effet de boomerang quantique en trois dimensions. Une autre piste de recherche intéressante serait de chercher des phénomènes similaires dans d'autres classes de symétrie (par exemple dans la classe unitaire où la compréhension qualitative de l'effet de boomerang quantique en termes de modes localisés réel ne s'applique pas).

Paquets d'ondes interagissant faiblement

Dans ce chapitre, on prend en compte les interactions atome-atome. On se place dans le contexte des gaz dilués de bosons condensés, qui décrit bien les expériences mises en œuvre à Palaiseau et Florence.

Dans une première partie, nous donnons une dérivation simple de l'équation de Gross-Pitaevskii. Cette dernière décrit l'évolution de la fonction d'onde du condensat. Cette description néglige les atomes non-condensés, et la possibilité pour les atomes de sortir du condensat. Néanmoins, l'équation de Gross-Pitaevskii explique très bien de nombreux résultats expérimentaux.

Fort de cette simplification, nous introduisons ensuite, dans une deuxième partie, un méthode numérique permettant de simuler l'évolution du gaz de bosons, régit par l'équation de Gross-Pitaevskii. Cette méthode s'appuie sur la méthode développée au chapitre précédent pour intégrer numériquement l'équation de Schrödinger. Nous montrons que l'inclusion de la non-linéarité revient à ajouter des phases avant et après l'application de la méthode linéaire. Cette méthode est asymptotiquement exacte quand le temps est infiniment discrétisé. En pratique, on peut s'appuyer sur le fait que l'erreur à temps fixé décroit comme le carré du pas en temps. Cette méthode est particulièrement adaptée à la limite de faibles interactions. Elle permet en effet de traiter efficacement la partie linéaire de l'équation de Gross-Pitaevskii, de faible interactions n'imposant que des pas temporels raisonnables.

Il reste néanmoins que l'on souhaite atteindre des temps relativement longs dans nos simulations numériques. Nous souhaitons en effet accéder à des régimes de temps où la non-linéarité se fait sentir. Pour cette raison, nous adoptons dans certaines sections un modèle réseau, plus facile à simuler numériquement. On notera que dans la limite linéaire et concernant la localisation d'Anderson, il n'y a essentiellement pas de différence entre la physique des réseaux et celle du continu. On peut donc espérer décrire, au moins qualitativement, la physique du continu.

Pour valider notre méthode numérique, nous considérons une situation qui a fait l'objet de nombreuses études. Elle consiste à placer un paquet d'ondes à un point d'un réseau désordonné et à le laisser l'étaler. On observe alors que la non-linéarité vient perturber la localisation d'Anderson, qui prédit une saturation de l'étalement. En effet, une dynamique sous-diffusive est attendue. Nous observons bien ce comportement sous-diffusif dans nos simulations avec un exposant de sous-diffusion en accord avec de précédents travaux.

Dans une troisième partie, nous nous tournons alors vers un problème nouveau, celui de l'effet de la non-linéarité sur l'effet de boomerang quantique. Nous étudions cette situation numériquement, et observons que la non-linéarité à l'air d'interrompre l'effet de boomerang quantique. Le boomerang quantique non-linéaire semble ne pas revenir à l'origine.

Pour comprendre un peu mieux ce phénomène, nous le comparons à un phénomène de décohérence. Ce dernier est étudié numériquement par l'introduction dans les simulations numérique d'un potentiel désordonné supplémentaire, dont l'amplitude varie dans le temps. Pour effectuer ces simulations, on utilise la même méthode numérique que pour le cas non-linéaire. On trouve que de façon surprenante, il est possible de reproduire presque à l'identique les courbes du mouvement du centre de masse non-linéaire avec ce modèle de décohérence. Ce résultat suggère que la non-linéarité agit ici comme une source de décohérence. On peut alors associer à la non-linéarité un temps de décohérence. Ce dernier est obtenu en considérant la diffusion associé au modèle de décohérence dont le mouvement du centre de masse reproduit celui obtenu avec l'équation de Gross-Pitaevskii.

On trouve alors qu'à la non-linéarité est associée un temps de décohérence inversement proportionnel à la force de la non-linéarité.

Dans une quatrième partie, nous considérons la dynamique de la distribution d'énergie du paquet d'ondes. En effet, contrairement au cas linéaire pour lequel la distribution d'énergie n'évolue pas, la non-linéarité est susceptible d'induire des collisions inélastiques et donc un changement de la distribution d'énergie.

Nous commençons cette partie par un réexamen du problème de l'étalement du paquet d'ondes, qui montre l'importance de la dynamique de la distribution d'énergie. En effet, nous faisons une expérience numérique relativement simple, qui consiste à comparer deux scénarios très proches. Dans les deux cas, nous considérons l'étalement d'un paquet d'ondes, simplement dans le premier cas l'énergie initiale du paquet d'ondes se trouve à un endroit arbitraire du spectre alors que dans le second cas, l'énergie du paquet d'ondes est choisie telle qu'elle corresponde à l'énergie pour laquelle la longueur de localisation est maximale. En effet, si dans le premier cas le paquet d'ondes est susceptible d'explorer des régions du spectre d'énergie où la longueur de localisation est grande, dans le second cas, le paquet d'ondes ne peut qu'explorer des régions où la longueur de localisation est relativement petite. Les simulations numériques révèlent que cette différence est fondamentale, avec un transport beaucoup moins efficace dans le cas où le paquet d'ondes est dès le départ au maximum de la longueur de localisation.

Bien que les simulations du paragraphe précédent soient faite en une dimension, nous considérons ensuite le cas tridimensionnel, plus simple en ce qu'il permet de négliger les effets de localisation. La dynamique de la distribution d'énergie peut alors être calculée. Nous comparons ce calcul à des simulations numériques, et trouvons un bon accord. Nous pouvons alors conclure que la distribution d'énergie évolue sur un temps caractéristique proportionnel au carré de l'inverse de la force de la

non-linéarité.

Nous observons cependant dans les simulations numériques une dynamique de la distribution d'énergie sur une échelle de temps beaucoup plus courte, celle du temps de diffusion. Nous attribuons cette dynamique à deux effets de temps courts, liés à la dynamique du paquet d'ondes sur cette échelle de temps.

Nous considérons finalement dans une dernière partie l'effet des interactions sur le pique de rétro-diffusion cohérente. De la même façon que pour la distribution d'énergie, les simulations révèlent deux temps caractéristiques. En premier lieu, aux temps courts (de l'ordre du temps de diffusion), on observe une construction incomplète du pique de rétro-diffusion cohérente. Ensuite, sur des temps plus longs, l'amplitude du pique diminue. Nous postulons que ces deux effets sont liés aux deux effets observés sur la distribution d'énergie.

Bien que nous ayons souligné les mécanismes physiques à l'œuvre, notre travail a été essentiellement numérique. Une caractérisation analytique des effets introduits dans ce chapitre devrait permettre d'affiner leur compréhension et offre des perspectives intéressantes pour de futurs travaux.

Le kick rotor, un simulateur paradigmatique de la localisation d'Anderson

Dans ce chapitre, nous changeons quelque peu de thématique. Nous considérons différentes variantes de kicks rotors, qui sont des modèles déterministes. La dynamique classique de ces modèles est cependant généralement chaotique, et leur dynamique quantique essentiellement identique à celle de modèles désordonnés.

Ce chapitre s'ouvre par une section d'introduction à la physique du kick rotor. Nous y discutons notamment les réalisations expérimentales avec des atomes froids, et introduisons quelques définitions utiles pour la suite.

Ensuite, dans une deuxième section, on introduit le concept des propriétés spectrales universelles et les ensemble de matrices aléatoires de Dyson. Nous discutons notamment du rôle central joué par les symétries par renversement du temps. Ainsi, nous introduisons les trois ensembles de Dyson, par une brève dérivation des propriétés statistiques de matrices invariantes par renversement du temps. Nous montrons notamment que les matrices appartenant à l'ensemble symplectique sont caractérisées par une dégénérescence de Kramers.

Nous donnons ensuite les formes approximées (Wigner surmise) des distributions d'espacement de niveau dans chacun des trois ensembles. Suite à quoi, nous discutons du rôle des symétries par renversement du temps pour les opérateurs de Floquet. Nous discutons aussi du lien entre les ensembles de Dyson et les classes d'universalité des systèmes désordonnés.

Après ces parties introductives, nous examinons la possibilité qu'un kick rotor sans spin soit dans la classe symplectique. On notera qu'il est communément accepté qu'une telle possibilité est exclue.

Pour trouver un kick rotor sans spin dans la classe symplectique, nous proposons de réfléchir autour du phénomène de localisation faible. Ce dernier se manifeste en effet très différemment dans la classe symplectique puisqu'il est transformé en *anti-localisation*. L'idée est alors de changer le signe de la localisation faible. Comme nous le montrons dans la thèse, ceci est possible par introduction d'un potentiel discontinu et d'une alternance de deux kicks d'amplitude différentes. Comme nous le montrons dans la thèse, ce modèle reproduit bien les signatures de l'*anti-localisation*, pourvu que la discontinuité soit placée le long d'une direction supplémentaire, composée d'un petit nombre de

sites.

Pour aller plus loin, on se tourne vers les propriétés spectrales introduites dans la section précédente. On retrouve les caractéristiques de l'ensemble symplectique, avec la présence de la dégénérescence de Kramers et la statistique des espacements de niveaux attendue dans cet ensemble. Nous montrons ensuite, qu'en effet, l'opérateur de Floquet commute avec un opérateur de renversement du temps, et que ce dernier est de carré -1.

Pour aller plus loin, nous proposons de considérer le cas tridimensionnel, par l'introduction de fréquences incommensurables. Cette astuce, permettant de simuler des problèmes désordonnés de dimensions entières arbitraires à l'aide de kicks rotors modulés dans le temps, n'a jusque là été appliquée qu'à des systèmes appartenant à la classe orthogonal. Avant de se lancer dans l'étude du modèle sans spin supposé symplectique, nous vérifions que l'astuce s'applique aussi au cas symplectique. Nous effectuons à cet effet des simulations numériques de kick rotor avec spin. Les résultats suggèrent que cette astuce ne s'applique pas dans la classe symplectique, l'exposant critique observé est en effet distinct de celui attendu pour un modèle désordonné équivalent. Nous sommes donc forcés de reporter l'étude du modèle sans spin supposé symplectique.

Pour essayer de comprendre pourquoi l'astuce usuelle, consistant à moduler l'amplitude des kicks par des produits de fonctions trigonométriques pour simuler des dimensions supplémentaires, ne fonctionne pas dans la classe symplectique, nous nous sommes intéressés à une nouvelle modulation. Plus précisément, nous avons essayé d'identifier les propriétés importantes des séquences issues de produits de fonctions trigonométriques pour simuler des problèmes désordonnés en dimensions non entière. Mise à part la compréhension des kicks rotors modulés, cette étude est aussi motivée par les perspectives intéressantes offertes par la simulation de problèmes désordonnés en dimensions non entières, telle que l'identification de la dimension critique inférieure dans l'ensemble symplectique (prédite strictement supérieur à 1 et strictement inférieur à 2) et d'explorer les conséquences de cette dimension critique inférieure non entière.

A cet effet, nous avons proposé une nouvelle séquence quasi-périodique. Cette dernière est obtenue de façon relativement similaire à la technique habituelle consistant à échantillonner des produits de fonctions trigonométriques. Plus précisément, nous proposons une fonction dont l'échantillonnage pour des arguments entiers génère une série quasi-périodique.

Les résultats sont surprenants, avec différents régimes de sous-diffusion dépendant de l'amplitude des kicks. Bien que l'objectif de simuler des problèmes désordonnés en dimensions non entières ne soit pas atteint, nous pensons que les résultats sont prometteurs.

Finalement, nous avons montré que le kick rotor constitue une excellente plate-forme pour caractériser divers aspects de la localisation d'Anderson, et avons identifié trois directions de recherche prometteuses pour de futurs travaux. Tout d'abord, défiant une hypothèse communément acceptée, nous avons présenté des éléments probants en faveur d'un kick rotor sans spin dans la classe symplectique. Deuxièmement, nous avons observé que l'astuce des séquences quasi périodiques de Casati *et al.* semble échouer dans la classe symplectique. Troisième, nous avons exploré la possibilité d'utiliser de nouveaux types de séquences quasi-périodiques. Nous pensons que notre étude préliminaire dans cette direction montre des résultats prometteurs et ouvre des perspectives passionnantes pour de futurs travaux.

Abstract

This thesis theoretically investigates several effects related to Anderson localization, focusing on the context of disordered and chaotic cold-atomic systems.

In cold-atomic systems, optical speckle patterns are often used to create the disorder. The resulting potentials felt by the atoms differ from Gaussian random potentials, commonly assumed in the description of condensed-matter systems. In the first part of the thesis, we discuss their specificities, with an emphasis on the spectral properties of atoms in such potentials. In particular, we derive several approximations for the spectral function.

Atom-optics experiments offer interesting possibilities, such as the possibility to directly probe the atoms inside the disordered potential. In view of these possibilities, we consider in the second part of the thesis the spreading of matter wave packets initially launched with a non-zero velocity. We find that after an initial ballistic motion, the packet center-of-mass experiences a retroreflection and slowly returns to its initial position, mimicking a boomerang. We show that this unexpected quantum boomerang effect is a consequence of Anderson localization, and describe it both numerically and analytically in dimension 1.

Atom-atom interactions are then introduced in a third part. We consider dilute condensed bosonic gases, and treat the interactions at the mean-field (Gross-Pitaevskii) level. Various situations are studied numerically, in particular the quantum boomerang scenario, and the dynamical spreading – both in momentum and energy – of matter waves prepared as plane waves.

In the last part, we show that chaotic models offer interesting prospects for the study of Anderson localization. On the one hand, going against common wisdom, we present strong evidences in favor of a spinless kicked rotor in the sympletic ensemble. On the other hand, a second look at a commonly studied quasi-periodically modulated kicked rotor reveals intriguing results.

Contents

1 Introduction **1**
- 1.1 From weak to strong localization: the self-consistent approach . . . 1
  - 1.1.1 Weak localization . . . 1
  - 1.1.2 Strong localization: the self-consistent approach . . . 3
- 1.2 Berezinskii diagrammatic technique . . . 3
- 1.3 Scaling theory of localization . . . 4
- 1.4 Experimental observations of Anderson localization . . . 6
  - 1.4.1 Early condensed-matter experiments . . . 6
  - 1.4.2 A wave phenomenon . . . 6
- 1.5 Anderson localization and interactions . . . 7
  - 1.5.1 Mean-field effects . . . 7
  - 1.5.2 Many-body effects . . . 8
- 1.6 Outline of the thesis . . . 8

2 Statistical properties of speckle patterns **9**
- 2.1 Dipolar potential for cold-atoms . . . 9
  - 2.1.1 Dipolar atom-laser interaction . . . 9
  - 2.1.2 Dipolar potential . . . 10
  - 2.1.3 Taking advantage of absorption or complex internal structures . . . 12
- 2.2 Speckle patterns: generalities . . . 12
  - 2.2.1 Fresnel integral . . . 13
  - 2.2.2 On-site intensity distribution . . . 14
  - 2.2.3 Correlation functions . . . 14
  - 2.2.4 Numerical implementation . . . 15
- 2.3 Statistics of intensity minima . . . 16
  - 2.3.1 Joint distribution $P(V,\omega)$ . . . 17
  - 2.3.2 Density of minima . . . 19
  - 2.3.3 Two-dimensional case . . . 20
- 2.4 Conclusion . . . 20

3 Semiclassical spectral function and density of states in speckle optical potentials **21**
- 3.1 Weak disorder, perturbative calculations . . . 21
  - 3.1.1 Perturbative treatment with Green functions . . . 22
  - 3.1.2 The self-energy . . . 23
  - 3.1.3 Scattering mean free time and scattering mean free path . . . 24
  - 3.1.4 The spectral function . . . 25
- 3.2 Importance of the spectral function in the dynamics of cold-atoms in random potentials 26
- 3.3 Strong disorder, semiclassical regime . . . 27
  - 3.3.1 Definitions and methods . . . 28
  - 3.3.2 Smooth quantum corrections . . . 29

3.3.3 Treatment of low energies . . . 32
3.3.4 Spectral function and density of states in one dimension: results . . . 35
3.3.5 Validity of the harmonic-oscillator approximation . . . 37
3.3.6 Validity of the inverted harmonic-oscillator approximation . . . 37
3.3.7 Higher dimensions . . . 38
3.4 Conclusion . . . 38
3.5 Article: *Semiclassical spectral function and density of states in speckle potentials* . . . 39

4 Quantum boomerang effect in one-dimensional random potentials 57
4.1 Initial condition . . . 57
4.2 Classical approach . . . 58
4.3 Numerical solution . . . 59
4.3.1 Chebyshev polynomials . . . 60
4.3.2 Expansion of the evolution operator over Chebyshev polynomials . . . 60
4.3.3 Practical implementation . . . 61
4.3.4 Results for $\langle x \rangle$ . . . 61
4.4 Convergence of the density to its infinite-time limit . . . 62
4.5 Center-of-mass motion from Berezinskii diagrammatic technique . . . 64
4.5.1 Center of mass in terms of Green functions . . . 64
4.5.2 Diagrammatics . . . 64
4.5.3 Equations for the center of mass . . . 69
4.5.4 Results . . . 73
4.6 General case . . . 73
4.6.1 Case of a non-Gaussian potential . . . 73
4.6.2 Case of a correlated potential . . . 74
4.6.3 Case of a broad initial wave packet . . . 75
4.7 A simple relation between $\langle x \rangle$ and $\langle x^2 \rangle$ . . . 76
4.8 Conclusion . . . 77
4.9 Article: *When Anderson localization makes quantum particles move backward* . . . 78
Appendix 4.A Solution of Berezinskii equations at long times . . . 84
Appendix 4.B Solution of Berezinskii equations from short times . . . 86

5 Weakly interacting wave packets 91
5.1 Bose-Einstein condensates in random potentials . . . 91
5.1.1 Many-body Hamiltonian . . . 91
5.1.2 Bogoliubov approximation . . . 92
5.1.3 Two-body low energy collisions and scattering potential . . . 92
5.1.4 Comments on the Gross-Pitaevskii equation . . . 93
5.2 Numerical integration of the Gross-Pitaevskii equation . . . 93
5.2.1 Numerical scheme and error estimate . . . 93
5.2.2 In practice . . . 94
5.2.3 Nonlinearity and spreading . . . 95
5.3 Nonlinear quantum boomerang . . . 96
5.3.1 Numerical experiment . . . 96
5.3.2 Comparison with decoherence . . . 97
5.4 Nonlinearity and energy distribution . . . 98
5.4.1 Motivations: a second look at spreading . . . 98
5.4.2 Numerical study of the energy distribution dynamics . . . 100
5.4.3 Short-time ($t \approx \tau$) picture: shifting and screening . . . 101
5.4.4 Intermediate-time picture: kinetic equation . . . 102

5.4.5 Density of states . . . 103
5.4.6 Comparison with numerics . . . 103
5.4.7 Infinite-time equilibrium . . . 104
5.5 Nonlinearity and the coherent back scattering peak . . . 105
5.5.1 Coherent back scattering peak . . . 105
5.5.2 Numerics . . . 106
5.5.3 Physical picture . . . 106
5.6 Conclusion . . . 107
Appendix 5.A Approximations of the density of states . . . 108
5.A.1 Density of states in term of self-energy . . . 108
5.A.2 Approximations of the self-energy . . . 109

6 The kicked rotor, a paradigmatic simulator for Anderson localization 111
6.1 From chaos to disorder . . . 111
6.1.1 Classical chaotic dynamics . . . 112
6.1.2 Quantum evolution: Floquet operator . . . 112
6.1.3 Quantum evolution: pseudo-random kicked rotor . . . 113
6.1.4 From classical diffusion to localization . . . 113
6.2 Universality classes and random matrix theory . . . 114
6.2.1 From a perturbative perspective . . . 114
6.2.2 Universal properties and random matrix theory . . . 115
6.2.3 Time reversal symmetry for Floquet models . . . 118
6.2.4 Critical exponents . . . 119
6.3 A spinless kicked rotor in the symplectic class? . . . 119
6.3.1 Weak antilocalization . . . 119
6.3.2 Eigenvalue statistics . . . 122
6.3.3 Time-reversal invariance . . . 124
6.3.4 Conclusion . . . 125
6.4 From incommensurate frequencies to higher dimensions . . . 125
6.4.1 Generalities . . . 125
6.4.2 Incommensurate frequencies in the symplectic class . . . 126
6.4.3 Beyond the incommensurate frequencies . . . 127
6.5 Conclusion . . . 130

7 Conclusion 133

Chapter 1

Introduction

Anderson localization, the absence of wave diffusion due to destructive interference between partial waves multiply scattered by a disordered potential, was predicted theoretically in 1958 [1]. Anderson formulated the problem of localization under the form of a perturbative expansion, for which he was able to derive a convergence criterion and thus a condition for localization to occur. Later on, various theories of Anderson localization emerged. The subject is also of interest to mathematicians, who were able to give mathematically rigorous proofs of localization [2].

In this chapter, we introduce several descriptions of Anderson localization that will be useful in the rest of the thesis. We start with the self-consistent theory of localization in section 1.1. This theory will allow us to gain intuition on the phenomenon of Anderson localization, and to introduce some important concepts. The self-consistent theory, which is a kind of mean-field approximation, is then compared with a more rigorous approach in one-dimension, Berezinskii diagrammatic technique, in section 1.2. The scaling theory of localization is then introduced in section 1.3. By adopting a macroscopic point of view, the latter offers a different perspective on Anderson localization.

Anderson localization has been experimentally observed in various contexts. In section 1.4, we give a brief account of these experimental developments, and discuss the specificities of cold-atom platforms in the field of Anderson localization. In section 1.5, we briefly discuss the role of interactions, often unavoidable in experiments.

We conclude this chapter with an outline of the thesis in section 1.6.

1.1 From weak to strong localization: the self-consistent approach

1.1.1 Weak localization

In this section, we present an intuitive picture of Anderson localization. To that end, we assume that a particle is initially placed at some point $\boldsymbol{r}'$ in a disordered medium, and formally express its density distribution at another point $\boldsymbol{r}$ at time t as a sum over all possible scattering paths:

$$n(\boldsymbol{r},t) = \left| \sum_{\text{paths i}} A_i \right|^2 = \underbrace{\sum_{\text{paths i}} A_i A_i^*}_{\text{classical}} + \underbrace{\sum_{\text{paths i}\neq\text{j}} A_i A_j^*}_{\text{quantum}}. \quad (1.1)$$

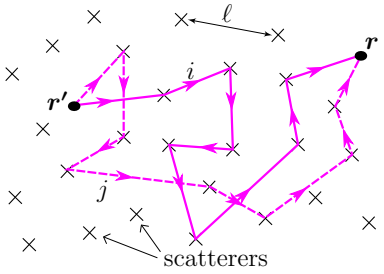

In this picture, A_i is the partial complex amplitude associated with the scattering path i. It has a phase which depends on the path i. In equation (1.1), we have separated two contributions to

the density distribution. On the one hand, the so-called "classical" contribution describes a random walk process where the various paths do not interfere and their intensity simply add up. The other "quantum" contribution, on the other hand, contains all possible interference effects. The pairs of paths responsible for the "quantum" contribution come with a phase factor of order $k\ell$. Here k is related to the De Broglie wave length of the particle λ, through $k = 2\pi/\lambda$, and ℓ is the scattering mean free path, the average distance traveled by the atoms between successive scattering events. If now we impose that $k\ell \gg 1$ (this defines a weak disorder criterion, see section 3.1 for details), the "quantum" contribution is negligible on average. Under this approximation, the particle experiences a classical diffusion process at large scales, with a diffusion coefficient D_0:

$$(\partial_t - D_0\nabla^2_{\boldsymbol{r}})\overline{n^{\rm cl}(\boldsymbol{r},t)} = \delta(\boldsymbol{r}-\boldsymbol{r'})\delta(t) \;\Leftrightarrow\; \overline{n^{\rm cl}(\boldsymbol{r},t)} = \int \frac{\mathrm{d}\omega}{2\pi}\frac{\mathrm{d}\boldsymbol{q}}{(2\pi)^d} e^{i\boldsymbol{q}.(\boldsymbol{r}-\boldsymbol{r'})-i\omega t}\frac{1}{-i\omega + D_0 q^2}, \quad (1.2)$$

where $\overline{n^{\rm cl}(\boldsymbol{r},t)}$ is the disorder averaged classical density. Note that $(-i\omega + D_0q^2)\overline{n^{\rm cl}(\boldsymbol{q},\omega)} = 1$ is the diffusion equation in Fourier space. This description is however incomplete. Indeed, some carefully designed pairs of paths turn out to survive the disorder average, provided each path accumulates the same phase during its propagation. When time-reversal invariance holds, this is precisely the case for a path and its time-reserved counterpart.

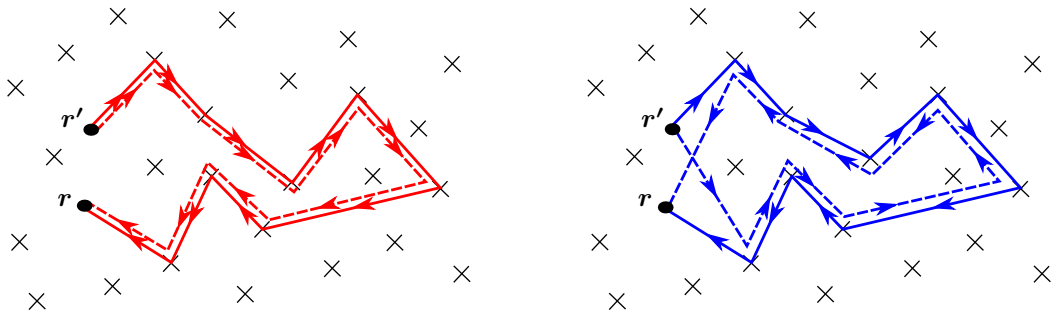

(a) Diffuson (b) Cooperon

Figure 1.1 – Two types of pairs of scattering paths contributing to the averaged density distribution: (a) the Diffuson: both paths follow the same sequence of scatterers in the same direction, and (b) the Cooperon: the two paths follow the same sequence of scatterers, but in opposite directions.

This argument leads us to keep two types of pairs of paths, the classical ones (called "Diffuson") and their time-reserved counterpart (called "Cooperon"). They are depicted in figure 1.1. Strictly speaking, Diffuson and Cooperon are symmetric upon time-reversal symmetry only when $\boldsymbol{r} = \boldsymbol{r'}$. This property makes the Cooperon play a singular role: it enhances the probability of observing the particle near its starting point.

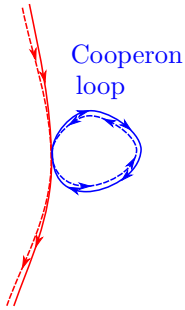

From the two building blocks in figure 1.1, we can build more complicated paths by chaining Diffusons and Cooperons (see figure opposite). The Cooperons can only appear as closed loops, their occurrence during the propagation leads to a reduction of the diffusion coefficient[1]:

[1] For a derivation of equation (1.3), see e.g. [3].

$$\overline{n^{\mathrm{WL}}(\boldsymbol{r},t)} = \int \frac{\mathrm{d}\omega}{2\pi}\frac{\mathrm{d}\boldsymbol{q}}{(2\pi)^d} e^{i\boldsymbol{q}.(\boldsymbol{r}-\boldsymbol{r}')-i\omega t}\frac{1}{-i\omega + D(\omega)q^2}$$
$$\frac{1}{D(\omega)} = \frac{1}{D_0} + \frac{1}{\pi\rho D_0}\underbrace{\int \frac{d\mathbf{Q}}{(2\pi)^d}\frac{1}{-i\omega + D_0\mathbf{Q}^2}}_{=\overline{n^{\mathrm{cl}}(\boldsymbol{r}',\omega)}}, \tag{1.3}$$

where ρ is the disorder-averaged density of states per unit volume. The reduction of the diffusion coefficient by interference effects is known as weak localization, and has been the subject of extensive research, in particular in condensed-matter physics, where it was tracked through its interplay with temperature, magnetic field, spin-orbit coupling or magnetic impurities (see e.g. the review [4] and the more recent experiment [5]). Note that one can alternatively observe the Cooperon contribution as a coherent enhancement of the return probability [6] or under the form of a coherent back scattering peak [7,8].

One sees that the reduction of the diffusion coefficient D_0 in equation (1.3) is proportional to the classical return probability $\overline{n^{\mathrm{cl}}(\boldsymbol{r}',\omega)}$. As it turns out, this correction becomes significant in low dimensions ($d \leq 2$) as well as at strong disorder in higher dimensions [3].

1.1.2 Strong localization: the self-consistent approach

In fact, if the quantum corrections (the Cooperon loops) become more important, more complex scattering paths appear, as shown in the figure on the right. These scattering paths may include loops nested into loops. The approximate solution to this problem has been provided by Vollhardt and Wölfle in 1980 [9], who suggested to renormalize the diffusion coefficient in the return probability itself:

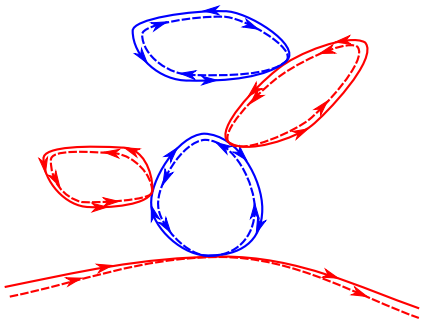

$$\overline{n^{\mathrm{SCTL}}(\boldsymbol{r},t)} = \int \frac{\mathrm{d}\omega}{2\pi}\frac{\mathrm{d}\boldsymbol{q}}{(2\pi)^d} e^{i\boldsymbol{q}.(\boldsymbol{r}-\boldsymbol{r}')-i\omega t}\frac{1}{-i\omega + D(\omega)q^2}$$
$$\frac{1}{D(\omega)} = \frac{1}{D_0} + \frac{1}{\pi\rho D_0}\underbrace{\int \frac{d\mathbf{Q}}{(2\pi)^d}\frac{1}{-i\omega + D(\omega)\mathbf{Q}^2}}_{=\overline{n^{\mathrm{SCTL}}(\boldsymbol{r}',\omega)}}, \tag{1.4}$$

Vollhardt and Wölfle self-consistent theory has enjoyed quite some success (see [10] for a recent review). It is however inaccurate in the vicinity of critical points, where its kind of mean-field nature[2] prevents accurate determinations of critical exponents [11].

Equation (1.4) can be fully solved in 1D [12], where the resulting infinite-time density profile takes the form

$$\overline{n^{\mathrm{SCTL}}(x,t=\infty)|^2} = \frac{e^{-|x|/2\ell}}{4\ell}. \tag{1.5}$$

1.2 Berezinskii diagrammatic technique

Berezinskii diagrammatic technique is a rigorous approach to localization restricted to the one-dimensional (1D) case. It was developed by Berezinskii in 1973 [13] and is discussed in details in

[2] The correction brought by each loop is an only an average correction, possible fluctuations from one loop to the other are not accounted for.

chapter 4. As the self-consistent theory, this method is based on the resummation of a diagrammatic expansion. However, in contrast with the self-consistent theory, the choice of relevant diagrams is rigorously controlled and their summation is exact. A particularly interesting result, obtained with this technique by Gogolin [14], is the infinite-time average density profile reached by an initially narrow wave packet spreading in a disordered potential[3],

$$\overline{n^{\mathrm{G}}(x,t=\infty)} = \int_0^\infty \frac{\mathrm{d}\eta\pi^2}{32\ell} \frac{\eta\left(1+\eta^2\right)^2 \sinh(\pi\eta) e^{-\left(1+\eta^2\right)|x|/8\ell}}{[1+\cosh(\pi\eta)]^2}. \tag{1.6}$$

Equation (1.6) can be interpreted as an average over exponentially localized profiles [$\propto \exp(-|x|/\xi)$], the integral over η accounting for the distribution of localization lengths ξ. As visible in figure 1.2, equation (1.6) somewhat differs from the result obtained using the self-consistent theory of localization, equation (1.5). The major difference occurs in the wings, where the exact result (1.6) decays as $\exp(-|x|/8\ell)$. This difference lies in the large fluctuations present in the wings, which make the average profile dominated by rare events not captured by the self-consistent theory, which only describes the typical profile [15]. In the center of the profile, fluctuations are much smaller [16, 17], and the self-consistent theory works well.

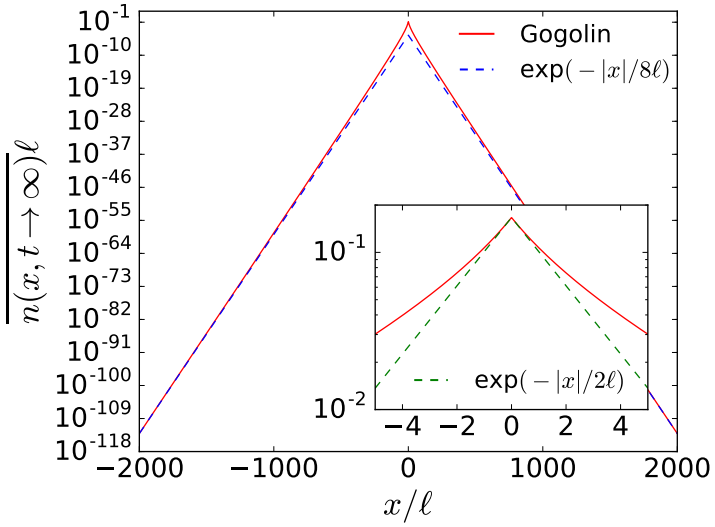

Figure 1.2 – Comparison between the exact Gogolin profile for the average density $\overline{n(x,t\to\infty)}$ (equation (1.6), red curve) and two simple exponential forms. In the main plot, the comparison is done with $\exp(-|x|/8\ell)$, shown as a dashed blue line. The inset presents a zoom on the small x part, where the comparison is done with $\exp(-|x|/2\ell)$, shown as a dashed green line. The latter is the prediction of the self-consistent theory.

1.3 Scaling theory of localization

The seemingly simple idea of considering how the properties of a system change when its size changes can be very fruitful for describing complex systems. Inspired by the ideas developed in the context of critical phenomena in statistical physics, Abrahams, Anderson, Licciardello and Ramakrishnan introduced a scaling theory of Anderson localization in disordered system of finite size [18]. In the present section, we give a brief account of their contribution.

[3] We will come back on the conditions under which equation (1.6) is valid in section 4.4.

The idea is to describe how the dimensionless conductance g of a disordered sample scales with its size L^d. Concretely speaking, one considers the Gell-Mann-Low β function, defined as

$$\beta = \frac{\mathrm{d}\,\ln(g)}{\mathrm{d}\,\ln(L)}. \tag{1.7}$$

The key ingredients allowing to characterize the β function are the following: (i) g is the only relevant variable, so that β depends only on g (hence the name *one-parameter scaling theory*), (ii) the β function is continuous and regular and (iii) the knowledge of the β function in its asymptotic regimes. On the one hand, the small g asymptotic follows from the exponential decay of the conductance, expected in the localization regime, and perturbation theory around this behavior [18],

$$\beta(g) \underset{g\to 0}{\sim} \ln(g)\,[1+\alpha g]\,, \tag{1.8}$$

with $\alpha > 0$. On the other hand, perturbation theory around the Ohm law provides the large g asymptotic [18]:

$$\beta(g) = d - 2 - a/g + \dots \tag{1.9}$$

with $a > 0$ for spinless time-reversal invariant systems. By interpolating between these two limits, Abrahams, Anderson, Licciardello and Ramakrishnan sketched the β function in all dimensions, as reproduced in figure 1.3.

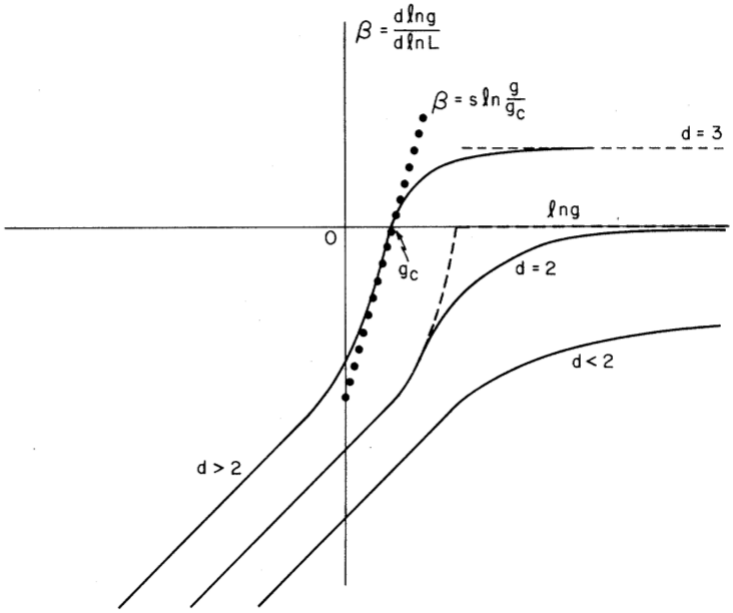

Figure 1.3 – Sketch (reproduced from [18]) of the β function versus $\ln(g)$ obtained by interpolating smoothly between the asymptotic limits (1.8) and (1.9). As discussed in the main text, in $d > 2$ the β function crosses 0, thus exhibiting a phase transition. Its slope across 0, shown as solid-circled line, encodes the critical exponent associated to this phase transition [18]. A jump of conductivity in $d = 2$, debated at the time [19], leads to the dashed line, inconsistent with the hypothesis of regularity, which instead rules in favor of localization of all states in $d = 2$.

Note that the β function (1.7) can be calculated from the self-consistent theory introduced in section 1.1. Its behavior is consistent with the general prediction of the scaling theory [20].

What conclusions can we draw from figure 1.3? On the one hand, for small dimensions ($d \leq 2$), the β function is always negative, i.e. the conductance decreases with increasing system size, and as

one moves along the curve of the β function, one ends up in the localization regime [$\beta(g) \sim \ln(g)$] for large systems. On the other hand, for higher dimensions ($d > 2$) the β function crosses 0. The point g_c such that $\beta(g_c) = 0$ separates two drastically different scaling behaviors. For $g < g_c$, one recovers the small dimension situation and localization eventually prevails for large enough systems. For $g > g_c$ in contrast, the conductance increases with increasing system size, signaling a regime of classical diffusion. g_c defines the so-called mobility edge, separating a localized phase from a delocalized phase for infinite systems. The associated transition is called Anderson transition, and was already predicted by Anderson in his seminal paper [1].

Interestingly, the two-dimensional (2D) case appears very sensitive to the sign of the correction in $1/g$ at large g [sign of a in (1.9)]. In the case of spinless time-reversal invariant systems considered so far, the weak localization correction was responsible for a small negative correction to $\beta(g \gg 1) = 0$. As it turns out, this perturbative correction strongly depends on the symmetries of the Hamiltonian. Assuming a weak magnetic field (thus breaking time-reversal invariance), the $1/g$ term of equation (1.9) disappears ($a = 0$), but the β function is not qualitatively affected, as the next order term, in $1/g^2$, bears a negative correction as well [21,22]. In sharp contrast, accounting for the electron spin through a spin-orbit term in the Hamiltonian turns the weak localization correction into a weak *antilocalization* correction and lead to a transition in two dimensions [22]. This is but one mechanism leading to criticality in 2D disordered systems [11].

1.4 Experimental observations of Anderson localization

1.4.1 Early condensed-matter experiments

One of the initial motivation that led to the theoretical prediction of localization was the understanding of spin transport in doped semiconductors, and in particular the observations of slow spin transport by Feher and Gere [23,24]. In the decades following Anderson's discovery of localization, a lot of experimental effort were devoted to the subject (see [25] for a review). Experiments were performed with solid-state samples such as thin metallic films or semiconductors. Correspondingly, theoretical works were primarily concerned with the conductivity (or related observables) of these systems (see review [25]).

The richness of solid-state system may however also constitute a difficulty. For instance, the effect of electron-electron interactions is *a priori* important in this context, their interplay with localization was intensively studied (see [26] for a review). The possibility of other mechanisms inhibiting transport (e.g. many-body effects for Mott insulators) makes the definite observation of Anderson localization difficult [27]. Furthermore, the coupling of electrons with external degrees of freedom (e.g. phonons) makes the localization phenomenon difficult to observe in "pure" conditions.

1.4.2 A wave phenomenon

As we have seen in section 1.1, Anderson localization is a manifestation of interferences between partial waves multiply scattered by the disorder. In other words, it is intrinsically a wave phenomenon [28]. As such, it was observed with various kinds of waves including microwaves [29], bending waves [30], light [31,32] (see however [33,34]) and ultrasound waves [35], to give the main examples.

Recently, Anderson localization of atomic matter waves has also been observed [36–40]. A major advantage of these setups is the possibility to control atom-atom interactions (through, e.g., Feshbach resonances), and to achieve a weak coupling to the environment. Furthermore, atom-optics experiments offer the possibility to directly probe localization phenomena *inside* the atomic system, as well as to follow their evolution in the course of time [41,42].

These key possibilities have led to an enrichment of Anderson localization phenomenology with the discovery of the coherent forward scattering peak [43], which can be used to characterize Anderson transitions [44]. In addition, cold-atom experiments based on a quench protocol [37–40, 45] impose to account for a broad spectrum of energy components [42, 46] (as opposed to condensed-matter experiments where only electrons near the Fermi energy contribute to transport). At last, the specificities of speckle optical potentials, often used to create the disorder [37–40, 45], lead to peculiar features, such as the existence of a series of apparent "mobility edges" between energy regions where localization lengths differ by orders of magnitude [47].

1.5 Anderson localization and interactions

The question of interactions is naturally important, as they are often unavoidable in experiments. Concerning this issue, two main trends have recently emerged. On the one hand, a large body of work tackles the question from the perspective of weakly interacting bosonic gases, and treat interactions at the mean-field level, possibly including perturbative corrections to the mean-field solution. On the other hand, a growing community has embarked into the subject of many-body localization, an extension of Anderson localization for many-body systems. The present thesis is only concerned with the former point of view, which is introduced in the next subsection. We have chosen to briefly discuss few aspects of many-body localization right afterwards, to offer a contrasting view.

1.5.1 Mean-field effects

At the mean-field level, the dynamics of cold bosonic gases is described by a nonlinear equation. This nonlinearity makes the physics very rich. Indeed, one expects the nonlinearity to have different effects depending on the initial conditions, as the superposition principle no longer holds. Four situations have attracted a lot of attention. First, the interplay between Anderson localization and interactions was tracked in the spreading of wave packets (see [48, 49] for recent reviews). It was found that Anderson localization is destroyed in favor of subdiffusion at long times as a result of a trade-off between destruction of localization and dilution of the nonlinearity. The destruction of Anderson localization in favor of subdiffusion was observed experimentally [50]. Subdiffusion is however predicted to breakdown at extremely long times, replaced by a slower spreading (if any) (see [51, 52] for rigorous proofs and [53, 54] for possible physical mechanisms). Second, the effects of inelastic collisions and the ensuing dynamics of the energy distribution was studied [55–59] as well as the eventual thermalization [60]. Third, the effect of interactions on the coherent backscattering peak was studied in an atom-laser-like configuration, where a static atomic beam is reflected from a nonlinear disordered medium [61,62]. It was found that interactions may transform the coherent backscattering peak into a dip. Note that one of the motivation for this work came from the optical context, where the effect of interactions on the coherent backscattering peak had been previously considered [63–66]. Fourth, in similar atom-laser-like configurations, the transmission of Bose-Einstein condensates through disordered regions was considered [67–69], reporting a destruction of Anderson localization in favor of superfluidity for small condensate velocities. At large velocities, Anderson localization prevails for small disordered regions (still, larger than the localization length) and an instability of the mean-field solution is expected for larger disordered regions.

The physics of perturbative corrections to the mean-field solution was also considered in the framework of Bogoliubov theory [70–76], through the truncated Wigner method [77], and with diagrammatic theory [78, 79].

1.5.2 Many-body effects

The field of many-body localization emerged after the pioneering work of Basko, Aleiner and Altshuler [80], who considered the possible localization of a many-body wave function in the Fock space of Anderson-localized states. From this formulation of the problem, they were able to build a reasoning somewhat similar to Anderson's original arguments for localization. This seminal paper generated a large body of works, see [81, 82] for recent reviews. These works confirmed the phenomenon of many-body localization and associated to it a whole phenomenology, with, in particular, the absence of thermalization and the logarithmic growth of entanglement entropy. The latter property should be contrasted with one-particle Anderson localization, for which the entanglement entropy is bounded [83]. Many-body localization has been recently observed experimentally [84,85]. Note that the many-body counterpart of the Cooperon (figure 1.1b) is predicted to be visible in Fock space [86]. Many-body localization has also found applications in gauge theories [87] and time crystals [88]. The subject is also of interest to mathematicians [89–91].

1.6 Outline of the thesis

The general goal of this thesis is to theoretically investigate several interesting effects related to Anderson localization, focusing on the context of cold-atomic systems. The study falls into three main categories. We first consider general aspects of cold-atom setups featuring speckle optical potentials, with an emphasis on the spectral properties of the atoms. The second facet of this work concerns new aspects of Anderson localization that can be explored with cold-atom setups. The third theme discusses the effect of interactions on various phenomena associated to Anderson localization, from the perspective of condensed bosons.

The thesis is organized as follows. We first present a theoretical approach to the energy distribution of atomic clouds in speckle potentials. This study consists of two stages. The first one is presented in chapter 2, where we consider statistical properties of speckle optical potentials, with an emphasis on intensity minima. In chapter 3, we present the second stage, a novel theoretical method for the calculation of the spectral function and the density of states in the strong disorder limit. Using the results obtained in chapter 2, we apply this method to the 1D case. The 2D case is treated in our published paper, reproduced in section 3.5.

In chapter 4, we come to the second facet of the work, with the characterization of the center-of-mass motion of wave packets launched with a finite velocity in random potentials. This study unveils a novel and unexpected manifestation of Anderson localization: after an initial ballistic motion, the packet center-of-mass experiences a retroreflection and slowly returns to its initial position. We dubbed this phenomenon the quantum boomerang effect. The core of chapter 4 consists in the analytical description of the quantum boomerang effect in one dimension.

In chapter 5, atom-atom interactions are introduced in the numerical simulations, at the mean-field (Gross-Pitaevskii) level. Their effects on the quantum boomerang phenomenon are first discussed. The effect of interactions is further investigated in the energy spreading of plane waves evolving in three-dimensional (3D) random potentials. Finally, we also discuss how they affect the coherent back scattering peak, and in particular reveal an unexpectedly small rise of the peak at short times.

In chapter 6, we take a different direction and consider a deterministic (albeit chaotic) model, the kicked rotor. We show that such kicked-rotor models offer interesting prospects for the study of Anderson localization. On the one hand, with strong experimental and theoretical motivations, we present compelling evidences in favor of a spinless kicked rotor in the sympletic ensemble. On the other hand, a second look at quasi-periodically modulated kicked rotors reveals intriguing results.

Finally, chapter 7 summarizes our findings and gives some perspectives.

Chapter 2

Statistical properties of speckle patterns

In cold-atom experiments, one takes advantage of the interaction between a laser and the atoms for various purposes. Of particular interest to us in this chapter is the possibility to shape the potential felt by the atoms. Indeed, under certain conditions, to be discussed in section 2.1, the laser acts for the atoms as a potential which is simply proportional to the laser intensity. In low dimensions, the common route to generate random potentials is to shine a laser on a rough plate. The resulting potential is then the complex diffraction pattern of the plate, and the randomness originates from the "random" local roughness of the plate. A precise understanding of the statistics of the resulting potential is of utmost importance for the analysis of such experiments.

This chapter is divided in three parts. First, we give a brief introduction to the cold-atom framework in section 2.1. Second, section 2.2 gives an introduction to the statistics of speckle potentials, and is concerned with general properties, such as the on-site distribution and correlation functions. This introductory section follows the book by Goodman [92]. It will also be the occasion to explain how speckle patterns are generated in the numerical simulations. Then, in section 2.3, we dive into more specific statistical properties, the statistical properties of intensity minima. The distributions considered there were derived during the thesis, and used to calculate spectral properties of atomic clouds in speckle potentials, which is the object of chapter 3.

2.1 Dipolar potential for cold-atoms

In this section, we show how one can take advantage of the interaction between a laser and the *internal* structure of an atom to influence the dynamics of its *external* degrees of freedom. This introductory section follows the courses by Dalibard at Collège de France [93].

For the sake of simplicity, throughout this section we consider a two-level atom interacting with a laser of frequency ω, as illustrated in figure 2.1. The ground state $|g\rangle$ and the excited state $|e\rangle$ of the atom describe its *internal* degrees of freedom, typically $|g\rangle$ is the orbital wave function of the outermost occupied shell in the ground state and $|e\rangle$ is an unoccupied orbital wave function. In cold-atom experiments, one takes advantage of the internal structure of the atom to induce the dynamics of its external degrees of freedom in a controlled way. The interaction between laser and atoms offers many possibilities. We detail only one of them in this manuscript, the possibility to tailor the external potential felt by the atoms. Other examples are briefly mentioned in subsection 2.1.3.

2.1.1 Dipolar atom-laser interaction

The atom is not charged, but possesses an internal structure, it can thus interact with the electric field of the laser through its dipole moment. For simplicity, we assume a linearly polarized (along

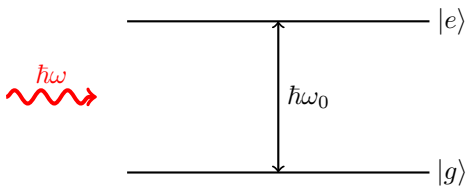

Figure 2.1 – Pictorial representation of a two-level atom, a ground state $|g\rangle$ and an excited state $|e\rangle$, separated by an energy $\hbar\omega_0$. A laser of frequency ω is shined on it.

u) classical electric field

$$\boldsymbol{\mathcal{E}}(\boldsymbol{r},t) = \mathcal{E}(\boldsymbol{r})\cos(\omega t + \phi(\boldsymbol{r}))\mathbf{u}. \tag{2.1}$$

Of course, $\boldsymbol{\mathcal{E}}(\boldsymbol{r},t)$ must obey Maxwell's equations, $\mathcal{E}(\boldsymbol{r})$ and $\phi(\boldsymbol{r})$ are not arbitrary functions. Note that the polarization is not crucial to the present discussion, it simply selects the possible excited states. At the dipolar approximation, the field only couples states of same angular momentum projection along **u**. The excited state is generally one among a degenerate set, the two levels are thus essentially always coupled at the dipolar approximation, making higher order multipole moments irrelevant.

At the dipolar approximation, the atom interacts with the electric field through

$$\widehat{V}_d = -\widehat{\mathbf{d}}.\boldsymbol{\mathcal{E}}(\boldsymbol{r}), \tag{2.2}$$

where the dipole operator writes $\widehat{\mathbf{d}} = -e\widehat{\boldsymbol{r}}_i$, with e the elementary electric charge and $\widehat{\boldsymbol{r}}_i$ the position operator of the electron in the reference frame of the atom. Here $\boldsymbol{r}$ is the atom center-of-mass. It is useful to express $\widehat{V}_d$ in the two-level basis,

$$\widehat{V}_d = -|e\rangle\langle e|\,\widehat{\mathbf{d}}\,|g\rangle\langle g|\,.\boldsymbol{\mathcal{E}}(\boldsymbol{r}) - |g\rangle\langle g|\,\widehat{\mathbf{d}}\,|e\rangle\langle e|\,.\boldsymbol{\mathcal{E}}(\boldsymbol{r}), \tag{2.3}$$

where we have not included $\langle e|\,\widehat{\mathbf{d}}\,|e\rangle$ and $\langle g|\,\widehat{\mathbf{d}}\,|g\rangle$ because they vanish by parity. To lighten the notations, we introduce the reduced atomic dipole (which can be chosen real for a two-level atom)

$$d_0 = \langle e|\,\widehat{\mathbf{d}}\,|g\rangle\,.\mathbf{u} = \langle g|\,\widehat{\mathbf{d}}\,|e\rangle\,.\mathbf{u}, \tag{2.4}$$

and two operators operating transitions between $|g\rangle$ and $|e\rangle$,

$$\widehat{\sigma}_+ = |e\rangle\langle g|\,, \qquad \widehat{\sigma}_- = |g\rangle\langle e|\,. \tag{2.5}$$

The dipolar atom-laser interaction reduces to

$$\widehat{V}_d(\boldsymbol{r},t) = -d_0\mathcal{E}(\boldsymbol{r})(\widehat{\sigma}_+ + \widehat{\sigma}_-)\cos(\omega t + \phi(\boldsymbol{r})). \tag{2.6}$$

2.1.2 Dipolar potential

Statement of the problem

Under certain conditions, to be specified in this subsection, the dipolar atom-field interaction mimicks an external potential: the center of mass of the atom in the electric field experiences an Hamiltonian dynamics, the dipolar interaction taking the form of an external potential. The goal of this subsection is to derive the corresponding effective Hamiltonian. To that end, we start from the full Hamiltonian

$$\widehat{H} = \frac{\widehat{\boldsymbol{p}}^2}{2m} + \widehat{V}_d(\boldsymbol{r},t) + \hbar\omega_0\,|e\rangle\langle e|\,, \tag{2.7}$$

where the first term accounts for the external kinetic degrees of freedom of the atom, the second term describes its coupling to the electric field at the dipolar approximation, and the last term is associated with the internal structure of the atom (we have chosen to count the energy starting from the ground state energy). We have already neglected spontaneous emission, which intrinsically cannot be described by an Hamiltonian dynamics, and thus assumed a small number of atoms in the excited state. The state of the atom is described by the density operator $\widehat{\rho}$, describing both its internal and external degrees of freedom. Of particular interest to us is its projection on the ground state of the atom, $\widehat{\rho}_{gg} = \langle g|\widehat{\rho}|g\rangle$.

Ground-state dynamics

The evolution of $\widehat{\rho}_{gg}$ is governed by the Heisenberg equation

$$\frac{\mathrm{d}\widehat{\rho}_{gg}}{\mathrm{d}t} = \frac{1}{i\hbar}\left[\widehat{H}, \widehat{\rho}_{gg}\right] = \frac{1}{i\hbar}\left[\frac{\widehat{\boldsymbol{p}}^2}{2m}, \widehat{\rho}_{gg}\right] - \cos(\omega t - \phi) i\Omega(\widehat{\boldsymbol{r}})\widehat{\rho}_{eg} + \cos(\omega t - \phi)\widehat{\rho}_{ge} i\Omega(\widehat{\boldsymbol{r}}), \tag{2.8}$$

where naturally $\widehat{\rho}_{eg} = \langle e|\widehat{\rho}|g\rangle$ and $\widehat{\rho}_{ge} = \widehat{\rho}_{eg}^\dagger$. We have also introduced the Rabi frequency $\Omega(\widehat{\boldsymbol{r}}) = -d_0\mathcal{E}(\widehat{\boldsymbol{r}})/\hbar$.

The evolution of $\widehat{\rho}_{gg}$ is coupled to the evolution of $\widehat{\rho}_{eg}$ that obeys

$$\frac{\mathrm{d}\widehat{\rho}_{eg}}{\mathrm{d}t} = \frac{1}{i\hbar}\left[\widehat{H}, \widehat{\rho}_{eg}\right] = \frac{1}{i\hbar}\left[\frac{\widehat{\boldsymbol{p}}^2}{2m}, \widehat{\rho}_{eg}\right] - i\omega_0\widehat{\rho}_{eg} - \cos(\omega t - \phi) i\Omega(\widehat{\boldsymbol{r}})\widehat{\rho}_{gg} + \cos(\omega t - \phi)\widehat{\rho}_{ee} i\Omega(\widehat{\boldsymbol{r}}), \tag{2.9}$$

where $\widehat{\rho}_{ee} = \langle e|\widehat{\rho}|e\rangle$. To simplify this equation, we make use of two assumptions. First, we assume that a negligible fraction of atoms are excited, i.e. $\widehat{\rho}_{ee} \approx 0$. Then we assume that internal degrees of freedom vary much faster than external ones, and thus neglect the kinetic part. Under this two assumptions, equation (2.9) provides

$$\widehat{\rho}_{eg} = \frac{\Omega(\widehat{\boldsymbol{r}})}{2}\left[\frac{e^{-i(\omega t-\phi)}}{\omega - \omega_0} - \frac{e^{i(\omega t-\phi)}}{\omega + \omega_0}\right]\widehat{\rho}_{gg}, \tag{2.10}$$

which we plug in equation (2.8) to find a closed equation for $\widehat{\rho}_{gg}$,

$$\begin{aligned}\frac{\mathrm{d}\widehat{\rho}_{gg}}{\mathrm{d}t} = \frac{1}{i\hbar}\left[\frac{\widehat{\boldsymbol{p}}^2}{2m}, \widehat{\rho}_{gg}\right] &+ \frac{\Omega^2(\widehat{\boldsymbol{r}})}{2i}\cos(\omega t - \phi)\left[\frac{e^{-i(\omega t-\phi)}}{\omega - \omega_0} - \frac{e^{i(\omega t-\phi)}}{\omega + \omega_0}\right]\widehat{\rho}_{gg} \\ &- \widehat{\rho}_{gg}\frac{\Omega^2(\widehat{\boldsymbol{r}})}{2i}\cos(\omega t - \phi)\left[\frac{e^{i(\omega t-\phi)}}{\omega - \omega_0} - \frac{e^{-i(\omega t-\phi)}}{\omega + \omega_0}\right],\end{aligned} \tag{2.11}$$

we have used $\widehat{\rho}_{gg} = \widehat{\rho}_{gg}^\dagger$. The optical frequency ω is very large. On time scales larger than $1/\omega$, we can neglect the micro-oscillations of the atomic center-of-mass induced by the rapidly oscillating terms (rotating wave approximation). Under this approximation, the dynamics is governed by

$$\frac{\mathrm{d}\widehat{\rho}_{gg}}{\mathrm{d}t} = \frac{1}{i\hbar}\left[\frac{\widehat{\boldsymbol{p}}^2}{2m} + V(\widehat{\boldsymbol{r}}), \widehat{\rho}_{gg}\right], \tag{2.12}$$

with, in the limit $\omega + \omega_0 \gg |\omega - \omega_0|$,

$$V(\widehat{\boldsymbol{r}}) \simeq \frac{d_0^2\mathcal{E}^2(\widehat{\boldsymbol{r}})}{4\hbar}\frac{1}{\omega - \omega_0}. \tag{2.13}$$

To make a more direct connection with the properties of the two-level atom, we express the reduced atomic dipole in terms of the decay rate of the excited state Γ [93]:

$$d_0^2 = \frac{3hc^3\epsilon_0\Gamma}{2\omega_0}, \tag{2.14}$$

where c is the speed of light. Plugging (2.14) in equation (2.13), and introducing the laser intensity $I(\boldsymbol{r}) = c\epsilon_0\mathcal{E}^2(\widehat{\boldsymbol{r}})/2$, we obtain the following expression for the potential

$$V(\widehat{\boldsymbol{r}}) \simeq \frac{3\pi c^2\Gamma}{2\omega_0}\frac{I(\boldsymbol{r})}{\delta}, \tag{2.15}$$

where $\delta = \omega - \omega_0$ is the laser detuning with respect to the two-level transition.

In conclusion, the ground state of the atom obeys an Hamiltonian dynamics and feels an external potential $V(\widehat{\boldsymbol{r}})$ proportional to the laser intensity. Depending on the laser frequency detuning with respect to the two-level transition considered, the sign of the potential can be positive or negative. The physical picture underlying the above calculation is the following: the incoming field polarizes the atom, which in turn interacts with it. Under the conditions detailed in the present subsection, this interaction, averaged over the rapid fluctuations of the electric field, acts as a potential for the external degrees of freedom of the atom.

Assumptions

In deriving equation (2.12), we have made various assumptions, which we now summarize and discuss. To begin with, we have considered a two-level atom. This is a good model for alkaline-earth metals (when they nuclear spin is vanishing), but it needs to be extended for alkali metals. For more complicated internal structures, the approach is somewhat similar and the conclusion is the same: for the atom, the laser mimicks an external potential. Another important assumption is that few atoms get excited by the laser, which is only possible if the laser frequency is far-enough detuned with respect to the two-level transition. Note that, in principle, it does not set a limit on the strength of the potential felt by the atom. Indeed, it is possible with large laser intensity and correspondingly large detuning to create strong potentials while preserving a small number of excitations. At last, we have assumed that internal degrees of freedom vary much faster than external ones, a condition generally met in cold-atom experiments.

2.1.3 Taking advantage of absorption or complex internal structures

So far, we have only seen photon absorption or more complex internal structures as annoyances without which we would be better off. In fact, photon absorption is the key to cool atoms down to very low temperatures, a step which preludes all the present discussion. On the other hand, one can use complex internal structures to mimick gauge fields. For more details about the cooling possibilities offered by atom-laser interaction see [94]. The reader interested in the generation of gauge fields in cold-atom experiments can consult the review [95]. Additionally, one can take advantage of the Zeeman effect to tune atom-atom interactions by application of a magnetic field, yet again a formidable subject we do not aim at covering in the present manuscript, see [96] for a recent review. The cold-atom technology is now widely used, as demonstrated by [97], and has allowed progress in many areas of quantum physics, as emphasized in [98, 99].

2.2 Speckle patterns: generalities

In the light of section 2.1, the generation of a random potential boils down to the generation of a sufficiently disordered intensity pattern $I(\boldsymbol{r}) = c\epsilon_0\mathcal{E}^2(\widehat{\boldsymbol{r}})/2$. The common way to achieve this

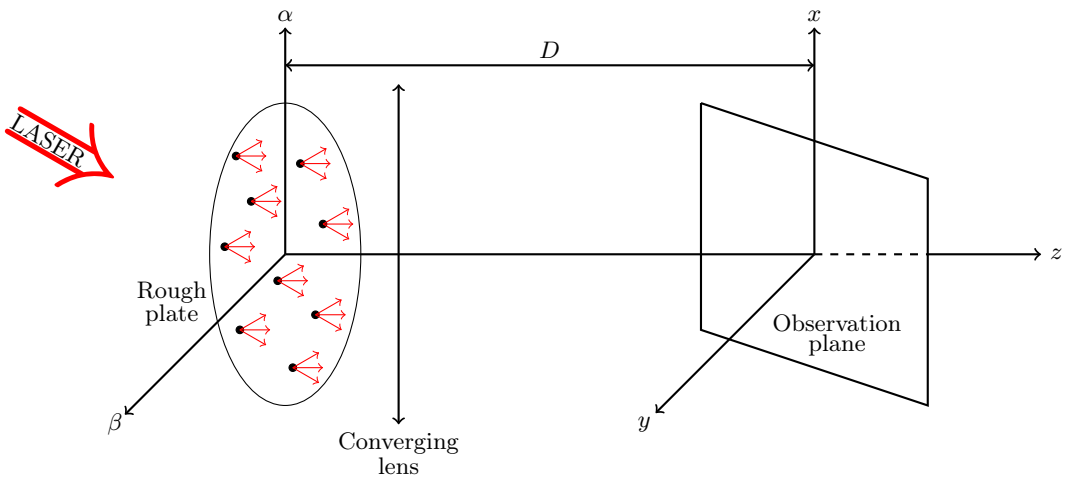

Figure 2.2 – Schematic representation of an experimental setup used to generate a speckle pattern in cold-atom experiments. A laser is shined on a rough plate, that scatters the electro-magnetic wave. The resulting interference pattern is observed in the observation plane, at a distance D from the plate. A lens is placed right after the rough plate, its focal plane corresponding to the observation plane, thus mimicking a far field configuration with a reasonable D.

goal consists in creating a speckle pattern, obtained by diffraction of a rough plate, as illustrated in figure 2.2. The resulting speckle pattern is observed in the far field and corresponds to the diffraction pattern of the plate. In practice, one places a lens right after the rough plate and uses the focal plane as observation plane, thus mimicking a far-field configuration with a reasonable distance between the plate and the observation plane. The electric field polarization does not play an important role, we assume a scalar field for the sake of simplicity.

2.2.1 Fresnel integral

The speckle pattern is characterized by a position-dependent intensity $I(x, y)$. To compute $I(x, y)$, we follow Huygens-Fresnel principle and break down the rough plate into many independent bits, each bit behaving as a secondary source. The observed speckle pattern is then the interference pattern of the electro-magnetic (EM) wave scattered by all the bits. Given a bit at (α, β), and its corresponding complex amplitude $a(\alpha, \beta)$ (in which we also include the phase accumulated when going through the lens), the resulting complex electric field at (x, y) writes

$$\mathcal{E}_{\alpha,\beta}(x, y) = \frac{a(\alpha, \beta)e^{ikr}}{i\lambda r}, \tag{2.16}$$

with $r = \sqrt{(x-\alpha)^2 + (y-\beta)^2 + D^2}$, $\lambda = 2\pi/k$ the wave length of the laser and D the distance between the rough plate and the observation plane. In the limit $D \gg x, y, \alpha, \beta$, one can resort to the Fresnel approximation:

$$r = D\sqrt{1 + \frac{(x-\alpha)^2 + (y-\beta)^2}{D^2}} \simeq D + \frac{(x-\alpha)^2 + (y-\beta)^2}{2D}. \tag{2.17}$$

The total complex field at (x, y) is obtained by integration over the bits constituting the rough plate:

$$\mathcal{E}(x, y) = \int \mathrm{d}\alpha\mathrm{d}\beta A_{\alpha,\beta}(x, y) = \frac{e^{ikD}}{i\lambda D} e^{\frac{ik}{2D}(x^2+y^2)} \int \mathrm{d}\alpha\mathrm{d}\beta e^{\frac{ik}{2D}(\alpha^2+\beta^2)} e^{-\frac{ik}{D}(x\alpha+y\beta)} a(\alpha, \beta). \tag{2.18}$$

The EM wave intensity follows from $I \propto |\mathcal{E}|^2$. In this section, the proportionality constant is irrelevant, we set it to 1 and use $I = |\mathcal{E}|^2$ to lighten the notations. The rough plate and its associated lens

are described by the function $a(\alpha, \beta)$, which contains the position-dependent scattering properties of the plate and the phase accumulated when going through the lens. We model it by a random function. For the present purposes, we do not need the full distribution of $a(\alpha, \beta)$, but only its correlation function. Assuming that the observation region is not large enough to allow the resolution of the details of the rough plate, we can neglect spatial correlations of $a(\alpha, \beta)$[1]:

$$\overline{a(\alpha,\beta)a^*(\alpha',\beta')} = I_{\rm rp}(\alpha,\beta)\delta^{(2)}(\alpha-\alpha',\beta-\beta'). \tag{2.19}$$

$I_{\rm rp}(\alpha, \beta)$ characterizes the average intensity transmission of the rough plate at (α, β). In experiments, it can be tuned by application of a mask.

2.2.2 On-site intensity distribution

We have laid out all the necessary ingredients for the statistical characterization of speckle potentials. Let us start with the intensity distribution at a given point (x, y). For an arbitrary speckle pattern, the complex electric field at (x, y) is given by equation (2.18) as the sum over contributions from a very large number of secondary sources. From the central limit theorem, it thus obeys a Gaussian law[2]:

$$P\left(\mathrm{Re}(\mathcal{E}),\mathrm{Im}(\mathcal{E})\right) = \frac{1}{2\pi\sigma_{\mathcal{E}}^2}\exp\left(-\frac{\mathrm{Re}(\mathcal{E})^2+\mathrm{Im}(\mathcal{E})^2}{2\sigma_{\mathcal{E}}^2}\right) \tag{2.20}$$

To obtain the distribution of the intensity, $I = |\mathcal{E}|^2$, we introduce the change of variables

$$\mathrm{Re}(\mathcal{E}) = I\cos(\theta), \tag{2.21}$$
$$\mathrm{Im}(\mathcal{E}) = I\sin(\theta), \tag{2.22}$$

the Jacobian is simply 1/2. The joint distribution of intensity and phase follows:

$$P\left(I,\phi\right) = \frac{\theta(I)}{4\pi\sigma_{\mathcal{E}}^2}\exp\left(-\frac{I}{2\sigma_{\mathcal{E}}^2}\right). \tag{2.23}$$

where θ is the Heaviside theta function. The phase is thus uniformly distributed, and the intensity obeys an exponential law:

$$P\left(I\right) = \frac{\theta(I)}{I_0}\exp\left(-\frac{I}{I_0}\right), \tag{2.24}$$

where we have introduced the average intensity

$$I_0 = \overline{I} = \sqrt{\overline{I^2}-\overline{I}^2} = 2\sigma_{\mathcal{E}}^2. \tag{2.25}$$

2.2.3 Correlation functions

Besides the on-site distribution, it is crucial to account for the spatial correlation of the potential. The complex electric field being a Gaussian random variable of vanishing mean value, all its correlations functions are encoded in its second-order correlation function

$$C_{\mathcal{E}}(x,y;x',y') = \overline{\mathcal{E}(x,y)\mathcal{E}^*(x',y')}. \tag{2.26}$$

[1] Note that these correlations are important in experiments to keep a small diffraction angle, so as to concentrate the speckle pattern in a limited region of space. Taking them into account only changes the large scale structure of the speckle pattern.

[2] To simplify the discussion, we assume that the complex electric field phase is uniformly distributed in $[0, 2\pi[$, such that $\overline{\mathcal{E}(x,y)} = 0$. Experimentally, this corresponds to using a plate rough at the scale of λ.

Similarly, the intensity correlation functions are deduced from $C_{\mathcal{E}}$, by application of Wick theorem, for example

$$\begin{aligned} C_I(x,y;x',y') =& \overline{I(x,y)I(x',y')} - \overline{I(x,y)}\ \overline{I(x',y')} \\ =& \overline{\mathcal{E}(x,y)\mathcal{E}^*(x,y)\mathcal{E}(x',y')\mathcal{E}^*(x',y')} - \overline{\mathcal{E}(x,y)\mathcal{E}^*(x,y)}\ \overline{\mathcal{E}(x',y')\mathcal{E}^*(x',y')} \\ =& \overline{\mathcal{E}(x,y)\mathcal{E}^*(x',y')}\ \overline{\mathcal{E}(x',y')\mathcal{E}^*(x,y)} \\ =& C_{\mathcal{E}}(x,y;x',y')C^*_{\mathcal{E}}(x,y;x',y') = |C_{\mathcal{E}}(x,y;x',y')|^2. \end{aligned} \tag{2.27}$$

In turn, $C_{\mathcal{E}}$ can be computed from equation (2.18):

$$C_{\mathcal{E}} = \frac{e^{\frac{ik}{2D}(x^2+y^2-x'^2-y'^2)}}{\lambda^2 D^2} \int \mathrm{d}\alpha\mathrm{d}\beta\mathrm{d}\alpha'\mathrm{d}\beta' \overline{a(\alpha,\beta)a^*(\alpha',\beta')} e^{\frac{ik}{2D}(\alpha^2+\beta^2-\alpha'^2-\beta'^2)} e^{-\frac{ik}{D}(x\alpha+y\beta-x'\alpha'-y'\beta')}. \tag{2.28}$$

Plugging in equation (2.19), we find

$$C_{\mathcal{E}} = \frac{e^{\frac{ik}{2D}(x^2+y^2-x'^2-y'^2)}}{\lambda^2 D^2} \int \mathrm{d}\alpha\mathrm{d}\beta e^{-\frac{ik}{D}((x-x')\alpha+(y-y')\beta)} I_{\mathrm{rp}}(\alpha,\beta). \tag{2.29}$$

We see that C_I ($= |C_{\mathcal{E}}|^2$, equation (2.27)) is the modulus square of the inverse Fourier transform of $I_{\mathrm{rp}}(\alpha,\beta)$, the intensity distribution of the laser in the rough plate, and depends only on $(x-x', y-y')$. The intensity distribution of the laser in the rough plate can be experimentally tuned by application of a mask on the rough plate (we assume that the converging lens transmit uniformly the EM wave). Physically, C_I corresponds to the diffraction pattern of the mask. Given a rough plate of size R, the intensity correlation function in the observation plane typically decays over a distance D/kR. This distance defines σ, the correlation length of the potential. Three examples of masks and their associated intensity correlation function are shown in table 2.1.

We have so far only considered 2D speckle patterns. A 1D speckle can easily be obtained from a 2D one, simply by cutting a slice in the 2D pattern. The generation of 3D speckle patterns is more involved. Indeed, the setup described here to generate speckle patterns has a small angular aperture, resulting in speckle grains elongated in the z direction. Recently, 3D speckle patterns were implemented in two experiments [38,40], by superimposing two 2D speckle patterns generated along two different directions, so that the resulting 3D speckle pattern remains anisotropic.

2.2.4 Numerical implementation

Having characterized the statistical properties of speckle potentials, we are now in position to implement them numerically. This implementation serves two purposes in the present thesis. On the one hand, we use them directly to study their properties in section 2.3. On the other hand, they from a key ingredient for the numerical simulations of chapters 3 and 4. Their implementation amounts to generating a spatially correlated random function. In practice, one generates the complex amplitude in two steps. First, one generates an uncorrelated grid of points with the desired distribution (e.g. complex Gaussian). Second, one convolutes the uncorrelated grid by the desired correlation function. The convolution can be conveniently performed in Fourier space, where it is simply a multiplication. Eventually, the speckle potential is obtained as the modulus square of the complex amplitude. In fact, this procedure exactly mimicks the experimental scenario discussed in the previous subsections, where the intensity correlation function is simply the modulus square of the inverse Fourier transform of the intensity distribution in the rough plate, the correlation function is thus imprinted "in Fourier space" by the rough plate mask.

Two realizations of 1D random potentials used in the numerical simulations of chapter 3 are shown in figure 2.3. They correspond to realizations of speckle optical potentials, with the following

	Square	Circle	Gaussian
Mask ($I_{\mathrm{rp}}(\alpha,\beta)$)	$\theta(R-\lvert\alpha\rvert)\theta(R-\lvert\beta\rvert)$ 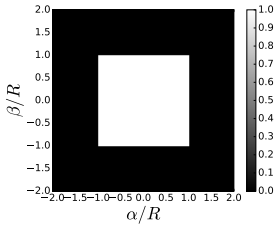	$\theta\left(R-\sqrt{\alpha^2+\beta^2}\right)$ 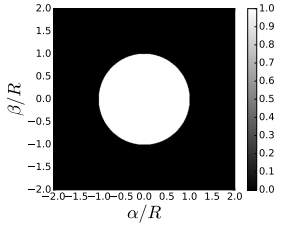	$\exp\left[-(\alpha^2+\beta^2)/2R^2\right]$ 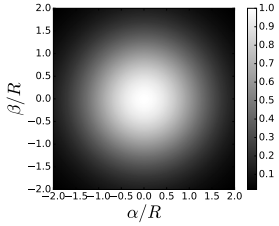
Intensity correlation function along $y=0$	$\mathrm{sinc}^2\left(\frac{x}{\sigma}\right)$ 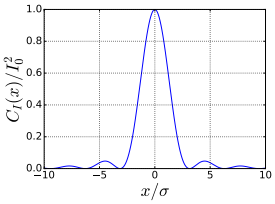	$\left[\frac{2J_1(x/\sigma)}{x/\sigma}\right]^2$ 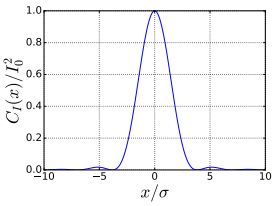	$\exp\left[-\frac{x^2}{2\sigma^2}\right]$ 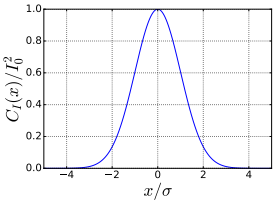
Correlation length	$\sigma = D/kR$	$\sigma = D/kR$	$\sigma = D/\sqrt{2}kR$

Table 2.1 – Three possible masks applied on the rough plate, and their resulting intensity correlation functions. α and β are expressed in arbitrary units. For the isotropic masks (the circle and the Gaussian), the correlation function is isotropic as well, however the correlation function associated to the square mask is anisotropic. θ is the Heaviside theta function, $\mathrm{sinc}(x) = \sin(x)/x$ and J_1 is the first order Bessel function of the first kind. We have introduced σ, the correlation length of the potential, which depends on the typical length over which $I_{\mathrm{rp}}(\alpha,\beta)$ decays R, the wave length of the laser λ ($= 2\pi/k$) and the distance between the rough plate and the observation plane D.

on-site distribution (we move from the intensity notation to the potential one for consistency with the rest of the thesis):

$$P\left[V(x)\right] = \frac{1}{V_0}\theta\left[\pm V(x)\right]\exp\left[\mp\frac{V(x)}{V_0}\right], \tag{2.30}$$

where θ is the Heaviside theta function. The disorder strength $V_0 > 0$ enters both the average $\overline{V(x)} = \pm V_0$ and the variance $\overline{V(x)^2} - \overline{V(x)}^2 = V_0^2$. In equation (2.30), the upper sign refers to a blue-detuned speckle potential ($\omega > \omega_0$ in equation (2.13)), bounded by zero from below, and the lower sign to a red-detuned speckle potential ($\omega < \omega_0$), bounded by zero from above. They are both characterized by a Gaussian correlation function:

$$\overline{V(x)V(x')} - \overline{V(x)}^2 = V_0^2\exp\left(-\frac{|x-x'|^2}{2\sigma^2}\right). \tag{2.31}$$

2.3 Statistics of intensity minima

The above statistical characterization of speckle potentials opens the way for calculating more specific statistical properties. We are interested in intensity minima, and more precisely the joint distribution of their depths and curvatures, together with the density of minima, in the 1D situation. We want eventually to apply these statistical properties to the calculation of spectral properties of atoms in chapter 3, we thus hereafter adopt the language of potential rather that of intensity. To set the notations, we introduce the potential on-site distribution,

$$P\left[V(x)\right] = \frac{1}{V_0}\theta\left[V(x)\right]\exp\left[-\frac{V(x)}{V_0}\right], \tag{2.32}$$

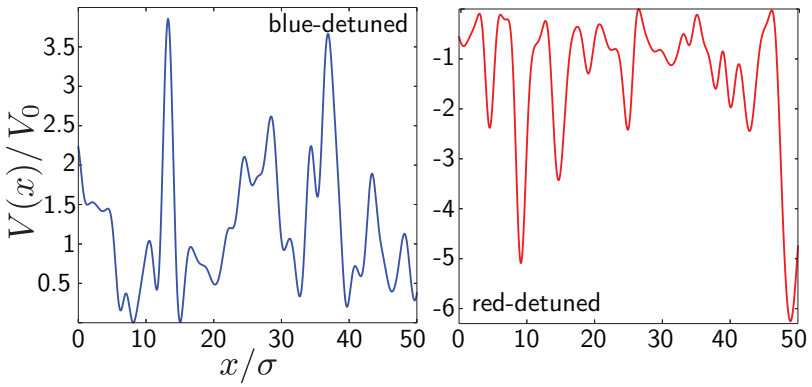

Figure 2.3 – Numerical realizations of a red- (left) and a blue-detuned (right) 1D speckle potential. The on-site distribution is exponential [equation (2.30)] and the two-point correlation function is Gaussian [equation (2.31)].

where θ is the Heaviside theta function. Along with the on-site distribution, the potential is characterized by a Gaussian correlation function [equation (2.31)]. The correlation function is set for definiteness, the calculation can be done for arbitrary correlation functions.

To be concrete, given the expansion of the potential near a minima

$$V(x) = V + \frac{1}{2}m\omega^2 x^2 + \ldots, \tag{2.33}$$

we are interested in the joint distribution of V and ω ($P(V,\omega)$), as well as the density of minima. Note that results on the 2D counterpart of $P(V,\omega)$ can be found in our published paper, reproduced in section 3.5. For the sake of brevity, we just briefly comment on these results in subsection 2.3.3. Throughout this section, we use a characteristic scale for ω,

$$\omega_0 = \sqrt{\frac{V_0}{m\sigma^2}}. \tag{2.34}$$

2.3.1 Joint distribution $P(V,\omega)$

In this subsection, we calculate the joint probability distribution $P(V,\omega)$ discussed above. The distribution $P(V,\omega)$ is closely related to the joint, conditional probability distribution of $V(x)$ and its second derivative $V''(x)$ given that $V'(x) = 0$ and $V''(x) > 0$, $P(V(x), V''(x)|V'(x) = 0, V''(x) > 0)$, that we propose to calculate first. From here on we use the following abbreviated notation for the potential and its derivatives at point x:

$$V \equiv V(x), \quad V_x \equiv V'(x), \quad V_{xx} \equiv V''(x). \tag{2.35}$$

The above distribution follows from

$$P(V, V_{xx}|V_x = 0, V_{xx} > 0) = N \times \lim_{V_x \to 0} \frac{P(V, V_x, V_{xx})}{P(V_x)}. \tag{2.36}$$

The numerical constant N that appears in equation (2.36) stems from the fact that only positive curvatures are selected on the left-hand side, whereas on the right-hand side all possible values are understood. It will be later determined from the normalization condition. In order to compute the joint distribution $P(V, V_x, V_{xx})$, we follow Goodman [92] and write the potential as

$$V = \Re(x)^2 + \Im(x)^2. \tag{2.37}$$

Up to a constant multiplicative factor, $\Re(x)$ and $\Im(x)$ respectively describe the real and imaginary part of the laser electric field at point x, from which the speckle potential V is built on, as explained in section 2.2. As for the potential, we introduce the following short-hand notations

$$\Re \equiv \Re(x), \quad \Re_x \equiv \Re'(x), \quad \Re_{xx} \equiv \Re''(x) \qquad \Im \equiv \Im(x), \quad \Im_x \equiv \Im'(x), \quad \Im_{xx} \equiv \Im''(x). \tag{2.38}$$

The motivation for introducing the fields $\Re$ and $\Im$ is that they are independent Gaussian variables with zero mean and equal variance [92]. Their derivatives are likewise Gaussian, since any linear transformation of a Gaussian retains Gaussian statistics. They also have a zero mean. As a consequence, the six random variables of interest obey the multi-dimensional Gaussian distribution

$$P(\Re, \Im, \Re_x, \Im_x, \Re_{xx}, \Im_{xx}) = \frac{e^{-\mathbf{u}^t C^{-1} \mathbf{u}/2}}{8\pi^3 \sqrt{\det(C)}}, \tag{2.39}$$

where $\mathbf{u}^t$ is a row vector with entries $(\Re, \Im, \Re_x, \Im_x, \Re_{xx}, \Im_{xx})$, and C is the covariance matrix.
We then introduce in equation (2.39) the change of variables

$$\Re = \sqrt{V}\cos\theta, \quad \Im = \sqrt{V}\sin\theta, \tag{2.40}$$

from which we calculate the distribution $P(V, \theta, V_x, \theta_x, V_{xx}, \theta_{xx})$, with a corresponding Jacobian equal to $1/8$. By explicitly evaluating the entries of the C matrix for the Gaussian correlation function (2.31) and calculating the remaining integrals over θ, θ_x and θ_{xx} with Mathematica [100], we find

$$\begin{aligned} P(V, V_x, V_{xx}) = &\frac{\sigma^4}{4\sqrt{2\pi} V_0^3 V} e^{-\frac{24V + 16 V_{xx}\sigma^2 + (V_x^2 - 2VV_{xx})^2\sigma^4/V^3}{16 V_0}} \sqrt{\frac{(-V_x^2 + 2VV_{xx})V_0}{V}}, \\ &\times \left\{ I_{-\frac{1}{4}}\left[\frac{(V_x^2 - 2VV_{xx})^2\sigma^4}{16V^3 V_0}\right] + I_{\frac{1}{4}}\left[\frac{(V_x^2 - 2VV_{xx})^2\sigma^4}{16V^3 V_0}\right] \right\}, \end{aligned} \tag{2.41}$$

where $I_{1/4}$ and $I_{-1/4}$ are the modified Bessel functions of the first kind. Note that this expression is valid only when $V_x^2 - 2VV_{xx} < 0$, a condition fulfilled since only minima of the potential are considered[3]. The distribution $P(V, V_x, V_{xx})$ is regular with respect to the limit $V_x \to 0$. In equation (2.36), we can thus take this limit separately in numerator and denominator, reducing the latter to a numerical constant which can be absorbed in the normalization prefactor N.
From the joint distribution (2.41), we are now in position to access the probability $P(V, V_{xx}|V_x = 0, V_{xx} > 0)$ using equation (2.36). The result is

$$P(V, V_{xx}|V_x = 0, V_{xx} > 0) = \frac{N\sqrt{V_{xx}}}{V} e^{-\frac{6V^2 + 4VV_{xx}\sigma^2 + V_{xx}^2\sigma^4}{4V_0 V}} \left[I_{-\frac{1}{4}}\left(\frac{V_{xx}^2\sigma^4}{4VV_0}\right) + I_{\frac{1}{4}}\left(\frac{V_{xx}^2\sigma^4}{4VV_0}\right)\right]. \tag{2.42}$$

By imposing that the distribution is normalized, we find $N = \sigma^5/(2cV_0^{5/2})$, where

$$c = \frac{\sqrt{3}\Gamma\left(1/4\right)\Gamma\left(5/4\right) - \Gamma\left(-1/4\right)\Gamma\left(7/4\right)}{3^{3/4}\sqrt{2}\pi} \simeq 1.00685, \tag{2.43}$$

which will be replaced by 1 in the following.

The last stage of the calculation consists in connecting $P(V, V_{xx}|V_x = 0, V_{xx} > 0)$ to the sought for distribution $P(V, \omega)$. This amounts to changing the variables from $V_x = 0$ to x such that $V_x(x) = 0$,

[3] The maxima of the potential could be studied along the same lines, but they are not relevant for our calculations of spectral properties in chapter 3.

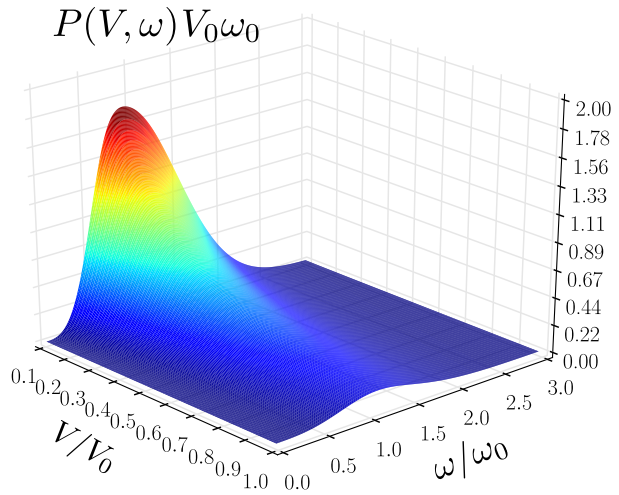

Figure 2.4 – Joint distribution $P(V,\omega)$ of minima and potential curvature around minima, for a 1D, blue-detuned speckle potential with Gaussian correlation function [equation (2.44)].

and from V_{xx} to ω such that $m\omega^2 = V_{xx}$. The associated Jacobian is $|dV_x/dx \times dV_{xx}/d\omega| = 2m^{5/2}\omega^3$. We finally infer

$$P(V,\omega) = \frac{1}{V\omega_0}\left(\frac{\omega}{\omega_0}\right)^4 e^{-\frac{3}{2}\left(\frac{V}{V_0}\right)^2-\left(\frac{\omega}{\omega_0}\right)^2-\frac{V_0}{4V}\left(\frac{\omega}{\omega_0}\right)^4}\left[I_{-\frac{1}{4}}\left(\frac{V_0}{4V}\left(\frac{\omega}{\omega_0}\right)^4\right)+I_{\frac{1}{4}}\left(\frac{V_0}{4V}\left(\frac{\omega}{\omega_0}\right)^4\right)\right]. \tag{2.44}$$

The joint distribution is shown in figure 2.4. At a given potential minimum V, we observe that it is maximum for $\omega \sim \omega_0$, at smaller ω, the distribution rapidly falls to zero.

Low energy minima, $V \ll V_0$, will turn out of special importance for the spectral properties of atoms in speckle potentials, it is thus interesting to express the distribution $P(V,\omega)$ in the limit $V \to 0$ [101]:

$$P(V,\omega)V_0\omega_0 \underset{V\to 0}{\sim} \sqrt{\frac{2}{\pi}}\sqrt{\frac{V_0}{V}}\left(\frac{\omega}{\omega_0}\right)^2 e^{-\left(\frac{\omega}{\omega_0}\right)^2}. \tag{2.45}$$

The $1/\sqrt{V}$ divergence at low V shows that most minima lie at very low $V \ll V_0$. The distribution of their associated frequency ω is peaked around ω_0.

2.3.2 Density of minima

We are also interested in the density of minima ρ. To evaluate it, we follow [102,103] and consider the general identity

$$\int \mathrm{d}x\delta(V'(x))f(x) = \sum_n \frac{1}{|V''(x_n)|}f(x_n), \tag{2.46}$$

valid for any function f. The sum is over all point x_n where $V'(x) \equiv V_x$ vanishes. If we choose $f(x)$ to be $|V''(x)| \equiv |V_{xx}|$, then the integral is equal to the number of points at which V_x vanishes. This defines the density of extrema per unit length as

$$\delta(V_x)|V_{xx}|. \tag{2.47}$$

The corresponding density restricted to minima of the potential is

$$\delta(V_x)V_{xx}\theta(V_{xx}), \tag{2.48}$$

with θ the Heaviside function. The disorder-averaged density of minima then reads

$$\rho = \int \mathrm{d}V_x \mathrm{d}V_{xx} P(V_x, V_{xx}) \delta(V_x) V_{xx} \theta(V_{xx}). \tag{2.49}$$

Using equation (2.41), we obtain $\rho = c'/\sigma$, where $c' \simeq 0.284026$.

2.3.3 Two-dimensional case

As we have shown at the end of subsection 2.3.1, most minima lie at very low $V \ll V_0$ in one-dimension, with a square-root singularity of the distribution of minima at small V [equation (2.45)]. It turns out that the two-dimensional case is even more singular, with a finite density of minima *exactly* at $V = 0$. The presence of such minima can be readily understood from the decomposition of V as $V = \Re^2 + \Im^2$ [equation (2.37)]. Indeed, they correspond to the intersections of the lines along which the Gaussian random functions $\Re$ and $\Im$ are vanishing. These particular minima play a crucial role for the calculation of spectral properties of atoms in speckle potentials in the next chapter. More precisely, from the expansion of V around a minima,

$$V(x, y) = \frac{1}{2} m\omega_x^2 x^2 + \frac{1}{2} m\omega_y^2 y^2 + \ldots, \tag{2.50}$$

where the basis if chosen such that the crossed term (in xy) is vanishing, the joint distribution of ω_x and ω_y is required. Its derivation is a bit technical and not very enlightening, we thus prefer to refer to our published paper, reproduced in section 3.5, for a detailed derivation. The situation is somewhat similar to the one-dimensional case with typical frequencies taking values around ω_0.

2.4 Conclusion

In this chapter, we have sketched out the generation of random potentials in cold-atom experiments and seen how to implement them numerically. We have characterized their statistical properties, as modulus square of complex Gaussian random variables, with various possible spatial correlations. From this characterization, we have then extracted important information for chapter 3, that of statistics of intensity minima in one-dimension. The intensity minima essentially lie at low energies, $V \ll V_0$, and the distribution of their proper frequency is peaked around $\omega_0 = \sqrt{V_0/(m\sigma^2)}$.

Chapter 3

Semiclassical spectral function and density of states in speckle optical potentials

As a prelude to the study of Anderson localization, it is important to characterize the spectral properties of the atoms in the random potential. In connection with cold-atom experiments, we are specifically concerned with speckle potentials, introduced in chapter 2. To get a first hand on the subject, we start with the weak disorder limit (section 3.1). In this limit, a perturbative treatment of the random potential is possible, allowing for a description of the atoms in terms of quasi-particles. It is a natural framework for introducing important quantities for the rest of the thesis. Among them, the spectral function, viz. the average energy distribution of a plane wave in the speckle potential, receives special attention, and its importance for the dynamics of atoms is discussed. A companion of the spectral function is the density of states. The latter is also an important quantity, in particular in the discussion of phases of dirty interacting bosons [60, 71, 104].

In the strong disorder regime, semiclassical methods turn out particularly valuable for calculating the above quantities. On the one hand, a perturbative expansion in $\hbar$ allows for systematic corrections to the classical limit in the large energy sector [105]. On the other hand, the low energy part requires a non-perturbative method. The perturbative expansion was recently carried out in [105], based on Wigner-Weyl formalism. In contrast, here we address the singular corrections that appear at low energy, using a new method based on stationary phase approximations, and applied to the one and two dimensional cases. These calculations are described and discussed in details in a published paper, reproduced in section 3.5. We choose here to present both the perturbative expansion in $\hbar$ (with a method differing from that of [105]) and the non-perturbative method, to offer a somewhat complete description of the semiclassical regime. As the two-dimensional case is qualitatively similar to the one-dimensional one, we prefer to detail only the former here, and refer to the article of section 3.5 for the latter.

Section 3.1 is introductory, the reader familiar with the Green function language may prefer to skip it. Section 3.2 motivates our study of the spectral function, and section 3.3 develops our contribution to the subject.

3.1 Weak disorder, perturbative calculations

In the weak disorder limit (to be defined shortly), one can resort to perturbation theory to get an understanding of the physics at play. We propose to carry out this program in the present section, within the Green function formalism. To lighten the notations, we assume a 1D system. The generalization of the mathematics to any dimension is straightforward. We closely follow the

book by Akkermans and Montambaux [3].

3.1.1 Perturbative treatment with Green functions

Green functions offer a powerful tool to carry out systematic perturbative calculations. In this respect, they are widely used in condensed matter physics [106]. Given an Hamiltonian

$$H = H_0 + V, \tag{3.1}$$

the (retarded) Green function is defined as

$$G(x_1, x_2, t) = \theta(t) \langle x_2 | e^{-iHt/\hbar} | x_1 \rangle , \tag{3.2}$$

with θ the Heaviside theta function. Its Fourier transform in turn writes

$$G(x_1, x_2, \epsilon) = \int_{-\infty}^{\infty} \mathrm{d}t e^{\frac{i(\epsilon + i0^+)t}{\hbar}} G(x_1, x_2, t) = \langle x_2 | \widehat{G} | x_1 \rangle , \tag{3.3}$$

where we have introduced the Green operator $\widehat{G}$:

$$\widehat{G} = \frac{1}{\epsilon - H + i0^+}, \tag{3.4}$$

$i0^+$ being an infinitesimal imaginary part ensuring the convergence of the Fourier transform at long times. The convenience of the Green function appears when one expresses the total Green operator $\widehat{G}$ in terms of the free Green operator $\widehat{G}_0 = 1/(\epsilon - H_0 + i0^+)$:

$$\widehat{G} = \widehat{G}_0 + \widehat{G}_0 V \widehat{G}, \tag{3.5}$$

which is easily obtained from the definitions of $\widehat{G}$ and $\widehat{G}_0$. Equation (3.5) is called the Lippmann–Schwinger equation. Iterating it generates a systematic perturbative expansion of $\widehat{G}$, the so-called Born series:

$$\widehat{G} = \widehat{G}_0 + \widehat{G}_0 V \widehat{G}_0 + \widehat{G}_0 V \widehat{G}_0 V \widehat{G}_0 + \dots \tag{3.6}$$

So far, H_0 and V can be arbitrary operators. In this thesis, we are primarily concerned with atoms subjected to disorder. It is thus natural to chose H_0 as the kinetic part of the Hamiltonian and V as the potential modeling the disorder. H_0 is diagonal in momentum space, so is G_0, which writes

$$G_0(k, k', \epsilon) = \iint \mathrm{d}x \mathrm{d}x' e^{-ikx + ik'x'} G_0(x, x', \epsilon) = \frac{1}{\epsilon - \epsilon_k + i0^+} \delta_{k,k'}, \tag{3.7}$$

where ϵ_k is the dispersion relation, $\epsilon_k = \hbar^2 k^2 / 2m$ for free atoms of mass m. $G_0(k, k', \epsilon)$ being diagonal, we introduce the short-hand notation

$$G_0(k, \epsilon) = G_0(k, k, \epsilon) = \frac{1}{\epsilon - \epsilon_k + i0^+}. \tag{3.8}$$

One expects the full Green function for a given disorder realization to be very complicated, and generally impractical. A more pertinent object is the distribution of the Green function. The distribution may however remains a difficult object to handle, so that one usually consider only the disorder-averaged Green function. According to equation (3.6), the latter can be expressed as

$$\begin{aligned} \overline{G}(x, x', \epsilon) =& G_0(x, x', \epsilon) + \int \mathrm{d}x_1 G_0(x, x_1, \epsilon) \overline{V(x_1)} G_0(x_1, x', \epsilon) \\ &+ \int \mathrm{d}x_1 \mathrm{d}x_2 G_0(x_1, x_2, \epsilon) \overline{V(x_1) G_0(x_1, x_2, \epsilon) V(x_2)} G_0(x_2, x', \epsilon) + \dots \end{aligned} \tag{3.9}$$

Choosing the origin of energies at $\overline{V}$, we can set the mean value of V to 0 in equation (3.9). From here on we assume that $\overline{V} = 0$, and define the potential correlation function as

$$\overline{V(x_1)V(x_2)} = B(x_1 - x_2). \tag{3.10}$$

With these definitions, equation (3.9) reduces to

$$\overline{G}(x, x', \epsilon) = G_0(x, x', \epsilon) + \int \mathrm{d}x_1 \mathrm{d}x_2 G_0(x, x_2, \epsilon) B(x_1 - x_2) G_0(x_1, x_2, \epsilon) G_0(x_2, x', \epsilon) + \dots \tag{3.11}$$

Translational invariance after disorder averaging suggests to express the average Green function in Fourier space, where it is diagonal:

$$\overline{G}(k, \epsilon) = \int \mathrm{d}(x - x') e^{-ik(x-x')} \overline{G}(x, x', \epsilon) = G_0(k, \epsilon) + G_0(k, \epsilon) \left[\int \frac{\mathrm{d}q}{2\pi} B(q) G_0(k + q, \epsilon) G_0(k, \epsilon) \right] + \dots \tag{3.12}$$

This expression of the average Green function provides a natural starting point for perturbative calculations in random potentials. Before embarking into specific calculations, it is useful to rearrange the above series, which is the object of the next subsection.

3.1.2 The self-energy

For simplicity, let us assume a Gaussian random potential for the moment, such that the n-correlation functions appearing in equation (3.9) reduce to products of B through application of Wick theorem. Interestingly, at order $2n$ in V, the above procedure generates a term of the form

$$G_0(k, \epsilon) \left[\int \frac{\mathrm{d}q}{2\pi} B(q) G_0(k + q, \epsilon) G_0(k, \epsilon) \right]^n. \tag{3.13}$$

In fact, equation (3.13) is but one example of high order contributions (here of order $2n$) that can be obtained by chaining lower order contributions (here n identical second order contributions). This property suggests to introduce a quantity, the so-called self-energy $\Sigma(k, \epsilon)$, gathering all contributions separable in lower order contributions. The average Green function then writes

$$\overline{G}(k, \epsilon) = G_0(k, \epsilon) + G_0(k, \epsilon) \sum_{n=1}^{\infty} \left[\Sigma(k, \epsilon) G_0(k, \epsilon) \right]^n. \tag{3.14}$$

where $\Sigma(k, \epsilon)$ contains only those contributions to $\overline{G}(k, \epsilon)$ that cannot be factorized. Upon summing the geometric series, equation (3.14) reduces to the so-called Dyson equation

$$\overline{G}(k, \epsilon) = G_0(k, \epsilon) + G_0(k, \epsilon) \Sigma(k, \epsilon) \overline{G}(k, \epsilon) \Leftrightarrow \overline{G}(k, \epsilon) = \frac{1}{\epsilon - \epsilon_k - \Sigma(k, \epsilon)}. \tag{3.15}$$

At this point, the physical meaning of the self-energy starts to appear. Indeed, we have recasted the average Green function under a form reminiscent of the free Green function [equation (3.8)], the self-energy encoding the difference between the two. To make the role of the self-energy more clear, it is useful to go back to time,

$$\overline{G}(k, t) = \int \frac{\mathrm{d}\epsilon}{2\pi\hbar} e^{-i\epsilon t/\hbar} \frac{1}{(\epsilon - \Sigma') - \epsilon_k - i\Sigma''} \tag{3.16}$$

where we have split the real and imaginary parts of the self-energy $\Sigma = \Sigma' + i\Sigma''$. To perform the integration, one needs to know how Σ depends on ϵ. Under the assumption that Σ is a smooth function of energy, we can use the residue theorem to find

$$\overline{G}(k, t) = \theta(t) e^{-i(\epsilon_k + \Sigma'(\epsilon_k, k))t/\hbar} e^{\Sigma''(\epsilon_k, k)t/\hbar}, \tag{3.17}$$

where we have used the fact that the imaginary part of the self-energy must always be negative to guarantee causality. In fact, the absence of poles in the upper half plane, which guarantees causality[1], also implies Kramers-Kronig relations between the real and imaginary parts of $\overline{G}(k,\epsilon)$. Equation (3.17) should be compared to the definition of $\overline{G}(k,t)$ (which follows from equation (3.2) through a Fourier transform):

$$\overline{G}(k,t) = \theta(t)\overline{\langle k|e^{-iHt/\hbar}|k\rangle}. \tag{3.18}$$

Σ' thus simply encodes an energy shift. Σ'', on the other hand, encodes the lifetime of plane waves in the disordered potential.

Note that the concept of self-energy is not restricted to the Gaussian potentials considered here. For example, in the case of speckle potentials, the introduction of the complex Gaussian field E ($V = \pm|E|^2$) allows for a similar introduction of the self-energy as a simplification of the Born series (see [107] for more details about this procedure). By studying the properties of the self-energy series, one can define a weak disorder criterion, which should be satisfied for the self-energy to be described by the first few terms of its Born series. For speckle potentials, one finds [107]

$$\eta \ll k\sigma, \tag{3.19}$$

where $\eta = V_0/E_\sigma$. Here V_0 and E_σ are characteristics of the speckle potential considered. V_0 corresponds to the amplitude of the fluctuations and $E_\sigma = \hbar^2/m\sigma^2$ is the characteristic energy associated to the spatial correlation length σ (see chapter 2 for details).

In some cases (e.g. when the potential distribution does not allow for the application of Wick theorem), it can be useful to introduce the self-energy simply through (3.15) (as opposed to through the Born series).

3.1.3 Scattering mean free time and scattering mean free path

The imaginary part of the self-energy (Σ'') encodes the lifetime of plane waves in a disordered potential. This lifetime is usually called scattering mean free time, and denoted by τ. Another approach to calculating this lifetime is the Fermi golden rule:

$$\frac{\hbar}{\tau} = \int \mathrm{d}k' \overline{|\langle k|V|k'\rangle|^2}\delta(\epsilon_k - \epsilon'_k), \tag{3.20}$$

which writes in our context

$$\frac{\hbar}{\tau} = \int \mathrm{d}k' B(k-k')\delta(\epsilon_k - \epsilon'_k). \tag{3.21}$$

The Fermi golden rule (3.21) turns out to give an approximation of the lifetime at lowest order in V, which should be compared with the calculation of the imaginary part of the self-energy at lowest order in V, given by [equation (3.12)]

$$\Sigma'' = \mathrm{Im}\left[\int \frac{\mathrm{d}k'}{2\pi} B(k-k')G_0(k',\epsilon)\right]. \tag{3.22}$$

To simplify this equation, we first use the parity of $B(x)$ to infer that $B(k)$ is real, and then use:

$$\mathrm{Im}\left[G_0(k',\epsilon)\right] = \mathrm{Im}\left[\frac{1}{\epsilon - \epsilon'_k + i0^+}\right] = -i\pi\delta(\epsilon - \epsilon'_k). \tag{3.23}$$

[1] To evaluate equation (3.16) at negative times, we use complex analysis and close the contour in the upper-half complex plane: the analyticity of $\overline{G}(k,\epsilon)$ guarantees that $\overline{G}(k,t<0) = 0$ (causality). If the imaginary part of the self-energy were positive, a pole in the upper-half complex plane would contribute to $\overline{G}(k,t<0)$, thus violating causality.

This leads to

$$\Sigma''(k,\epsilon) = -\frac{1}{2}\int \mathrm{d}k' B(k-k')\delta(\epsilon-\epsilon'_k). \tag{3.24}$$

This results coincides with the Fermi golden rule (3.21). The factor 2 stems from the self-energy dealing with $|k\rangle$, while the Fermi golden rule deals with $|\,|k\rangle\,|^2$. The scattering mean free time is thus given by $\tau = -\hbar/(2\Sigma''(k,\epsilon_k))$.

A companion of the scattering mean free time is the scattering mean free path. To introduce it, we consider the Green function in real space,

$$\overline{G}(x,x',\epsilon) = \int \frac{\mathrm{d}k}{2\pi} e^{ik(x'-x)}\overline{G}(k,\epsilon) = \int \frac{\mathrm{d}k}{2\pi} e^{ik(x'-x)} \frac{1}{(\epsilon-\Sigma')-\epsilon_k - i\Sigma''}. \tag{3.25}$$

We assume again that the self-energy simply shifts the pole, such that

$$\overline{G}(x,x',\epsilon) = G_0(x,x',\epsilon-\Sigma')e^{-|x-x'|/2\ell}, \tag{3.26}$$

with

$$\ell = -\left[\frac{\hbar^2 k_{\tilde{\epsilon}}}{2m\Sigma''(k_{\tilde{\epsilon}},\tilde{\epsilon})}\right]_{\tilde{\epsilon}=\epsilon-\Sigma'} \qquad \left(k_{\tilde{\epsilon}} = \sqrt{2m\tilde{\epsilon}}/\hbar\right). \tag{3.27}$$

The average Green function can be viewed as a free Green function decaying over a distance ℓ. The particle (described by the modulus square of the wave function) thus typically propagates freely over a distance ℓ before being scattered, hence the name scattering mean free path for ℓ.

In a weak disordered potential, the plane waves have a finite lifetime τ, during which they typically travel a distance ℓ, with τ and ℓ set by the imaginary part of the self-energy. In the present context, these plane waves and associated self-energy form the quasi-particles which are commonly used as building blocks for the description of coherent effects (see e.g. [9]). Interestingly, one can generally recast the weak disorder criterion, equation (3.19) for speckle potentials, under the form $k_\epsilon \ell \gg 1$ [107]. Expressed in terms of the wave length $\lambda_\epsilon = 2\pi/k_\epsilon$, the weak disorder criterion becomes $\ell \gg \lambda_\epsilon$, which corresponds to well separated scattering events [108].

3.1.4 The spectral function

The two effects of the self-energy are clearly visible in the spectral function, defined as

$$A_k(\epsilon) = -\frac{1}{\pi}\mathrm{Im}\left[\overline{G}(k,\epsilon)\right] = \frac{|\Sigma''|}{\pi}\frac{1}{(\epsilon-\Sigma'-\epsilon_k)^2+\Sigma''^2}. \tag{3.28}$$

In the free case, $\Sigma = 0$, the spectral function is a delta function centered at ϵ_k. The effect of the disorder is twofold. On the one hand, the real part of the self-energy (Σ') shifts the maximum of the spectral function. On the other hand, the imaginary part of the self-energy (Σ'') broadens the peak. These two effects are illustrated in figure 3.1a. The broadening effect is also visible in figure 3.1b, which compares a numerically computed spectral function (details in the caption of figure 3.1) and equation (3.28) with the self-energy calculated at lowest order in V (Born approximation):

$$\Sigma = \int \frac{\mathrm{d}q}{2\pi} B(q) G_0(k+q,\epsilon) = \int \frac{\mathrm{d}q}{2\pi} \frac{B(q-k)}{\epsilon-\epsilon_q+i0^+}. \tag{3.29}$$

As visible in figure 3.1b, at weak disorder, the real part of the self-energy has a small effect. At stronger disorder, a precise account of the real part of the self-energy can be crucial, in particular for the calculation of the mobility edge [109].

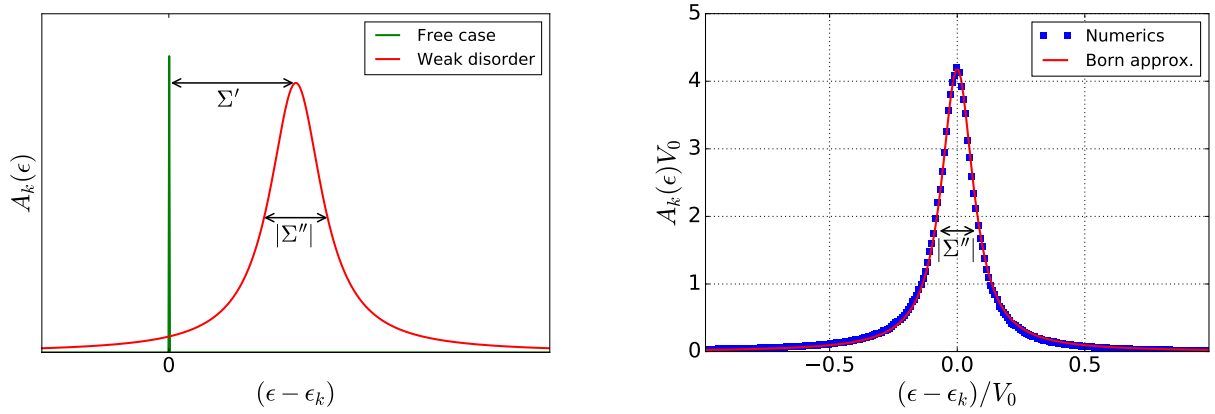

Figure 3.1 – a) Schematic representation of the effects of a weak disorder on the spectral function, through the self-energy Σ. The self-energy Σ is decomposed into its real part Σ' (shift of the peak) and its imaginary part Σ'' (width of the peak). b) Spectral function as a function of energy, for a weak, delta-correlated Gaussian potential ($\overline{V(x)V(x')} = V_0^2\delta(x-x')/k$, with $V_0 \simeq 0.076\ \hbar^2k^2/m$). The red line shows the perturbative result, equation (3.28), with Σ evaluated at the Born approximation [equation (3.29)]: $\Sigma \simeq -iV_0^2m/\hbar^2k^2 \simeq i\Sigma''$. This result is compared with numerical simulations, obtained by propagating a plane wave, $|k\rangle$, in a system of size $5000\pi/k$, discretized with 78540 grid points. The results are averaged over 2500 disorder realizations and periodic boundary conditions are used.

The physical meaning of the spectral function appears clear if one re-expresses (3.28) as

$$A_k(\epsilon) = -\frac{1}{\pi}\mathrm{Im}\left[\overline{G}(k,\epsilon)\right] = -\frac{1}{\pi}\overline{\mathrm{Im}\left[\langle k|\,\frac{1}{\epsilon - H + i0^+}\,|k\rangle\right]} = \overline{\langle k|\,\delta(\epsilon - H)\,|k\rangle}. \tag{3.30}$$

$A_k(\epsilon)$ is the average energy distribution of a plane wave $|k\rangle$ in the presence of the disorder. At weak disorder, the spectral function is sharply peaked, so that energies and momenta are generally used interchangeably.

The spectral function is a ubiquitous quantity for the characterization of the cold-atoms in random potentials. Its role in the description of the dynamics of atoms in random potentials is the object of the next section. Note that it has very recently been experimentally measured in 3D speckle potentials [110].

3.2 Importance of the spectral function in the dynamics of cold-atoms in random potentials

Let us consider a common experimental scenario in the context of Anderson localization: the spreading of a wave packet. In such an experiment, one tracks manifestations of Anderson localization in the freezing of the average density profile. What is really observed can however be more subtle, for the wave packet is generally made of several energy components ϵ. To see this, we introduce a central object, $P_\epsilon(x-x',t)$, the average probability for a particle of energy ϵ to go from x' to x given a time span t. The dynamics of the wave packet results from both the integration over the wave packet energy distribution and the convolution of $P_\epsilon(x-x',t)$ with the initial spatial profile. The wave packet energy distribution is essentially given by the spectral function $A_k(\epsilon)$, which has to

be weighted by the initial momentum distribution of the wave packet. To express the wave packet density, we introduce the joint position-momentum distribution, referred to as Wigner distribution,

$$W(x,p,t) = \frac{1}{2\pi\hbar}\int_{-\infty}^{\infty} \mathrm{d}y \psi^*(x+y/2,t)\psi(x-y/2,t)e^{-iyp/\hbar}. \tag{3.31}$$

The average density at time t is then written as

$$\overline{|\psi(x,t)|^2} = \int W(x',k,t=0)A_k(\epsilon)P_\epsilon(x-x',t)\mathrm{d}x'\mathrm{d}\epsilon\mathrm{d}k. \tag{3.32}$$

Note that this somewhat natural decomposition of the average density can be derived using the diagrammatic formalisms discussed in subsection 1.1 [42] and section 1.2 [111]. In equation (3.32), one identifies $\int \mathrm{d}k W(x',k,t=0)A_k(\epsilon)$ as the joint energy-position initial distribution. The wave packet density at time t then follows from the propagation of each energy component, starting from the initial spatial profile.

In the above decomposition, $P_\epsilon(x-x',t)$ plays a prominent role as it contains all the physics associated with Anderson localization. Nonetheless, forgetting completely about the rest would be dangerous. Indeed, the energy distribution can have drastic effects on the dynamics, even at reasonably weak disorder. Concretely speaking, let us consider the situation experimentally realized in [37], where an initially narrow wave packet evolves in a 1D speckle potential. This particular speckle potential has an intriguing feature: at weak disorder, the scattering mean path is strongly energy dependent, exhibiting sharp crossovers when the energy goes through specific values [47]. Following equation (3.32), the total evolution, integrated over all energy components of the wave packet, may thus differ from the evolution of an individual energy component. Indeed, at large distances, the (usually expected) Anderson exponential localization is turned into algebraic localization [112].

Conversely, as was pointed out in [46,113], a wave packet made of only diffusive atoms can appear close to localized because of the spectral function. Indeed, even if for a given energy ϵ, $P_\epsilon(x-x',t)$ is a diffusive kernel, the total evolution may appear subdiffusive due to the specific energy dependence of the diffusion coefficient. The total evolution in this case looks as if a single energy component with a subdiffusive kernel was at play, thus mimicking the onset of Anderson localization.

As demonstrated in [38, 40, 45], a precise account of the energy distribution is also required in the characterization of the Anderson transition in three dimensions. Indeed, in this case the energy distribution spreads on both sides of the mobility edge, making the complete dynamics a superposition of localized and diffusive behaviors. The knowledge of the energy distribution is then needed to extract physically relevant quantities (e.g. the position of the mobility edge) from the complete dynamics [114, 115].

All these reasons motived us to have a closer look at $A_k(\epsilon)$. This is the central question addressed in this chapter.

3.3 Strong disorder, semiclassical regime

We have seen in sections 3.1 and 3.2 that the spectral function is an important quantity to characterize the dynamics of wave packets in random potentials. We have been able to obtain it perturbatively in the weak disorder limit. The present section is devoted to the strong disorder limit (to be defined shortly), for which semiclassical approximations turn out to offer valuable tools.

3.3.1 Definitions and methods

We recall the definition of the spectral function [equation (3.30)]:

$$A_{\boldsymbol{k}}(\epsilon) = \overline{\langle \boldsymbol{k}| \, \delta\left(\epsilon - H\right) |\boldsymbol{k}\rangle}. \tag{3.33}$$

Introducing the Fourier representation of the Dirac delta function in equation (3.33), it follows that

$$A_{\boldsymbol{k}}(\epsilon) = \int_{-\infty}^{\infty} \frac{\mathrm{d}t}{2\pi\hbar} e^{i\epsilon t/\hbar} \overline{\langle \boldsymbol{k}| \, e^{-iHt/\hbar} \, |\boldsymbol{k}\rangle}, \tag{3.34}$$

which establishes the connection with the evolution operator $e^{-iHt/\hbar}$. The spectral function is related to the density of states per unit volume (DoS), $\nu(\epsilon)$, through the relation

$$\nu(\epsilon) = \frac{1}{L^d} \mathrm{Tr}\, \overline{\delta\left(\epsilon - H\right)} = \int \frac{\mathrm{d}^d \boldsymbol{k}}{(2\pi)^d} A_{\boldsymbol{k}}(\epsilon). \tag{3.35}$$

The amplitude of the potential fluctuations (V_0) defines a natural energy scale in the problem. Besides its fluctuations, the potential is characterized by its correlation length (σ), which defines another important energy scale, $E_\sigma = \hbar^2/m\sigma^2$. The ratio of these two energy scales,

$$\eta = \frac{V_0}{E_\sigma} = \frac{m\sigma^2 V_0}{\hbar^2}, \tag{3.36}$$

is of special importance. In the following, we focus on the so-called *semiclassical regime* characterized by the condition

$$\eta \gg 1. \tag{3.37}$$

Anticipating on the results presented below, we have represented pictorially the semiclassical limit in figure 3.2.

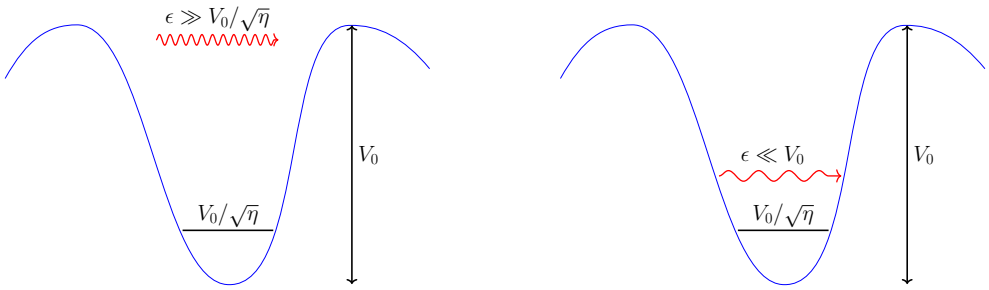

(a) High energies (b) Low energies

Figure 3.2 – Pictorial representation of the semiclassical limit for a blue-detuned speckle potential. The semiclassical condition $\eta \gg 1$ implies the existence of many states in typical minima of the potential (the typical lowest harmonic-state lying at $\hbar\omega_0 = V_0/\sqrt{\eta}$, see section 2.3 for more details). At higher energies (a), an expansion in powers of $\hbar$ is possible. This is the object of subsection 3.3.2. At low energies, on the contrary, corrections to the classical limit are singular. We present in subsection 3.3.3 a semiclassical approach, based on stationary phase approximations, allowing us to describe these singular quantum corrections.

In the classical limit $\eta \to \infty$, the non-commutation between position and momentum can be neglected, so that $\overline{\langle \boldsymbol{k}| \, e^{-iHt/\hbar} \, |\boldsymbol{k}\rangle} \approx e^{-i\hbar k^2 t/2m} \, \overline{e^{-iV(\boldsymbol{r})t/\hbar}}$. With in addition

$$\overline{e^{-iV(\boldsymbol{r})t/\hbar}} = \int \mathrm{d}V P(V) e^{-iVt/\hbar} = \frac{1}{1 \pm itV_0/\hbar}, \tag{3.38}$$

where $P(V)$ is the speckle on-site potential distribution [equation (2.30)], equation (3.34) yields

$$A^{\mathrm{cl}}_{\boldsymbol{k}}(\epsilon) = \int_{-\infty}^{\infty} \frac{\mathrm{d}t}{2\pi\hbar} \frac{e^{i(\epsilon-\epsilon_k)t/\hbar}}{1 \pm itV_0/\hbar} = P(\epsilon - \epsilon_k)\,, \tag{3.39}$$

with $\epsilon_k = \hbar^2\boldsymbol{k}^2/(2m)$. Note that in equations (3.38) and (3.39), V_0 encodes the variance of the potential. Note also that the slow decay in time of (3.38) is rooted in the discontinuity of the speckle on-site distribution [in contrast, the counterpart of (3.38) for a Gaussian potential decays as $\exp(-\alpha t^2)$]. In the classical limit, the spectral function thus mimics the on-site distribution [105]. With this result in hand, the classical DoS follows from equation (3.35):

$$\nu^{\mathrm{cl}}(\epsilon) = \int_0^{\infty} \mathrm{d}\epsilon_k \nu_0(\epsilon_k) P(\epsilon - \epsilon_k), \tag{3.40}$$

where ν_0 is the free-space DoS [105, 116].

The classical limit for the spectral function [equation (3.39)] is compared with numerical simulations in figure 3.3 for three different on-site distributions: a Gaussian (figure 3.3a), a red-detuned (figure 3.3b) and a blue-detuned speckle (figure 3.3c). Remarkably, the classical limit describes reasonably well the Gaussian case, which is smooth, but is completely inadequate near the discontinuity of the speckle distribution. This already suggests that perturbation theory around the classical limit should be sufficient for the description of the spectral function when the distribution is smooth. In contrast, a completely different starting point is probably more suited near the discontinuity of the speckle distribution.

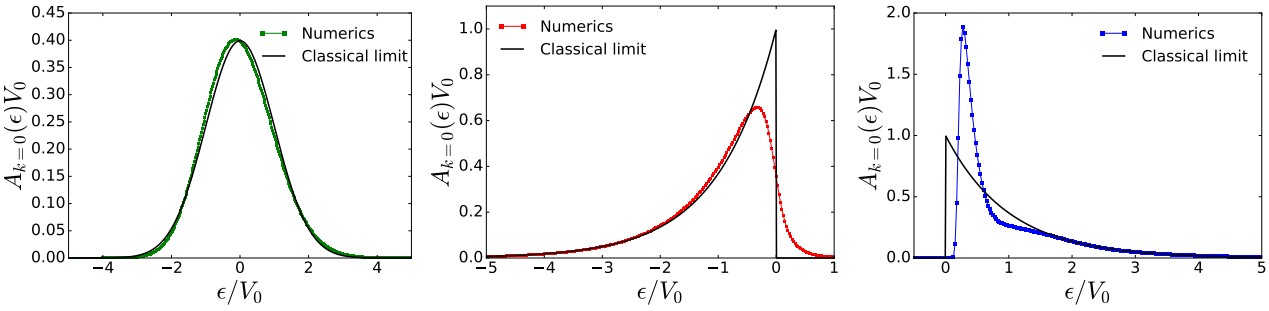

(a) Gaussian (b) Red-detuned speckle (c) Blue-detuned speckle

Figure 3.3 – Spectral function as a function of energy in a 2D random potential, for three different on-site distributions. In all three cases $\eta = 4$. The classical limit (3.39), shown as a black curve, is systematically compared with numerical results shown as colored squares. The on-site distributions are a) Gaussian, b) red-detuned speckle and c) blue-detuned speckle. The numerical results are taken from [105]. On the one hand, one observes than the spectral function is reasonably well described by the classical limit for the smooth Gaussian distribution. On the other hand, the exact spectral function differs widely from its classical limit near the discontinuity of the speckle distribution.

3.3.2 Smooth quantum corrections

To go beyond the classical limit, equation (3.39) for the spectral function and equation (3.40) for the DoS, it is natural to look for a expansion in powers of $\hbar$, where the leading order would be the classical limit and the next orders would bring corrections to it. This expansion can be worked out in two ways. One possibility is to work directly in the energy domain, and use Wigner-Weyl formalism [117]. The other possibility is to start from the representation of the spectral function in terms of the evolution operator, equation (3.34), and proceed with a commutator expansion of

the latter, followed by a cumulant expansion. Of course, either way leads to the same result. In this thesis, we touch upon the main steps of the commutator-cumulant expansion, and refer to our published paper, reproduced in section 3.5, for more details. The reader interested in the first way, based on the Wigner-Weyl formalism, can find the calculation in [105].

Note that while the results presented below for the spectral function extend directly to the DoS, through equation (3.35), we focus in this subsection on the spectral function only. As the DoS directly follows from the spectral function in equation (3.35), we felt that a specific discussion on the DoS would be redundant. This feeling is strengthened by the difficulty of getting reliable numerical results at large energy for the DoS, preventing quantitative comparison with exact numerical simulations.

Both the expansion in powers of $\hbar$ (present subsection) and the method based on a stationary phase approximation (subsection 3.3.3) apply to potentials with arbitrary correlation functions. For the sake of concreteness, we consider speckle potentials with a Gaussian correlation function:

$$\overline{V(\boldsymbol{r})V(\boldsymbol{r}')} = V_0^2 \exp\left(-\frac{|\boldsymbol{r}-\boldsymbol{r}'|^2}{2\sigma^2}\right). \tag{3.41}$$

Commutator-cumulant expansion of the evolution operator

We here present an expansion in powers of $\hbar$ of the evolution operator expectation value

$$\langle k|\, e^{-i\left(p^2/2m+V\right)t/\hbar}\, |k\rangle\,. \tag{3.42}$$

In the limit $\hbar \to 0$, p^2 and V commute and we have

$$\langle k|\, e^{-i\left(p^2/2m+V\right)t/\hbar}\, |k\rangle \xrightarrow[\hbar\to 0]{} e^{-i\frac{\hbar^2 k^2}{2m}\frac{t}{\hbar}}\, \langle k|\, e^{-iVt/\hbar}\, |k\rangle\,. \tag{3.43}$$

Corrections to this limit involve commutators of p^2 and V. This is encoded in Zassenhaus formula [118]:

$$e^{\tilde{t}(X+Y)} = e^{\tilde{t}X}\; e^{\tilde{t}Y}\; e^{-\frac{\tilde{t}^2}{2}[X,Y]}\; e^{\frac{\tilde{t}^3}{6}(2[Y,[X,Y]]+[X,[X,Y]])} + O(\tilde{t}^4). \tag{3.44}$$

To reveal the small parameter of the commutator expansion of (3.42), we introduce $\tilde{t} = tV_0/\hbar$, the time expressed in the natural units of the problem. With this definition, one natural recovers the classical limit (3.43) in the commutator expansion of (3.42) when $\hbar \to 0$. The following calculation is performed with the natural time $\tilde{t}$, to leading order in $\hbar$. The expansion of (3.42) involves a few commutators. Their calculation is tedious but straightforward, let us skip it and directly move on to the disorder average. Averaging over disorder can be done by mean of the following cumulant expansion:

$$\overline{\exp(X)} = \exp\left[\sum_{n=1}^{\infty} \frac{\kappa_n(X)}{n!}\right], \tag{3.45}$$

where $\kappa_n(X)$ denotes the n^{th} cumulant of X. In the present context, X is a sum of random variables. Cumulants of sum of random variables can be conveniently expressed with joint cumulants [119], which are basically a generalization of the notion of cumulant to several variables ($K_2(X)$ becomes $K_{\text{joint}}(X,X)$, allowing to consider $K_{\text{joint}}(X,Y)$ as well). Note that even at lowest order in $\hbar$, an infinite number of cumulants must be kept. The present expansion generates a wealth of terms which we do not want to show here, we prefer to restrict ourselves and only give the flavor of the calculation. The basic idea is to write the potential as[2]

$$V = \pm\left(E_1^2 + E_2^2\right), \tag{3.46}$$

[2]See section 2.2 for more details about this decomposition.

with the + (resp. −) sign for blue-(resp. red-)detuned speckles. Since E_1 and E_2 are independent Gaussian variables with zero mean and equal variance, the decomposition (3.46) is convenient when working with cumulants. The rest of the calculation is centered around a theorem due to Leonov and Shiryaev [120], which allows to disentangle the joint cumulants containing powers of the E_1 or E_2 into joint cumulants containing only E_1 or E_2 at first order, at the price of some combinatorics. Indeed, after writing the expansion in terms of joint cumulants containing only E_1 or E_2 at first order, the calculation is not difficult to carry out in Fourier space. Eventually, it boils down to the summation of geometric and logarithmic series. We find

$$\overline{\langle k|\, e^{-i\left[\frac{p^2}{2m}+V\right]\frac{t}{\hbar}}\, |k\rangle} = \frac{e^{-i\epsilon_k \tilde{t}/V_0}}{1 \pm i\tilde{t}} \times \left[1 + \frac{di\tilde{t}^3}{12\eta(1 \pm i\tilde{t})} + \frac{\tilde{t}^4}{12\eta(1 \pm i\tilde{t})}\frac{\epsilon_k}{V_0} + \dots\right], \tag{3.47}$$

where d is the space dimension. We recall that $\tilde{t} = tV_0/\hbar$. In the limit $k = 0$, the quantum correction is small when $\widehat{t} = \tilde{t}/\sqrt{\eta} = tV_0/\hbar\sqrt{\eta} \ll 1$. It defines the natural frequency unit in this context:

$$\omega_0 = \frac{V_0}{\hbar\sqrt{\eta}} = \sqrt{\frac{V_0}{m\sigma^2}}, \tag{3.48}$$

which is the typical oscillation frequency in a potential well of height V_0 and size σ. The condition of validity of equation (3.47) simply reads $\omega_0 t \ll 1$. The Fourier integral over time is then well approximated if:

$$|\epsilon| \gg \hbar\omega_0 = \frac{V_0}{\sqrt{\eta}}. \tag{3.49}$$

This discussion is put on a more solid ground in the next subsection through comparison with exact numerical simulations. For the sake of clarity, the limit (3.49) will be referred to as high energy limit in the following. The opposite low energy limit corresponding to $|\epsilon| \simeq \hbar\omega_0 = V_0/\sqrt{\eta}$.

Results and validity

The present subsection is largely based on [105] where the same results for the spectral function have been obtained using Wigner-Weyl formalism. The first-order correction to the classical limit, equation (3.47), is compared with exact numerical simulations in the insets of figure 3.4. The results confirm the discussion of subsection 3.3.2, namely the classical limit plus the small correction describe very well the high-energy limit, whereas as ϵ approaches $\hbar\omega_0 = V_0/\sqrt{\eta}$, the spectral function starts to deviate strongly from the classical approximation (main plots of figure 3.4) and the expansion loses its accuracy (insets of figure 3.4). In fact, for speckle potentials the low-energy region is non trivial. While the classical spectral function, equation (3.39), has a discontinuity at $\epsilon - \epsilon_k$, the exact spectral function is widely different: for a blue-detuned speckle, it rigorously vanishes below $\epsilon = 0$ and, for $k = 0$, it rapidly increases between $\epsilon = 0$ and $\epsilon \sim V_0/\sqrt{\eta}$.

To get some understanding on the low energy part, it is useful to repeat the calculation for a Gaussian potential, i.e. to trade the speckle on-site distribution, equation (2.30), to

$$P_{\text{Gaussian}}\left[V(\mathbf{r})\right] = \frac{1}{V_0\sqrt{2\pi}} \exp\left[-\frac{V(\boldsymbol{r})^2}{2V_0^2}\right]. \tag{3.50}$$

The calculation is much simpler in this case, as the Gaussian nature of the potential helps to carry out the cumulant expansion. The result is

$$\overline{\langle k|\, e^{-i\left[\frac{p^2}{2m}+V\right]\frac{t}{\hbar}}\, |k\rangle} = e^{-i\epsilon_k \tilde{t}/V_0} e^{-\tilde{t}^2} \times \left[1 + \frac{di\tilde{t}^3}{12\eta} + \frac{\tilde{t}^4}{12\eta}\frac{\epsilon_k}{V_0} + \dots\right]. \tag{3.51}$$

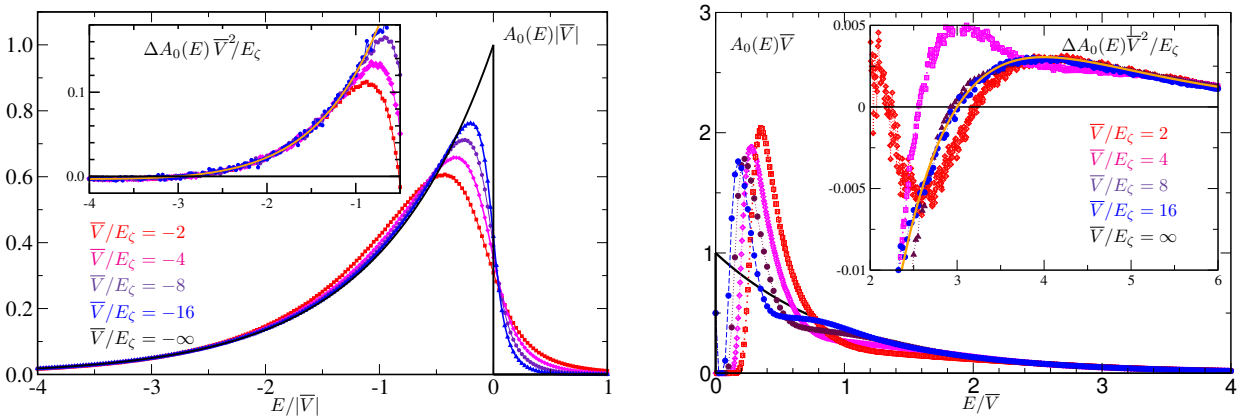

(a) Red-detuned speckle.

(b) Blue-detuned speckle.

Figure 3.4 – Figures from [105] showing the spectral function $A_{k=0}(\epsilon)$ as a function of energy ϵ in two dimensions, (a) red- and (b) blue-detuned, speckle potential with Gaussian correlation function. Note the following correspondences with our notations, $E = \epsilon$, $|\overline{V}/E_\zeta| = \eta$ and $|\overline{V}| = V_0$. Inset: focus on the correction to the classical limit, $\Delta A_k(\epsilon) = A_k(\epsilon) - A_k^{\mathrm{cl}}(\epsilon)$, The prediction (3.47) is shown as the solid orange curve.

The result exhibits a remarkable difference with its counterpart for speckle potentials, equation (3.47): the classical part decays exponentially with time, whereas it decays only as $1/t$ for speckle potentials. This difference has important manifestations in the spectral function, deduced from equations (3.47) and (3.51) by Fourier transform [equation (3.34)]. For speckle potentials, the quantum corrections generate unphysical singularities (delta functions and derivatives). In contrast, for Gaussian potentials, they remain small and the classical limit already offers an decent approximation of the spectral function, as visible in figure 3.5a. As shown in figures 3.5b and 3.5c, accounting for the quantum corrections only refines the description of the spectral function.

In conclusion, the expansion in powers of $\hbar$ is perfectly suited to describe the high energy limit for speckle potentials and fails at low energies, with in particular unphysical singularities (delta functions and derivatives). These difficulties are absent for Gaussian potentials, and are rooted in the discontinuity of the potential on-site distribution.

3.3.3 Treatment of low energies

Harmonic-oscillator approximation

We now would like to describe the quantum corrections to the classical limit in the low-energy region $\epsilon \sim V_0/\sqrt{\eta}$ for speckle potentials. As we have seen in subsection 3.3.2, an expansion in powers of $\hbar$ is not suited to tackle this regime, the quantum corrections to the classical expressions being singular. A non-perturbative method is called for. We propose an approach inspired of Gutwiller theory [121], for which we here sketch the essential ideas. The starting point is the Van Vleck form of the propagator, valid in the semiclassical regime [122, 123]:

$$\overline{\langle \boldsymbol{r}|\, e^{-iHt/\hbar}\, |\boldsymbol{r}'\rangle} \simeq \overline{\sum_\alpha (\dots)\, e^{iS^\alpha(\boldsymbol{r},\boldsymbol{r}',t)/\hbar}}, \tag{3.52}$$

where the sum runs over classical trajectories leading from $\boldsymbol{r}'$ to $\boldsymbol{r}$ during the time span t. $S^\alpha(\boldsymbol{r},\boldsymbol{r}',t)$ is the classical action associated with the classical trajectory α. We do not give the expression of the prefactors here. Their exact value is not important for the present preliminary discussion, where we remain at a qualitative level and want only to discuss which classical trajectories give

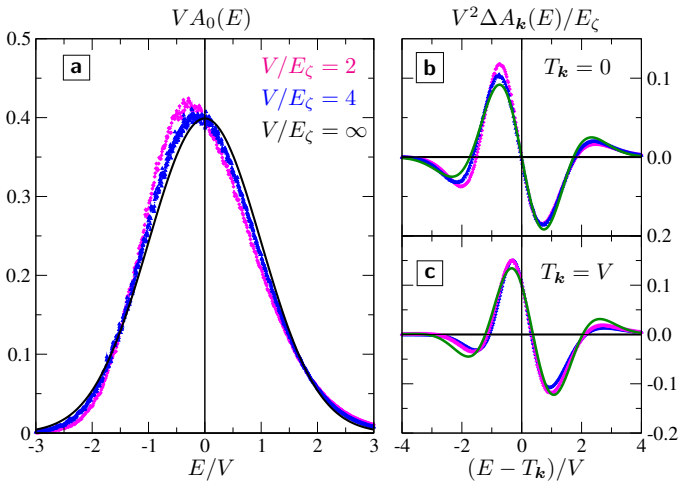

Figure 3.5 – Figures from [105] showing the spectral function $A_k(\epsilon)$ as a function of energy ϵ in a 2D Gaussian potential with Gaussian correlation function. Note the following correspondences with our notations, $E = \epsilon$, $V = V_0$, $E_\zeta = E_\sigma$, $T_k = \epsilon_k$. Figure (a) shows the spectral function, while figures (b) and (c) focus on the correction to the classical limit, $\Delta A_k(\epsilon) = A_k(\epsilon) - A_k^{\rm cl}(\epsilon)$. The prediction (3.51) is shown as the solid green curve.

the most important contributions. The sum over all classical trajectories is a very complicated one, obviously different for each disorder realization, making the averaging *a priori* rather complex. One can nevertheless convince oneself that the statistical properties of the potential will have a strong influence. For instance, for a blue-detuned speckle at low energy, there will be essentially short trajectories trapped in the potential wells, so that the peculiar distribution of energy minima will play a crucial role.

The spectral function is related to the propagator (3.52) through the relation

$$A_{\boldsymbol{k}}(\epsilon) = \int \frac{\mathrm{d}t}{2\pi\hbar} \int \frac{\mathrm{d}^d\Delta\boldsymbol{r}}{L^d} e^{i\epsilon t/\hbar - i\boldsymbol{k}\cdot\Delta\boldsymbol{r}} \overline{\langle \boldsymbol{r}|\, e^{-iHt/\hbar}\, |\boldsymbol{r}'\rangle}, \tag{3.53}$$

where $\Delta\boldsymbol{r} = \boldsymbol{r} - \boldsymbol{r}'$. The integral over time can be performed by a stationary phase approximation, which restricts the contributing classical trajectories to those with energy ϵ [123]. At the low energies $\epsilon < \hbar\omega_0$ we are targeting, such classical trajectories lie in potential wells (resp. inverted potential wells) for blue-detuned (resp. red-detuned) speckles. We propose to approximate these (inverted) wells by independent (inverted) harmonic oscillators[3]. Under this approximation, the stationary phase approximation becomes exact so one can simply replace the propagator (3.52) by the known propagator of an (inverted) harmonic oscillator [126].

Blue-detuned speckle

Within the harmonic oscillator approximation described above, equation (3.53) simply reduces to a sum of spectral functions of infinitely many random harmonic oscillators i whose minima V_i are centered at x_i. For the case of a 1D, blue-detuned speckle potential, this reads

$$A_k(\epsilon) \simeq \frac{1}{L} \overline{\sum_{x_i} \sum_{n=0}^{\infty} |\psi_n^i(k)|^2 \delta\left(\epsilon - \epsilon_n^i\right)}, \tag{3.54}$$

[3]Note that for blue-detuned speckle potentials, the spectral function and the density of states exhibit a Lifshitz tail at very small energies [124, 125]. This tail is intrinsically quantum and cannot be described by semiclassical approximations.

where $\psi_n^i(k)$ is the eigenfunction of the 1D i^{th} oscillator in k space:

$$\psi_n^i(k) = \frac{(2\pi)^{1/2}}{\sqrt{2^n n!}} \left(\frac{\hbar}{\pi m\omega_i}\right)^{1/4} e^{-\frac{\hbar k^2}{2m\omega_i} + ikx_i} H_n\left(\sqrt{\frac{\hbar k^2}{m\omega_i}}\right), \tag{3.55}$$

normalized according to $\int dk/(2\pi)|\psi_n^i(k)|^2 = 1$ and with associated eigenenergy $\epsilon_n^i = V_i + \hbar\omega_i(n + 1/2)$.

We now make use of the assumption that the harmonic wells are statistically independent, which allows us to take the sum over x_i out of the disorder average. The latter is then over the random frequency ω_i and the potential minimum V_i of a single oscillator only. To lighten the notations, we drop the now unnecessary i index. By introducing the joint distribution $P(V,\omega)$ of these two random variables, we rewrite equation (3.54) as

$$A_k(\epsilon) = \rho \sum_{n=0}^{\infty} \int dV d\omega P(V,\omega) |\psi_n(k)|^2 \delta(\epsilon - \epsilon_n), \tag{3.56}$$

where ρ is the average density of potential minima. ρ and the distribution $P(V,\omega)$ have been derived in section 2.3 for speckle potentials. Note that equation (3.56) is only justified if a typical harmonic well accommodates many states. In the semiclassical regime (3.37), this is indeed the case: as the typical frequency of the oscillator will be ω_0 and the typical depth of a potential well V_0, the number of states contained in the well is $\sim V_0/\hbar\omega_0 = \sqrt{\eta} \gg 1$.

Red-detuned speckle

For the red-detuned speckle potential, we proceed similarly. Here however, we do not care much about the potential wells which have energy minima typically of the order of $-V_0$, that is, in a range where the classical approximation works well (see figure 3.4a). Indeed, we are interested here in the energy range around $\epsilon = 0$, so that it is the potential *maxima* which are relevant. We thus make use of an inverted harmonic-oscillator approximation. In this case however, the representation (3.54) of the spectral function is not convenient due to the continuous nature of the spectrum of the inverted harmonic oscillator[4]. We therefore prefer to work in the time domain, using formulation (3.34) for the spectral function (written for a 1D speckle):

$$A_k(\epsilon) \simeq \rho \int_{-\infty}^{\infty} \frac{\mathrm{d}t}{2\pi\hbar} e^{i\epsilon t/\hbar} \overline{\langle k|\, e^{-iH_{\text{IHO}}t/\hbar}\, |k\rangle}, \tag{3.57}$$

where $H_{\text{IHO}} = p^2/(2m) - V_i - m\omega^2(x - x_i)^2/2$. The 1D inverted harmonic-oscillator propagator in k space is given by [126]

$$\langle k|\, e^{-iH_{\text{IHO}}t/\hbar}\, |k\rangle = 2\pi e^{iVt/\hbar} \sqrt{\frac{i\hbar}{2\pi m\omega \sinh(\omega t)}} \exp\left\{-\frac{i\hbar k^2}{m\omega}\left[\coth(\omega t) - \frac{1}{\sinh(\omega t)}\right]\right\}. \tag{3.58}$$

The disorder average is then carried out as in equation (3.56), by averaging over V and ω with the help of the joint distribution $P(V,\omega)$. By "returning" the potential $V(x) \to -V(x)$, we are back to the blue-detuned potential so the joint distribution of the maxima $P_{\text{red}}(V,\omega)$ is nothing but the joint distribution $P_{\text{blue}}(V,\omega)$ for the minima of a blue-detuned speckle. This symmetry also implies that the density of maxima for a red-detuned speckle is equal to the density of minima ρ for a blue-detuned speckle.

[4] It could be possible to perform a Wick rotation and express everything as a sum of imaginary "energies". This treatment is not very enlightening.

Note that, in principle, one could use the propagator of the harmonic oscillator in the time domain for calculating the spectral function of the blue-detuned speckle potential as well. This approach turns however inadequate due to the presence of an infinite number of singularities – when ωt is an integer multiple of π – arising in the time integral over the propagator.

In principle, the present method applies to any dimension, with the counterpart of the joint distribution $P(V,\omega)$ becoming a priori increasingly difficult to calculate as the dimension increases. We have successfully applied this method to the 1D and 2D cases in a published paper, reproduced in section 3.5. We here detail only the 1D case. The 2D case is quite similar, we merely comment on it in subsection 3.3.7.

3.3.4 Spectral function and density of states in one dimension: results

Plugging the joint distribution of minima and curvature around minima (2.45), as well as the density of minima (2.49), in the formulas of subsection 3.3.3, it is not difficult to obtain the spectral function and the DoS. The resulting predictions are however a bit cumbersome and not very enlightening, we thus choose not to reproduce them here. The interested reader can find them in our published paper, reproduced in section 3.5. It is more appealing to compare them to numerical simulations. This is done in figure 3.6 where we show systematically the (inverted) harmonic oscillator prediction as a red curve and the results from numerical simulations as blue points. For comparison, we also show the classical limits [equations (3.39) and (3.40)] as solid green curves.

As visible in figures 3.6a and 3.6b, in the blue-detuned case, the harmonic oscillator approximation describes very well the spectral function (figure 3.6a) and the DoS (figure 3.6b) at low energies. We can thus interpret the low-energy features of the spectral function and the DoS from this perspective. The peak of the spectral function in the blue-detuned case originates from the ground state of the harmonic oscillators. Its relatively narrow character comes from the ω distribution in equation (2.44) rather well peaked around $\omega = \omega_0$. The ensuing bump builds up upon adding excited states[5]. The narrow peak in turn results in a bump in the DoS at low energy, see figure 3.6b. Indeed, upon increasing k the peak of the spectral function becomes less and less pronounced but remains at the same energy, which results in a smooth bump after summation over k. At larger energies $\epsilon > V_0$ (not shown for the DoS in figure 3.6b), the harmonic-oscillator approximation breaks down and the purely classical limit takes over, eventually leading to $A_{k=0}(\epsilon) = \exp\left(-\epsilon/V_0\right)/V_0$ and $\nu(\epsilon) \simeq \nu_0(\epsilon) = \sqrt{m/(2\epsilon)}/(\pi\hbar)$ for $\epsilon \to \infty$ [116].

In the red-detuned spectral function case, shown in figure 3.6c, the inverted harmonic-oscillator prediction is in good agreement with the numerical results for energies near 0. At smaller energies ($\epsilon \lesssim -V_0$), the description of the speckle potential in terms of inverse harmonic oscillators becomes poor, while the classical limit provides an excellent approximation.

At variance with the blue-detuned DoS (figure 3.6b), the red-detuned DoS (figure 3.6d) is well described by the classical limit at all energies. This can be understood qualitatively from the Gutzwiller trace formula [121,127], which expresses the DoS as the sum of the classical contribution, equation (3.40), and of oscillatory contributions coming from periodic orbits. Around $\epsilon = 0$, the periodic orbits in a red-detuned speckle are long ones with characteristic properties (action, period...) which strongly depend on the disorder realization, so that all oscillatory contributions cancel out. This is indeed in stark contrast with the blue-detuned speckle where periodic orbits around $\epsilon = 0$ are short orbits trapped in the deep potential minima and collectively contribute to "bumps" in the DoS. The absence of inverted-harmonic oscillator prediction for the red-detuned DoS comes from an ultraviolet divergence. This divergence already appears in the DoS of the inverted harmonic oscillator, for which it originates of the continuous nature of the spectrum. It thus appears that for the DoS of red-detuned speckles, the description of singular quantum corrections requires to go

[5]Note that $|\psi_n(k=0)|^2$ vanishes for odd n, such that only even n contribute to $A_{k=0}(\epsilon)$ in equation (3.56).

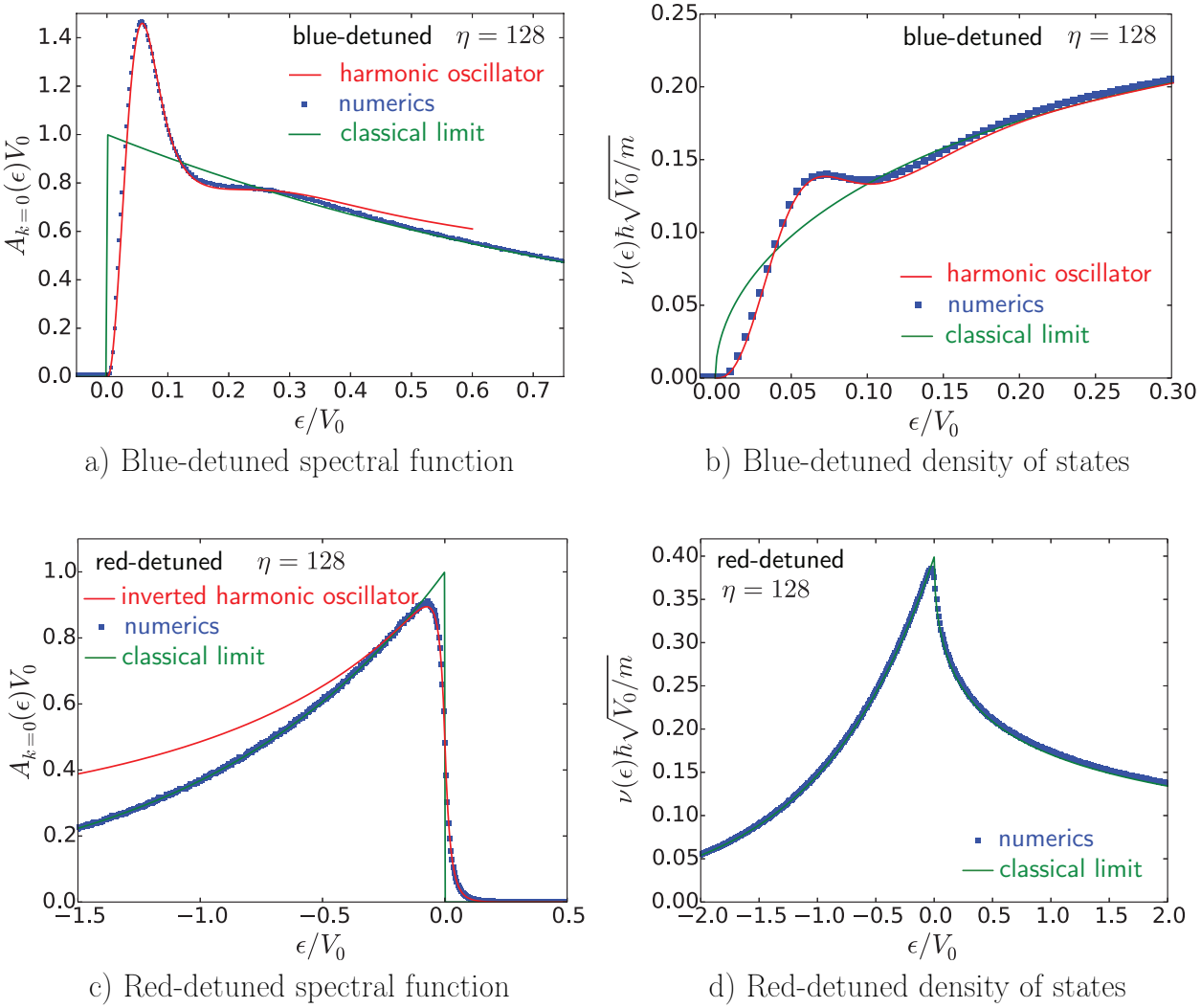

a) Blue-detuned spectral function

b) Blue-detuned density of states

c) Red-detuned spectral function

d) Red-detuned density of states

Figure 3.6 – Spectral function $A_{k=0}(\epsilon)$ and density of states $\nu(\epsilon)$ as a function of energy in a 1D blue(red-)-detuned speckle potential with Gaussian correlation function, for $\eta = 128$. The (inverted) harmonic-oscillator approximation of subsection 3.3.3 is systematically shown as a solid red curve, and the classical limit, equations (3.39) and (3.40) for the spectral function and the density of states respectively, as a solid green curve. Blue dots are the result of exact numerical simulations. The parameters used in the numerical simulations can be found in our published paper, reproduced in section 3.5.

beyond the inverted harmonic-oscillator approximation. In any case, these corrections are extremely small, as visible in figure 3.6d.

Note that very recent experimental measurements of the spectral function [110] corroborate these results at a qualitative level. In particular, the predicted dissymmetry between red- and blue-detuned speckles, as well as the peaked structure of the blue-detuned spectral function, were unambiguously observed. A quantitative comparison is impossible, as the experiment was performed with 3D speckles.

3.3.5 Validity of the harmonic-oscillator approximation

A simple argument can be used to estimate the energy range where the harmonic-oscillator approximation is valid. According to the virial theorem, equipartition between kinetic and potential energy imposes that $\epsilon_n = m\omega^2 \langle x^2 \rangle_n$ for the energy of an eigenstate. In order for the speckle potential to be correctly described by an harmonic-oscillator approximation, all states such that $\epsilon_n = \epsilon$ in equation (3.54) should have an extension $\sqrt{\langle x^2 \rangle_n}$ much smaller than the correlation length σ, which imposes an upper limit for the energy: $\epsilon \ll m\omega^2\sigma^2$ (in case this condition is not fulfilled, anharmonic terms would also come into play). As seen in subsection 2.3.1, the most likely value of ω is ω_0, so the condition becomes

$$\epsilon \ll V_0. \tag{3.59}$$

On the other hand, the classical approximation is expected to describe well the spectral function down to energies of order $V_0/\sqrt{\eta}$ [105]. Therefore, in the region $V_0/\sqrt{\eta} \ll \epsilon \ll V_0$ both the harmonic-oscillator and the classical approximation provide a good description of the spectral function and of the DoS.

Equation (3.59) provides a restriction on the high-energy tail of the spectral function $A_k(\epsilon)$ for the latter to be correctly described by our harmonic-oscillator approximation. A similar argument imposes an additional restriction for the momentum k. Indeed, equipartition between kinetic and potential energy for the harmonic oscillator also implies

$$\frac{\hbar^2 \langle k^2 \rangle_n}{2m} = \frac{1}{2} m\omega^2 \langle x^2 \rangle_n , \tag{3.60}$$

where $\sqrt{\langle x^2 \rangle_n}$ should be again much smaller than σ for the harmonic-oscillator approximation to hold. With $\omega \sim \omega_0$, condition (3.60) reads

$$\frac{\hbar^2 \langle k^2 \rangle_n}{m} \ll V_0. \tag{3.61}$$

The contribution of each eigenstate to the sum in equation (3.54) being proportional to $|\psi_n(k)|^2$, the sum is dominated by eigenstates having $\sqrt{\langle k^2 \rangle_n}$ of the order of k, such that criterion (3.61) leads to

$$\epsilon_k \ll V_0. \tag{3.62}$$

In any case, the harmonic oscillator approximation is a good one in the region $\epsilon, \epsilon_k \sim \hbar\omega_0$ where the quantum corrections are important, while the purely classical result (3.39) takes over at higher energy $\epsilon, \epsilon_k \sim V_0$.

3.3.6 Validity of the inverted harmonic-oscillator approximation

The breakdown of the inverted harmonic-oscillator approximation at energies $\epsilon \lesssim -V_0$ can be understood from a reasoning on the classical action that appears in equation (3.52). Indeed, for the stationary phase approximation to be valid, the time span t associated with a classical trajectory should be such that the classical action $V_0 t/\hbar$ is large, imposing $t \gg \hbar/V_0$. Energies corresponding to such long times fulfill

$$|\epsilon| \ll V_0. \tag{3.63}$$

Note that this condition is fully similar to that for blue-detuned speckles, equation (3.59), though it is here deduced from a slightly different argument. Then, the motion of a classical atom of energy $\epsilon = \epsilon_k - m\omega x^2/2$ describes well the dynamics in a red-detuned speckle as long as the excursion x^2 remains much smaller than σ, namely as long as $\epsilon_k + |\epsilon| \ll m\omega\sigma^2/2$. Since $\omega \sim \omega_0$ and $|\epsilon| \ll V_0$, this leads to

$$\epsilon_k \ll V_0, \tag{3.64}$$

which is the same validity condition as for blue-detuned speckles.

3.3.7 Higher dimensions

Having settled the 1D situation, we now briefly comment on the case of higher dimensions. The sharp behavior of the blue-detuned spectral function at low energy observed in one dimension is rooted in the presence of most minima at very low $V \ll V_0$ (see subsection 2.3.1). In this respect, one expects a sharper spectral function in two dimensions, reminiscent of the minima sitting *exactly* at $V = 0$ (see subsection 2.3.3). This is indeed what is numerically observed in figure 3.7 where the spectral function for a 1D and 2D blue-detuned speckle potentials are shown respectively as blue and green squares. We note that the 3D spectral function, shown as red squares, is even sharper. On the other hand, at high energies the 1D, 2D and 3D spectral functions all collapse on the classical limit [equation (3.39)] shown as a solid black curve.

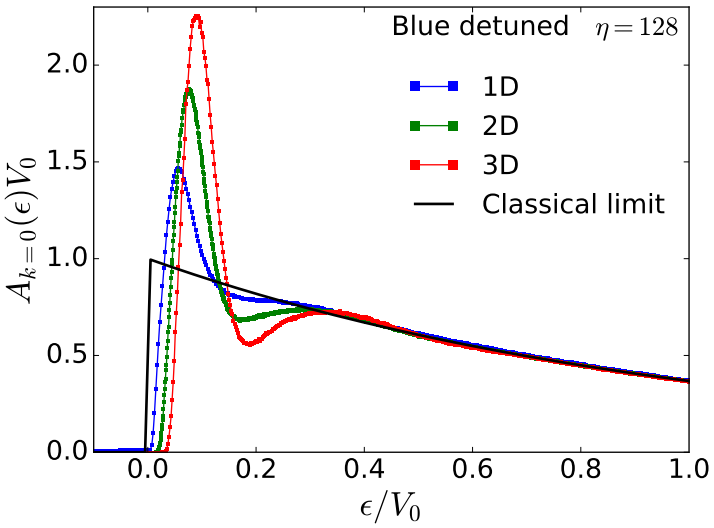

Figure 3.7 – Spectral function $A_{k=0}(\epsilon)$ as a function of energy in blue-detuned speckle potentials with Gaussian correlation function, for $\eta = 128$. The result for the one-dimensional case is shown as blue squares and is compared with the results obtained in two and three dimensions, respectively shown as green and red squares. The classical limit, equation (3.39), is the same in all dimensions and is shown as a solid black curve. The parameters used in the 1D and 2D numerical simulations can be found in our published paper, reproduced in section 3.5. In three dimensions, we have used a discrete grid of size $L^3 = (6\pi\sigma)^3$ with 120^3 grid points, and averaged the results over 720 disorder realizations.

Aside from the minima *exactly* at $V = 0$, the 2D case is quite similar to the 1D one. Results similar to those presented in subsection 3.3.4 can be found in our published paper, reproduced in section 3.5. The 3D case constitutes a technical challenge, because the points of vanishing potential responsible for the sharp 2D blue-detuned spectral function turn to curves. The approximation of isolated harmonic oscillators used throughout this section thus breaks down, one has to cope with valleys instead of isolated minima. We leave this challenging task for later work.

3.4 Conclusion

In this chapter, we have discussed many properties of the spectral function, a fundamental building block in the description of matter wave packets. We have introduced this concept by starting from the weak-disorder limit, and we have then discussed its importance in the characterization of the energy distribution, and thus the dynamics of wave packets. Directly connected with the spectral

function, the density of states came along. Although we have put less emphasis on it, it is also an important quantity, particularly in the discussion of phases of dirty interacting bosons [60, 71, 104].

In the core of this chapter, we have introduced two semiclassical methods aiming to describe the spectral function and the density of states in speckle potentials. We have seen how the corrections to the classical limit can be obtained through an expansion in powers of $\hbar$ of the spectral function or the density of states in the large energy sector. This expansion is however not sufficient at low energies, due to the discontinuity of the on-site potential distribution. In order to overcome this difficulty, we have developed a novel analytical method based on a semiclassical description of the dynamics combined with the statistical properties of potential extrema. Applying this approach to 1D blue- and red-detuned speckles, we have carried out the calculation of the spectral function and the DoS. The 2D case is very similar to the 1D one with some additional technical difficulties, we have preferred to left it aside here and refer the interested reader to our published paper, reproduced in section 3.5. In both the 1D and 2D cases, by connecting the two methods, a rather complete description of the whole energy spectrum is possible.

Our semiclassical description additionally provides a simple interpretation of intriguing features of the spectral function and DoS. In particular, for blue-detuned potentials we have shown that the low-energy peak of spectral functions is essentially associated with the ground state of an atom in a potential well of the speckle, while the secondary bump is associated with excited states. We have also emphasized that in spite of their simple symmetry, red- and blue-detuned speckles exhibit remarkably different features in the semiclassical regime, coming from the fundamental different nature of the classical trajectories involved near zero energy: for blue-detuned speckles, these classical trajectories lie in deep potential wells, while for red-detuned speckles they lie in the vicinity of the top of inverted wells.

As a logical continuation of this work, it would be of great interest to address the case of three-dimensional speckle potentials, involved in important questions related to Anderson localization [38, 40, 44, 109, 115, 128]. This task appears challenging though, due to the existence of curves along which the potential is vanishing, making the application of a harmonic oscillator approximation less obvious.

3.5 Article: *Semiclassical spectral function and density of states in speckle potentials* [Phys. Rev. A 94, 022114 (2016)]

Semiclassical spectral function and density of states in speckle potentials

Tony Prat, Nicolas Cherroret, and Dominique Delande
Laboratoire Kastler Brossel, UPMC-Sorbonne Universités, CNRS, ENS-PSL Research University, Collège de France; 4 Place Jussieu, 75005 Paris, France

(Received 8 June 2016; published 19 August 2016)

We present an analytical method for calculating the spectral function and the density of states in speckle potentials, valid in the semiclassical regime. Our approach relies on stationary phase approximations, allowing us to describe the singular quantum corrections at low energies. We apply it to the calculation of the spectral function and the density of states in one- and two-dimensional speckle potentials. By connecting our results with those of previous work valid in the high-energy sector, we end up with a consistent description of the whole energy spectrum, in good agreement with numerical simulations.

DOI: 10.1103/PhysRevA.94.022114

I. INTRODUCTION

Anderson localization, the absence of wave diffusion due to destructive interference between partial waves multiply scattered by a disordered potential [1], has been observed in a number of experiments involving atomic matter waves quasiperiodically kicked by laser pulses [2,3] or subjected to one-dimensional (1D) [4] and three-dimensional (3D) [5,6] quenched speckle potentials, as well as ultrasound waves in 3D disordered dielectric media [7]. In cold-atom setups, the control of atom-atom interactions (through, e.g., Feshbach resonances) together with a weak coupling to the environment constitute precious assets for the observation of interference effects in disorder. Furthermore, atom-optics experiments offer the possibility to directly probe localization phenomena *inside* the atomic system, as well as to follow their evolution in the course of time [8,9].

If atoms are injected into a disordered potential with an initial momentum $\boldsymbol{k}$, they no longer have a well defined energy ϵ but rather an energy distribution called the spectral function, denoted by $A_{\boldsymbol{k}}(\epsilon)$. The spectral function thus defines a quasiparticle, and generally speaking can provide important physical insights to the complex problem of disorder scattering even without the knowledge of the system's eigenstates [10]. Even more, it turns out that to achieve a quantitative understanding of cold-atom experiments in speckle potentials and in particular to properly characterize Anderson localization, a good knowledge of the spectral function is crucial. Indeed, when disorder is strong enough the spectral function is broad, which can have important consequences for the global motion of an atomic cloud. For instance, a cloud of atoms that are individually diffusive may exhibit a global subdiffusive behavior as a result of the superposition of the various energy-dependent atomic diffusion coefficients, thus mimicking the onset of localization [11,12]. Furthermore, even if the cloud contains localized atoms, usually a finite part of it remains diffusive and a precise characterization of the spectral function is then required in order to pinpoint the location of the mobility edge [6,13]. Related to the spectral function, the density of states (DOS) in strong speckle potentials is also poorly understood. This question is however essential as the DOS plays a central role in atomic physics, in particular in the discussion of phases of interacting bosons [14–16].

Despite its importance, the calculation of the spectral function of speckle potentials in the strong disorder regime has been little addressed, the main difficulty stemming from the inapplicability of weak-disorder approximations in this regime. Recently however, a systematic semiclassical expansion of the spectral function around the classical solution has been proposed [17]. Although successful in the large-energy sector, the approach of [17] fails at capturing the singular quantum corrections at low energies. As far as the DOS is concerned, important progress has been recently accomplished by Falco *et al.* [18], who used a classical approximation for describing high energies in speckle potentials. Again however, this approach remains inaccurate to capture the low-energy sector. As a matter of fact, the difficulty of treating low energies in speckle potentials lies in the singular nature of quantum corrections in this region of the spectrum. Such singular corrections are absent for Gaussian random potentials [17] frequently used in condensed-matter physics [19]. To our knowledge, they have not been described yet.

In this paper, we calculate the spectral function and the density of states in one- (1D) and two-dimensional (2D) speckle potentials, making use of a semiclassical approach based on stationary phase approximations, thereby allowing for a nonanalytic perturbation expansion in $\hbar$. Our theoretical predictions are in good agreement with exact numerical simulations in the low-energy sector where quantum corrections are singular. By connecting our results with those of [17], we eventually end up with a consistent description of the whole energy spectrum. Section II is devoted to the definition of the relevant quantities and to a discussion of the results previously obtained in [17]. Our semiclassical approach is also introduced and discussed. In Sec. III, we derive important statistical properties of 1D speckles needed to implement our semiclassical theory. Results for the 1D spectral function and DOS are presented in Sec. IV. The approach is then extended to the 2D case in Secs. V and VI. In Sec. VII, we finally summarize our findings and discuss some open questions.

II. DEFINITIONS AND METHODS

A. Framework

We consider a cloud of noninteracting atoms of mass m, subjected to a random potential $V(\boldsymbol{r})$. Its dynamics is governed by the Hamiltonian

$$H = \frac{\boldsymbol{p}^2}{2m} + V(\boldsymbol{r}), \tag{1}$$

where $\boldsymbol{p} = -i\hbar\nabla$. The coordinate vector $\boldsymbol{r} \in [0,L]^d$ lies in a d-dimensional cubic volume of linear size L that we will eventually make tend to infinity. In the following, averaging over the random potential will be indicated by an overline: $\overline{(\dots)}$. In practice, speckle potentials are obtained by transmission or reflection of a laser through a rough plate. The resulting potential $V(\boldsymbol{r})$ felt by atoms subjected to this light is proportional to the square of a complex Gaussian field [20], with a sign that depends on the laser detuning with respect to the considered two-level transition. This potential has the following on-site distribution:

$$P[V(\mathbf{r})] = \frac{1}{V_0}\theta[\pm V(\boldsymbol{r})]\exp\left[\mp\frac{V(\boldsymbol{r})}{V_0}\right], \tag{2}$$

where $\theta(\dots)$ is the Heaviside θ function. The disorder strength $V_0 > 0$ enters both the average $\overline{V(\boldsymbol{r})} = \pm V_0$ and the variance $\overline{V(\mathbf{r})^2} - \overline{V(\mathbf{r})}^2 = V_0^2$. In Eq. (2), the upper sign refers to a blue-detuned speckle potential, bounded by zero from below, and the lower sign to a red-detuned speckle potential, bounded by zero from above. Another quantity that we will frequently encounter in the following is the two-point correlation function $\overline{V(\boldsymbol{r})V(\boldsymbol{r}')} - \overline{V(\boldsymbol{r})}^2$. For the isotropic speckles considered in this paper, the two-point correlation function depends only on $|\boldsymbol{r} - \boldsymbol{r}'|$. It decays over a typical distance σ, referred to as the correlation length [20]. σ defines an important characteristic energy scale, the so-called correlation energy [21]:

$$E_\sigma = \frac{\hbar^2}{m\sigma^2}. \tag{3}$$

The two-point correlation function can take various forms depending on the experimental setup [20]. The approach developed in this paper in principle applies to any shape of the correlation function, but the results for the spectral function and the DOS turn out to very weakly depend on it, provided the proper value of σ is chosen. Consequently, for definiteness we will only consider the Gaussian case in the following:

$$\overline{V(\mathbf{r})V(\boldsymbol{r}')} - \overline{V(\boldsymbol{r})}^2 = V_0^2\exp\left(-\frac{|\boldsymbol{r} - \boldsymbol{r}'|^2}{2\sigma^2}\right). \tag{4}$$

As an example, we show in Fig. 1 a numerical disorder realization of both a blue and a red-detuned 1D speckle potential. To generate these realizations, we use a numerical procedure that precisely describes the experimental scenario: we first generate a spatially uncorrelated complex random Gaussian field in Fourier space, simulating the transmission through the rough plate. This field is then multiplied by a proper cutoff function—that physically describes the shape of the plate—which we take Gaussian to reproduce the two-point correlation function (4). Finally, (the opposite of) the modulus square of the field in coordinate space gives the blue-(red-)detuned speckle potential visible in the observation plane [20].

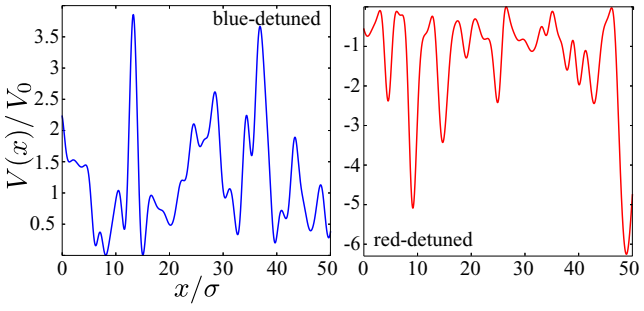

FIG. 1. Numerical realizations of a red- (left) and a blue-detuned (right) 1D speckle potential. The on-site distribution is given by Eq. (2) and the two-point correlation function by Eq. (4). The procedure used to numerically generate the speckle is explained in the main text.

B. Definitions, semiclassical regime

The figure of merit of this paper is the spectral function, defined as

$$A_{\boldsymbol{k}}(\epsilon) = \overline{\langle\boldsymbol{k}|\,\delta(\epsilon - H)\,|\boldsymbol{k}\rangle}. \tag{5}$$

Physically, the spectral function is the probability density for a plane wave $|\boldsymbol{k}\rangle$ to have energy ϵ in the potential $V(\boldsymbol{r})$. At vanishing disorder, the spectral function is a Dirac δ function centered at energy $\hbar^2k^2/2m$. Upon increasing the disorder, this peak acquires a finite width and, at strong disorder, starts to develop intriguing structures that we wish to explore. Introducing the Fourier representation of the Dirac δ function in Eq. (5), it follows that

$$A_{\boldsymbol{k}}(\epsilon) = \int_{-\infty}^{\infty}\frac{dt}{2\pi\hbar}e^{i\epsilon t/\hbar}\overline{\langle\boldsymbol{k}|\,e^{-iHt/\hbar}\,|\boldsymbol{k}\rangle}, \tag{6}$$

which establishes the connection with the evolution operator $e^{-iHt/\hbar}$. The spectral function is related to the DOS per unit volume $\nu(\epsilon)$ through the relation

$$\nu(\epsilon) = \frac{1}{L^d}\mathrm{Tr}\,\overline{\delta(\epsilon - H)} = \int\frac{d^d\boldsymbol{k}}{(2\pi)^d}A_{\boldsymbol{k}}(\epsilon). \tag{7}$$

There are several energy scales in the problem: E, E_σ, V_0, and only their ratio matter. Of special importance is the parameter

$$\eta = \frac{V_0}{E_\sigma} = \frac{m\sigma^2V_0}{\hbar^2}. \tag{8}$$

In this paper, we focus on the so-called *semiclassical regime* characterized by the condition [17,18]

$$\eta \gg 1. \tag{9}$$

This inequality has a simple interpretation: $\sqrt{\eta}$ is the ratio of the disorder correlation length σ to the de Broglie wavelength of a particle with energy V_0, so that, in the semiclassical regime, the quantum particle can resolve all the potential fluctuations. Alternatively, a quantum particle with energy V_0 encountering a potential barrier of height V_0 and thickness σ will have a vanishingly small probability $\exp(-\sqrt{\eta})$ to tunnel through it, making the dynamics almost classical.

In the deep semiclassical limit $\eta \to \infty$, the noncommutation between position and momentum can be neglected, so that $\overline{\langle\boldsymbol{k}|\,e^{-iHt/\hbar}\,|\boldsymbol{k}\rangle} \approx e^{-i\hbar k^2t/2m}\,\overline{e^{-iV(\boldsymbol{r})t/\hbar}}$ and Eq. (6) yields

$$A_{\boldsymbol{k}}^{\mathrm{cl}}(\epsilon) = \int_{-\infty}^{\infty}\frac{dt}{2\pi\hbar}\frac{e^{i(\epsilon-\epsilon_k)t/\hbar}}{1 \pm itV_0/\hbar} = P(\epsilon - \epsilon_k), \tag{10}$$

where $\epsilon_k = \hbar^2 \boldsymbol{k}^2/(2m)$ and $P(\epsilon)$ is the on-site potential distribution [Eq. (2)]. In the classical limit, the spectral function thus mimics the on-site distribution (2) [17]. With this result in hand, the classical DOS then follows from Eq. (7):

$$\nu^{\rm cl}(\epsilon) = \int_0^\infty d\epsilon_k \nu_0(\epsilon_k) P(\epsilon - \epsilon_k), \tag{11}$$

where ν_0 is the free-space DOS [17,18].

C. Smooth quantum corrections

For both the spectral function and the density of states, it is possible to calculate the smooth quantum corrections to the classical limits (10) and (11) from an analytic expansion in $\hbar$. The calculation of the first quantum correction has been recently carried out in [17] in the energy domain from Wigner-Weyl formalism [22]. The calculation is also possible in the time domain from an expansion of the evolution operator, as we show in Appendix A. In any dimension d, either of the two approaches leads to

$$A_{\boldsymbol{k}}(\epsilon) = \int_{-\infty}^{\infty} \frac{dt}{2\pi\hbar} \frac{e^{i(\epsilon-\epsilon_k)t/\hbar}}{1 \pm i t V_0/\hbar} \times \left[1 + \frac{dit^3 V_0^2 E_\sigma/\hbar^3}{12(1 \pm i t V_0/\hbar)} + \frac{t^4 V_0^2 E_\sigma/\hbar^4}{12(1 \pm i t V_0/\hbar)} \epsilon_k\right], \tag{12}$$

with again the $+$ $(-)$ sign for the blue-(red-)detuned speckle. As was noticed in [17], Eq. (12) is correct only at large energies. For $\boldsymbol{k} = 0$, this can be readily seen from the observation that the first quantum correction term should remain small for the perturbation theory to be valid. This term is of the order of $t^2 V_0 E_\sigma/\hbar^2 \sim (t/\hbar)^2 V_0^2/\eta$. It is useful to define the natural frequency unit in this context:

$$\omega_0 = \sqrt{\frac{V_0}{m\sigma^2}} = \frac{V_0}{\hbar\sqrt{\eta}}, \tag{13}$$

which is the typical oscillation frequency in a potential well of height V_0 and size σ. The condition of validity of Eq. (12) simply reads $\omega_0 t \ll 1$. The Fourier integral over time is then well approximated if

$$\epsilon \gg \hbar\omega_0 = \frac{V_0}{\sqrt{\eta}}. \tag{14}$$

If one performs the Fourier integral in Eq. (12) at energies smaller than $V_0/\sqrt{\eta}$, the failure of the perturbation expansion manifests itself as unphysical singularities (δ functions and derivatives). One should then resort to another approach, which is the object of the next section. In fact, as noted in [17], for speckle potentials the low-energy region is nontrivial. While the classical spectral function, Eq. (10), has a discontinuity at $\epsilon - \epsilon_k$, the exact spectral function is widely different: for a blue-detuned speckle, it rigorously vanishes below $\epsilon = 0$ and, for $k = 0$, it rapidly increases between $\epsilon = 0$ and $\epsilon \sim V_0/\sqrt{\eta}$. These difficulties are absent for Gaussian potentials [17].

D. Treatment of low energies

1. Harmonic-oscillator approximation

We now would like to describe the quantum corrections to the classical limit in the low-energy region $\epsilon \sim V_0/\sqrt{\eta}$ for speckle potentials. For this purpose, we propose an approach inspired of Gutwiller theory [23], for which we here sketch the essential ideas. The starting point is the Van Vleck form of the propagator, valid in the semiclassical regime [24,25]:

$$\overline{\langle \boldsymbol{r}|\, e^{-iHt/\hbar}\, |\boldsymbol{r}'\rangle} \simeq \overline{\sum_\alpha (\dots) e^{iS^\alpha(\boldsymbol{r},\boldsymbol{r}',t)/\hbar}}, \tag{15}$$

where the sum runs over classical trajectories leading from $\boldsymbol{r}'$ to $\boldsymbol{r}$ during the time span t. $S^\alpha(\boldsymbol{r},\boldsymbol{r}',t)$ is the classical action associated with the classical trajectory α. We do not give the expression of the prefactors here. Their exact value is not important for the present preliminary discussion, where we remain at a qualitative level and want only to discuss which classical trajectories give the most important contributions. The sum over all classical trajectories is a very complicated one, obviously different for each disorder realization, making the averaging *a priori* rather complex. One can nevertheless envision that the statistical properties of the potential may have a strong influence. For a blue-detuned speckle at low energy, there will be essentially short trajectories trapped in the potential wells, so that it is easy to understand that the peculiar distribution of energy minima will play a crucial role.

The spectral function is related to the propagator (15) through the relation

$$A_{\boldsymbol{k}}(\epsilon) = \int \frac{dt}{2\pi\hbar} \int \frac{d^d\Delta\boldsymbol{r}}{L^d} e^{i\epsilon t/\hbar - i\boldsymbol{k}\cdot\Delta\boldsymbol{r}} \overline{\langle \boldsymbol{r}|\, e^{-iHt/\hbar}\, |\boldsymbol{r}'\rangle}, \tag{16}$$

where $\Delta\boldsymbol{r} = \boldsymbol{r} - \boldsymbol{r}'$. The integral over time can be performed by a stationary phase approximation, which restricts the contributing classical trajectories to those with energy ϵ [25]. At the low energies $\epsilon < \hbar\omega_0$ we are targeting, such classical trajectories lie in potential wells (respectively inverted potential wells) for blue-detuned (respectively red-detuned) speckles. We propose to approximate these wells by independent harmonic oscillators [26]. Under this approximation, the stationary phase approximation becomes exact so one can simply replace the propagator (15) by the known propagator of a harmonic oscillator (respectively inverted harmonic oscillator) [29].

2. Blue-detuned speckle

Within the harmonic oscillator approximation described above, Eq. (16) simply reduces to a sum of spectral functions of infinitely many random harmonic oscillators i whose minima V_i are centered at $\boldsymbol{r}_i$. For the case of a 1D, blue-detuned speckle potential, this reads

$$A_k(\epsilon) \simeq \frac{1}{L} \overline{\sum_{x_i} \sum_{n=0}^{\infty} \left|\psi_n^i(k)\right|^2 \delta\left(\epsilon - \epsilon_n^i\right)}, \tag{17}$$

where $\psi_n^i(k)$ is the eigenfunction of the 1D ith oscillator in k space:

$$\psi_n^i(k) = \frac{(2\pi)^{1/2}}{\sqrt{2^n n!}}\left(\frac{\hbar}{\pi m\omega_i}\right)^{1/4} e^{-\hbar k^2/2m\omega_i + ikx_i} H_n\left(\sqrt{\frac{\hbar k^2}{m\omega_i}}\right),$$

normalized according to $\int dk/(2\pi)|\psi_n^i(k)|^2 = 1$ and with associated eigenenergy $\epsilon_n^i = V_i + \hbar\omega_i(n+1/2)$.

We now make use of the assumption that the harmonic wells are statistically independent, which allows us to take the sum over x_i out of the disorder average. The latter is then over the random frequency ω_i and the potential minimum V_i of a single oscillator only. By introducing the joint distribution $P(V_i,\omega_i)$ of these two random variables, we rewrite Eq. (17) as

$$A_k(\epsilon) = \rho\sum_{n=0}^{\infty}\int dV_i d\omega_i P(V_i,\omega_i)\left|\psi_n^i(k)\right|^2\delta\left(\epsilon-\epsilon_n^i\right), \quad (18)$$

where ρ is the average density of potential minima. Calculation of the distribution $P(V_i,\omega_i)$ will be the object of Sec. III. Note that Eq. (18) is only justified if a typical harmonic well accommodates many states. In the semiclassical regime (9), this is indeed the case: as the typical frequency of the oscillator will be ω_0 and the typical depth of a potential well V_0, the number of states contained in the well is $\sim V_0/\hbar\omega_0 = \sqrt{\eta} \gg 1$.

3. *Red-detuned speckle*

For the red-detuned speckle potential, we proceed similarly. The potential wells which can accommodate a harmonic series of bound states have energy minima typically of the order of $-V_0$, that is in a range where the classical approximation works well (see below). In contrast, we are interested in the energy range around $E = 0$, near the maximum allowed potential, and it is the potential *maxima* which are relevant. We thus make use of an inverted harmonic-oscillator approximation. In this case however, the representation (17) of the spectral function is not convenient due to the continuous nature of the spectrum of the inverted harmonic oscillator [30]. We therefore prefer to work in the time domain, using formulation (6) for the spectral function (written for a 1D speckle):

$$A_k(\epsilon) \simeq \rho\int_{-\infty}^{\infty}\frac{dt}{2\pi\hbar}e^{i\epsilon t/\hbar}\overline{\langle k|\, e^{-iH_{\rm IHO}t/\hbar}\,|k\rangle}, \quad (19)$$

where $H_{\rm IHO} = p^2/(2m) - V_i - m\omega_i^2(x-x_i)^2/2$. The 1D inverted harmonic-oscillator propagator in k space is given by [29]

$$\begin{aligned}\langle k|e^{-iH_{\rm IHO}t/\hbar}|k\rangle &= 2\pi e^{iV_i t/\hbar}\sqrt{\frac{i\hbar}{2\pi m\omega_i \mathrm{sh}(\omega_i t)}}\\ &\times\exp\left\{-\frac{i\hbar k^2}{m\omega_i}\left[\coth(\omega_i t)-\frac{1}{\mathrm{sh}(\omega_i t)}\right]\right\}. \quad (20)\end{aligned}$$

The disorder average is then carried out as in Eq. (18), by averaging over V_i and ω_i with the help of the joint distribution $P(V_i,\omega_i)$. By "returning" the potential $V(x) \to -V(x)$, we are back to the blue-detuned potential so the joint distribution of the maxima $P_{\rm red}(V_i,\omega_i)$ is nothing but the joint distribution $P_{\rm blue}(V_i,\omega_i)$ for the minima of a blue-detuned speckle. This symmetry also implies that the density of maxima for a red-detuned speckle is equal to the density of minima ρ for a blue-detuned speckle.

Note that, in principle, one could use the propagator of the harmonic oscillator in the time domain for calculating the spectral function of the blue-detuned speckle potential as well. This approach turns however inadequate due to the presence of an infinite number of singularities—when $\omega_i t$ is an integer multiple of π—arising in the time integral over the propagator.

III. STATISTICS OF 1D SPECKLE POTENTIALS

A. Joint distribution $P(V_i,\omega_i)$

In this section, we calculate the joint probability distribution $P(V_i,\omega_i)$ discussed above. From here on we drop the subscript i and merely write $P(V,\omega)$ to lighten the notations. We derive it for the blue-detuned speckle potential, for which it corresponds to the joint probability of minima and potential curvature around minima.

The distribution $P(V,\omega)$ is closely related to the joint, conditional probability distribution $P(V(x),\, V''(x)|V'(x) = 0,\, V''(x) > 0)$ of $V(x)$ and its second derivative $V''(x)$ given that $V'(x) = 0$ and $V''(x) > 0$, that we propose to calculate first. From here on we use the following abbreviated notation for the potential and its derivatives at point x:

$$V \equiv V(x),\;\; V_x \equiv V'(x),\;\; V_{xx} \equiv V''(x). \quad (21)$$

The above distribution follows from

$$P(V,V_{xx}|V_x = 0, V_{xx} > 0) = N \times \lim_{V_x\to 0}\frac{P(V,V_x,V_{xx})}{P(V_x)}. \quad (22)$$

The numerical constant N that appears in Eq. (22) stems from the fact that only positive curvatures are selected on the left-hand side, whereas on the right-hand side all possible values are understood. It will be later determined from the normalization condition. In order to compute the joint distribution $P(V,V_x,V_{xx})$, we follow Goodman [20] and write the potential as

$$V = \mathrm{Re}(x)^2 + \mathrm{Im}(x)^2. \quad (23)$$

Up to a constant multiplicative factor, $\mathrm{Re}(x)$ and $\mathrm{Im}(x)$ respectively describe the real and imaginary parts of the laser electric field at point x, from which the speckle potential V is built. As for the potential, we introduce the following short-hand notations:

$$\begin{aligned}&\Re \equiv \mathrm{Re}(x),\;\; \Re_x \equiv \frac{d}{dx}\mathrm{Re}(x),\;\; \Re_{xx} \equiv \frac{d^2}{dx^2}\mathrm{Re}(x)\\ &\Im \equiv \mathrm{Im}(x),\;\; \Im_x \equiv \frac{d}{dx}\mathrm{Im}(x),\;\; \Im_{xx} \equiv \frac{d^2}{dx^2}\mathrm{Im}(x).\end{aligned} \quad (24)$$

The motivation for introducing the fields $\Re$ and $\Im$ is that they are independent Gaussian variables with zero mean and equal variance [20]. Their derivatives are likewise Gaussian, since any linear transformation of a Gaussian retains Gaussian statistics. They also have a zero mean. As a consequence, the six random variables of interest obey the multidimensional

Gaussian distribution

$$P(\Re,\Im,\Re_x,\Im_x,\Re_{xx},\Im_{xx}) = \frac{e^{-\mathbf{u}^t C^{-1}\mathbf{u}/2}}{8\pi^3\sqrt{\det(C)}}, \tag{25}$$

where $\mathbf{u}^t$ is a row vector with entries $(\Re,\Im,\Re_x,\Im_x,\Re_{xx},\Im_{xx})$, and C is the covariance matrix

$$C = \begin{pmatrix} \overline{\Re\Re} & \overline{\Re\Im} & \overline{\Re\Re_x} & \overline{\Re\Im_x} & \overline{\Re\Re_{xx}} & \overline{\Re\Im_{xx}} \\ \overline{\Im\Re} & \overline{\Im\Im} & \overline{\Im\Re_x} & \overline{\Im\Im_x} & \overline{\Im\Re_{xx}} & \overline{\Im\Im_{xx}} \\ \overline{\Re_x\Re} & \overline{\Re_x\Im} & \overline{\Re_x\Re_x} & \overline{\Re_x\Im_x} & \overline{\Re_x\Re_{xx}} & \overline{\Re_x\Im_{xx}} \\ \overline{\Im_x\Re} & \overline{\Im_x\Im} & \overline{\Im_x\Re_x} & \overline{\Im_x\Im_x} & \overline{\Im_x\Re_{xx}} & \overline{\Im_x\Im_{xx}} \\ \overline{\Re_{xx}\Re} & \overline{\Re_{xx}\Im} & \overline{\Re_{xx}\Re_x} & \overline{\Re_{xx}\Im_x} & \overline{\Re_{xx}\Re_{xx}} & \overline{\Re_{xx}\Im_{xx}} \\ \overline{\Im_{xx}\Re} & \overline{\Im_{xx}\Im} & \overline{\Im_{xx}\Re_x} & \overline{\Im_{xx}\Im_x} & \overline{\Im_{xx}\Re_{xx}} & \overline{\Im_{xx}\Im_{xx}} \end{pmatrix}.$$

The entries of this matrix can be explicitly calculated for a blue-detuned speckle potential. This yields

$$C = \begin{pmatrix} F(0) & 0 & 0 & 0 & F''(0) & 0 \\ 0 & F(0) & 0 & 0 & 0 & F''(0) \\ 0 & 0 & -F''(0) & 0 & 0 & 0 \\ 0 & 0 & 0 & -F''(0) & 0 & 0 \\ F''(0) & 0 & 0 & 0 & F^{(4)}(0) & 0 \\ 0 & F''(0) & 0 & 0 & 0 & F^{(4)}(0) \end{pmatrix},$$

where $F(x)$ is related to the two-point correlation function of the potential V through

$$F(x-x') = \tfrac{1}{2}\sqrt{\overline{V(x)V(x')} - \overline{V(x)}^2}. \tag{26}$$

We then introduce in Eq. (25) the change of variables

$$\Re = \sqrt{V}\cos\theta, \quad \Im = \sqrt{V}\sin\theta, \tag{27}$$

from which we calculate the distribution $P(V,\theta,V_x,\theta_x, V_{xx},\theta_{xx})$, with a corresponding Jacobian equal to $1/8$. By explicitly evaluating the entries of the C matrix for the Gaussian correlation function (4) and calculating the remaining integrals over θ, θ_x, and θ_{xx} with Mathematica [31], we find

$$\begin{aligned} &P(V,V_x,V_{xx}) \\ &= \frac{\sigma^4}{4\sqrt{2\pi}V_0^3 V} e^{-[24V+16V_{xx}\sigma^2+(V_x^2-2VV_{xx})^2\sigma^4/V^3]/16V_0} \\ &\quad\times\left\{ I_{-1/4}\left[\frac{(V_x^2-2VV_{xx})^2\sigma^4}{16V^3V_0}\right] \right. \\ &\quad\left. + I_{1/4}\left[\frac{(V_x^2-2VV_{xx})^2\sigma^4}{16V^3V_0}\right]\right\}\sqrt{\frac{(-V_x^2+2VV_{xx})V_0}{V}}, \end{aligned} \tag{28}$$

where $I_{1/4}$ and $I_{-1/4}$ are the modified Bessel functions of the first kind. Note that this expression is valid only when $V_x^2 - 2VV_{xx} < 0$, a condition fulfilled since only minima of the potential are considered [32]. The distribution $P(V,V_x,V_{xx})$ is regular with respect to the limit $V_x \to 0$. In Eq. (22), we can thus take this limit separately in the numerator and denominator, reducing the latter to a numerical constant which can be absorbed in the normalization prefactor N.

From the joint distribution (28), we are now in position to access the probability $P(V,V_{xx}|V_x=0,V_{xx}>0)$ using Eq. (22). The result is

$$\begin{aligned} &P(V,V_{xx}|V_x=0,V_{xx}>0) \\ &= \frac{N\sqrt{V_{xx}}}{V} e^{-(6V^2+4VV_{xx}\sigma^2+V_{xx}^2\sigma^4)/4V_0V} \\ &\quad\times\left[I_{-1/4}\left(\frac{V_{xx}^2\sigma^4}{4VV_0}\right) + I_{1/4}\left(\frac{V_{xx}^2\sigma^4}{4VV_0}\right)\right]. \end{aligned} \tag{29}$$

By imposing that the distribution is normalized, we find $N = \sigma^5/(2cV_0^{5/2})$, where $c = [\sqrt{3}\Gamma(1/4)\Gamma(5/4) - \Gamma(-1/4)\Gamma(7/4)]/(3^{3/4}\sqrt{2\pi}) \simeq 1.006\,85$, which will be replaced by 1 in the following.

The last stage of the calculation consists of connecting $P(V,V_{xx}|V_x=0,V_{xx}>0)$ to the sought for distribution $P(V,\omega)$. This amounts to changing the variables from $V_x = 0$ to x such that $V_x(x) = 0$, and from V_{xx} to ω such that $m\omega^2 = V_{xx}$. The associated Jacobian is $|dV_x/dx \times dV_{xx}/d\omega| = 2m^{5/2}\omega^3$. We finally infer

$$\begin{aligned} P(V,\omega) &= \frac{1}{V\omega_0}\left(\frac{\omega}{\omega_0}\right)^4 e^{-3/2(V/V_0)^2-(\omega/\omega_0)^2-V_0/4V(\omega/\omega_0)^4} \\ &\quad\times\left\{ I_{-1/4}\left[\frac{V_0}{4V}\left(\frac{\omega}{\omega_0}\right)^4\right] + I_{1/4}\left[\frac{V_0}{4V}\left(\frac{\omega}{\omega_0}\right)^4\right]\right\}. \end{aligned} \tag{30}$$

The joint distribution is shown in Fig. 2. At a given potential minimum V, we observe that it is maximum for $\omega \sim \omega_0$. At smaller ω, the distribution rapidly falls to zero, which supports our description of the speckle potential landscape in terms of purely harmonic wells at low energies.

As we are primarily interested in low-energy minima $V \ll V_0$, it is instructive to express the distribution $P(V,\omega)$ in the

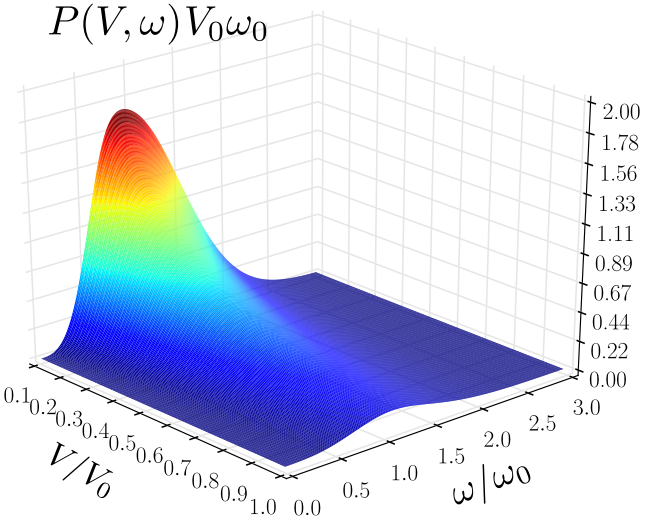

FIG. 2. Joint distribution $P(V,\omega)$ of minima and potential curvature around minima, for a 1D, blue-detuned speckle potential with Gaussian correlation function [Eq. (30)].

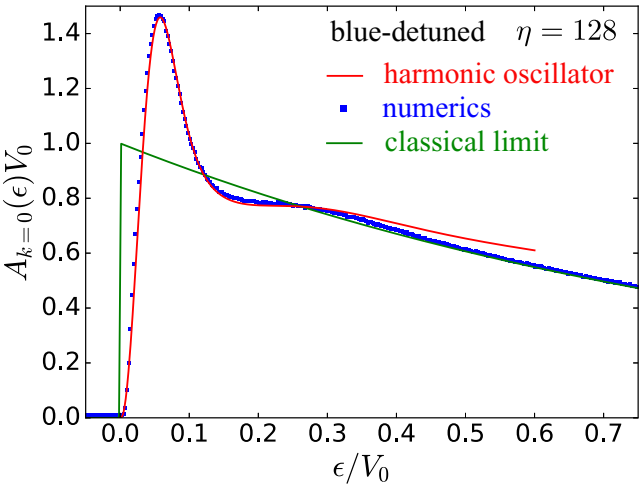

FIG. 3. Spectral function $A_{k=0}(\epsilon)$ as a function of energy in a 1D, blue-detuned speckle potential with Gaussian correlation function, for $\eta = 128$. The harmonic-oscillator approximation, Eq. (36), is shown as a solid red curve, and the classical limit, Eq. (10), as a solid green curve. Blue dots are the result of exact numerical simulations.

limit $V \to 0$ [33]:

$$P(V,\omega)V_0\omega_0 \underset{V\to 0}{\sim} \sqrt{\frac{2}{\pi}}\sqrt{\frac{V_0}{V}}\left(\frac{\omega}{\omega_0}\right)^2 e^{-(\omega/\omega_0)^2}. \tag{31}$$

This asymptotic expression shows that most minima lie at very low $V \ll V_0$. This phenomenon is ultimately responsible for the sharp behavior of the spectral function at low energy. A broader distribution of energy minima would smooth out all peaks and oscillations in the spectral function and DOS, as visible in Figs. 3 and 4.

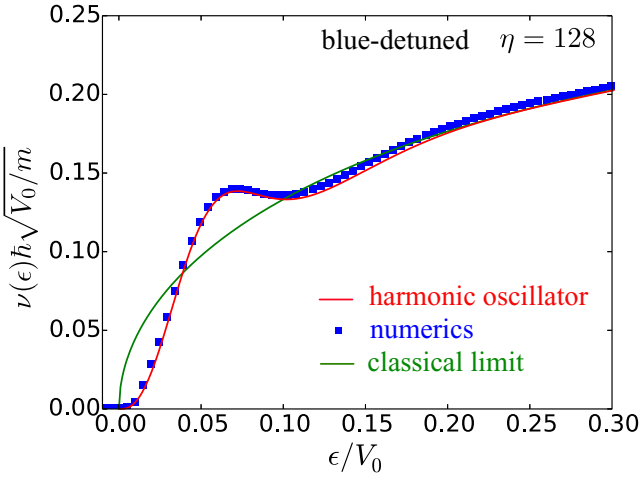

FIG. 4. Density of states $\nu(\epsilon)$ as a function of energy in a 1D, blue-detuned speckle potential with Gaussian correlation function. The harmonic oscillator-approximation, Eq. (37), is shown as a solid red curve, and the classical limit, Eq. (11), as a solid green curve. Blue dots are the result of exact numerical simulations.

B. Density of minima

The last unknown quantity is the density of minima ρ. To evaluate it, we follow [34,35] and consider the general identity

$$\int dx\delta[V'(x)]f(x) = \sum_n \frac{1}{|V''(x_n)|}f(x_n), \tag{32}$$

valid for any function f. The sum is over all points x_n where $V'(x) \equiv V_x$ vanishes. If we choose $f(x)$ to be $|V''(x)| \equiv |V_{xx}|$, then the integral is equal to the number of points at which V_x vanishes. This defines the density of extrema per unit length as

$$\delta(V_x)|V_{xx}|. \tag{33}$$

The corresponding density restricted to minima of the potential is

$$\delta(V_x)V_{xx}\theta(V_{xx}), \tag{34}$$

with θ the Heaviside function. The disorder-averaged density of minima then reads

$$\rho = \int dV_x dV_{xx}\, P(V_x, V_{xx})\delta(V_x)V_{xx}\theta(V_{xx}). \tag{35}$$

Using Eq. (28), we obtain $\rho = c'/\sigma$, where $c' \simeq 0.284\,026$.

IV. 1D SPECTRAL FUNCTION AND DOS: RESULTS

A. Spectral function for 1D blue-detuned speckles

We now evaluate the theoretical prediction (18) of the spectral function for 1D, blue-detuned speckle potentials, using Eq. (30) for the joint distribution of minima and curvature around minima. By carrying out the integral over ω_i that ranges from 0 to ∞, we find

$$A_k(\epsilon) = \frac{c'}{\sigma}\sum_n \int_0^\epsilon dV \frac{|\psi_n(k)|^2}{\hbar(n+1/2)} P\left(V, \frac{\epsilon - V}{\hbar(n+1/2)}\right)\theta(\epsilon). \tag{36}$$

This prediction is shown in Fig. 3 as a function of energy, for $k = 0$ and $\eta = 128$ (solid red curve). As discussed in Sec. II D 1, we expect it to describe low energies. At large energies, the classical limit (10) (solid green curve in Fig. 3)—and its smooth quantum corrections (12)—is on the other hand a very good approximation. In order to assess the accuracy of these two limits, we have performed numerical simulations of the spectral function. For these simulations we use a discrete grid of size $L = 200\sigma$ with 4000 grid points and periodic boundary conditions, and compute the spectral function from definition (6), using the same approach as described in [17] to carry out the time evolution. The results are averaged over 50 000 disorder realizations, and are shown in Fig. 3 as blue dots. We see that the harmonic-oscillator prediction is in excellent agreement with the numerics at low energies. In particular, the high and narrow peak near $\epsilon/V_0 \sim 0.05$ and the secondary "bump" near $\epsilon/V_0 \sim 0.25$ are very well described. The peak originates from the ground state of the harmonic oscillator [term $n = 0$ in the sum (36)]; its relatively narrow character originates from the ω distribution in Eq. (30) rather well peaked around $\omega = \omega_0$. The bump comes from the excited states.

B. Density of states for 1D blue-detuned speckles

From definition (7) and Eq. (36), we can compute the DOS for 1D blue-detuned speckles. Carrying out the integral over k, we find

$$\nu(\epsilon) = \frac{c'}{\sigma} \sum_n \int_0^\epsilon dV \frac{1}{\hbar(n+1/2)} P\left(V, \frac{\epsilon - V}{\hbar(n+1/2)}\right) \theta(\epsilon). \tag{37}$$

This prediction is shown in Fig. 4 as a function of energy, for $\eta = 128$ (solid red curve), together with the classical limit, Eq. (11) (solid green curve). We have also performed numerical simulations of the DOS, by first computing many spectral functions for k ranging from 0 to $13\sigma^{-1}$ and then summing over k, using a number of grid points between 4000 (at small k) and 40 000 (for the largest k). These results are shown in Fig. 4 as blue dots. The DOS displays a bump at low energies, which is reminiscent of the narrow peak that shows up in the profiles of the spectral function; see Fig. 3. Indeed, upon increasing k the peak of the spectral function becomes less and less pronounced but remains at the same energy, which results in a smooth bump after summation over k. As seen in Fig. 4, at low energies numerical results are very well captured by the harmonic-oscillator prediction. At larger energies $\epsilon > V_0$ (not shown in Fig. 4), the harmonic-oscillator approximation breaks down and the purely classical limit takes over, eventually leading to $\nu(\epsilon) \simeq \nu_0(\epsilon) = \sqrt{m/(2\epsilon)}/(\pi\hbar)$ for $\epsilon \to \infty$ [18].

C. Validity of the harmonic-oscillator approximation

A simple argument can be used to estimate the energy range where the harmonic-oscillator approximation is valid. According to the Virial theorem, equipartition between kinetic and potential energy imposes that $\epsilon_n = m\omega^2 \langle x^2 \rangle_n$ for the mean energy of an eigenstate. In order for the speckle potential to be correctly described by a harmonic-oscillator approximation, all states such that $\epsilon_n = \epsilon$ in Eq. (17) should have an extension $\sqrt{\langle x^2 \rangle_n}$ much smaller than the correlation length σ, which imposes an upper limit for the energy: $\epsilon \ll m\omega^2\sigma^2$ (in case this condition is not fulfilled, anharmonic terms would also come into play). As seen in Sec. III A, the most likely value of ω is ω_0, so the condition becomes

$$\epsilon \ll V_0. \tag{38}$$

On the other hand, the classical approximation is expected to describe well the spectral function down to energies of order $V_0/\sqrt{\eta}$ [17]. Therefore, in the region $V_0/\sqrt{\eta} \ll \epsilon \ll V_0$ both the harmonic-oscillator and the classical approximation provide a good description of the spectral function and of the DOS.

Equation (38) provides a restriction on the high-energy tail of the spectral function $A_k(\epsilon)$ for the latter to be correctly described by our harmonic-oscillator approximation. A similar argument imposes an additional restriction for the momentum k. Indeed, equipartition between kinetic and potential energy for the harmonic oscillator also implies

$$\frac{\hbar^2 \langle k^2 \rangle_n}{2m} = \frac{1}{2} m\omega^2 \langle x^2 \rangle_n, \tag{39}$$

where $\sqrt{\langle x^2 \rangle_n}$ should be again much smaller than σ for the harmonic-oscillator approximation to hold. With $\omega \sim \omega_0$, condition (39) reads

$$\frac{\hbar^2 \langle k^2 \rangle_n}{m} \ll V_0. \tag{40}$$

The contribution of each eigenstate to the sum in Eq. (17) being proportional to $|\psi_n(k)|^2$, the sum is dominated by eigenstates having $\sqrt{\langle k^2 \rangle_n}$ of the order of k, such that criterion (40) leads to

$$\epsilon_k \ll V_0. \tag{41}$$

In any case, the harmonic oscillator approximation is a good one in the region $\epsilon, \epsilon_k \sim \hbar\omega_0$ where the quantum corrections are important, while the purely classical result (10) takes over at higher energy $\epsilon, \epsilon_k \sim V_0$.

D. Spectral function for 1D red-detuned speckles

For 1D, red-detuned speckle potentials, we make use of the approach explained in Sec. II D 3 to calculate the spectral function. Using Eq. (19) and (20) together with the joint distribution (30) and carrying out the integral over V, we find

$$A_k(\epsilon) = \frac{(2\pi)^2 c' \sigma^4 m^{5/2}}{\sqrt{2} V_0^{5/2}} \int_{-\infty}^{\infty} \frac{dt}{2\pi\hbar} e^{i\epsilon t/\hbar} \int_0^\infty d\omega\, \omega^4 \left[I^2_{-1/4}\left(\frac{m\omega^2\sigma^2}{2V_0}\sqrt{3 - 2itV_0/\hbar}\right) - I^2_{1/4}\left(\frac{m\omega^2\sigma^2}{2V_0}\sqrt{3 - 2itV_0/\hbar}\right)\right]$$
$$\times \sqrt{\frac{i\hbar}{2\pi m\omega \mathrm{sh}(\omega t)}} \exp\left\{ -\frac{i\hbar k^2}{m\omega}\left[\coth(\omega t) - \frac{1}{\mathrm{sh}(\omega t)}\right] - \frac{m\omega^2\sigma^2}{V_0}\right\}. \tag{42}$$

This prediction is shown in Fig. 5 for $k = 0$ (solid red curve), together with the classical limit, Eq. (10) (solid green curve). Both limits are compared with the result of numerical simulations (blue dots) that use a discrete grid of size $L = 200\sigma$ with 4000 grid points, periodic boundary conditions, and 50 000 disorder realizations.

As seen in Fig. 5, the harmonic-oscillator prediction is in good agreement with the numerical results for energies near 0. At smaller energies ($\epsilon \lesssim -V_0$), the description of the speckle potential in terms of inverse harmonic oscillators becomes poor, while the classical limit provides an excellent approximation.

E. Validity of the inverted harmonic-oscillator approximation

The breakdown of the inverted harmonic-oscillator approximation at energies $\epsilon \lesssim -V_0$ can be understood from a

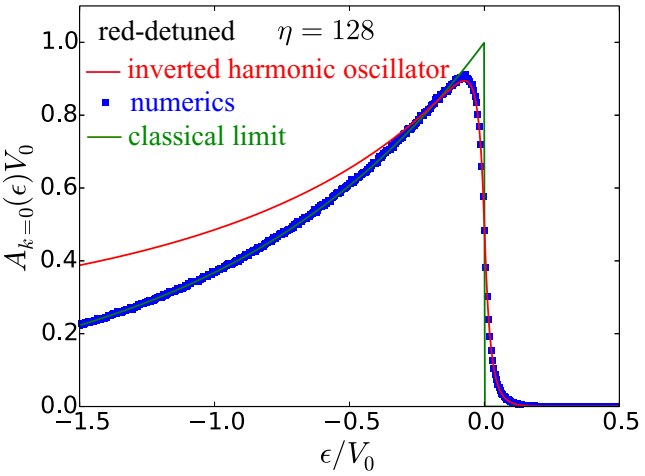

FIG. 5. Spectral function $A_{k=0}(\epsilon)$ as a function of energy in a 1D, red-detuned speckle potential with Gaussian correlation function, for $\eta = 128$. The inverted harmonic-oscillator approximation, Eq. (42), is shown as a solid red curve, and the classical limit, Eq. (10), as a solid green curve. Blue dots are the result of exact numerical simulations.

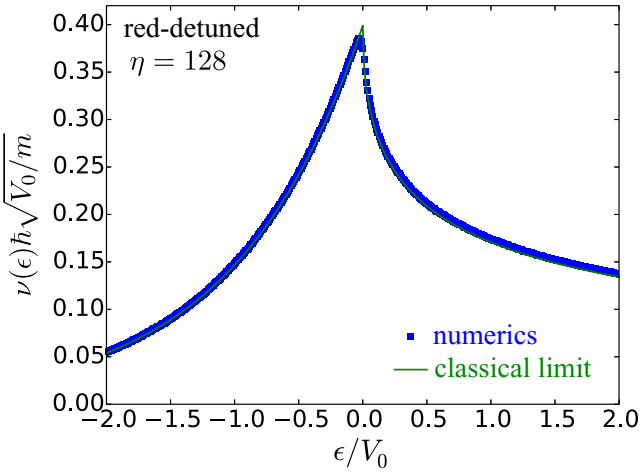

FIG. 6. Density of states $\nu(\epsilon)$ as a function of energy in a 1D, red-detuned speckle potential with Gaussian correlation function. The classical limit, Eq. (11), is shown as a solid green curve. Blue dots are the result of exact numerical simulations.

reasoning on the classical action that appears in Eq. (15). Indeed, for the stationary phase approximation to be valid, the time span t associated with a classical trajectory should be such that the classical action $V_0 t/\hbar$ is large, imposing $t \gg \hbar/V_0$. Energies corresponding to such long times fulfill

$$|\epsilon| \ll V_0. \tag{43}$$

Note that this condition is fully similar to that for blue-detuned speckles, Eq. (38), though it is here deduced from a slightly different argument. Then, the motion of a classical atom of energy $\epsilon = \epsilon_k - m\omega x^2/2$ describes well the dynamics in a red-detuned speckle as long as the excursion x^2 remains much smaller than σ, namely as long as $\epsilon_k + |\epsilon| \ll m\omega\sigma^2/2$. Since $\omega \sim \omega_0$ and $|\epsilon| \ll V_0$, this leads to

$$\epsilon_k \ll V_0, \tag{44}$$

which is the same validity condition as for blue-detuned speckles.

F. Density of states for 1D red-detuned speckles

We show in Fig. 6 as blue dots the DOS in a 1D, red-detuned speckle potential, computed from numerical simulations where we have summed over 208 spectral functions with k ranging from 0 to $13\sigma^{-1}$, varying the number of grid points from 4000 (for small k) to 40 000 (for the largest k). We also show as the solid green curve the classical prediction (11). As seen in the figure, the latter already provides an excellent description of the exact results. This can be understood qualitatively from the Gutzwiller trace formula [23,36] which expresses the density of states as the sum of the classical contribution, Eq. (11), and of oscillatory contributions coming from periodic orbits. Around $E = 0$, the periodic orbits in a red-detuned speckle are long ones with characteristic properties (action, period...) which strongly depend on the disorder realization, so that all oscillatory contributions cancel out. This is in stark contrast with the blue-detuned speckle where periodic orbits around $E = 0$ are short orbits trapped in the deep potential minima and collectively contribute to "bumps" in the DoS.

In principle, quantum corrections to the DOS can be obtained from Eq. (42) by evaluating the Fresnel integral over k; see Eq. (7). The latter can be performed, but the remaining integral over t displays an ultraviolet divergence. This divergence already appears in the DOS of the inverted harmonic oscillator, for which it originates of the continuous nature of the spectrum. It thus appears that for the DOS of red-detuned speckles, the description of singular quantum corrections requires to go beyond the inverted harmonic-oscillator approximation, a task that we leave for later work.

V. STATISTICS OF 2D SPECKLE POTENTIALS

We now turn to the study of 2D speckle potentials which we aim to describe, at low energies, by a 2D harmonic-oscillator approximation. By analogy with the 1D case, we propose to model the speckle potential around an extremum $V(x_i, y_i)$ by a 2D harmonic oscillator (respectively inverted harmonic oscillator) of the form $\pm V \pm m\omega_x^2(x - x_i)^2/2 \pm m\omega_y^2(y - y_i)^2/2$ with again the $+$ (respectively $-$) sign for blue (respectively red)-detuned speckles, with random frequencies ω_x and ω_y. Such a description requires the preliminary knowledge of the joint probability distribution $P(V, \omega_x, \omega_y)$ of extrema and potential curvature around extrema. Study of this quantity is the object of the present section. We here focus on blue-detuned speckle potentials, and then infer the corresponding distribution for red-detuned speckles by the same symmetry argument as in one dimension.

A. Density of minima at $V = 0$

2D speckle potentials have a important difference with 1D potentials: they present a finite density of points exactly at $V = 0$ [34]. In writing the blue-detuned speckle potential as

$$V(x, y) = \mathrm{Re}(x, y)^2 + \mathrm{Im}(x, y)^2, \tag{45}$$

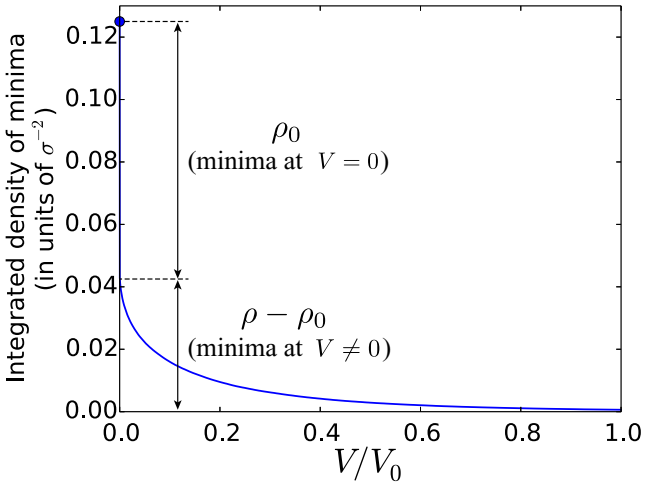

FIG. 7. Blue curve: integrated density of minima (density of minima whose depth is greater than V) for a 2D, blue-detuned speckle potential with Gaussian correlation function. The results have been obtained numerically on a discrete grid of size $L \times L = 400\sigma \times 400\sigma$.

these points are minima that correspond to the intersections of the curves $\mathrm{Re}(x,y) = 0$ and $\mathrm{Im}(x,y) = 0$. Before considering the distribution $P(V,\omega_x,\omega_y)$, let us first examine the proportion of minima at $V = 0$ and at $V \neq 0$. To this end, we have numerically computed the integrated density of minima, i.e., the density of minima whose depth is greater than V. To distinguish between minima at $V = 0$ and minima at $V \neq 0$, we have exploited the sensitivity (respectively insensitivity) of the minima at $V = 0$ (respectively $V \neq 0$) with respect to a change in the spatial discretization (number of grid points). The results of these simulations are shown in Fig. 7. They have been obtained on a discrete grid of size $L \times L = 400\sigma \times 400\sigma$, by varying the number of grid points between 18 000 and 26 000 along x and y. The discontinuity of the integrated density of minima at $V = 0$ visible in Fig. 7 defines ρ_0, the density of minima at $V = 0$. We find that approximately $\rho_0/\rho \sim 65\%$ of all minima lie at $V = 0$ [37]. Note that this result is confirmed by an analytical prediction derived in [34]:

$$\rho_0 = \left[\frac{-4\pi F(0)}{\boldsymbol{\nabla}_{\boldsymbol{r}}^2 F(\boldsymbol{r})|_{\boldsymbol{r}=0}}\right]^{-1}, \tag{46}$$

where $F(\boldsymbol{r}-\boldsymbol{r}') = \sqrt{\overline{V(\boldsymbol{r})V(\boldsymbol{r}')} - \overline{V(\boldsymbol{r})}^2}/2$. For the Gaussian correlation function (4), this explicitly gives $\rho_0 = 1/(4\pi\sigma^2) \simeq 0.08/\sigma^2$.

In two dimensions, the majority of minima thus lies at $V = 0$. To keep the discussion and the calculation as simple as possible, as a first approximation, we keep only the minima at $V = 0$ in the 2D semiclassical description. We will discuss the validity of this approximation in Sec. VI A. The joint distribution of interest $P(V,\omega_x,\omega_y)$ reduces to

$$P(V,\omega_x,\omega_y) \simeq P(\omega_x,\omega_y)\delta(V), \tag{47}$$

where $P(\omega_x,\omega_y)$ is the 2D joint distribution of potential curvatures around a minimum (x_i,y_i) where $V(x_i,y_i) = 0$.

B. Joint distribution $P(\omega_x,\omega_y)$

The distribution $P(\omega_x,\omega_y)$ is closely related to the joint, conditional probability distribution $P(\omega_x,\omega_y|V(x_i,y_i) = 0)$ of potential curvatures given that $V(x_i,y_i) = 0$. To calculate this distribution, we first expand $V(x,y)$ up to second order in the vicinity of (x_i,y_i) as

$$V(x,y) \simeq \tfrac{1}{2} X A X^t, \tag{48}$$

where $X = (x - x_i, y - y_i)$ and

$$A = \begin{pmatrix} \partial_x^2 V(x,y) & \partial_x\partial_y V(x,y) \\ \partial_y\partial_x V(x,y) & \partial_y^2 V(x,y) \end{pmatrix}. \tag{49}$$

By diagonalizing the quadratic form (48) (which is possible since the matrix A is symmetric), we can describe a well of the speckle potential in terms of two independent 1D harmonic oscillators, whose curvatures ω_x and ω_y are related to the eigenvalues λ_1 and λ_2 of A through $\omega_x = \sqrt{\lambda_1/m}$ and $\omega_y = \sqrt{\lambda_2/m}$. The calculation of the joint distribution of the eigenvalues (λ_1,λ_2) is done in Appendix B for clarity. The corresponding result for $P(\omega_x,\omega_y|V = 0)$ is

$$P(\omega_x,\omega_y|V = 0) = \frac{2}{\omega_0^4}\left|\omega_y^2 - \omega_x^2\right| e^{-(\omega_x^2+\omega_y^2)/\omega_0^2}. \tag{50}$$

The sought for distribution $P(\omega_x,\omega_y)$ then follows from the change of variables from $V(x_i,y_i) = 0$ to (x_i,y_i) such that $V(x_i,y_i) = 0$: $P(\omega_x,\omega_y) = (d^2V/dxdy)P(\omega_x,\omega_y|V = 0)$, where d^2V is the change in the surface element defined by the 2D curve $V(x,y)$ when x varies from x_i to $x_i + dx$ and y varies from y_i to $y_i + dy$. Since $V(x,y) \simeq m\omega_x^2(x - x_i)^2/2 + m\omega_y^2(y - y_i)^2/2$ in the vicinity of a minimum, we expect this change to be proportional to $\omega_x\omega_y dxdy$, such that

$$P(\omega_x,\omega_y) \propto \omega_x\omega_y P(\omega_x,\omega_y|V = 0). \tag{51}$$

The unknown prefactor is determined from normalization, which eventually leads to

$$P(\omega_x,\omega_y) = \frac{4}{\omega_0^6}\omega_x\omega_y\left|\omega_y^2 - \omega_x^2\right| e^{-(\omega_x^2+\omega_y^2)/\omega_0^2}. \tag{52}$$

A density plot of $P(\omega_x,\omega_y)$ is shown in Fig. 8. As in one dimension, the distribution rapidly falls to zero at small frequencies, which again supports our description of the speckle potential landscape in terms of purely harmonic wells at low energies. We have confirmed Eq. (52) by numerical simulations of the distribution $P(\omega_x,\omega_y)$, deduced from numerically generated speckle potentials. We show in Fig. 9 the numerical cut $P(\omega_x,\omega_y = 1.25\omega_0)$ as a function of ω_x (blue dots), together with Eq. (52) (red curve), and find a very good agreement.

VI. 2D SPECTRAL FUNCTION AND DOS: RESULTS

A. Spectral function for 2D blue-detuned speckles

We are now in position to compute the spectral function for 2D, blue-detuned speckle potentials. The 2D counterpart

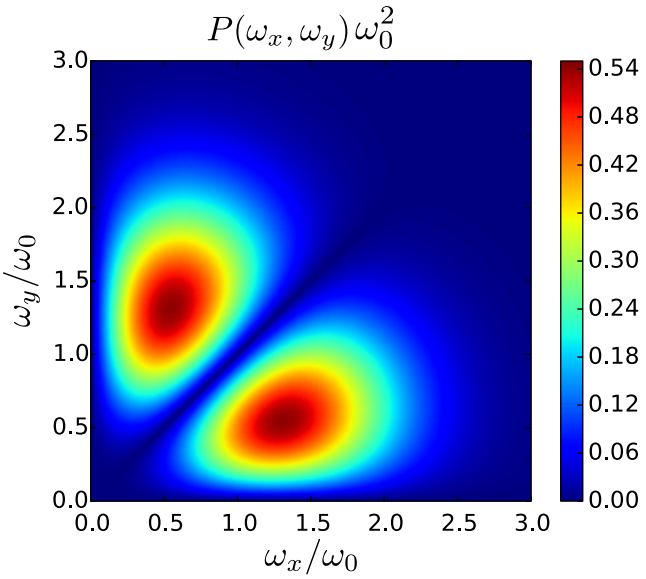

FIG. 8. Density plot of the joint distribution $P(\omega_x,\omega_y)$ at a point where $V = 0$ for a 2D, blue-detuned speckle potential with Gaussian correlation function.

of Eq. (18) reads

$$A_{\boldsymbol{k}}(\epsilon) = \rho_0 \sum_{n_x,n_y=0}^{\infty} \int d\omega_x d\omega_y P(\omega_x,\omega_y) \times |\psi_{n_x}(k_x)|^2 |\psi_{n_y}(k_y)|^2 \delta(\epsilon - \epsilon_{n_x,n_y}), \quad (53)$$

where $P(\omega_x,\omega_y)$ is the joint distribution of curvatures around minima at $V = 0$ given by Eq. (52), $\epsilon_{n_x,n_y} = \hbar\omega_x(n_x + 1/2) + \hbar\omega_y(n_y + 1/2)$ and the eigenfunctions $\psi_{n_x}(k_x)$ are given by Eq. (17) with n replaced by n_x and k replaced by k_x, and similarly for $\psi_{n_y}(k_y)$. By performing the integral over ω_y and

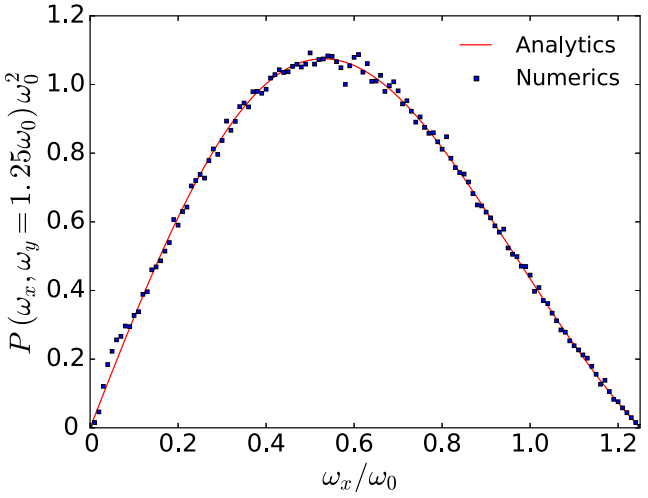

FIG. 9. Cut $P(\omega_x,\omega_y = 1.25\omega_0)$ of the joint distribution of curvatures around a minima at $V = 0$ for a 2D, blue-detuned speckle potential. Blue dots are the results of numerical simulations and the red curve is Eq. (52).

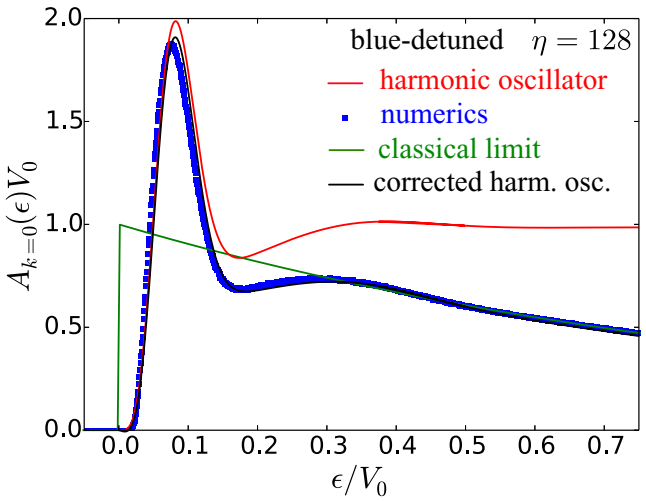

FIG. 10. Spectral function $A_{k=0}(\epsilon)$ as a function of energy in a 2D, blue-detuned speckle potential with Gaussian correlation function, for $\eta = 128$. The harmonic-oscillator approximation, Eq. (54), is shown as a solid red curve, and the classical limit, Eq. (10), as a solid green curve. The corrected harmonic-oscillator approximation, Eq. (56), is shown as a solid black curve. Blue dots are the results of exact numerical simulations.

using that $\rho_0 = 1/(4\pi\sigma^2)$, we find

$$A_{\boldsymbol{k}}(\epsilon) = \frac{1}{4\pi\sigma^2} \sum_{n_x,n_y} \int_0^{\epsilon/\hbar(n_x+1/2)} d\omega_x \frac{|\psi_{n_x}(k_x)|^2}{\hbar(n_y+1/2)} \theta(\epsilon) \times |\psi_{n_y}(k_y)|^2 P(\omega_x,\omega_y)|_{\omega_y=(\epsilon-\hbar\omega_x(n_x+1/2))/\hbar(n_y+1/2)}. \quad (54)$$

This prediction is shown in Fig. 10 as a function of energy, for $k = 0$ and $\eta = 128$ (solid red curve). The classical limit (10), expected to describe large energies, is also shown as a solid green curve. These results are compared to numerical simulations of the spectral function (blue dots) which use a system size $L \times L = (20\pi\sigma)^2$ with 600 grid points along x and y, periodic boundary conditions and 40 000 disorder realizations. Several observations can de made. Like in one dimension, the harmonic approximation quantitatively describes the spectral function for energies $\sim V_0/\sqrt{\eta} = \hbar\omega_0$. The large peak is at an energy about twice larger than in one dimension—compare with Fig. 3—because it is the ground-state energy of a 2D (instead of 1D) harmonic oscillator. It is also slightly higher and the minimum around $\epsilon/V_0 = 0.2$ as well as the second bump above are slightly more visible than in one dimension. This is because most potential minima are exactly at $V = 0$ in two dimensions, while this is not true in one dimension, so that an additional smoothing takes place in the latter case. This must however be taken with a grain of salt: the 2D low-energy peak of the spectral function is not entirely controlled by the ground state of the harmonic oscillator: excited states also contribute for roughly 25% of the peak height. As seen in Fig. 10, deviations of the harmonic-oscillator prediction from the numerical result occur at smaller energy than in one dimension. This phenomenon can be understood from the expression of the spectral function in terms of the propagator

of the 2D harmonic oscillator:

$$A_{\boldsymbol{k}}(\epsilon) = \rho_0 \int_{-\infty}^{\infty} \frac{dt}{2\pi\hbar} e^{i\epsilon t/\hbar} \overline{\langle \boldsymbol{k}| \, e^{-iH_{\rm HO}t/\hbar} \, |\boldsymbol{k}\rangle}, \qquad (55)$$

where $H_{\rm HO} = \boldsymbol{p}^2/(2m) + m\omega_x^2 x^2/2 + m\omega_y^2 y^2/2$. In two dimensions, the propagator $\langle \boldsymbol{k}| \, e^{-iH_{\rm HO}t/\hbar} \, |\boldsymbol{k}\rangle \propto 1/t$ at short times [29]. This singularity is more pronounced than in one dimension where the propagator diverges as $1/\sqrt{t}$. In two dimensions there is thus more weight on short times, which are by construction not well captured by the harmonic-oscillator approximation. On the other hand, we know that short times are fairly well described by the classical limit, Eq. (10). To improve on the quality of the harmonic-oscillator description, we thus propose to replace the contribution from the pole at $t = 0$ by the classical contribution. The contribution from this pole is simple to calculate from Eq. (55): we find $\theta(\epsilon)/V_0$. The classical contribution is given in Eq. (10). The above prescription thus leads to

$$A_{\boldsymbol{k}}^{\rm corr}(\epsilon) \simeq A_{\boldsymbol{k}}(\epsilon) - \frac{\theta(\epsilon)}{V_0} + \frac{\theta(\epsilon)}{V_0} \exp\left(-\frac{\epsilon - \epsilon_k}{V_0}\right), \qquad (56)$$

where $A_{\boldsymbol{k}}(\epsilon)$ is the prediction of the harmonic-oscillator description, Eq. (54). Equation (56) is shown in Fig. 10 as a solid black curve, and is in very good agreement with the numerical simulations.

The excellent agreement with the numerical calculations justifies *a posteriori* the approximation of keeping only the minima at $V = 0$. Such an agreement may surprise the attentive reader as approximately 35% of the minima have been left aside. The reason for it lies in two mechanisms reducing the contribution to the spectral function of minima at $V \neq 0$ as compared to minima at $V = 0$. First, among the 35% of minima at $V \neq 0$, only a fraction contributes to the spectral function: as we are interested in very low energies ($\epsilon \ll V_0$), we should keep only the harmonic wells with associated minimum smaller than ϵ. Second, the smoothing due to the dispersion in V—compare the 1D oscillations in Fig. 3 with such a dispersion and the 2D oscillations in Fig. 10 where the dispersion is absent—makes the contribution of minima at $V \neq 0$ negligible after application of the corrected harmonic-oscillator prescription [Eq. (56)].

B. Density of states for 2D blue-detuned speckles

From definition (7) and Eq. (54), we can compute the DOS for 2D blue-detuned speckles. Carrying out the integral over k, we readily find

$$\nu(\epsilon) = \frac{1}{4\pi\sigma^2} \sum_{n_x,n_y} \int_0^{\epsilon/\hbar(n_x+1/2)} d\omega_x \frac{\theta(\epsilon)}{\hbar(n_y+1/2)} \times P\left(\omega_x, \frac{\epsilon - \hbar\omega_x(n_x+1/2)}{\hbar(n_y+1/2)}\right). \qquad (57)$$

This prediction is shown in Fig. 11 as a function of energy, for $\eta = 128$ (solid red curve), together with the classical limit, Eq. (11) (solid green curve). We have also performed numerical simulations of the DOS. In two dimensions however, the strategy of numerically computing first spectral functions at different $\boldsymbol{k}$ and then summing of $\boldsymbol{k}$ is numerically demanding. We have thus used a different scheme that consists of

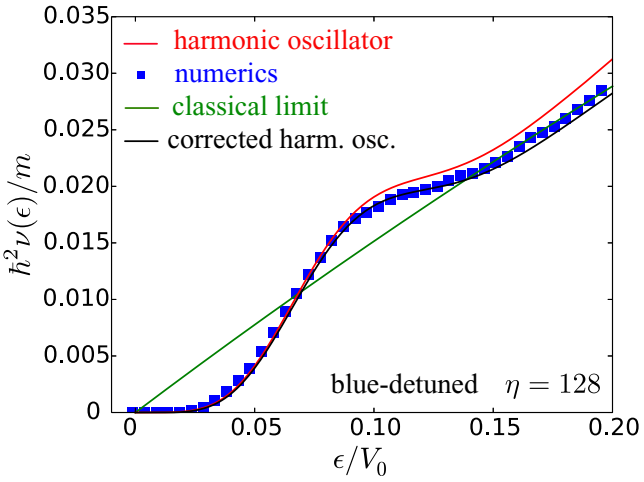

FIG. 11. Density of states $\nu(\epsilon)$ as a function of energy in a 2D, blue-detuned speckle potential with Gaussian correlation function. The harmonic-oscillator approximation, Eq. (57), is shown as a solid red curve, and the classical limit, Eq. (11), as a solid green curve. The corrected harmonic-oscillator description, Eq. (60), is shown as a solid black curve. Blue dots are the result of exact numerical simulations.

expressing the trace in Eq. (7) in real space rather than in momentum space:

$$\nu(\epsilon) = \frac{1}{L^2} \mathrm{Tr}\, \overline{\delta(\epsilon - H)} = \frac{1}{L^2} \int d^2\boldsymbol{r} \, \langle \boldsymbol{r}| \, \overline{\delta(\epsilon - H)} |\boldsymbol{r}\rangle. \qquad (58)$$

The system being translation invariant on average, the integrand is in fact independent of $\boldsymbol{r}$ so

$$\nu(\epsilon) = \langle \boldsymbol{r} = 0| \, \overline{\delta(\epsilon - H)} \, |\boldsymbol{r} = 0\rangle = \int_{-\infty}^{\infty} \frac{dt}{2\pi\hbar} e^{i\epsilon t/\hbar} \overline{\langle 0| \, e^{-iHt/\hbar} \, |0\rangle}. \qquad (59)$$

From Eq. (59), it thus appears that the DOS can be obtained by numerically propagating a particle initially located at the origin, then recording the value of the wave function at the origin for many different times t, and finally taking the Fourier transform with respect to time and averaging over disorder. We have applied this strategy for a system size $L \times L = (10\pi\sigma)^2$ with 400 grid points along x and y and 40 000 disorder realizations. Results are shown in Fig. 11 as blue dots. As for the 2D spectral function, we observe deviations of the theoretical prediction (59) from the numerical results at relatively small energies due to a pole $\propto 1/t^2$ in the propagator in (59). We again correct them by replacing the contribution of this pole by the classical result (11). This gives

$$\nu^{\rm cor}(\epsilon) = \nu(\epsilon) - \frac{m\epsilon\theta(\epsilon)}{2\pi\hbar^2 V_0} + \frac{m\theta(\epsilon)}{2\pi\hbar^2}\left(1 - e^{-\epsilon/V_0}\right). \qquad (60)$$

This prediction is plotted in Fig. 11 (solid black curve), and describes very well the exact numerical results.

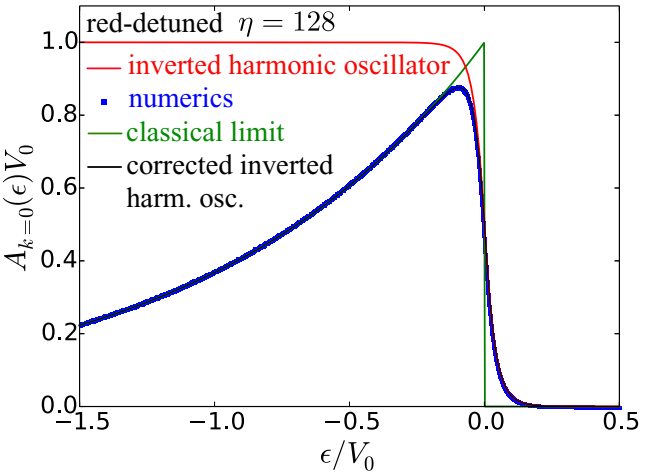

FIG. 12. Spectral function $A_{k=0}(\epsilon)$ as a function of energy in a 2D, red-detuned speckle potential with Gaussian correlation function, for $\eta = 128$. The inverted harmonic-oscillator approximation, Eq. (62), is shown as a solid red curve, and the classical limit, Eq. (10), as a solid green curve. The corrected inverted harmonic-oscillator approximation, Eq. (63), is shown as a solid black curve. Blue dots are the results of exact numerical simulations.

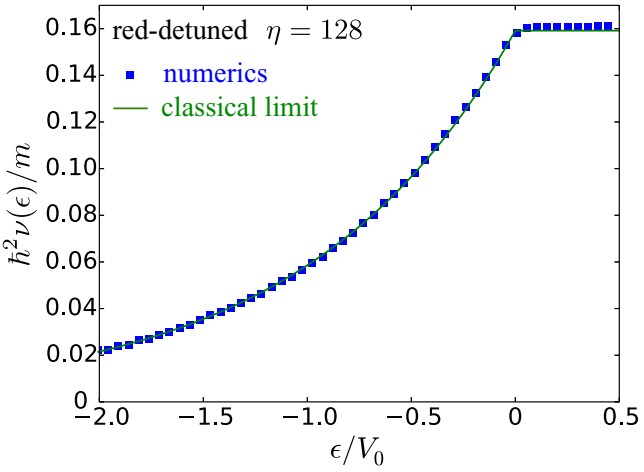

FIG. 13. Density of states $\nu(\epsilon)$ as a function of energy in a 2D, red-detuned speckle potential with Gaussian correlation function. The classical limit, Eq. (11), is shown as a solid green curve. Blue dots are the results from exact numerical simulations based on Eq. (59).

C. Spectral function for 2D red-detuned speckles

To evaluate the spectral function for 2D, red-detuned speckle potentials, we proceed as in one dimension and write

$$A_{\boldsymbol{k}}(\epsilon) \simeq \rho_0 \int_{-\infty}^{\infty} \frac{dt}{2\pi\hbar} e^{i\epsilon t/\hbar} \overline{\langle \boldsymbol{k}|\, e^{-iH_{\rm IHO}t/\hbar}\, |\boldsymbol{k}\rangle}, \qquad (61)$$

where $H_{\rm IHO} = \boldsymbol{p}^2/(2m) - m\omega_x^2 x^2/2 - m\omega_y^2 y^2/2$. Making the average over disorder explicit, we have

$$\begin{aligned} A_{\boldsymbol{k}}(\epsilon) = \frac{1}{4\pi\sigma^2} \int_{-\infty}^{\infty} \frac{dt}{2\pi\hbar} e^{i\epsilon t/\hbar} \int_0^{\infty} d\omega_x d\omega_y P(\omega_x,\omega_y) \\ \times \langle k_x|\, e^{-i[p_x^2/(2m) - m\omega_x^2 x^2/2]t/\hbar} |k_x\rangle \\ \times \langle k_y|\, e^{-i[p_y^2/(2m) - m\omega_y^2 y^2/2]t/\hbar} |k_y\rangle, \end{aligned} \qquad (62)$$

where the 1D inverted harmonic-oscillator propagator is given by Eq. (20).

Equation (62) is shown in Fig. 12 (solid red curve), together with the classical limit, Eq. (10) (solid green curve). Results of numerical simulations that use a system size $L \times L = (20\pi\sigma)^2$ with 600 grid points along x and y and 40 000 disorder realizations are also shown (blue dots). As for the blue-detuned speckle, the pole $1/t$ in the propagator gives rise to deviations of the oscillator description from the exact numerical results that are more significant than in one dimension. We again cure them by replacing the contribution of the pole by the classical limit:

$$A_{\boldsymbol{k}}^{\rm cor}(\epsilon) = A_{\boldsymbol{k}}(\epsilon) - \frac{\theta(-\epsilon)}{V_0} + \frac{\theta(-\epsilon)}{V_0} e^{(\epsilon-\epsilon_k)/V_0}. \qquad (63)$$

This prediction is plotted in Fig. 12 (solid black curve), and describes very well the exact numerical results.

D. Density of states for 2D red-detuned speckles

We show in Fig. 13 the DOS in a 2D, red-detuned speckle potential computed from numerical simulations using a system size $L \times L = (10\pi\sigma)^2$ with 2000 grid points in each direction and 8000 disorder realizations, based on Eq. (59) (blue dots). As for 1D red-detuned speckles, the oscillator correction to the DOS diverges due to an ultraviolet divergence in the propagator; see Sec. IV F. Nevertheless, as seen in Fig. 13, the classical prediction (11) (solid green curve) already constitutes an excellent approximation of the exact result.

VII. CONCLUSION

In this paper, we have pointed out that an expansion in powers of $\hbar$ of the spectral function or the density of states in speckle potentials is not sufficient at low energies, due to the discontinuity of the potential distribution. In order to overcome this difficulty, we have developed an analytical method based on a semiclassical description of the dynamics combined with the statistical properties of potential extrema. Applying this approach to 1D and 2D blue- and red-detuned speckles, we have carried out the calculation of the spectral function and the DOS. By connecting our results with those of previous works valid at high energies [17,18], we have been able to describe the whole energy spectrum, and have found a good agreement with exact numerical simulations.

Our semiclassical description additionally provides a simple interpretation of intriguing features of the spectral function and DOS. In particular, for blue-detuned potentials we have shown that the low-energy peak of spectral functions is essentially associated with the ground state of an atom in a potential well of the speckle, while the secondary bump is associated with excited states. We have also emphasized that in spite of their simple symmetry, red- and blue-detuned speckles exhibit remarkably different features in the semiclassical regime, coming from the fundamental different nature of the classical trajectories involved near zero energy: for blue-detuned speckles, these classical trajectories lie in deep

potential wells, while for red-detuned speckles they lie in the vicinity of the top of inverted wells.

As a logical continuation of this work, it would be of great interest to address the case of three-dimensional speckle potentials, involved in important questions related to Anderson localization [5,6,38,39]. This task appears challenging though, as the isolated points of zero potential in two dimensions become curves in three dimensions, making the application of a harmonic-oscillator approximation less obvious.

ACKNOWLEDGMENTS

The authors would like to thank T. Thiery and C. Müller for useful discussions. This work was granted access to the HPC resources of TGCC under the allocation 2016-057083 made by GENCI (Grand Equipement National de Calcul Intensif).

APPENDIX A

In this Appendix, we calculate the leading-order smooth quantum corrections to the classical limit of the spectral function, Eq. (12), using an alternative approach to the one used in [17]. The calculation is first carried out for 1D, blue-detuned speckles, then generalized to any dimension, and finally to red-detuned speckles by a simple symmetry argument.

The first stage of our approach is a commutator expansion of the evolution operator based on the Zassenhaus formula [40]:

$$\begin{aligned}&\langle k|e^{-i[p^2/2m+V]t}\,|k\rangle\\&\quad= e^{-iV(x)t}e^{(i\hbar^2t^3/3m)[\partial_xV(x)]^2}\\&\qquad\times e^{(-\hbar^2t^2/4m)[2ik\partial_xV(x)+\partial_x^2V(x)]-(it^3\hbar^2/3m)[\partial_x^2V(x)]\epsilon_k}e^{O(\hbar^3)}.\end{aligned}\tag{A1}$$

The second stage consists of carrying out the disorder average. This can be done by mean of the following cumulant expansion:

$$\overline{\exp(X)}=\exp\left[\sum_{n=1}^{\infty}\frac{\kappa_n(X)}{n!}\right],\tag{A2}$$

where κ_n denotes the nth cumulant. To evaluate the cumulants of sums of random variables that appear in Eq. (A2), we make use of the expansion

$$\kappa_n(X+Y)=\sum_{j=0}^{n}\binom{n}{j}\kappa(\underbrace{X,\ldots,X}_{j\text{ terms}},\underbrace{Y,\ldots,Y}_{n-j\text{ terms}}),\tag{A3}$$

where we have introduced the joint cumulants κ, defined as [41]

$$\kappa(X_1,\ldots,X_n)=\sum_{\pi}(|\pi|-1)!(-1)^{|\pi|-1}\prod_{B\in\pi}\overline{\left[\prod_{i\in B}X_i\right]}.\tag{A4}$$

Here π runs through the list of all partitions of $\{1,\ldots,n\}$, B runs through the list of all blocks of the partition π, and $|\pi|$ is the number of parts in the partition. Joint cumulants have the following important properties [41]:

(1) they are linear in all variables;

(2) $\kappa(X,\ldots,X)=\kappa_n(X)$;

(3) $\kappa(X_1,\ldots,X_n)=0$ if any set of the X_i's are independent of the remaining $X_{j\neq i}$'s.

After these premises, let us now write the random potential as

$$V(x)=E_1(x)^2+E_2(x)^2,\tag{A5}$$

where E_1 and E_2 are independent Gaussian variables with zero mean and equal variance [20]. Defining $X=-iV(x)t$ and denoting by Y_i the $\hbar$ corrections appearing in Eq. (A2), we obtain for the nth cumulant:

$$\begin{aligned}&\kappa_n\left(X+\sum_{i=1}^{m}Y_i\right)\\&\quad=\kappa_n(X)+\sum_{i=1}^{m}n\kappa(\underbrace{X,\ldots,X}_{n-1\text{ terms}},Y_i)\\&\qquad+\sum_{j=1}^{2}\binom{n}{2}\kappa\left(\underbrace{X,\ldots,X}_{n-2\text{ terms}},-\frac{\hbar t^2}{2m}\left[\partial_xE_j^2(x)\right]i\hbar k,\right.\\&\qquad\left.-\frac{\hbar t^2}{2m}\left[\partial_xE_j^2(x)\right]i\hbar k\right)+O\left(\hbar^3\right).\end{aligned}\tag{A6}$$

We now need to calculate the various cumulants entering this equation. For this purpose, we use a theorem due to Leonov and Shiryaev [42,43]. Before discussing the theorem itself, it is useful to introduce some terminology. Consider the matrix

$$\begin{pmatrix}X_{11}&\ldots&X_{1J}\\.&&.\\.&&.\\.&&.\\X_{J1}&\ldots&X_{JJ}\end{pmatrix},\tag{A7}$$

and a partition $P_1\cup P_2\cup\cdots\cup P_M$ of its entries. We choose this matrix square for simplicity, but the formalism is straightforwardly generalizable to rectangular matrices. If the rows are denoted by $R_1,\ldots,R_J$, then a partition is said to be indecomposable if and only if there exist no sets $P_{m_1},\ldots,P_{m_N}$, $(N<M)$, and rows $R_{i_1},\ldots,R_{i_P}$, $(P<J)$, with

$$P_{m_1}\cup\cdots\cup P_{m_N}=R_{i_1}\cup\cdots\cup R_{i_P}.\tag{A8}$$

The theorem then goes as follows [42]. Consider a matrix of random entries X_{ij} $(i,j=1,\ldots,J)$ and the J random variables

$$Y_i=\prod_{j=1}^{J}X_{ij},\ i=1,\ldots,J.\tag{A9}$$

The joint cumulant $\kappa(Y_1,\ldots,Y_J)$ is then given by

$$\begin{aligned}\kappa(Y_1,\ldots,Y_J)=\sum_{P}&\kappa(\underbrace{X_{i_1j_1},\ldots,X_{i_mj_m}}_{\{i_1j_1,\ldots,i_mj_m\}=P_1})\\&\ldots\kappa(\underbrace{X_{i_nj_n},\ldots,X_{i_oj_o}}_{\{i_nj_n,\ldots,i_oj_o\}=P_p}),\end{aligned}\tag{A10}$$

where the summation is over all indecomposable partitions $P=P_1\cup\cdots\cup P_p$ of matrix (A7).

Let us now tackle one of the terms involved in Eq. (A6): $\kappa(E_1^2,\ldots,E_1^2,\partial_x^2E_1^2)$. It is simpler to work in Fourier space,

hence defining

$$E_j(x) = \int \frac{dp_i}{2\pi} e^{ipx} E_j(p). \tag{A11}$$

The cumulant of interest then reads

$$\kappa\left(E_1^2,\ldots,E_1^2,\partial_x^2 E_1^2\right) = -\int \left[\prod_{i=1}^{2n} \frac{dp_i}{2\pi}\right](p_{2n-1}+p_{2n})^2 \kappa[E_1(p_1)E_1(p_2), \ldots, E_1(p_{2n-3})E_1(p_{2n-2}), E_1(p_{2n-1})E_1(p_{2n})]. \tag{A12}$$

The corresponding matrix (A7) is

$$\begin{pmatrix} E_1(p_1) & E_1(p_2) \\ \cdot & \cdot \\ \cdot & \cdot \\ \cdot & \cdot \\ E_1(p_{2n-1}) & E_1(p_{2n}) \end{pmatrix}. \tag{A13}$$

As E_1 is Gaussian distributed, only joint cumulants involving two fields should be kept in the right-hand side of Eq. (A10). Our indecomposable partitions are then made of pairs of E_1 and all give the same contribution. Let us now count them, taking into account the two following constraints for making pairs so to obtain an indecomposable partition:

(i) A pair cannot be formed out of two fields lying on the same line, i.e., the choice

$$\begin{pmatrix} \overline{E_1(p_1)} & \overline{E_1(p_2)} \\ \cdot & \cdot \\ \cdot & \cdot \\ \cdot & \cdot \\ E_1(p_{2n-1}) & E_1(p_{2n}) \end{pmatrix} \tag{A14}$$

is forbidden.

(ii) Two pairs right nearby cannot be formed, i.e., the choice

$$\begin{pmatrix} \overline{E_1(p_1)} & \overline{E_1(p_2)} \\ \overline{E_1(p_1)} & \overline{E_1(p_2)} \\ \cdot & \cdot \\ \cdot & \cdot \\ \cdot & \cdot \\ E_1(p_{2n-1}) & E_1(p_{2n}) \end{pmatrix} \tag{A15}$$

is forbidden.

Therefore, to form the first pair, we have $(2n)$ choices for the first field and $(2n-2)$ choices for the second, and similarly for the next pairs. This leaves us with $2n(2n-2)^2(2n-4)^2\ldots = 2^{2n}n!^2/(2n)$ choices of pairing. There is however a redundancy in this counting, due to the invariance of the partition with respect to both swapping of the two fields inside one pair (2^n possibilities) and swapping of different pairs ($n!$ possibilities). This leaves us with only $2^n n!^2/(2n2^n n!) = 2^n n!/(2n)$ choices of pairing. Calculating the contribution from one of them, we obtain

$$\kappa\Big(\underbrace{E_1^2,\ldots,E_1^2}_{n-1 \text{ terms}},\partial_x^2 E_1^2\Big) = \frac{2^n n!}{2n} F^{n-2}(0) 2 \times [F(0)F''(0) + F'^2(0)], \tag{A16}$$

where $F(x)$ is defined by Eq. (26).

A similar derivation is then performed for all terms in Eq. (A6) that are not found to vanish on the basis of the property (3) above [41]. Upon summing various geometric series and recognizing the expansion of a logarithm, we find

$$\overline{\langle k|\, e^{-i[p^2/2m+V](t/\hbar)}\, |k\rangle} = \frac{e^{-i\epsilon_k t/\hbar}}{1 \pm i t V_0/\hbar}\left[1 + \frac{i t^3 V_0^2 E_\sigma/\hbar^3}{12(1+itV_0/\hbar)} + \frac{t^4 V_0^2 E_\sigma/\hbar^4}{12(1+itV_0/\hbar)}\epsilon_k\right]. \tag{A17}$$

This result is not difficult to generalize to dimension d, where Eq. (A2) becomes

$$\begin{aligned}\langle \boldsymbol{k}|\, e^{-i[\boldsymbol{p}^2/2m+V](t/\hbar)}\, |\boldsymbol{k}\rangle &= e^{-iV(\boldsymbol{r})t} e^{(i\hbar^2 t^3/3m)\sum_{i=1}^d [\partial_{x_i} V(\boldsymbol{r})]^2} \\ &\quad \times e^{(-\hbar^2 t^2/4m)[2i\boldsymbol{k}\cdot\nabla V(\boldsymbol{r}) + \nabla^2 V(\boldsymbol{r})]} \\ &\quad \times e^{-(i\hbar^2 t^3/3m)\sum_{i,j=1}^d [\partial_{x_i}\partial_{x_j} V(\boldsymbol{r})](\hbar^2 k_i k_j/2m)} e^{O(\hbar^3)}.\end{aligned} \tag{A18}$$

In the sum $\sum_{i,j=1}^d [\partial_{x_i}\partial_{x_j} V(\boldsymbol{r})]\hbar^2 k_i k_j/2m$, to leading order in $\hbar$ the crossed terms ($i \neq j$) do not contribute to the disorder-averaged propagator as their contributions are proportional to first-order derivatives of the field correlation function (26) evaluated at 0, which vanish. Also, derivatives of the potential with respect to different directions are independent. Therefore, the propagator in dimension d is simply the product of d 1D propagators. Finally, the result for the red-detuned speckle is deduced by changing m to $-m$ and t to $-t$ (which amounts to changing the sign of V). The general result then reads

$$\overline{\langle k|\, e^{-i[p^2/2m+V](t/\hbar)}\, |k\rangle} = \frac{e^{-i\epsilon_k t/\hbar}}{1 \pm i t V_0/\hbar}\left[1 + \frac{d i t^3 V_0^2 E_\sigma/\hbar^3}{12(1 \pm itV_0/\hbar)} + \frac{t^4 V_0^2 E_\sigma/\hbar^4}{12(1 \pm itV_0/\hbar)}\epsilon_k\right], \tag{A19}$$

with the $+$ (respectively $-$) sign for blue-(respectively red-)detuned speckles. This immediately leads to Eq. (12) of the main text.

APPENDIX B

In this Appendix, we derive the joint probability distribution $P(\lambda_1,\lambda_2)$ of the eigenvalues λ_1 and λ_2 of the matrix

$$A = \begin{pmatrix} \partial_x^2 V(x,y) & \partial_x\partial_y V(x,y) \\ \partial_y\partial_x V(x,y) & \partial_y^2 V(x,y) \end{pmatrix}, \tag{B1}$$

in the vicinity of a minimum $V(x,y) = 0$. As in Sec. III A we write the potential as

$$V(x,y) = \mathrm{Re}(x,y)^2 + \mathrm{Im}(x,y)^2, \tag{B2}$$

where $\mathrm{Re}(x,y)$ and $\mathrm{Im}(x,y)$ are independent Gaussian variables with zero mean and equal variance $\sigma_c^2 = V_0/(4\sigma^2)$ [20]. Making use of the shorthand notation

$$\begin{aligned} \Re_x &\equiv \partial_x \mathrm{Re}(x,y), \quad \Im_x \equiv \partial_x \mathrm{Im}(x,y), \\ \Re_y &\equiv \partial_y \mathrm{Re}(x,y), \quad \Im_y \equiv \partial_y \mathrm{Im}(x,y), \end{aligned} \tag{B3}$$

we rewrite the matrix A as

$$A = 2\begin{pmatrix} \Re_x^2 + \Im_x^2 & \Re_x\Re_y + \Im_x\Im_y \\ \Re_x\Re_y + \Im_x\Im_y & \Re_y^2 + \Im_y^2 \end{pmatrix}. \tag{B4}$$

$\Re_x$, $\Re_y$, $\Im_x$, and $\Im_y$ are independent, Gaussian distributed random variables with zero mean and variance σ_c. The distribution $P(u,v)$ can then be expressed as

$$\begin{aligned} P(u,v) = &\int d\Re_x d\Re_y d\Im_x d\Im_y P(\Re_x)P(\Re_y)P(\Im_x)P(\Im_y) \\ &\times \delta[u - \lambda_1(\Re_x,\Re_y,\Im_x,\Im_y)]\delta[v - \lambda_2(\Re_x,\Re_y,\Im_x,\Im_y)]. \end{aligned}$$

To tackle this integral, we first change variables to "intensity" and "phase":

$$\begin{aligned} \Re_x &= \sqrt{I_1}\cos\theta_1, \quad \Im_x = \sqrt{I_1}\sin\theta_1, \\ \Re_y &= \sqrt{I_2}\cos\theta_2, \quad \Im_y = \sqrt{I_2}\sin\theta_2. \end{aligned} \tag{B5}$$

The Jacobian of the transformation is $1/4$, and $I_1, I_2 \in [0, +\infty[$ and $\theta_1, \theta_2 \in [-\pi, \pi]$. The integral reduces to

$$\begin{aligned} &P(\lambda_1,\lambda_2) \\ &= \frac{1}{32\pi^2\sigma_c^4}\int_0^{+\infty} dI_1 dI_2 \int_{-\pi}^{\pi} d\theta_1 d\theta_2 e^{-(I_1+I_2)/2\sigma_c^2} \\ &\times\delta\big(\lambda_1 - \big[I_1 + I_2 - \sqrt{I_1^2 + I_2^2 + 2I_1I_2\cos 2(\theta_1-\theta_2)}\big]\big) \\ &\times\delta\big(\lambda_2 - \big[I_1 + I_2 + \sqrt{I_1^2 + I_2^2 + 2I_1I_2\cos 2(\theta_1-\theta_2)}\big]\big), \end{aligned}$$

where we have assumed $\lambda_2 > \lambda_1$ without loss of generality, and added a corresponding renormalization prefactor $1/2$. We then introduce

$$\varphi = \theta_1 + \theta_2, \quad \phi = 2(\theta_1 - \theta_2), \tag{B6}$$

and carry out the integral over φ. This eventually yields

$$\begin{aligned} P(\lambda_1,\lambda_2) = &\frac{1}{8\pi\sigma_c^4}\int_0^{+\infty} dI_1 dI_2 \int_0^{\pi} d\phi e^{-(I_1+I_2)/2\sigma_c^2} \\ &\times\delta\big(\lambda_1 - \big[I_1 + I_2 - \sqrt{I_1^2 + I_2^2 + 2I_1I_2\cos\phi}\big]\big) \\ &\times\delta\big(\lambda_2 - \big[I_1 + I_2 + \sqrt{I_1^2 + I_2^2 + 2I_1I_2\cos\phi}\big]\big). \end{aligned}$$

This expression can be further simplified by writing $\int_0^{\infty} dI_1 dI_2 = \int_0^{\infty} dI_1 \int_0^{I_1} dI_2 + \int_0^{\infty} dI_1 \int_{I_1}^{\infty} dI_2$ and noticing the equality of these two integrals due to the symmetric role played by I_1 and I_2:

$$\begin{aligned} P(\lambda_1,\lambda_2) = &\frac{1}{4\pi\sigma_c^4}\int_0^{+\infty} dI_1 \int_0^{I_1} dI_2 \int_0^{\pi} d\phi e^{-(I_1+I_2)/2\sigma_c^2} \\ &\times\delta\big(\lambda_1 - \big[I_1 + I_2 - \sqrt{I_1^2 + I_2^2 + 2I_1I_2\cos\phi}\big]\big) \\ &\times\delta\big(\lambda_2 - \big[I_1 + I_2 + \sqrt{I_1^2 + I_2^2 + 2I_1I_2\cos\phi}\big]\big). \end{aligned}$$

We then change the variable ϕ to z so that

$$z = I_1 + I_2 + \sqrt{I_1^2 + I_2^2 + 2I_1I_2\cos\phi}, \tag{B7}$$

where z spans the interval $[0, 2I_2]$. The corresponding Jacobian is

$$\left|\frac{\partial\phi}{\partial z}\right| = \frac{2|I_1 + I_2 - z|}{\sqrt{z(2I_1 - z)(2I_2 - z)(2I_1 + 2I_2 + z)}}. \tag{B8}$$

Performing the integrals over I_2 and z, we straightforwardly find

$$\begin{aligned} P(\lambda_1,\lambda_2) = &\frac{1}{8\pi\sigma_c^4}\int_{(\lambda_1+\lambda_2)/4}^{\lambda_2/2} dI_1 e^{-(\lambda_1+\lambda_2)/4\sigma_c^2} \\ &\times\frac{(\lambda_2 - \lambda_1)\theta(\lambda_1)}{\sqrt{\lambda_1\lambda_2(\lambda_2 - 2I_1)(2I_1 - \lambda_1)}}. \end{aligned} \tag{B9}$$

The remaining integral can be done analytically, yielding

$$P(\lambda_1,\lambda_2) = \frac{(\lambda_2 - \lambda_1)e^{-(\lambda_1+\lambda_2)/4\sigma_c^2}}{32\sigma_c^4\sqrt{\lambda_1\lambda_2}}\theta(\lambda_1) \ (\lambda_2 > \lambda_1). \tag{B10}$$

This relation has been obtained assuming $\lambda_2 > \lambda_1$. The opposite case $\lambda_1 < \lambda_2$ is fully symmetric:

$$P(\lambda_1,\lambda_2) = \frac{(\lambda_1 - \lambda_2)e^{-(\lambda_1+\lambda_2)/4\sigma_c^2}}{32\sigma_c^4\sqrt{\lambda_1\lambda_2}}\theta(\lambda_2) \ (\lambda_2 < \lambda_1). \tag{B11}$$

Using Eqs. (B10) and (B11) together with the relations $\lambda_1 = m\omega_x^2$, $\lambda_2 = m\omega_x^2$, we finally obtain Eq. (50) of the main text.

[1] P. W. Anderson, Phys. Rev. **109**, 1492 (1958).

[2] J. Chabé, G. Lemarié, B. Grémaud, D. Delande, P. Szriftgiser, and J. C. Garreau, Phys. Rev. Lett. **101**, 255702 (2008).

[3] I. Manai, J. F. Clément, R. Chicireanu, C. Hainaut, J. C. Garreau, P. Szriftgiser, and D. Delande, Phys. Rev. Lett. **115**, 240603 (2015).

[4] J. Billy, V. Josse, Z. Zuo, A. Bernard, B. Hambrecht, P. Lugan, D. Clément, L. Sanchez-Palencia, P. Bouyer, and A. Aspect, Nature (London) **453**, 891 (2008).

[5] F. Jendrzejewski, A. Bernard, K. Müller, P. Cheinet, V. Josse, M. Piraud, L. Pezzé, L. Sanchez-Palencia, A. Aspect, and P. Bouyer, Nat. Phys. **8**, 398 (2012).

[6] G. Semeghini, M. Landini, P. Castilho, S. Roy, G. Spagnolli, A. Trenkwalder, M. Fattori, M. Inguscio, and G. Modugno, Nat. Phys. **11**, 554 (2015).

[7] H. Hu, A. Strybulevych, J. H. Page, S. E. Skipetrov, and B. A. Van Tiggelen, Nat. Phys. **4**, 945 (2008).

[8] G. Modugno, Rep. Prog. Phys. **73**, 102401 (2010).

[9] B. Shapiro, J. Phys. A: Math. Theor. **45**, 143001 (2012).
[10] P. W. Anderson, *Basic Notions of Condensed Matter Physics* (Westview/Addison-Wesley, Reading, MA, 1997).
[11] W. R. McGehee, S. S. Kondov, W. Xu, J. J. Zirbel, and B. DeMarco, Phys. Rev. Lett. **111**, 145303 (2013).
[12] C. A. Müller and B. Shapiro, Phys. Rev. Lett. **113**, 099601 (2014).
[13] C. A. Müller, D. Delande, and B. Shapiro, arXiv:1605.04329.
[14] P. Lugan, D. Clement, P. Bouyer, A. Aspect, and L. Sanchez-Palencia, Phys. Rev. Lett. **99**, 180402 (2007).
[15] I. L. Aleiner, B. L. Altshuler, and G. V. Shlyapnikov, Nat. Phys. **6**, 900 (2010).
[16] N. Cherroret, T. Karpiuk, B. Grémaud, and C. Miniatura, Phys. Rev. A **92**, 063614 (2015).
[17] M. I. Trappe, D. Delande, and C. A. Müller, J. Phys. A: Math. Theor. **48**, 245102 (2015).
[18] G. M. Falco, A. A. Fedorenko, J. Giacomelli, and M. Modugno, Phys. Rev. A **82**, 053405 (2010).
[19] S. John, M. Y. Chou, M. H. Cohen, and C. M. Soukoulis, Phys. Rev. B **37**, 6963 (1988).
[20] J. W. Goodman, *Statistical Properties of Laser Speckle Patterns* (Springer, New York, 2008).
[21] R. C. Kuhn, O. Sigwarth, C. Miniatura, D. Delande, and C. A. Müller, New J. Phys. **9**, 161 (2007).
[22] B. Grammaticos and A. Voros, Ann. Phys. **123**, 359 (1979).
[23] M. C. Gutzwiller, *Chaos in Classical and Quantum Mechanics* (Springer, New York, 1990).
[24] M. Tabor, Physica D **6**, 195 (1983).
[25] F. Haake, *Quantum Signatures of Chaos* (Springer, New York, 2010).
[26] Note that for blue-detuned speckle potentials, the spectral function and the density of states exhibit a Lifshitz tail at very small energies [27,28]. This tail is intrinsically quantum and cannot be described by semiclassical approximations.
[27] I. M. Lifshitz, Adv. Phys. **13**, 483 (1964).
[28] G. M. Falco and A. A. Fedorenko, Phys. Rev. A **92**, 023412 (2015).
[29] A. Altland and B. Simons, *Condensed Matter Field Theory* (Cambridge University Press, Cambridge, England, 2010).
[30] It could be possible to perform a Wick rotation and express everything as a sum of imaginary energies. This treatment is not very enlightening.
[31] Wolfram Research, Inc., Mathematica, Version 10.3, Champaign, IL, 2015.
[32] The maxima of blue-detuned speckle—or equivalently the minima of a red-detuned one—could be studied along the same lines, but they are not relevant for the behavior of the spectral function.
[33] G. N. Watson, *A Treatise on the Theory of Bessel Functions* (Cambridge University Press, Cambridge, England, 1966).
[34] A. Weinrib, Phys. Rev. B **26**, 1352 (1982).
[35] A. Weinrib and B. I. Halperin, Phys. Rev. B **26**, 1362 (1982).
[36] M. C. Gutzwiller, Physica D **5**, 183 (1982).
[37] We remind that this value corresponds to a speckle potential with Gaussian correlation function. For circular speckles [20], this number goes up to roughly 75%.
[38] M. Pasek, Z. Zhao, D. Delande, and G. Orso, Phys. Rev. A **92**, 053618 (2015).
[39] S. Ghosh, D. Delande, C. Miniatura, and N. Cherroret, Phys. Rev. Lett. **115**, 200602 (2015).
[40] W. Magnus, Commun. Pure Appl. Math. **7**, 649 (1954).
[41] D. R. Brillinger, *Time Series Data Analysis and Theory* (Society for Industrial and Applied Mathematics, Philadelphia, USA, 2001).
[42] V. P. Leonov and A. N. Shiryaev, Theor. Probab. Appl. **4**, 319 (1959). Note that "semi-invariant" is another word for joint cumulant.
[43] Here we use a somewhat simpler and less general version of Leonov and Shiryaev theorem, proposed in [41].

Chapter 4

Quantum boomerang effect in one-dimensional random potentials

Having clarified how random potentials are generated in cold-atom experiments in chapter 2, and discussed the general framework for describing the dynamics of wave packets in section 3.2, we now consider a concrete dynamical scenario. The latter resembles the experiment performed in Palaiseau in 2008 [37], where an initially narrow wave packet spreads in a one-dimensional random potential, and the density profile is recorded in the course of time. Here however, we propose to additionally give the atoms a finite average velocity and track the wave packet center-of-mass motion.

The chapter starts with a brief statement of the problem in section 4.1. In section 4.2, we develop an intuitive derivation of the packet center-of-mass, based on classical arguments. This somewhat naive approach is compared to numerical simulations in section 4.3. The numerical simulations reveal an unexpected phenomenon: after an initial ballistic motion, the packet center-of-mass experiences a retroreflection and appears to slowly return to its initial position. We dubbed this phenomenon the quantum boomerang effect. We show in section 4.4 that it is triggered by Anderson localization. Section 4.5 is devoted to an analytical treatment of the center of mass, based on Berezinskii diagrammatic technique [13]. This derivation is supplemented by appendices 4.A and 4.B. In applying Berezinskii diagrammatic technique, we make some assumptions on the random potential and on the initial wave packet, which are discussed in section 4.6. In section 4.7 finally, we derive a surprising relation between center of mass and mean square displacement. Section 4.8 concludes the chapter and gives some perspectives for future work.

4.1 Initial condition

We consider the evolution of an initial Gaussian wave packet with a phase,

$$\psi(x, t = 0) = \Psi_{k_0}(x) = \frac{\exp\left(-x^2/2\sigma^2 + ik_0x\right)}{\pi^{1/4}\sigma^{1/2}}, \tag{4.1}$$

which we will refer to as "kicked" Gaussian wave packet in the following. At variance with the initial wave packet used in Palaiseau in 2008 [37], (4.1) is imprinted with a mean velocity $\hbar k_0/m$. The evolution is governed by the Hamiltonian

$$H = -\hbar^2\Delta/2m + V, \tag{4.2}$$

where V is a Gaussian[1], uncorrelated random potential:

$$\overline{V(x)} = 0 \quad \text{and} \quad \overline{V(x)V(x')} = \gamma\delta(x - x'), \tag{4.3}$$

the overbar denoting averaging over disorder realizations. Starting from a Gaussian-correlated potential, equation (2.31), the uncorrelated potential (4.3) is obtained by taking the limit $\sigma \to 0$ and $V_0 \to \infty$ with $\gamma = V_0^2\sigma\sqrt{2\pi}$. Of course the dynamics of the wave packet for positive and negative k_0 is perfectly symmetric. Without loss of generality, from here on we consider only $k_0 > 0$.

For the sake of simplicity, we assume in the following that the wave packet can be approximated by a quasi-monochromatic wave packet (i.e. its dynamics is supported by only one energy component). This approximation is justified in the limit of an initially narrow momentum distribution, $k_0\sigma \gg 1$, and of a weak energy broadening by the disorder ($k_0\ell \gg 1$). To make it clear, we adopt the language of section 3.2 and write the energy distribution $P(\epsilon)$ as

$$P(\epsilon) = \int W(x,p)A_p(\epsilon)\mathrm{d}x\mathrm{d}p, \tag{4.4}$$

where $A_p(\epsilon)$ is the spectral function and $W(x,p)$ is the Wigner distribution of the initial wave packet (4.1):

$$W(x,p) = \frac{1}{\pi}\exp\left(-x^2/\sigma^2\right)\exp\left[-(p-\hbar k_0)^2\sigma^2\right]. \tag{4.5}$$

Under the assumption $k_0\sigma \gg 1$, we can simplify the initial Wigner distribution to

$$W(x,p) \simeq \frac{1}{\sqrt{\pi}\sigma}\exp\left(-x^2/\sigma^2\right)\delta(p-\hbar k_0), \tag{4.6}$$

such that equation (4.4) reduces to $P(\epsilon) = A_{\hbar k_0}(\epsilon)$. By further assuming weak disorder ($k_0\ell \gg 1$), the spectral function can be approximated by its free form $A_{\hbar k_0}(\epsilon) \simeq \delta(\epsilon - \hbar^2k_0^2/2m)$, such that $P(\epsilon) \simeq \delta(\epsilon - \hbar^2k_0^2/2m)$. Only one energy component ($\epsilon_0 = \hbar^2k_0^2/2m$) is indeed at play. In section 4.5, we will come back more rigorously on this and rely directly on the assumptions $k_0\sigma \gg 1$ and $k_0\ell \gg 1$.

The disorder parameter $k_0\ell$ introduced above involves the scattering mean free path $\ell = \hbar k_0\tau/m$, related to the scattering mean free time τ, given by (subsection 3.1.3)

$$\tau = \frac{k_0\hbar^3}{2m\gamma} \tag{4.7}$$

at the Born approximation.

We focus primarily on the visual case of a wave packet which is initially much smaller than the mean free path. As it turns out, what we discuss in the following holds as well for wave packet broader than the mean free path, as shown in subsection 4.6.3.

4.2 Classical approach

To get a first insight on the dynamics of the kicked wave packet, let us start with classical considerations. To that end, we first relate the center of mass to the average momentum, through Ehrenfest theorem:

$$\partial_t \langle x\rangle = \frac{\langle p\rangle}{m}. \tag{4.8}$$

[1] As discussed in chapter 2, this model of random potential is not realistic for cold-atom experiments. It is chosen here because it allows for much simpler perturbative developments thanks to Wick theorem (see subsection 3.1.2 for more details), and eventually to fully solve the problem in section 4.5. In the weak disorder limit, the choice of potential on-site distribution, if reasonable, is anyhow not expected to change the physics discussed in this chapter [42]. This issue is further discussed in section 4.6.1.

In this notation, the symbol $\langle . \rangle$ refers to both the quantum expectation value and the disorder average.

Equation (4.8) provides a good starting point in that the evolution of the momentum distribution takes a rather simple form in the classical framework. Indeed, under the conditions introduced in section 4.1, atoms have either a positive momentum $\hbar k_0$ or a negative one $-\hbar k_0$, and they are scattered from one momentum state to the other at a rate $1/2\tau$ (see subsection 3.1.3 for more details), leading to two coupled Boltzmann equations for the evolution of the average population in $\hbar k_0$ (n_+) and $-\hbar k_0$ (n_-):

$$\begin{cases} \frac{\mathrm{d}n_+}{\mathrm{d}t} = \frac{n_-}{2\tau} - \frac{n_+}{2\tau}, \\ \frac{\mathrm{d}n_-}{\mathrm{d}t} = \frac{n_+}{2\tau} - \frac{n_-}{2\tau}, \end{cases} \tag{4.9}$$

with of course $n_+ + n_- = 1$. These two equations are straightforward to solve. With the initial condition $n_+ = 1$, we find

$$n_+ = \frac{1 + e^{-t/\tau}}{2} \quad \text{and} \quad n_- = \frac{1 - e^{-t/\tau}}{2}. \tag{4.10}$$

Plugging this result back in equation (4.8),

$$\partial_t \langle x \rangle_{\text{class}} = \frac{\hbar k_0}{m} (n_+ - n_-), \tag{4.11}$$

and using $\langle x(t=0) \rangle = 0$, we find the following classical solution for the center of mass:

$$\langle x \rangle_{\text{class}} = \ell \left(1 - e^{-t/\tau} \right). \tag{4.12}$$

Within a classical approach, the initial ballistic motion of the center of mass thus quickly saturates at a scattering mean free path. Is this the full story, or does Anderson localization modify this intuitive behavior? To answer this question, we propose to perform numerical simulations. Before doing so, we note that equation (4.12) applies in any dimension.

4.3 Numerical solution

This section being devoted to a numerical technique, we set $\hbar$ to 1 to lighten the notations.

To propagate numerically the initial wave packet, equation (4.1), we start by discretizing the space on a grid. The Laplacian in the Schrödinger equation thus becomes a discrete one. In order to correctly describe the continuous limit, the discretization should be fine enough to capture the spatial variations of the wave function. When using correlated potentials, one should also make sure that the discretization allows to resolve the correlation length. The space being of finite size, we have to impose boundary conditions. Throughout this thesis, we use periodic boundary conditions. Note that we use large enough systems for the wave packet not to reach the boundaries.

The way random potentials are numerically generated was discussed in subsection 2.2.4. It remains to perform the evolution, for that we follow [129,130]. The idea is to take advantage of the formal solution of the Schrödinger equation as

$$|\psi(t)\rangle = \hat{U}(t) |\psi(t=0)\rangle = e^{-i\hat{H}t} |\psi(t=0)\rangle. \tag{4.13}$$

The challenge is then to find a representation of $\hat{U}(t)$ which can be implemented efficiently. This is achieved with Chebyshev polynomials.

4.3.1 Chebyshev polynomials

The Chebyshev polynomial of order k is defined as $T_k(x) = \cos(k\arccos(x))$. Chebyshev polynomials have the following orthogonality properties [131]:

$$\int_{-1}^{1} \mathrm{d}x \frac{T_n(x)T_m(x)}{\sqrt{1-x^2}} = \frac{\pi}{2}\delta_{n,m}(2-\delta_{n,0}), \tag{4.14}$$

and they can be determined iteratively using [131]

$$\begin{cases} T_{n+1}(x) = 2xT_n(x) - T_{n-1}(x), \\ T_0(x) = 1,\, T_1(x) = x. \end{cases} \tag{4.15}$$

Importantly, the Chebyshev polynomials form a complete basis, and the Chebyshev series of a given function f:

$$f(x) = \sum_n c_n T_n(x), \tag{4.16}$$

converges to f, for $x \in [-1,1]$, if f is piecewise smooth and continuous [131]. The series (4.16) generally diverges for $|x| > 1$ [131].

4.3.2 Expansion of the evolution operator over Chebyshev polynomials

Since the Chebyshev series converges only in $[-1,1]$, it cannot be directly used to expand the evolution operator $\hat{U}(t)$. To achieve this goal, it is convenient to introduce the quantities

$$R = \frac{E_{\max} - E_{\min}}{2}, \tag{4.17}$$

$$G = E_{\min}, \tag{4.18}$$

$$\hat{H}_{\mathrm{norm}} = \frac{\hat{H} - (R+G)}{R}, \tag{4.19}$$

where $E_{\min}$ and $E_{\max}$ are respectively a lower and an upper bound of the Hamiltonian spectrum (such bounds always exist in the discrete finite systems used in numerical simulations). With these definitions, the eigenvalues of $\hat{H}_{\mathrm{norm}}$ are in $[-1,1]$ and

$$\hat{U}(t) = \mathrm{e}^{-i\hat{H}t} = \mathrm{e}^{-i(R+G)t}\mathrm{e}^{-iR\hat{H}_{\mathrm{norm}}t}. \tag{4.20}$$

We can now write $\mathrm{e}^{-iR\hat{H}_{\mathrm{norm}}t}$ as a sum of Chebyshev polynomials:

$$\mathrm{e}^{-iR\hat{H}_{\mathrm{norm}}t} = \sum_{k=0}^{\infty} a_k T_k(\hat{H}_{\mathrm{norm}}). \tag{4.21}$$

The a_k are determined from the Chebyshev polynomials orthogonality relations (4.14),

$$a_k \frac{\pi}{2}(2-\delta_{k,0}) = \int_{-1}^{1} \mathrm{d}x \frac{T_k(x)\mathrm{e}^{-iRxt}}{\sqrt{1-x^2}} = \pi(-i)^k J_k(Rt), \tag{4.22}$$

where J_k denotes the k^{th} order Bessel function of the first kind.

4.3.3 Practical implementation

Numerically, we cannot sum the infinite series in (4.21), we have to stop at some point. This is where the choice of Chebyshev polynomials proves useful, since for large enough k, a_k decays exponentially with k [101].

At this stage, two important comments are in order. First, the efficiency of the procedure strongly depends on the bounds on the Hamiltonian spectrum that one is able to provide [$E_{\max}$ and $E_{\min}$ in equation (4.19)]. Absolute bounds are not difficult to obtain by minimizing/maximizing separately the kinetic and potential energies:

$$E_{\min}^{\text{abs}} = V_{\min} \quad \text{and} \quad E_{\max}^{\text{abs}} = \frac{1}{2m}\left(\frac{\pi}{\Delta x}\right)^2 + V_{\max} \tag{4.23}$$

where $V_{\min}$ ($V_{\max}$) is the smallest (largest) value taken by the given realization of the random potential and Δx is the grid step. However, it is generally more effective to use tighter bounds $E_{\min}$ and $E_{\max}$, which can be estimated from

$$\left|(\hat{H} - E_{\max}^{\text{abs}})^n |\psi\rangle\right|^2 \underset{n\to\infty}{\sim} \left(E_{\min} - E_{\max}^{\text{abs}}\right)^{2n}, \tag{4.24}$$

$$\left|(\hat{H} + E_{\min}^{\text{abs}})^n |\psi\rangle\right|^2 \underset{n\to\infty}{\sim} \left(E_{\max} + E_{\min}^{\text{abs}}\right)^{2n}, \tag{4.25}$$

with $|\psi\rangle$ an arbitrary state with non vanishing projection on the eigenstate with lowest (resp. highest) eigenvalue of $\hat{H}$. In practice, at weak disorder we use the eigenstate minimizing or maximizing the kinetic energy, while at strong disorder, the eigenstates minimizing and maximizing the potential energy are used. We assume that the asymptotic behaviors (4.24) and (4.25) are reached when we observe an essentially geometrical progression (i.e. when the ratio of two consecutive values is roughly constant). To be on the safe side, $E_{\min}$ ($E_{\max}$) is eventually reduced (increased) by a few percents.

A second important point is the question of numerical stability. Indeed, computing the Chebyshev polynomials in (4.21) iteratively using equation (4.15) up to high order may lead to numerical instabilities. To avoid such troubles, it is generally preferable to divide the full evolution into small time steps. Indeed, the maximum order in the Chebyshev expansion decreases when the time step decreases. The maximum order in the Chebyshev expansion being inversely proportional to the time step [$J_k(Rt)$ in equation (4.22) takes non-negligible values for $k \lesssim Rt$], the division of the full evolution in small time steps does not impact much the performances. We have also noticed that a rearrangement of the series (4.21) tends to impact the numerical stability as well as the performances. Practically, we have observed that rearranging the series (4.21) under the form

$$\sum_{k=0}^{k_{\max}} a_k T_k(\hat{H}_{\text{norm}}) = \sum_{k=0}^{k_{\max}} b_k \hat{H}_{\text{norm}}^k, \tag{4.26}$$

with time steps allowing for $k_{\max}$ to be around 20, is both numerically stable and efficient. Equation (4.26) simply rearranges the Chebyshev polynomials (e.g. $T_1 = x$, $T_2 = -1+2x^2$) in monomials (e.g. -1, x, $2x^2$).

4.3.4 Results for $\langle x \rangle$

We are now in position to perform the numerical simulations for $\langle x \rangle$. To meet the conditions of section 4.1, we discretize the Hamiltonian on a 1D grid of size $16000\pi/k_0$, divided into 251352 grid points (roughly five grid points per k_0^{-1}). The initial wave-packet width is set to $\sigma = 10/k_0$, and $\gamma = 5.8\ 10^{-3}\ \hbar^4 k_0^3/m^2$ ($k_0\ell \simeq 86.5$). The resulting center of mass, averaged over 45000 disorder

realizations, is shown in figure 4.1a as blue points, with statistical error bars. As visible in figure 4.1a, while at short times the initial ballistic motion is well described by the classical prediction (4.12) (in green), the center of mass experiences a retroreflection instead of saturating at a mean free path (quantum boomerang effect). This surprising behavior is due to Anderson localization, as demonstrated in the next section.

We note nevertheless that the classical prediction is an excellent approximation at short times. Indeed, anticipating on the results presented in section 4.5, we have compared the classical prediction (4.12) to the exact short-time expansion [equation (4.69)] in figure 4.1b. One needs to keep the first six terms of the short-time expansion (magenta curve) to improve upon the classical prediction.

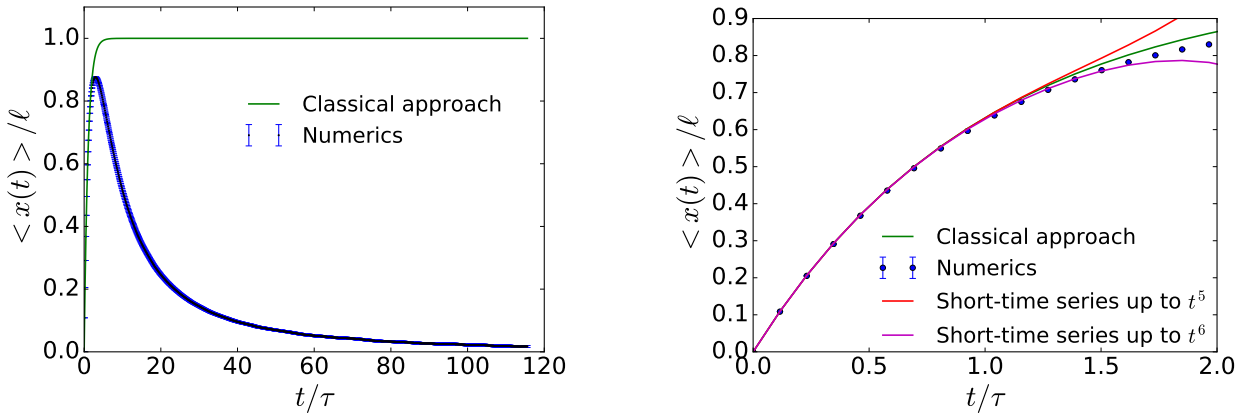

(a) (b)

Figure 4.1 – Center of mass $\langle x \rangle$ as a function of time, respectively in units of the scattering mean free path and time, of a wave packet initially launched with finite velocity in a random potential. The classical prediction, equation (4.12), shown as a green curve, is compared with numerical simulations shown as blue points. Figure a): after an initial ballistic motion, the packet center-of-mass experiences a retroreflection, in sharp contrast with the classical expectation. Figure b): focus on short times, with a comparison between the classical prediction and the exact short-time expansion [equation (4.69)], the classical prediction is an excellent approximation in this limit, six terms of the short-time expansion (magenta curve) are needed to improve upon it. The parameters used in the numerical simulations are given in the main text, in subsection 4.3.4.

4.4 Convergence of the density to its infinite-time limit

The reason why quantum wave packets behave so differently can be understood by the following argument. At any time, the density distribution can be expanded over the eigenbasis $\{\epsilon_n, |\phi_n\rangle\}$ of H as

$$|\Psi(x,t)|^2 = \sum_{n,m} \langle \phi_n | \Psi_{k_0} \rangle \langle \Psi_{k_0} | \phi_m \rangle \, \phi_n(x) \phi_m^*(x) e^{-i(\epsilon_n - \epsilon_m)t/\hbar}. \tag{4.27}$$

Since eigenstates are localized, the system is constrained to a volume set by the localization length $\xi = 2\ell$ [132]. This defines a typical mean level spacing $\Delta = 1/(\rho\xi)$ (ρ is the density of states per unit volume), with a corresponding Heisenberg time $\tau_{\mathrm{H}} = 2\pi\hbar/\Delta = 4\tau$ beyond which the off-diagonal oscillatory terms $n \neq m$ in equation (4.27) vanish, leaving:

$$\overline{|\Psi(x,\infty)|^2} = \sum_n \overline{|\langle \phi_n | \Psi_{k_0} \rangle|^2} |\phi_n(x)|^2, \tag{4.28}$$

where the overbar $\overline{(\dots)}$ denotes averaging over the random potential. Due to time-reversal invariance, the localized eigenstates ϕ_n can be chosen real. Furthermore, we have $|\langle\phi_n|\Psi_{k_0}\rangle|^2 = |\langle\phi_n^*|\Psi_{k_0}^*\rangle|^2 = |\langle\phi_n|\Psi_{-k_0}\rangle|^2$: equation (4.28) is independent of the sign of k_0. Equation (4.28) thus coincides with the long-time, spatially symmetric, averaged density distribution that would have been obtained with an initial wave packet having a symmetric velocity distribution. This shows that the center of mass *must* return to its initial position at long times, as a result of Anderson localization.

In order to clarify which specific behavior of the spatial distribution $\overline{|\Psi(x,t)|^2}$ actually gives rise to the quantum boomerang effect, we show in figure 4.2 the $x > 0$ (blue curve) and $x < 0$ (red curve) components of the spatial profile $\overline{|\Psi(x,t)|^2}$, obtained numerically at three successive times. As shown above, this distribution is expected to converge toward a symmetric one, equation (4.28), which coincides with the final distribution associated to an initial wave packet of the form $\Psi_{k_0}(x) \propto \exp(-x^2/2\sigma^2)\cos(k_0 x)$ (i.e. a state having a momentum distribution symmetric with respect to $k = 0$). As it turns out, this final distribution is the so-called Gogolin density profile [14]:

$$\overline{|\Psi(x,\infty)|^2} = \int_0^\infty \frac{\mathrm{d}\eta\pi^2}{32\ell} \frac{\eta\left(1+\eta^2\right)^2 \sinh(\pi\eta) e^{-\left(1+\eta^2\right)|x|/8\ell}}{[1+\cosh(\pi\eta)]^2}. \tag{4.29}$$

Equation (4.29) is derived in [14] using Berezinskii diagrammatic technique [13]. The latter is discussed in details in section 4.5 and applies in the conditions detailed in section 4.1 (quasi-monochromatic narrow initial wave packet and weak disorder). Equation (4.29) is also shown in figure 4.2 for comparison. At short times, the initial ballistic motion is visible as a peak moving with velocity $v_0 = \hbar k_0/m$. After this peak has been attenuated, one sees that the retroreflection does not stem from a rigid, forth and back motion of the wave packet, but rather from a process of re-symmetrization of the shape of the profile around $x = 0$.

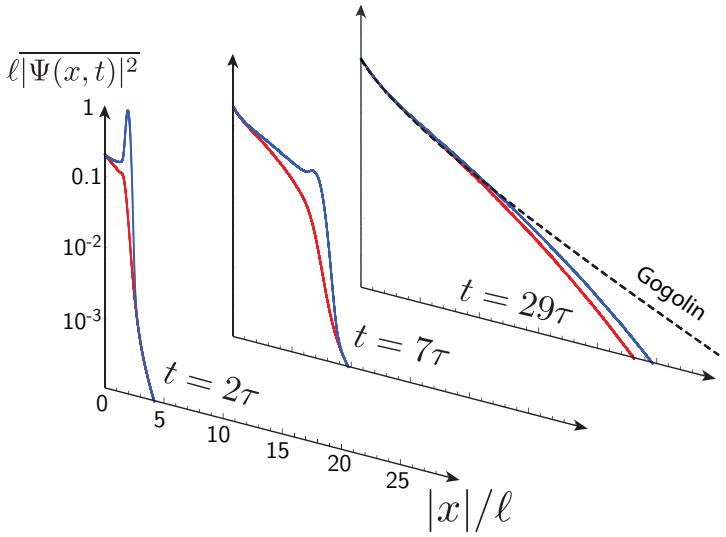

Figure 4.2 – Average density profile obtained numerically at three different times. The solid upper blue and lower red curves are the $x > 0$ and $x < 0$ components of the profile, respectively. The long-time limit of the profile, equation (4.29), is shown as a dashed black curve.

Having clarified the origin of the quantum boomerang effect, we now would like to analyze the center of mass at finite times from an analytical perspective.

4.5 Center-of-mass motion from Berezinskii diagrammatic technique

To lighten the notations, we use $\hbar = 1$ throughout this section.

4.5.1 Center of mass in terms of Green functions

To begin with, we express the quantity of interest, here $\langle x \rangle$, in terms of Green functions (the reader not familiar with Green functions may find subsection 3.1.1 useful). This is most conveniently done by first making use of the Erenhfest theorem, $\partial_t \langle x \rangle = \langle p \rangle / m$, which leads to

$$\langle p \rangle = \int \frac{\mathrm{d}p}{2\pi} \overline{|\psi(p,t)|^2} p = \frac{i}{4\pi} \int \mathrm{d}x_a \mathrm{d}x_b \mathrm{d}p \left(\partial_{x_a} - \partial_{x_b}\right) e^{-ip(x_a - x_b)} \overline{\psi(x_a,t)\psi^*(x_b,t)}. \tag{4.30}$$

Then, we express $\psi(x_a,t)$ [resp. $\psi^*(x_b,t)$] in terms of $G^R(x_a,x_c,t)$ [resp. $G^A(x_b,x_d,t)$]:

$$\psi(x_a,t) = \int \mathrm{d}x_c G^R(x_a,x_c,t)\Psi_{k_0}(x_c) \quad \left[\text{resp. } \psi^*(x_b,t) = \int \mathrm{d}x_d G^A(x_b,x_d,t)\Psi^*_{k_0}(x_d)\right]. \tag{4.31}$$

We can perform the integral over p, equal to $2\pi\delta(x_a - x_b)$, to find

$$\langle p \rangle = \frac{i}{2} \int \mathrm{d}x \mathrm{d}x_c \mathrm{d}x_d \left[\left(\partial_{x_a} - \partial_{x_b}\right) \overline{G^R(x_a,x_c,t)G^A(x_b,x_d,t)}\right]_{x_a = x_b = x} \Psi_{k_0}(x_c)\Psi^*_{k_0}(x_d). \tag{4.32}$$

It is easier to work in the frequency domain than in time domain, we thus introduce the Fourier transforms

$$G^R(x_a,x_c,\omega_1) = \int \mathrm{d}t e^{i\omega_1 t} G^R(x_a,x_c,t) \text{ and } G^A(x_b,x_d,\omega_2) = \int \mathrm{d}t e^{-i\omega_2 t} G^A(x_b,x_d,t). \tag{4.33}$$

Changing variables to ϵ and ω through $\omega_1 = \epsilon$ and $\omega_2 = \epsilon - \omega$, we obtain

$$\langle p(\omega) \rangle = \frac{i}{4\pi} \int \mathrm{d}x \mathrm{d}x_c \mathrm{d}x_d \mathrm{d}\epsilon \left[\left(\partial_{x_a} - \partial_{x_b}\right) \overline{G^R(x_a,x_c,\epsilon)G^A(x_b,x_d,\epsilon-\omega)}\right]_{x_a = x_b = x} \Psi_{k_0}(x_c)\Psi^*_{k_0}(x_d), \tag{4.34}$$

where $\langle p(\omega) \rangle = \int \mathrm{d}t e^{i\omega t} \langle p(t) \rangle$. The Fourier transform of the center of mass, $\langle x(\omega) \rangle = \int \mathrm{d}t e^{i\omega t} \langle x(t) \rangle$, immediately follows from

$$\partial_t \langle x(t) \rangle = \langle p(t) \rangle / m \Leftrightarrow \langle x(\omega) \rangle = -\frac{1}{im\omega} \langle p(\omega) \rangle . \tag{4.35}$$

Equation (4.34) is fully general and does not rely on any assumption.

4.5.2 Diagrammatics

As we have seen in subsection 3.1.1, Green functions are very convenient for perturbative calculations. A perturbative treatment is however insufficient here, because the quantum boomerang effect is due to Anderson localization, which is in essence a non-perturbative phenomenon. The Berezinskii diagrammatic technique [13] allows for a systematic resummation of the perturbative series, thus providing an analytical description of Anderson localization in one dimension. Berezinskii diagrammatic technique operates in a frequency range where $\omega \ll \epsilon$, hence *a priori* describing only times longer than $1/\epsilon$. Note that, anticipating on the results presented below, we can replace ϵ by ϵ_0, such that the weak disorder limit $k_0\ell \gg 1$ can equivalently be written $\epsilon_0\tau \gg 1$, and the condition $t > 1/\epsilon_0$ does not impose anything on t/τ.

Diagrammatic representation of $\overline{G^R(x_a,x_c,\epsilon)G^A(x_b,x_d,\epsilon-\omega)}$

We start by expanding the Green function, under the form of a Born series [equation (3.6)],

$$G^{A/R}(x,x',\epsilon) = G_0^{A/R}(x-x',\epsilon) + \int \mathrm{d}x_1 G_0^{A/R}(x-x_1,\epsilon)V(x_1)G_0^{A/R}(x_1-x',\epsilon) + \int \mathrm{d}x_1\mathrm{d}x_2 G_0^{A/R}(x-x_1,\epsilon)V(x_1)G_0^{A/R}(x_1-x_2,\epsilon)V(x_2)G_0^{A/R}(x_2-x',\epsilon)+\ldots, \tag{4.36}$$

where $G_0^{A/R}(x-x',\epsilon)$ is the Green function of the free-particle Hamiltonian, given by

$$G_0^{A/R}(x-x',\epsilon) = \pm i\frac{m}{k}e^{\mp ik|x-x'|}, \tag{4.37}$$

with $k=\sqrt{2m\epsilon}$. The following formula will be useful in what follows:

$$G_0^{A}(x-x',\epsilon-\omega) = i\frac{m}{k}e^{-ik\left(1-\frac{\omega}{2\epsilon}\right)|x-x'|} \text{ when } |\omega|\ll\epsilon. \tag{4.38}$$

The different terms appearing in the right-hand side of equation (4.36) are represented as diagrams: the unaveraged diagrams consist of two particle lines going respectively from x_c to x_a and x_d to x_b (respectively for G^R and G^A). Each line consists of segments $(x',x_1),\ldots,(x_i,x_{i+1}),\ldots,(x_n,x)$; the segments are the free Green functions while the points x_i refer to the factors $V(x_i)$. After averaging, these factors group together in pairs (by application of Wick theorem), each pair being associated with the potential correlation function (4.3). In the diagrams, the potential correlation functions are represented by wavy lines and free Green functions by ordinary (for the retarded Green function, G^R) and dashed lines (for the advanced Green function G^A). An example of such a diagram is shown in figure 4.3 (for the sake of clarity with $x_a=x_b=x$ and $x_c=x_d=x'$).

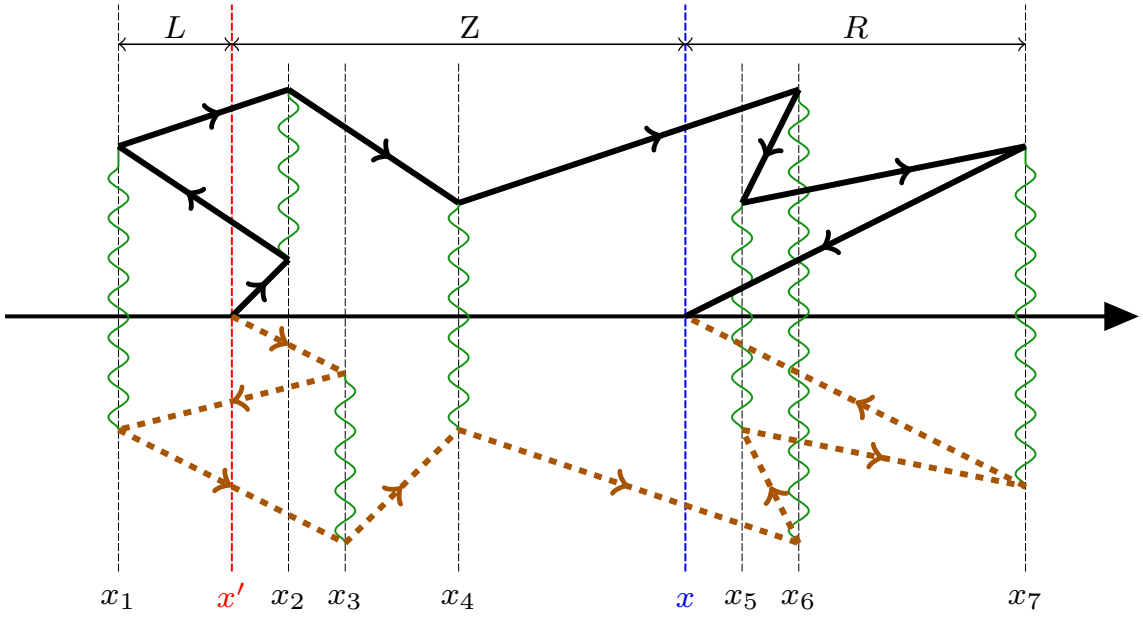

Figure 4.3 – Example of diagram contributing to $\overline{G^R(x,x',\epsilon)G^A(x,x',\epsilon-\omega)}$. The wavy lines represent the potential correlation function, the ordinary (dashed) lines represent the free Green functions for the retarded (advanced) Green function. The vertical unfolding is necessary to represent the diagram, the vertical direction has no substance.

Initial vertices

In principle, to sum all the diagrams, we should consider all possible initial vertices. They are depicted in figure 4.4. Under the weak-disorder condition introduced in section 4.1 ($k_0\ell \gg 1$), only two of them matter. To exhibit these relevant initial vertices, the first step is to order the scattering points x_i (over which the integration is performed to calculate a diagram) as

$$-\infty < x_1 \leq \cdots \leq x_i \leq x' \leq x_{i+1} \leq \cdots \leq x_j \leq x \leq x_{j+1} \leq \cdots \leq x_n < \infty. \tag{4.39}$$

With this ordering, the free Green functions are now factorable thanks to the fixed sign of $x_i - x_j$ over the region of integration [given by equation (4.39)]. For example, if $x_i > x_j$, we have

$$G_0^R(x_i - x_j, \epsilon) = -i\frac{m}{k}e^{ik|x_i - x_j|} = \sqrt{-i\frac{m}{k}}e^{ikx_i}\sqrt{-i\frac{m}{k}}e^{-ikx_j}. \tag{4.40}$$

This allows us to formally associate the first factor to the vertex x_i and the second one to the vertex x_j. We generalize this procedure to all G_0^R and G_0^A lines of the diagrams, thereby transferring the dependence on the x_i's from the lines to the vertices.

In each diagram, we can now consider the initial vertices separately from the rest. The different initial vertices are shown in figure 4.4. Vertices 4.4c and 4.4d carry a rapidly oscillating factor $e^{\pm ik(x_c + x_d)}$, integrating it makes a negligible contribution to $\overline{G^R G^A}$. We thus keep only initial vertices 4.4a and 4.4b.

(a) (b) (c) (d)

Figure 4.4 – Different vertices at the starting point. To those vertices correspond the following factors: $(m/k)\exp(ik(x_d - x_c))\exp(-i\omega k x_d/(2\epsilon))$ [a], $(m/k)\exp(ik(x_c - x_d))\exp(i\omega k x_d/(2\epsilon))$ [b], $(m/k)\exp(ik(x_c + x_d))\exp(-i\omega k x_d/(2\epsilon))$ [c], $(m/k)\exp(-ik(x_c + x_d))\exp(i\omega k x_d/(2\epsilon))$ [d].

As specified in section 4.1, the initial wave packet is assumed much smaller than the scattering mean free path: $|x_c - x_d| \ll \ell$, allowing us to perform the integral over $x_c - x_d$ in equation (4.34). To this end, we change variable to $r = x_c - x_d$ and $x' = (x_c + x_d)/2$ in equation (4.34) (we also use equation (4.35) to express the center of mass $\langle x \rangle$ in terms of the momentum expectation value $\langle p \rangle$):

$$\langle x(\omega) \rangle = -\frac{1}{4\pi m\omega}\int \mathrm{d}x\mathrm{d}x'\mathrm{d}r\mathrm{d}\epsilon \left[\left(\partial_{x_a} - \partial_{x_b}\right)\overline{G^R(x_a, x' + r/2, \epsilon)G^A(x_b, x' - r/2, \epsilon - \omega)}\right]_{x_a = x_b = x} \times \Psi_{k_0}(x' + r/2)\Psi_{k_0}^*(x' - r/2). \tag{4.41}$$

The range of Ψ_{k_0} being much smaller than the scattering mean free path, we can assume that no scattering event takes place between x_c and x_d, and factorize $e^{\pm ikr}$ in the product $G^R G^A$ as illustrated in figure 4.5:

$$\overline{G^R(x_a, x' + r/2, \epsilon)G^A(x_b, x' - r/2, \epsilon - \omega)} \simeq e^{\mp ikr}\overline{G^R(x_a, x', \epsilon)G^A(x_b, x', \epsilon - \omega)}, \tag{4.42}$$

with the upper sign for the vertex 4.4a and the lower sign for the vertex 4.4b.

We are now in position to perform the integration over r. For vertices 4.4a and 4.4b we obtain:

$$\int \mathrm{d}r e^{\mp ikr}\Psi_{k_0}(x' + r/2)\Psi_{k_0}^*(x' - r/2) = \frac{2\pi k}{m}\int_0^\infty \mathrm{d}p W(x', \pm p)\delta(\epsilon - p^2/2m), \tag{4.43}$$

(a) (b)

Figure 4.5 – Relevant vertices at the starting point: operation of changing variables from (x_c, x_d) to (r, x') through $r = x_c - x_d$ and $x' = (x_c + x_d)/2$, under the condition $|r| \ll \ell$ (no scattering event between x_c and x_d).

where we have introduced (we remind that $k = \sqrt{2m\epsilon}$)

$$1 = \frac{k}{m}\int_0^\infty \mathrm{d}p\,\delta(\epsilon - p^2/2m), \tag{4.44}$$

and the Wigner distribution of the initial wave packet $W(r,p)$ [equation (4.5)]. We identify $\delta(\epsilon - p^2/2m)$ as the free spectral function $A_p^0(\epsilon)$ (see subsection 3.1.4 for more details).

Plugging equations (4.42) and (4.43) in equation (4.41), we obtain

$$\begin{aligned}\langle x(\omega)\rangle = -\int \mathrm{d}x\mathrm{d}x'\mathrm{d}p\mathrm{d}\epsilon \frac{k}{2m^2\omega}\left[\left(\partial_{x_a} - \partial_{x_b}\right)\overline{G^R(x_a,x',\epsilon)G^A(x_b,x',\epsilon-\omega)}\right]_{x_a=x_b=x} \\ \times\left[\underbrace{W(x',p)}_{\text{vertex 4.4a}} + \underbrace{W(x',-p)}_{\text{vertex 4.4b}}\right] A_p^0(\epsilon).\end{aligned} \tag{4.45}$$

Note that the free spectral function $A_p^0(\epsilon)$ appears here instead of the average spectral function $A_p(\epsilon)$ in the presence of the random potential. This is due to our approximation of no scattering event between x_c and x_d [111]. Anyway, the free spectral function $A_p^0(\epsilon)$ is an excellent approximation of $A_p(\epsilon)$ in the weak disorder limit we are considering. Under the conditions of section 4.1 [$A_p(\epsilon) = A_p^0(\epsilon) = \delta(\epsilon - p^2/2m)$ and $W(x',p) = \delta(x')\delta(p - k_0)$], equation (4.45) simplifies to

$$\langle x(\omega)\rangle = -\frac{k_0}{2m^2\omega}\int \mathrm{d}x\left[\left(\partial_{x_a} - \partial_{x_b}\right)\overline{G^R(x_a,0,\epsilon_0)G^A(x_b,0,\epsilon_0-\omega)}\right]_{x_a=x_b=x}, \tag{4.46}$$

with vertex 4.4a as only possible initial vertex in the diagrammatic representation of $\overline{G^R G^A}$. Equation (4.46) constitutes our starting point for the calculation of $\langle x\rangle$ with Berezinskii diagrammatic technique.

To summarize, the conditions allowing us to simplify equations (4.34) and (4.35) to equation (4.46) are i) the quasi-monochromaticity, which makes the integral over ϵ dominated by ϵ_0, ii) the initially narrow wave packet, allowing for $\Psi_{k_0}(x) \simeq \delta(x)$, iii) the kicking term, $\exp(ik_0x)$, together with the assumption $k_0\sigma \gg 1$, which impose an initial motion to the right (i.e. initial vertex 4.4a only).

Selection of relevant diagrams

For the sake of generality, we momentarily forget the restriction to the initial vertex 4.4a in the diagrammatic representation of $\overline{G^R G^A}$, and include the initial vertex 4.4b as well.

In order to evaluate $\overline{G^R G^A}$ exactly, one should in principle sum all possible diagrams, which is a formidable task. As for initial vertices, at weak disorder ($k_0\ell \gg 1$) only a subclass of diagrams matters. To exhibit these diagrams, we consider the intervals delimited by the successive scattering

points of equation (4.39) and to each associate a number pair (g, g'), where g and g' are the number of G_0^R and G_0^A lines in the interval. For example, to the diagram in figure 4.3 corresponds the sequence (from left to right) (2,2),(3,3),(3,1),(1,1),(1,1),(2,2),(4,4),(2,2). When going from one interval to a neighboring one, the numbers g and g' undergo definite changes Δg and $\Delta g'$ which are uniquely determined by the type of vertex separating the two intervals. Different types of vertices are displayed in figure 4.6. As an example, the diagram f in figure 4.6 corresponds to $\Delta g = \Delta g' = 2$. Such a vertex appears in figure 4.3 between the intervals at the left and at the right of x_1.

We are now in position to distinguish two families of vertices. On the one hand, the first family has the property that $\Delta g = \Delta g'$. As can be seen from equation (4.38), in the limit $\omega/\epsilon_0 \to 0$, the vertices of this family are phaseless. On the other hand, the remaining vertices carry a phase $e^{i(\Delta g' - \Delta g)k_0 x}$. Integrating this rapidly oscillating factor makes a negligible contribution to $\overline{G^R G^A}$. We thus keep only diagrams made of vertices having the property $\Delta g = \Delta g'$. Such vertices are represented in figure 4.6 (for the inner ones) and 4.7 (for the external ones).

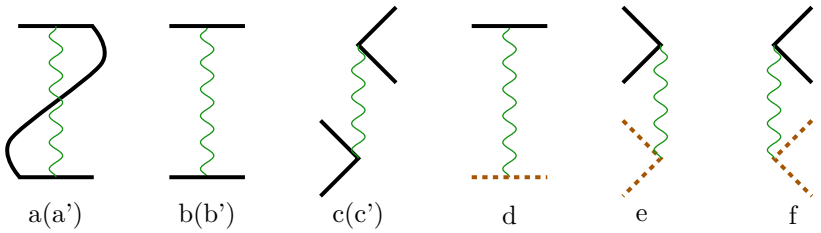

Figure 4.6 – Different inner vertices that form the relevant diagrams when $\omega \ll \epsilon_0$. The vertices a',b' and c', not shown on the figure, differ from the vertices a, b and c by having dashed brown lines in place of ordinary lines. The vertex a(a') corresponds to a term of the form $G_0(x_{i-1}-x_i)V(x_i)G_0(x_i-x_i)V(x_i)G_0(x_i-x_{i+1})$. To those vertices correspond the following factors: $-\gamma(m/k_0)^2$ [a,a',b,b',c,c'], $\gamma(m/k_0)^2$ [d], $\gamma(m/k_0)^2 \exp(i\omega k_0 x_i/\epsilon_0)$ [e], $\gamma(m/k_0)^2 \exp(-i\omega k_0 x_i/\epsilon_0)$ [f].

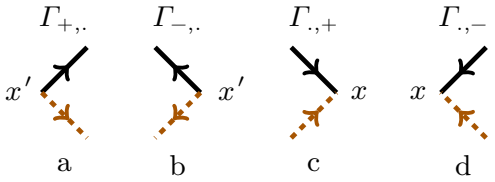

Figure 4.7 – Different vertices at the starting point x' and the ending point x entering the relevant diagrams when $\omega \ll \epsilon_0$. We denote such diagrams by $\Gamma_{\pm,\pm}$, the left subscript $\pm$ indicates the type of x' vertex (a or b), while the right subscript indicates the type of x vertex (c or d) (e.g. a diagram containing b and c will be denoted $\Gamma_{-,+}$). To those vertices correspond the following factors: $(m/k_0)\exp(-i\omega k_0 x'/(2\epsilon_0))$ [a], $(m/k_0)\exp(i\omega k_0 x'/(2\epsilon_0))$ [b], $(m/k_0)\exp(i\omega k_0 x/(2\epsilon_0))$ [c], $(m/k_0)\exp(-i\omega k_0 x/(2\epsilon_0))$ [d].

$\langle x \rangle$ in terms of diagrams

Coming back to our initial problem, the calculation of $\langle x \rangle$ through equation (4.46), we see that two important points should be taken into account: i) we should only keep diagrams with initial vertices of type 4.4a and ii) we should account for the derivatives with respect to the initial point. i) amounts to keeping only diagrams of type $\Gamma_{+,\cdot}$ in figure 4.7 and ii) simply introduces prefactors (from the caption of figure 4.4, $\mp 2ik_0$ for $\Gamma_{\cdot,\pm}$). Taking i) and ii) into account, we obtain

$$\langle x(\omega) \rangle = -\frac{1}{i\omega} \int \mathrm{d}(x - x') \left[\Gamma_{+,+}(x - x') - \Gamma_{+,-}(x - x') \right], \tag{4.47}$$

where we have used the fact that $\overline{G^R G^A}$ depends only on $|x-x'|$, due to translational invariance after averaging over the random potential. For latter convenience, it is useful to symmetrize equation (4.47), which presently describes the center of mass of a wave packet initially kicked to the right, by adding the corresponding equation for a wave packet initially kicked to the left

$$\langle x(\omega)\rangle_{-k_0} = -\frac{1}{i\omega}\int \mathrm{d}(x-x')\left[\Gamma_{-,+}(x-x') - \Gamma_{-,-}(x-x')\right], \tag{4.48}$$

through $\langle x\rangle_{k_0} = (\langle x\rangle_{k_0} - \langle x\rangle_{-k_0})/2$, to obtain

$$\langle x(\omega)\rangle = -\frac{1}{2i\omega}\int \mathrm{d}(x-x')\left[\Gamma_{+,+}(x-x') - \Gamma_{+,-}(x-x') - \Gamma_{-,+}(x-x') + \Gamma_{-,-}(x-x')\right]. \tag{4.49}$$

Indeed, under this form $\langle x(\omega)\rangle$ can be treated on the same footing as the current-current correlation function with the Berezinskii approach[2] [13]. We will come back to the connection between center of mass and the current-current correlation function in section 4.7.

4.5.3 Equations for the center of mass

Setting up the equations

From this point on, we use Berezinskii convention $\hbar = 2m = k_0 = 1$. $\hbar$, m and k_0 will be reintroduced in the final results.

To calculate the diagrams involved in equation (4.49), we start by distinguishing the left-hand, right-hand and central parts of the diagrams as the part of the diagrams lying to the left of x', to the right of x, and between x' and x respectively (we assume $x > x'$ for the moment). In figure 4.3, these respectively correspond to L, R and Z. Since for all the selected vertices (see figure 4.6) $\Delta g = \Delta g' = 0, \pm 2$, in each interval belonging to the left-hand and right-hand part we have $g = g' = 2n$, while in each interval belonging to the central part we have $g = g' = 2n+1$, where n is an integer which may depend on the interval.

The contribution of each diagram is an integral over the region (4.39). This integral breaks up into product of three integrals over $(x_1, \ldots, x_i)$, $(x_{i+1}, \ldots, x_j)$ and $(x_{j+1}, \ldots, x_n)$, which we call respectively the contributions of the left-hand, central and right-hand part. Let us denote by $\tilde{R}_m(x)$ the sum of the contributions of all the right-hand parts that have at the boundary with the central part (i.e. immediately to the right of point x) the state $g = g' = 2m$, by $\tilde{R}_{m'}(x')$ the analogous sum of the contributions of the left-hand parts, and by $Z_{m',m}(x',x)$ the sum of the contributions made by the central parts with left and right boundary states $g = g' = 2m'+1$ and $g = g' = 2m+1$.

To calculate $\tilde{R}_m(x)$, the idea is to consider how it varies as x is increased of an infinitesimal amount δx. In practice, one can relate $\tilde{R}_m(x-\delta x)$ to $\tilde{R}_m(x)$ by adding all the possible vertices in figure 4.6 between $x-\delta x$ and x. However, in doing this, one should be careful not to obtain diagrams with particle loops or diagrams that bear no relation with the original diagrams. In particular, one must only keep diagrams for which the lines G_0^R and G_0^A are continuous from x' to x. For this purpose, we can number the lines on the boundary of the right-hand part by assigning #1 to the segment corresponding to the first entry of the particle line into the right-hand part, #2 to the first emergence from it, #3 to the second entry, and so forth from 1 to $2m$. Then, in constructing the diagrams, we should keep in mind that the angles at the vertices in figure 4.6 can only be formed by the segments of the G_0-lines with consecutive numbers. Applying this procedure to $\tilde{R}_m$ in figure 4.8,

[2] Note that using directly the results of [13] to calculate $\langle x\rangle$, we find a result off by a factor of 2.

we derive the equation

$$\begin{aligned}\tilde{R}_m(x-\delta x) =&\tilde{R}_m(x) + \frac{\gamma}{4}\left[\underbrace{-4m\delta x}_{\text{a and a'}} - \underbrace{2m^2\delta x - 2m(m-1)\delta x}_{\text{b and b'}} - \underbrace{2m(m-1)\delta x}_{\text{c and c'}} + \underbrace{4m^2\delta x}_{\text{d}}\right]\tilde{R}_m(x)\\ &+\frac{\gamma}{4}\left[\underbrace{m^2\tilde{R}_{m-1}(x)e^{i\omega x}\delta x}_{\text{e}} + \underbrace{m^2\tilde{R}_{m+1}(x)e^{-i\omega x}\delta x}_{\text{f}}\right] + O(\delta x^2).\end{aligned} \tag{4.50}$$

Taking the limit $\delta x \to 0$, we obtain

$$-\frac{\mathrm{d}\tilde{R}_m(x)}{\mathrm{d}x} = \frac{\gamma}{4}\left[-2m^2\tilde{R}_m(x) + m^2\tilde{R}_{m-1}(x)e^{i\omega x} + m^2\tilde{R}_{m+1}(x)e^{-i\omega x}\right]. \tag{4.51}$$

This equation can be solved under the form $\tilde{R}_m(x) = e^{i\omega m x}R_m$, with R_m solution of

$$i\nu R_m + m\left(R_{m+1} + R_{m-1} - 2R_m\right) = 0 \text{ for } m > 0 \text{ and } R_0 = 1, \tag{4.52}$$

where $\nu = 4\omega/\gamma$.

For $\tilde{R}_{m'}(x')$, the procedure is identical with $x + \delta x$ instead of $x - \delta x$ and e $\leftrightarrow$ f [figure 4.6]. One finds

$$\frac{\mathrm{d}\tilde{R}_{m'}(x')}{\mathrm{d}x'} = \frac{\gamma}{4}\left[-2m'^2\tilde{R}_{m'}(x') + m'^2\tilde{R}_{m'-1}(x')e^{-i\omega x'} + m'^2\tilde{R}_{m'+1}(x')e^{i\omega x'}\right], \tag{4.53}$$

i.e. $\tilde{R}_{m'}(x) = \tilde{R}_m(-x)$.

For $Z_{.,m}(x)$, on should separate the "ending vertex" (the one at x, c and d in figure 4.7) from the rest, formally

$$\begin{aligned}\frac{\mathrm{d}Z_{.,m}(x)}{\mathrm{d}x} &= \frac{\mathrm{d}\left(\text{“ending vertex”} \times \text{“the rest”}\right)}{\mathrm{d}x}\\ &= \frac{\mathrm{d}\text{ “ending vertex”}}{\mathrm{d}x}\text{“the rest”} + \frac{\mathrm{d}\text{ “the rest”}}{\mathrm{d}x}\text{“ending vertex”},\end{aligned} \tag{4.54}$$

and one finds

$$\frac{\mathrm{d}Z_{.,m}(x)}{\mathrm{d}x} = \pm\frac{i\omega}{2}Z_{.,m}(x) + \frac{\gamma}{4}\left[m^2e^{-i\omega x}Z_{.,m-1} + (m+1)^2e^{i\omega x}Z_{.,m+1} - (m^2+(m+1)^2)Z_{.,m}\right], \tag{4.55}$$

$\pm$ depending on the kind of "ending vertex", $+$ for $\Gamma_{.,+}$ and $-$ for $\Gamma_{.,-}$. $Z_{m,.}(x')$ is in turn found equal to $Z_{.,m}(-x)$.

From the initial and final vertices presented in figure 4.7, we see that the Γ introduced in equations (4.49) can be expressed as

$$\begin{pmatrix}\Gamma_{++} & \Gamma_{+-}\\ \Gamma_{-+} & \Gamma_{--}\end{pmatrix} = \sum_{m'=0}^{\infty}\sum_{m=0}^{\infty}\begin{pmatrix}\tilde{R}_{m'}Z_{m',m}\tilde{R}_m & \tilde{R}_{m'}Z_{m',m}\tilde{R}_{m+1}\\ \tilde{R}_{m'+1}Z_{m',m}\tilde{R}_m & \tilde{R}_{m'+1}Z_{m',m}\tilde{R}_{m+1}\end{pmatrix}. \tag{4.56}$$

Some simplifications

Let us come back to equation (4.49). We first consider the contribution of $\Gamma_{+,+}(x' < x)$. We express it through[3]

$$\int_{x'<x}\mathrm{d}(x'-x)e^{ik(x'-x)}\Gamma_{+,+}(x'-x) = 4\gamma\sum_{m'=0}^{\infty}R_{m'}(\omega)\tilde{Q}^{++}_{m'}(\omega,k), \tag{4.57}$$

[3] k is absent in the equation for $\langle x\rangle$ [equation (4.49)], and thus set to 0 in the final expressions [equations (4.63) and (4.65)]. It is here introduced for the sake of generality, to conform with Berezinskii notations [13].

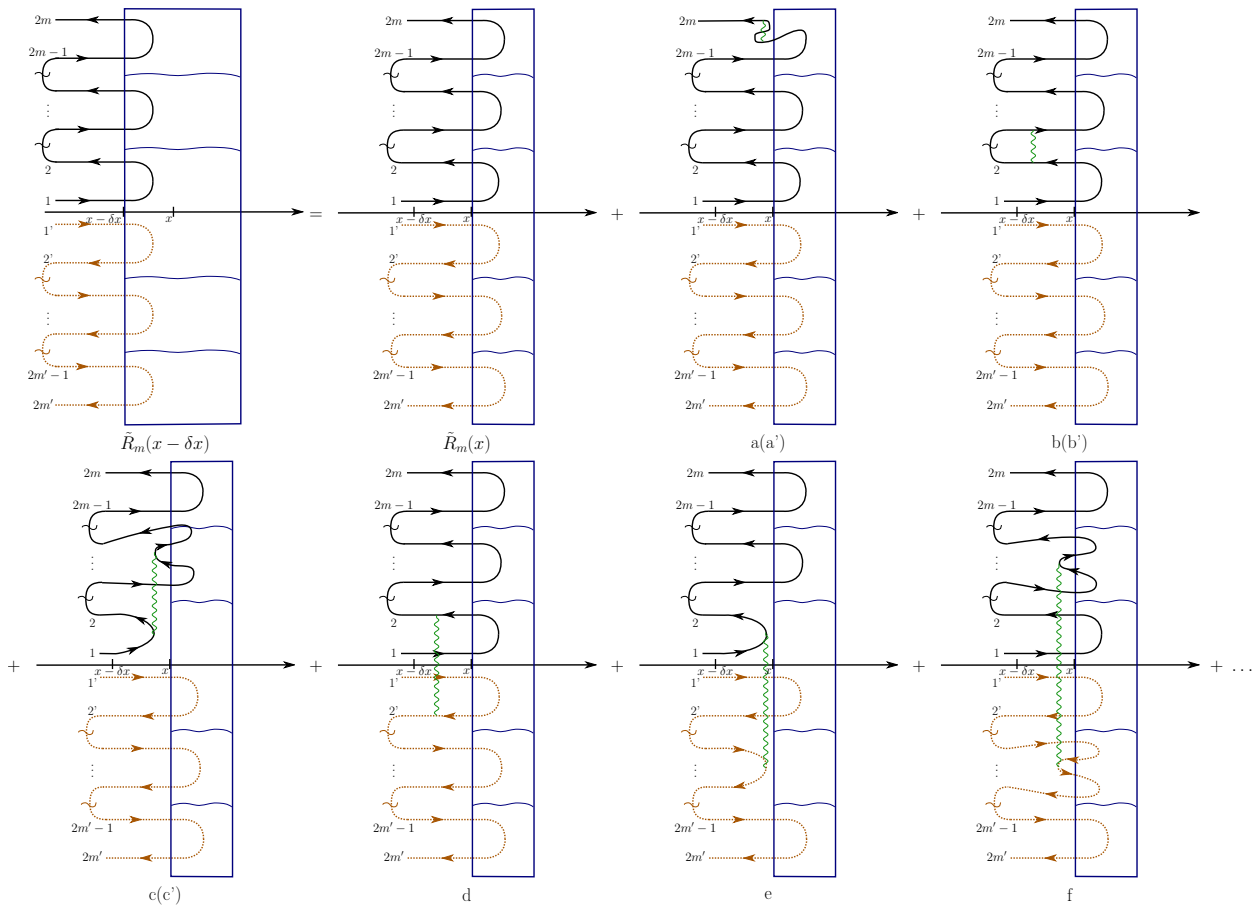

Figure 4.8 – Schematic representation of the process of constructing the right hand parts and equation (4.50). The right-hand parts are represented with rectangles ; the curves are the particle lines inside the right-hand part and the central part. The diagrams a',b' and c' are the same as a, b and c with the vertex below the x-axis. Only one example for each kind of vertex is represented, summation over all possible choice for incoming and outgoing legs is implied.

where, according to (4.56),

$$R_{m'}\tilde{Q}^{++}_{m'}(\omega,k) = \frac{\gamma}{4}\sum_{m=0}^{\infty}\int_0^{\infty} \mathrm{d}r e^{-ikr}\tilde{R}_{m'}(x-r)Z_{m',m}(x-r,x)\tilde{R}_m(x). \tag{4.58}$$

$\tilde{Q}^{++}_{m'}$ is then defined as

$$\tilde{Q}^{++}_{m'}(\omega,k) = \frac{\gamma}{4}\sum_{m=0}^{\infty}\int_{-\infty}^{x} \mathrm{d}x' e^{ik(x'-x)}e^{-i\omega m'x'}Z_{m',m}(x',x)e^{i\omega m x}R_m. \tag{4.59}$$

We recall that $\tilde{R}_{m'}(r) = e^{-i\omega m' r}R_{m'}$, with $R_{m'}$ independent of r. To derive an equation for $\tilde{Q}^{++}_{m'}(\omega,k)$, we start by the following integration by part:

$$\begin{aligned}&\int_{-\infty}^{x} \mathrm{d}x' e^{ik(x'-x)}e^{-i\omega m'x'}Z_{m',m}(x',x)e^{i\omega m x}R_m \\ &= \left[\frac{e^{ik(x'-x)}e^{-i\omega m'x'}}{ik-i\omega m'}Z_{m',m}(x',x)e^{i\omega m x}R_m\right]_{-\infty}^{x} - \int_{-\infty}^{x}\mathrm{d}x'\frac{e^{ik(x'-x)}e^{-i\omega m'x'}}{ik-i\omega m'}\frac{\mathrm{d}Z_{m',m}(x',x)}{\mathrm{d}x'}e^{i\omega m x}R_m.\end{aligned} \tag{4.60}$$

We have the condition $Z_{m',m}(x',x') = \delta_{m',m}$, and the equation for $Z_{m',m}$ (from equation (4.55) and $Z_{m,.}(x') = Z_{.,m}(-x)$)

$$-\frac{\mathrm{d}Z_{m',.}}{\mathrm{d}x'} = \frac{i\omega}{2}Z_{m',.} + \frac{\gamma}{4}\left[m'^2 e^{i\omega x'}Z_{m'-1,.} + (m'+1)^2 e^{-i\omega x'}Z_{m'+1,.} - (m'^2+(m'+1)^2)Z_{m',.}\right]. \tag{4.61}$$

Plugging it in equation (4.60), we find the sought for equation

$$R_{m'} - \frac{4ik}{\gamma}\tilde{Q}^{++}_{m'} + \frac{4i\omega}{\gamma}\left(m'+\frac{1}{2}\right)\tilde{Q}^{++}_{m'} + (m'+1)^2(\tilde{Q}^{++}_{m'+1} - \tilde{Q}^{++}_{m'}) - m'^2(\tilde{Q}^{++}_{m'} - \tilde{Q}^{++}_{m'-1}) = 0. \tag{4.62}$$

The same procedure is then carried out for $\Gamma_{+,-}(x' < x)$. The contributions from $\Gamma_{+,+}(x' < x)$ and $\Gamma_{+,-}(x' < x)$ are gathered through the introduction of $Q^1_m(\omega,k) = \tilde{Q}^{++}_m - \tilde{Q}^{+-}_m$. $\Gamma_{+,+}(x' > x)$ and $\Gamma_{+,-}(x' > x)$ give the same contribution with an opposite k, $Q^1_m(\omega,-k)$. Gathering the contributions from the $\Gamma_{+,.}$ we obtain

$$\langle x(\omega)\rangle_{\Gamma_{+,.}} = -\frac{2}{i\omega\gamma}\sum_{m=0}^{\infty} R_m\left[Q^1_m(\omega,k=0) + Q^1_m(\omega,-k=0)\right], \tag{4.63}$$

with

$$P^1_m - i\kappa Q^1_m + i\nu\left(m+\frac{1}{2}\right)Q^1_m + (m+1)^2(Q^1_{m+1} - Q^1_m) - m^2(Q^1_m - Q^1_{m-1}) = 0, \tag{4.64}$$

where we have introduced $\nu = 4\omega/\gamma$, $\kappa = 4k/\gamma$ and $P^1_m = R_m - R_{m+1}$. Adding the contribution from $\Gamma_{-,.}$, we eventually obtain

$$\langle x(\omega)\rangle = -\frac{2}{i\omega\gamma}\sum_{m=0}^{\infty} P^1_m\left[Q^1_m(\omega,k=0) + Q^1_m(\omega,-k=0)\right]. \tag{4.65}$$

The problem is reduced to solving equations (4.52) for R_m, (4.64) for Q^1_m and summing them as prescribed by equation (4.65). The solution of equation (4.52) has an explicit form [133]:

$$R_m(s) = s\Gamma(m+1)\Psi(m+1,2;-s), \tag{4.66}$$

where Ψ is the confluent hypergeometric function of the second kind, and $s = i\nu$. It is sometimes more convenient to work with the integral representation of R_m, which reads

$$R_m = -i\nu\int_0^\infty \mathrm{d}s e^{i\nu s}\left(\frac{s}{s+1}\right)^m = -i\nu\int_0^\infty \mathrm{d}s e^{i\nu s}\left(1+s^{-1}\right)^{-m}. \tag{4.67}$$

Equation (4.67) can be directly checked from equation (4.52) through integration by part. On the other hand, to the best of our knowledge no closed form solution for Q^1_m exists.

Note that the derivation of Gogolin density profile [equation (4.29)] presented in [14] involves an equation akin to (4.65). More precisely, the infinite-time density profile is similarly written as a sum over P^0_m and Q^0_m. $P^0_m = (R_m + R_{m+1})/2$ is the counterpart of P^1_m, and the equation for Q^0_m differs from (4.64) only through the upper index. The infinite-time limit then allows to approximate m by a continuous variable, making the calculation tractable.

4.5.4 Results

The problem is now only of mathematical nature. To extract the long time asymptotic behavior of $\langle x\rangle$, one can use the generating functions of R_m and Q_m^1 to derive an integro-differential equation for $\langle x\rangle$. This integro-differential equation cannot be solved in full generality but can be used to extract the limit of long times. This program is carried out in appendix 4.A, the result writes

$$\langle x\rangle = \ell\frac{64\ln(t/4\tau)\tau^2}{t^2} + \mathcal{O}\left(\frac{1}{t^2}\right). \tag{4.68}$$

Equation (4.68) is shown in figure 4.9, as a solid red curve, and is in excellent agreement with the numerical simulations at long times.

We can also solve equation (4.64) for Q_m^1 by making use of an expansion in powers of t. The method is presented in appendix 4.B and allows to extract the short-time expansion of $\langle x\rangle$ up to arbitrary order. Keeping only the first few terms, we obtain the short-time series

$$\langle x\rangle = \ell\left[\frac{t}{\tau} - \frac{t^2}{2\tau^2} + \frac{t^3}{6\tau^3} - \frac{3t^4}{64\tau^4} + \frac{7t^5}{576\tau^5} - \frac{629t^6}{207360\tau^6}\right] + \mathcal{O}\left(t^7\right). \tag{4.69}$$

The series has a finite convergence radius (estimated at 4τ from the first 100 terms). Equation (4.69) is compared with numerical simulations at short-times in figure 4.1, it describes very well the numerical results up to $t \approx \tau$.

To describe the center of mass beyond the convergence radius of the short-time series (4.69), we propose a Padé resummation. The knowledge of the long-time limit (4.68) suggests to express $\langle x\rangle$ at any time under the form

$$\langle x\rangle = \ell\frac{\ln(1+t/4\tau)\tau^2}{t^2}\lim_{N\to\infty}\underbrace{\frac{\sum_{n=0}^{N} a_n\left(t/\tau\right)^n}{\sum_{n=0}^{N} b_n\left(t/\tau\right)^n}}_{\text{Padé approximant}}, \tag{4.70}$$

the coefficients a_n and b_n are deduced from the short-time series (4.69). In practice, (4.70) converges quickly, and an excellent approximation of $\langle x\rangle$ for times up to 120τ is obtained with $N = 7$. This is demonstrated by the solid green curve in figure 4.9a, which perfectly coincides with the numerical results.

4.6 General case

So far, we have only considered the case of a Gaussian uncorrelated potential. As discussed in section 2.2, this model for the random potential is not realistic for cold-atom experiments. It was chosen here to allow for the full analytical treatment of section 4.5. Nevertheless, in the weak disorder limit, a kind of universality with respect to the potential on-site distribution and correlation function is expected [42].

4.6.1 Case of a non-Gaussian potential

The on-site distribution, if reasonable, is not expected to have any qualitative effect on the dynamics. This is indeed what we observe in figure 4.10b, where the numerical simulations using a blue-detuned speckle uncorrelated potential[4] are in excellent agreement with our prediction for a Gaussian potential. This is in agreement with the one-parameter scaling theory [section 1.3], which states that the dynamics depends on the microscopic details only through the non-interferential (classical) limit [ℓ and τ here, see equation (4.12)].

[4] This potential has an on-site exponential distribution and is defined only for positive V, see section 2.2 for more details.

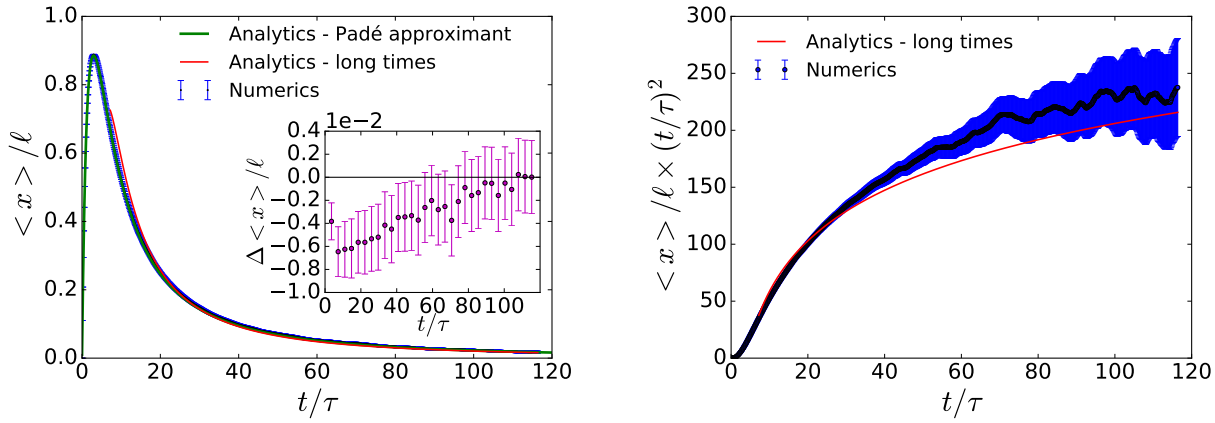

(a) (b)

Figure 4.9 – Figure a): center of mass $\langle x \rangle$ of a wave packet initially launched with finite velocity in a random potential, as a function of time. The analytical results, equation (4.68) for the long time asymptotic and the Padé approximant (4.70), respectively shown as red and green curves, are compared with numerical simulations shown as blue points, with statistical error bars. Inset of figure a): difference between the Padé approximant of $\langle x \rangle$ and the numerical result ($\Delta x = \langle x \rangle_{\text{green}} - \langle x \rangle_{\text{blue}}$) as a function of time. Figure b): center of mass multiplied by $(t/\tau)^2$ as a function of time. The asymptotic result (4.68) [red curve] is compared to the numerical prediction. The parameters used in the numerical simulations are given in subsection 4.3.4. To allow for a more accurate comparison, we have used more precise estimates (only by roughly a percent) of the scattering mean free path and time, $\ell = \hbar^4(1-\cos^2(k_0 a))/2m^2a^2\gamma$ and $\tau = \ell ma/\hbar \sin(k_0 a)$ respectively [134], where $a = 0.2/k_0$ is the lattice spacing used in the numerical simulations. Just like (4.7), these forms are valid to lowest order in the potential, the only difference is that they take the spatial discretization into account [(4.7) corresponds to the limit $a \to 0$].

4.6.2 Case of a correlated potential

The introduction of correlations requires some care. Indeed, the scattering on correlated potentials is described by two time scales, the scattering (τ) and transport mean free time (τ_b). The latter is defined as the average time it takes for an atom to experience a significative change in its direction of propagation. In the case of an uncorrelated potential, the scattering is isotropic and the transport mean free time is equal to the scattering mean free time. In strongly correlated potentials in contrast, scattering is strongly anisotropic and the transport mean free time well exceeds the scattering mean free time [135]. Correspondingly, the transport mean free path ($\ell_b = \hbar k_0 \tau_b/m$) is the average time traveled by the atoms before experiencing a significative change in their direction of propagation. As it turns out, Berezinskii equations can be derived for correlated potentials, the net result is that the replacement $(\tau, \ell) \to (\tau_b, \ell_b)$ fully accounts for the correlations [14]. This is again fully consistent with the one-parameter scaling theory, as here the classical limit is set by ℓ_b and τ_b (in section 4.2, describing the classical limit, the replacement $(\tau, \ell) \to (\tau_b, \ell_b)$ is immediate).

When performing the simple replacement $(\tau, \ell) \to (\tau_b, \ell_b)$ to describe the correlated case, one should ensure that the variations of τ_b and ℓ_b with energy are not too important in the energy range covered by the wave packet. Indeed, as discussed in section 3.2, not fulfilling this condition can lead to surprises. As an example, one can imagine having energy components with sharply distinct localization lengths, as can be the case in speckle potentials [47]. If this happens, it could lead to an apparent halt of the quantum boomerang effect, waiting for the retroreflection of slow energy

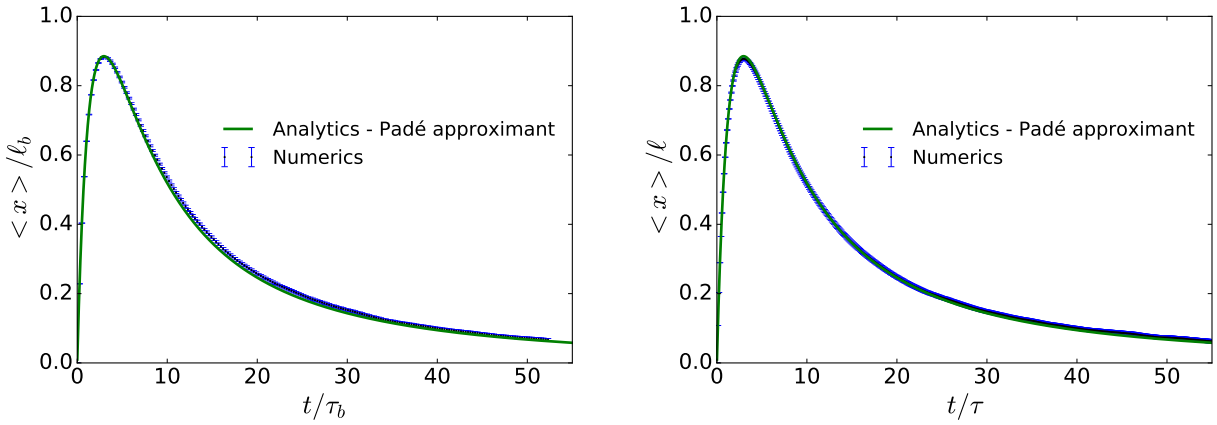

(a) Correlated Gaussian potential

(b) Uncorrelated speckle potential

Figure 4.10 – Center of mass as a function of time for two types of random potentials. The numerical results for a Gaussian correlated potential (a) and an uncorrelated potential with on-site blue-detuned speckle distribution (b) are shown in blue, with their error bars, and are compared to the analytical prediction obtained in section 4.5. For a), the potential correlation function is given by (4.71). The speckle distribution (b) corresponds to an exponential distribution, defined only for positive V. For a) [resp. b)], we have used a disorder strength $V_0 = 0.1\ \hbar^2 k_0^2/m$ [resp. $\gamma = 0.0058\ \hbar^4 k_0^3/m^2$]. In both cases, we have used an initial wave packet of size $\sigma = 10/k_0$. The results are averaged over 25000 [resp. 15000] disorder realizations for a) [resp. b)]. In the correlated case (a), the correlation length σ_c is equal to $0.5/k_0$. To guarantee that the correlations are correctly resolved, we have used a thinner discretization of roughly 10 points per k_0^{-1} in the correlated case (a) than in the uncorrelated case (b) for which roughly 5 points per k_0^{-1} were sufficient. Transport (a) and scattering (b) mean free time and path are obtained by fitting the short times with the classical prediction (4.12) (with ℓ and τ replaced by τ_b and ℓ_b for a), see main text for more details). The fitted values [$\ell \simeq 87$ and $\ell_b \simeq 96$] are close to the predictions of perturbation theory [$\ell \simeq 86$ from equation (4.7) and $\ell_b \simeq 100$ from equation (4.72)]. Note that in the correlated case (a), $\ell_b \simeq 1.5\ell$.

components. To avoid the appearance of such effects, we have chosen to use a correlated potential that has smooth variations of the transport mean free path and time. This potential is described by an exponential correlation function:

$$\overline{V(x)V(x')} = V_0^2 \exp\left(-\frac{|x-x'|}{\sigma_c}\right), \tag{4.71}$$

from which we infer the scattering and transport mean free path at the Born approximation [3]:

$$\ell = \frac{\hbar^4 k_0^2}{m^2 V_0^2}\left[2\sigma_c + \frac{2\sigma_c}{1+4k_0^2\sigma_c^2}\right]^{-1} \quad \text{and} \quad \ell_b = \frac{\hbar^4 k_0^2}{2m^2 V_0^2}\frac{1+4k_0^2\sigma_c^2}{2\sigma_c}. \tag{4.72}$$

Figure 4.10a shows that in this case, the simple replacements $(\tau, \ell) \to (\tau_b, \ell_b)$ in the results of section 4.5 is indeed sufficient to describe the correlated case.

4.6.3 Case of a broad initial wave packet

We have so far restricted ourselves to the case of a wave packet initially much smaller than the mean free path. What happens to the quantum boomerang effect if we relax this assumption? To

answer this question, we elaborate on the reasoning leading to equation (3.32). We assume that the initial wave packet plays only a role through its convolution with a propagator:

$$\overline{|\psi(x,t)|^2} = \int \mathrm{d}x' P(x'-x,t)|\Psi_{k_0}(x')|^2, \tag{4.73}$$

with $P(x'-x,t)$ the probability for a particle initially at x' to reach x in a time span t and $|\Psi_{k_0}(x')|^2$ the initial wave packet. The center of mass follows from integration over x weighted by x. The change of variable $\tilde{x} = x - x'$ then allows to immediately conclude that the width of the initial wave packet plays no role.

To validate the above reasoning, we have performed numerical simulations starting from wave packets much broader than the mean free path. The results are reported in figure 4.11 and confirm the minor role (if any) played by the initial wave packet width on the quantum boomerang effect.

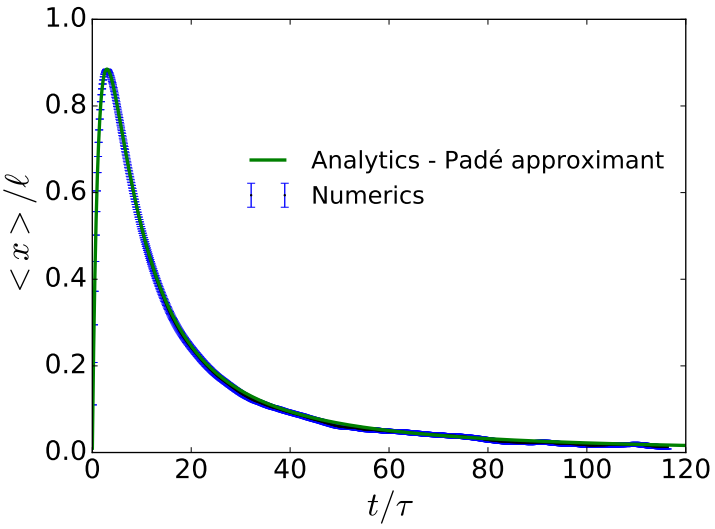

Figure 4.11 – Center of mass as a function of time in the case of an initially broad wave packet ($\sigma \gg \ell$). The center of mass obtained numerically, starting from a broad wave packet, is shown in blue, with its error bars and is compared to the analytical prediction obtained in section 4.5. The numerical parameters match the ones used for the numerical results of figure 4.9, except for the initial width of the wave packet, equal to $\sigma = 750/k_0 \simeq 9\ell$. The scattering mean free path (ℓ) and time (τ) are calculated using the formula given in the caption of figure 4.9.

In conclusion, although a broad wave packet appears essentially motionless at the scale of its size, a fine analysis reveals that it experiences the same quantum boomerang effect than a narrow wave packet.

4.7 A simple relation between $\langle x \rangle$ and $\langle x^2 \rangle$

Interestingly, the similarity of the calculation of $\langle x \rangle$ and of the current-current correlation function, observed in subsection 4.5.2, is rooted in a simple relation between $\langle x \rangle$ and $\langle x^2 \rangle$ (note that $\langle x^2 \rangle$ is directly related to the diffusion coefficient and thus to the conductivity, which in turn is related to the current-current correlation function). To exhibit this connection, we start by applying Ehrenfest theorem to the mean-square displacement, $\partial_t \langle x^2 \rangle = \langle [x^2, p^2] \rangle / (2i\hbar m)$, and split the particle distribution into two classes of positive and negative velocities: $\overline{|\Psi(x,t)|^2} = n_+(x,t) + n_-(x,t)$. This

leads to[5]

$$\partial_t \langle x^2 \rangle = 2v_0 \langle x \rangle_+ - 2v_0 \langle x \rangle_- , \tag{4.74}$$

where $v_0 = \hbar k_0/m$. Here $\langle x \rangle_\pm = \int_{-\infty}^{\infty} x\, n_\pm(x,t)\, dx$, with obviously $\langle x \rangle = \langle x \rangle_+ + \langle x \rangle_-$.

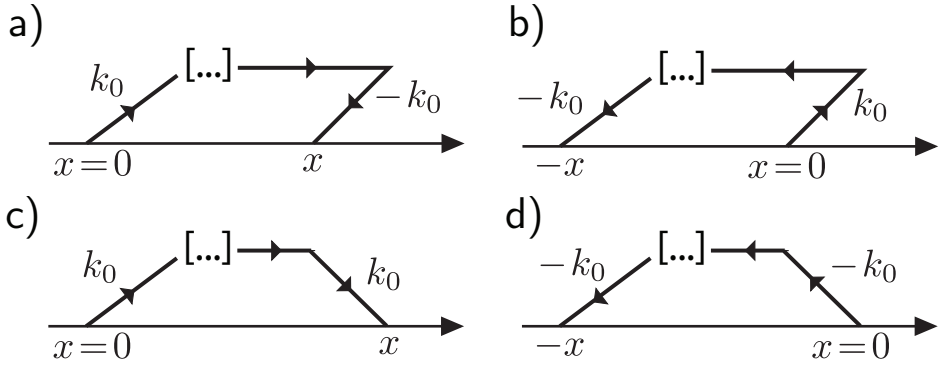

Figure 4.12 – a) Arbitrary multiple scattering path going from $x = 0$ to x, contributing to $\langle x \rangle_-$ (the path is unfolded to the top for clarity). By time-reversing and translating this path by $-x$, we obtain path b), which gives an opposite contribution to $\langle x \rangle_-$, ensuring that $\langle x \rangle_-$ vanishes. c) Path contributing to $\langle x \rangle_+$. Its time-reversed and translated counterpart d) starts with momentum $-k_0$ and is thus not populated at $t = 0$, so that $\langle x \rangle_+$ can be non-vanishing.

We now consider an arbitrary path contributing to $\langle x \rangle_-$ [figure 4.12a]. The path starts at $x = 0$ with momentum $\hbar k_0$ and reaches x with momentum $-\hbar k_0$ at time t. By time-reversing and translating this path of a distance $-x$, one can always find a complementary path starting with momentum $\hbar k_0$ at $x = 0$ and reaching $-x$ at time t [figure 4.12b]. Due to time-reversal and translational invariance, these two paths contribute with the same weight to $n_-(x,t)$, which is thus an even function of x, yielding $\langle x \rangle_- = 0$. This reasoning does not apply to $\langle x \rangle_+$ since the time-reversed/translated counterpart of an arbitrary path contributing to $\langle x \rangle_+$ starts by construction with a momentum $-\hbar k_0$ which is not initially populated (see figures 4.12c-d). We have thus shown

$$\partial_t \langle x^2 \rangle = 2v_0 \langle x \rangle. \tag{4.75}$$

4.8 Conclusion

In this chapter, we have considered the evolution in a 1D disordered potential of an initial wave packet carrying a finite velocity. We have first observed numerically that, unexpectedly, after an initial ballistic motion, the packet center-of-mass experiences a retroreflection and slowly returns to its initial position (quantum boomerang effect). We have attributed this phenomenon to Anderson localization.

The core of this chapter consisted in applying Berezinskii diagrammatic theory [13] to this scenario. We have been able to derive the long-time asymptotic return of the packet center-of-mass to its initial position. Further, we have presented a new method to solve Berezinskii equations under the form of a Padé approximant, allowing for a description of the center-of-mass motion at all times. We have also derived an intriguing relation between the center of mass and the mean square displacement, which turns out to be at the root of our calculations.

We have then tested the robustness our results with respect to a change in the statistics of the random potential and of the size of the initial wave packet. We have found that, at least for weak

[5] This can be justified more rigorously by using the phase space Wigner representation $\overline{W(x,p,t)}$ of the wave packet (see section 3.2 for more details). Under the conditions of section 4.1, $\overline{W(x,p,t)}$ is non vanishing only near $p = \pm\hbar k_0$, so that it can be split in two parts $\overline{W(x,p,t)} \approx n_+(x,t)\delta(p - \hbar k_0) + n_-(x,t)\delta(p + \hbar k_0)$.

disorder, the statistics of the potential (including on-site distribution and possible correlations) does not visibly affect the center-of-mass motion. Similarly, the center-of-mass motion appears independent of the width of the initial wave packet.

The reasoning presented in section 4.4, and explaining the quantum boomerang effect in terms of real localized modes, applies in any dimension. The quantum boomerang effect is thus expected to take place in higher dimensions as well, provided the dynamics is Anderson localized. This offers interesting perspectives for future work. For example, along with recent works on the coherent backward and forward scattering peaks across Anderson transition [44,128], it would be very interesting to perform a fine numerical analysis of the quantum boomerang effect in three dimensions. Another interesting direction of research would be to look for similar phenomena in other symmetry classes (e.g. in the unitary class where the qualitative understanding of retroreflection in terms of *real* localized modes does not apply).

4.9 Article: *When Anderson localization makes quantum particles move backward* [Submitted to Phys. Rev. Lett. (arXiv:1704.05241)]

When Anderson localization makes quantum particles move backward

Tony Prat[1], Dominique Delande[1], Nicolas Cherroret[1]
[1]*Laboratoire Kastler Brossel, UPMC-Sorbonne Universités, CNRS, ENS-PSL Research University, Collège de France; 4 Place Jussieu, 75005 Paris, France*
(Dated: 19/04/2017)

We unveil a novel and unexpected manifestation of Anderson localization of matter wave packets that carry a finite average velocity: after an initial ballistic motion, the packet center-of-mass experiences a retroreflection and slowly returns to its initial position. We describe this effect both numerically and analytically in dimension 1, and show that it is destroyed by weak particle interactions which act as a decoherence process. The retroreflection is also present in higher dimensions, provided the dynamics is Anderson localized.

PACS numbers: 72.15.Rn, 67.85.–d, 05.60.Gg

Anderson localization (AL), the absence of wave diffusion due to destructive interference in disordered potentials [1], is ubiquitous in condensed-matter systems, wave physics or atom optics. This offers many experimental platforms for its characterization, as was recently demonstrated experimentally with light [2, 3] (see however [4, 5]) or ultrasound waves [6]. Very recently, AL of atomic matter waves has also been observed [7–11], as well as its many-body counterpart [12, 13]. A precious asset of atom optics experiments is to allow for direct tests of fundamental manifestations of AL, such as the time evolution of wave packets. In this context, a common experimental scenario for probing localization consists in preparing a spatially narrow atomic wave packet in a trap, then opening the trap and recording the time evolution of the gas [14, 15]. After it has been released, the wave packet spreads symmetrically around its initial position and, after a transient ballistic expansion, quickly becomes localized in space. What happens, now, if a nonzero average velocity is additionally imprinted to the gas? In a naive picture, one expects the randomization of velocities due to scattering on the random potential to stop the initial ballistic motion of the wave packet center-of-mass (CoM) at roughly a mean free path ℓ, and then a symmetric localization of the packet around this new central position due to AL. We show in this Letter that the evolution is in fact very different. Quite unexpectedly, after an initial ballistic motion where the CoM indeed increases up to ℓ, the wave packet slowly *returns to its initial position*, recovering a symmetric shape at long times. The final state of the system is in turn identical to the one that would have been reached if no velocity had been transferred to the gas.

In this Letter, we thoroughly study this phenomenon both numerically and analytically. In dimension 1, we give an exact solution to this problem. We then study the CoM retroreflection in the presence of a weak nonlinearity describing particle interactions in the mean field approximation. The CoM freezes at a position that depends on the strength of interactions, very much like a decoherence process.

Let us consider a one-dimensional (1D) system described by the Hamiltonian $H = -\hbar^2\Delta/(2m) + V(x)$, where $V(x)$ is a Gaussian, uncorrelated random potential: $\overline{V(x)} = 0$ and $\overline{V(x)V(x')} = \gamma\delta(x-x')$, where the overbar denotes averaging over disorder realizations. We wish to study the time evolution of a normalized Gaussian wave packet, $\Psi_{k_0}(x) \propto \exp\left[-x^2/(2\sigma^2) + ik_0x\right]$, to which a finite momentum $\hbar k_0$ is imprinted. We choose $k_0 > 0$ without loss of generality. To simplify the discussion, we assume throughout this Letter a sharp initial velocity distribution, $k_0\sigma \gg 1$, and weak disorder, $k_0\ell \gg 1$, thereby allowing for a simple description of the wave packet in terms of two velocity components $\pm\hbar k_0/m$, with energy $E_0 = \hbar^2k_0^2/(2m)$.

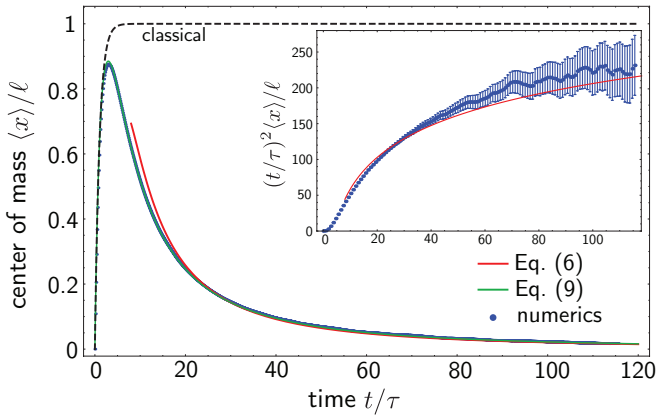

FIG. 1. (Color online) Main plot: center of mass as a function of time. Its long-time asymptotics, Eq. (6), is shown as a solid red curve, and the re-summation of the short-time series, Eq. (10), as a solid green curve. The latter perfectly overlaps with the numerical result (blue dots). The dashed curve is the classical result, Eq. (1). Inset: center of mass multiplied by $(t/\tau)^2$ as a function of time. The asymptotic result (6) (red curve) is compared to the numerical prediction, displayed with its statistical error bars. The parameters used in the simulations are given in the main text.

The average evolution in the random potential is governed by two microscopic scales, the scattering mean free time τ and the scattering mean free path $\ell = v_0\tau$, where

$v_0 = \hbar k_0/m$. Throughout this Letter, τ and ℓ are calculated to the leading order in $1/(k_0\ell) \ll 1$, using the Born approximation at energy E_0 [16]. The assumption of uncorrelated random potential is not crucial for our discussion: all the results that follow hold as well for short-range correlated potentials, provided that ℓ and τ are replaced by the transport mean free path and time, respectively [17, 18].

By numerically propagating $\Psi_{k_0}(x)$, we obtain the disorder-averaged density profile $\overline{|\Psi(x,t)|^2}$, from which we infer the CoM $\langle x\rangle \equiv \int x\overline{|\Psi(x,t)|^2}dx$. The result is shown in Fig. 1 : $\langle x\rangle$ first increases rapidly, reaches a maximum at $t \sim \tau$ and then slowly decreases to zero. In other words, after a transient motion rightward, the center of mass of the wave packet slowly *returns to its initial position* $x = 0$. For these simulations we discretize the Hamiltonian on a 1D grid of size $16000\pi/k_0$, divided into 251352 grid points. The initial wave-packet width is set to $\sigma = 10/k_0$, and $\gamma = 0.0058\hbar^4k_0^3/m^2$ ($k_0\ell = \hbar^4k_0^3/(2m^2\gamma) \simeq 86.5$). The results are averaged over 45000 disorder realizations. In the simulations, the evolution operator is expanded in a series of Chebyshev polynomials, as explained in [19, 20]. The surprising behavior observed in Fig. 1 is dramatically different from the classical expectation, which can be simply deduced from Ehrenfest theorem: $\partial_t \langle x\rangle_{\rm class} = \langle p\rangle/m = \hbar k_0(n_+ - n_-)/m$ where $n_\pm$ is the population of particles with momentum $\pm\hbar k_0$ ($n_+ + n_- = 1$). Using the classical Boltzmann equations $\partial_t n_\pm = (n_\mp - n_\pm)/(2\tau)$ with the initial condition $n_+ = 0$, we find

$$\langle x\rangle_{\rm class} = \ell\left(1 - e^{-t/\tau}\right), \tag{1}$$

which is shown in Fig. 1 as a dashed curve. Within the classical picture, the CoM thus quickly saturates to the mean free path ℓ, but never experiences retroreflection. The reason why quantum wave packets behave so differently can be understood by the following argument. At any time, the density distribution can be expanded over the eigenbasis $\{\epsilon_n, |\phi_n\rangle\}$ of H as

$$|\Psi(x,t)|^2 = \sum_{n,m} \langle\phi_n|\Psi_{k_0}\rangle\langle\Psi_{k_0}|\phi_m\rangle \times \phi_n(x)\phi_m^*(x)e^{-i(\epsilon_n-\epsilon_m)t}. \tag{2}$$

Since eigenstates are localized, the system is constrained to a volume set by the localization length $\xi = 2\ell$. This defines a typical mean level spacing $\Delta = 1/(\rho\xi)$ (ρ is the density of states per unit volume), with a corresponding localization time $\tau_{\rm loc} = 2\pi\hbar/\Delta = 4\tau$ beyond which the off-diagonal oscillatory terms $n \neq m$ in Eq. (2) vanish, leaving:

$$\overline{|\Psi(x,\infty)|^2} = \sum_n \overline{|\langle\phi_n|\Psi_{k_0}\rangle|^2}|\phi_n(x)|^2. \tag{3}$$

Due to time-reversal invariance, the $\phi_n(x)$ are real so that $\langle\phi_n|\Psi_{k_0}\rangle = \langle\phi_n|\Psi_{-k_0}\rangle^*$: Eq. (3) is independent of the sign of k_0, and thus coincides with the long-time, spatially symmetric density distribution that would have been obtained with an initial wave packet having a symmetric velocity distribution. This shows that the CoM *must* return to its initial position at long times, as a result of AL.

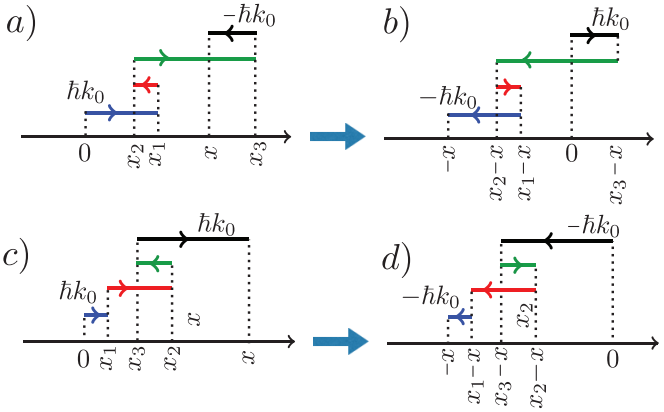

FIG. 2. a) A typical multiple scattering path going from $x = 0$ to x, contributing to $\langle x\rangle_-$ (the path is unfolded to the top for clarity). The momentum reverses at each scattering event. By time-reversing and translating this path by $-x$, we obtain path b), which gives an opposite contribution to $\langle x\rangle_-$, ensuring that $\langle x\rangle_-$ vanishes. c) Path contributing to $\langle x\rangle_+$. Its time-reversed and translated counterpart d) starts with momentum $-k_0$ and is thus not populated at $t = 0$, so that $\langle x\rangle_+ \neq 0$.

Let us now be more quantitative and analyze the CoM at finite times. For this purpose, we start by applying Ehrenfest theorem to the mean-square displacement, $\partial_t\langle x^2\rangle = \langle[x^2, p^2]\rangle/(2i\hbar m)$, and split the particle distribution into two classes of positive and negative velocities: $\overline{|\Psi(x,t)|^2} = n_+(x,t) + n_-(x,t)$. This leads to [21]

$$\partial_t\langle x^2\rangle = 2v_0\langle x\rangle_+ - 2v_0\langle x\rangle_-. \tag{4}$$

Here $\langle x\rangle_\pm = \int_{-\infty}^{\infty} x\ n_\pm(x,t)\ dx$, with obviously $\langle x\rangle = \langle x\rangle_+ + \langle x\rangle_-$. We now consider an arbitrary path contributing to $\langle x\rangle_-$ [Fig. 2(a)]. The path starts at $x = 0$ with momentum $\hbar k_0$ and reaches x with momentum $-\hbar k_0$ at time t. By time-reversing and translating this path of a distance $-x$, one can always find a complementary path starting with momentum $\hbar k_0$ at $x = 0$ and reaching $-x$ at time t (Fig. 2b). Due to time-reversal and translational invariance, these two paths contribute with the same weight to $n_-(x,t)$, which is thus an even function of x, yielding $\langle x\rangle_- = 0$. This reasoning does not apply to $\langle x\rangle_+$ since the time-reversed/translated counterpart of an arbitrary path contributing to $\langle x\rangle_+$ starts by construction with a momentum $-\hbar k_0$ which is not initially populated (see Figs. 2c-d). We have thus

$$\partial_t\langle x^2\rangle = 2v_0\langle x\rangle, \tag{5}$$

a property that we can use to infer the long-time limit of $\langle x\rangle$ from $\langle x^2\rangle$, which was previously studied in [22]. This yields [23]

$$\langle x\rangle = \ell\frac{64\ln(t/4\tau)\tau^2}{t^2} + \mathcal{O}\left(\frac{1}{t^2}\right). \quad (6)$$

Eq. (6) is shown in Fig. 1 and matches well the exact numerical prediction at long times. The inset of Fig. 1 also confirms the presence of the logarithmic term in Eq. (6).

In fact, one can go one step further and exploit Eq. (5) to compute $\langle x\rangle$ at *any time*. For this purpose, we use Berezinskii diagrammatic technique [24] which, combined with Eq. (5), gives [23]

$$\langle x\rangle = \int\frac{\mathrm{d}\omega}{2\pi}e^{-i\omega t}\left[-\frac{2\ell}{i\omega}\sum_{m=0}^{\infty}P_m^1(\omega)Q_m^1(\omega)\right], \quad (7)$$

where $P_m^1(\omega) = s\Gamma(m+1)[\Psi(m+1,2;-s)-(m+1)\Psi(m+2,2;-s)]$, with $s = 4i\omega\tau$, Γ the Gamma function and Ψ the confluent hypergeometric function of the second kind. The $Q_m^1(\omega)$ are solutions of

$$[4i\tau(m+1/2)\omega - (m+1)^2 - m^2]Q_m^1(\omega) + (m+1)^2Q_{m+1}^1(\omega) + m^2Q_{m-1}^1(\omega) + P_m^1(\omega) = 0. \quad (8)$$

At short times, one can solve these equations with the expansion $Q_m^1(\omega) = \sum_{n=0}^{+\infty}q_{m,n}/(i\omega)^n$. To compute the $q_{m,n}$, we first notice that $q_{m,i} = 0$ if $i \le m$, which follows from the large-frequency expansion of $P_m^1(\omega)$ (which has no terms $1/\omega^i$ with $i < m$). We use this result to expand Eqs. (8) order by order in $1/\omega$ and reduce them to a triangular system. This method provides us with the coefficients χ_n of the expansion $\langle x\rangle = \ell\sum_n\chi_n(t/\tau)^n$ at arbitrary order [18]. We find for instance

$$\langle x\rangle = \ell\left[\frac{t}{\tau} - \frac{t^2}{2\tau^2} + \frac{t^3}{6\tau^3} - \frac{3t^4}{64\tau^4}\right] + \mathcal{O}\left(t^5\right). \quad (9)$$

The method cannot be directly used to estimate $\langle x\rangle$ at any time because the series has a finite convergence radius, estimated at 4τ from the first 100 terms. Nevertheless, the observed exponential decay of the χ_n makes this series a good candidate for a Padé resummation. The knowledge of the long-time limit (6) suggests to express the CoM at any time under the form

$$\langle x\rangle = \ell\frac{\ln(1+t/4\tau)\tau^2}{t^2}\lim_{n\to\infty}R_n(t), \quad (10)$$

where $R_n(t)$ is a diagonal Padé approximant of order n, deduced from the χ_n coefficients [25]. In practice, $R_n(t)$ converges quickly, and an excellent approximation of $\langle x\rangle$ for times up to 120τ is obtained with $n = 7$. This is demonstrated by the solid green curve in Fig. 1, which perfectly coincides with the numerical results.

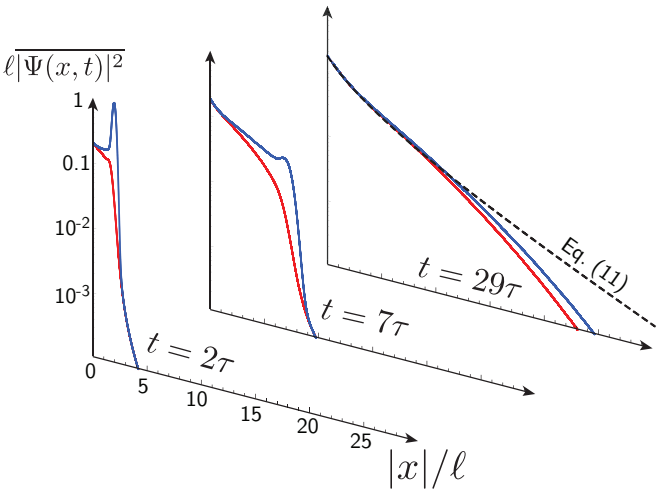

FIG. 3. (Color online) Average density profile obtained numerically at three different times. The solid upper blue and lower red curves are the $x > 0$ and $x < 0$ components of the profile, respectively. The long-time limit of the profile, Eq. (11), is shown as a dashed black curve.

In order to clarify which specific behavior of the spatial distribution $\overline{|\Psi(x,t)|^2}$ actually gives rise to the phenomenon of retroreflection, we show in Fig. 3 the $x > 0$ (blue curve) and $x < 0$ (red curve) components of the spatial profile $\overline{|\Psi(x,t)|^2}$, obtained numerically at three successive times. The profiles display a ballistic peak responsible for the increase of $\langle x\rangle$ at short times. After this peak has been attenuated, the profile re-symmetrizes itself around $x = 0$, which gives rise to the retroreflection phenonemon. As discussed above, this distribution is expected to converge toward a symmetric one, Eq. (3), which coincides with the so-called Gogolin density profile [17, 26]:

$$\overline{|\Psi(x,\infty)|^2} = \int_0^\infty\frac{\mathrm{d}\eta\pi^2}{32\ell}\frac{\eta\left(1+\eta^2\right)^2\sinh(\pi\eta)e^{-\left(1+\eta^2\right)|x|/8\ell}}{[1+\cosh(\pi\eta)]^2}, \quad (11)$$

which is shown in Fig. 3 for comparison. Note that although we start from a rather narrow wave packet with $\sigma < \ell$ in our simulations, the retroreflection phenomenon is present as well when $\sigma > \ell$.

We finally discuss the effect of particle interactions on $\langle x\rangle(t)$, by considering a weakly interacting, condensed bosonic gas. Its dynamics is governed, at the mean field level, by the Gross-Pitaevskii equation $i\hbar\partial_t\Psi = [-\hbar^2\Delta/2m + V(x) + g|\Psi|^2]\Psi$. For wave packets with $k_0 = 0$, it was shown that the interaction term $g|\Psi|^2$ leads to a destruction of AL at very long times, in favor of a regime of subdiffusion where $\langle x^2\rangle \sim t^\alpha$ with $\alpha < 1$ [27, 28]. Here we take a different perspective and investigate numerically how the nonlinearity affects $\langle x\rangle$. For these simulations, we write the evolution operator over a small time step

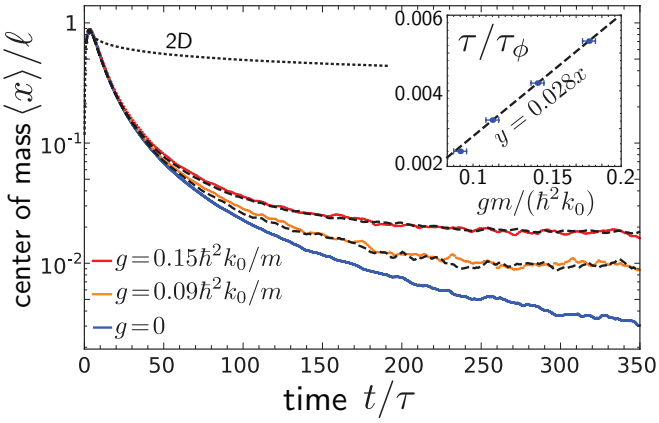

FIG. 4. (Color online) Main plot: center of mass $\langle x\rangle_g$ as a function of time, for $g = 0$ (solid lower blue curve), $g = 0.09\hbar^2k_0/m$ (solid middle orange curve) and $g = 0.15\hbar^2k_0/m$ (solid upper magenta curve). Two dashed curves show the center of mass $\langle x\rangle_\phi$ obtained with the model of decoherence, for $A_f = 0.02, 0.03$. Dotted curve: CoM in 2D. Inset: $\tau/\tau_\phi(g)$, well fitted by a linear regression. The effective decoherence time $\tau_\phi(g)$ associated with the nonlinearity thus behaves like $\hbar/\tau_\phi(g) \sim g/\ell$.

δt as $U(\delta t) = \exp[-ig\left|\Psi(\delta t)\right|^2\delta t/2]\exp[-i(-\hbar^2\Delta/2m + V)\delta t]\exp[-ig\left|\Psi(0)\right|^2\delta t/2]$ and treat the linear part as before, through an expansion in a series of Chebyshev polynomials. We use a system of size $7500\pi/k_0$ discretized into 23562 grid points, and propagate a wave packet of width $\sigma = 10/k_0$ in a random potential of strength $\gamma = 0.0196\hbar^4k_0^3/m^2$ ($k_0\ell \simeq 18.1$). The results are averaged over 600000 (8.85 millions) disorder realizations when $g \neq 0$ (respectively $g = 0$). We show in Fig. 4 the CoM $\langle x\rangle_g$ as a function of time obtained with this procedure, for two values of $g \neq 0$. We observe that $\langle x\rangle_g$ decreases more slowly than in the non-interacting limit and *saturates* at a finite value at long times. The CoM retroreflection is thus interrupted by the nonlinearity.

To better understand the role of the nonlinearity, we have also studied how the CoM is affected by *decoherence*, modeled by the Hamiltonian $H = -\hbar^2\Delta/(2m) + V(x) + V_\phi(x,t)$. Here $V(x)$ is the same random potential as above and $V_\phi(x,t) = h(x)f(t)$, where $h(x)$ has the same statistical properties as $V(x)$ and $f(t)$ is a random, Gaussian distributed function of time with zero average. $f(t)$ is fully characterized by its time-time correlation function which we choose Gaussian, $\overline{f(t)f(t')} = A_f^2\exp[-(t-t')^2/2\sigma_t^2]$, with $A_f \ll 1$ to ensure that the fluctuating potential is weaker than the static one. We have checked that the potential $V_\phi(x,t)$ does induce decoherence: at long times, it restores classical diffusion with $\langle x^2\rangle = 2D_\phi t$, where $D_\phi = \xi^2/\tau_\phi = 4\ell^2/\tau_\phi$ is the diffusion coefficient and τ_ϕ the decoherence time [17]. Because $V_\phi(x,t)$ preserves time-reversal and translational invariance after a disorder average, Eq. (5) still holds for this model, demonstrating that the CoM, $\langle x\rangle_\phi$, converges to a finite value $4\ell\tau/\tau_\phi$ at long times. $\langle x\rangle_\phi$ is displayed in Fig. 4 (dashed curves), for two values of A_f. The two values of g chosen in the Gross-Pitaevskii model were adjusted so that $\langle x\rangle_g$ coincides with these two curves $\langle x\rangle_\phi$ in the long-time limit. Surprisingly, the obtained curves $\langle x\rangle_\phi$ match extremely well the nonlinear curves $\langle x\rangle_g$ *in the whole time window*. This suggests that at least regarding $\langle x\rangle$ and for times short enough for subdiffusion not to play a major role, the nonlinearity acts similarly to a decoherence process. From this observation, we associate to the nonlinearity an effective decoherence time $\tau_\phi(g)$. To find this quantity, we first determine D_ϕ from the evolution of $\langle x^2\rangle$ with time in the model of decoherence, and then find the associated g by matching the curves $\langle x\rangle_\phi$ and $\langle x\rangle_g$ at long time. The results, shown in the inset of Fig. 4, demonstrate that $\hbar/\tau_\phi(g) \propto g/\xi$, which can be interpreted as the average interaction energy within a localization volume $\xi = 2\ell$. A similar time scale for the dynamical alteration of localization by interactions was found in [29, 30].

We expect the retroreflection phenomenon to be a rather general property of systems displaying Anderson localization. In particular, it is not restricted to 1D systems, as can be inferred from a straightforward extension to any dimension of the reasoning leading to Eq. (3). We have also numerically checked that the CoM indeed goes back to its initial position in two-dimensional (2D) random potentials, see the dotted curve in Fig. 4, obtained using the 2D version of the potential $V(x)$ (with $k_0\ell \simeq 2.5$). At weak disorder, the decay of $\langle x\rangle(t)$ is however much slower in 2D because the localization time is much longer than in 1D. The fact that the retroreflection is significantly affected by weak interactions at short times suggests that it could be advantageously used as a sensitive probe of Anderson localization in interacting disordered systems.

We thank Christian Miniatura for discussions at the early stages of this work.

[1] P. W. Anderson, Phys. Rev. **109**, 1492 (1958).
[2] A. A. Chabanov, M. Stoytchev, and A. Z. Genack, Nature **404**, 850 (2000).
[3] T. Schwartz, G. Bartal, S. Fishman, and M. Segev, Nature **446**, 52 (2007).
[4] M. Störzer, P. Gross, C. M. Aegerter, and G. Maret, Phys. Rev. Lett. **96**, 063904 (2006).
[5] T. Sperling, L. Schertel, M. Ackermann, G. J. Aubry, C. M. Aegerter, and G. Maret, New J. Phys. **18**, 013039 (2016).
[6] H. Hu, A. Strybulevych, J. H. Page, S. E. Skipetrov, and B. A. Van Tiggelen, Nature Phys. **4**, 945 (2008).
[7] J. Chabé, G. Lemarié, B. Grémaud, D. Delande, P. Szriftgiser, and J. C. Garreau, Phys. Rev. Lett. **101**, 255702

(2008).
[8] J. Billy, V. Josse, Z. Zuo, A. Bernard, B. Hambrecht, P. Lugan, D. Clément, L. Sanchez-Palencia, P. Bouyer, and A. Aspect, Nature **453**, 891 (2008).
[9] F. Jendrzejewski, A. Bernard, K. Müller, P. Cheinet, V. Josse, M. Piraud, L. Pezzé, L. Sanchez-Palencia, A. Aspect, and P. Bouyer, Nature Phys. **8**, 398 (2012).
[10] I. Manai, J. F. Clément, R. Chicireanu, C. Hainaut, J. C. Garreau, P. Szriftgiser, and D. Delande, Phys. Rev. Lett. **115**, 240603 (2015).
[11] G. Semeghini, M. Landini, P. Castilho, S. Roy, G. Spagnolli, A. Trenkwalder, M. Fattori, M. Inguscio, and G. Modugno, Nature Phys. **11**, 554 (2015).
[12] M. Schreiber, S. S. Hodgman, P. Bordia, H. P. Lüschen, M. H. Fischer, R. Vosk, E. Altman, U. Schneider, and I. Bloch, Science **349**, 842 (2015).
[13] J. Choi, S. Hild, J. Zeiher, P. Schauß, A. Rubio-Abadal, T. Yefsah, V. Khemani, D. A. Huse, I. Bloch, and C. Gross, Science **352**, 1547 (2016).
[14] G. Modugno, Rep. Prog. Phys. **73**, 102401 (2010).
[15] B. Shapiro, J. Phys. A: Math. Theor. **45**, 143001 (2012).
[16] E. Akkermans and G. Montambaux, *Mesoscopic physics of electrons and photons* (Cambridge University Press, 2007).
[17] A. A. Gogolin, Physics Reports **86**, 1 (1982).
[18] T. Prat, D. Delande, and N. Cherroret, to be published.
[19] S. Roche and D. Mayou, Phys. Rev. Lett. **79**, 2518 (1997).
[20] H. Fehske, J. Schleede, G. Schubert, G. Wellein, V. S. Filinov, and A. R. Bishop, Phys. Lett. A **373**, 2182 (2009).
[21] This can be justified more rigorously by using the phase space Wigner representation $\overline{W(x,p,t)}$ of the wave packet. In the weak-disorder approximation, $\overline{W(x,p,t)}$ is non vanishing only near $p = \pm\hbar k_0$, so that it can be split in two parts $\overline{W(x,p,t)} \approx n_+(x,t)\delta(p-\hbar k_0)+n_-(x,t)\delta(p+\hbar k_0)$.
[22] E. P. Nakhmedov, V. N. Prigodin, and Yu. A. Firsov, Zh. Eksp. Teor. Fiz. **92**, 2133 (1987) [Sov. Phys. JETP **65**, 1202 (1987)].
[23] Although the calculations in [22, 24] are correct, there are occasionally factors 2 missing in some equations.
[24] V. L. Berezinsky, Zh. Eksp. Teor. Fiz. **65**, 1251 (1973) [Sov. Phys. JETP **38**, 620 (1974)].
[25] G. A. Baker Jr., *Essentials of Padé Approximants*, Academic Press (New York).
[26] To obtain Eq. (11), one starts from $\Psi_{k_0}(x) \propto \exp(-x^2/2\sigma^2)\cos(k_0 x)$, i.e. from a state having a momentum distribution symmetric with respect to $k = 0$.
[27] M. Mulansky, K. Ahnert, A. Pikovsky, and D. L. Shepelyansky, Phys. Rev. E **80**, 056212 (2009).
[28] S. Flach, Springer Proc. Phys. **173**, 45 (2016).
[29] A. Iomin, Phys. Rev. E **81**, 017601 (2010).
[30] N. Cherroret, J. Phys.: Condens. Matter **29**, 024002 (2017).

Appendix 4.A Solution of Berezinskii equations at long times

In this appendix, we use the Berezinskii convention $\hbar = 2m = k_0 = 1$.

To obtain the long-time (small frequency) asymptotic behavior of $\langle x \rangle$ from Berezinskii equations [equations (4.64), (4.65) and (4.66)], it is convenient to introduce the generating functions

$$R(\zeta) = \sum_{m=0}^{\infty} R_m \zeta^m \text{ and } Q(\zeta) = \sum_{m=0}^{\infty} Q_m^1 \zeta^m. \tag{4.76}$$

$R(\zeta)$ can be deduced from the closed-form solution of R_m [equation (4.67)], the result writes

$$R(\zeta) = \frac{1}{1-\zeta}\left[1 - \zeta F\left(\frac{i\nu}{1-\zeta}\right)\right], \; F(z) = ze^{-z}\mathrm{Ei}(z), \tag{4.77}$$

where $\mathrm{Ei}(z)$ is the exponential integral function. For $Q(\zeta)$ we can only infer a differential equation from equation (4.64):

$$i\nu\left(\zeta\frac{\mathrm{d}Q}{\mathrm{d}\zeta} + \frac{1}{2}Q\right) + (1-\zeta)\frac{\mathrm{d}}{\mathrm{d}\zeta}\left\{\zeta\frac{\mathrm{d}}{\mathrm{d}\zeta}\left[(1-\zeta)Q\right]\right\} + P(\zeta) = 0, \tag{4.78}$$

where $P(\zeta) = \sum_{m=0}^{\infty} P_m^1 \zeta^m$ is straightforward to deduce from $R(\zeta)$.

Coming back to equation (4.65), we introduce the solution for R_m [equation (4.67)] and obtain

$$\langle x \rangle = -\frac{4\nu}{\omega\gamma}\int_0^{\infty} \mathrm{d}s e^{i\nu s} \sum_{m=0}^{\infty} \frac{1}{s+1} Q_m(\omega, k=0)\left(\frac{s}{s+1}\right)^m = -\frac{4\nu}{\omega\gamma}\int_0^{\infty} \mathrm{d}s e^{i\nu s} B(s), \tag{4.79}$$

where $B(s)$ is then given by

$$B(s) = \frac{1}{s+1} Q\left(\frac{s}{s+1}\right) = \frac{1}{s+1}\sum_{m=0}^{\infty} Q_m(\omega, k=0)\left(\frac{s}{s+1}\right)^m. \tag{4.80}$$

From equation (4.78), we deduce the equation obeyed by $B(s)$:

$$\frac{\mathrm{d}}{\mathrm{d}s}\left(s(s+1)\frac{\mathrm{d}B(s)}{\mathrm{d}s}\right) + i\nu\left[s\frac{\mathrm{d}}{\mathrm{d}s}((s+1B(s)) + \frac{B(s)}{2}\right] + i\nu e^{-i\nu(s+1)}\mathrm{Ei}(i\nu(s+1)) = 0. \tag{4.81}$$

It is convenient to use the alternative form

$$\langle x \rangle = -\frac{4\nu}{i\omega}\int_0^{\infty} \mathrm{d}s (e^{i\nu s} - 1)\frac{\mathrm{d}B(s)}{\mathrm{d}s}, \tag{4.82}$$

obtained through integration by part.

We are now in position to address the small frequency (ν) expansion. We start by changing variable to $u = -i\nu s$,

$$\langle x \rangle = -\frac{\nu^2}{i\omega\gamma}\int_0^{-i\infty} (e^{-u} - 1)\frac{\mathrm{d}B(u)}{\mathrm{d}u}\mathrm{d}u. \tag{4.83}$$

Equation (4.81) becomes

$$\begin{aligned} &\frac{\mathrm{d}}{\mathrm{d}u}\left(u^2\frac{\mathrm{d}B(u)}{\mathrm{d}u}\right) - u\frac{\mathrm{d}}{\mathrm{d}u}\left(uB(u)\right) \\ &+ i\nu\left\{-\frac{\mathrm{d}}{\mathrm{d}u}\left(uB(u)\right) + u\frac{\mathrm{d}B(u)}{\mathrm{d}u} + \frac{B(u)}{2}\right\} + i\nu e^{-i\nu}e^{u}\mathrm{Ei}(-u + i\nu) = 0. \end{aligned} \tag{4.84}$$

We are interested in the few first orders in ν, we can therefore readily neglect the term enclosed in the braces, to simplify equation (4.84) to

$$\frac{\mathrm{d}}{\mathrm{d}u}\left(u^2\frac{\mathrm{d}B(u)}{\mathrm{d}u}\right) - u\frac{\mathrm{d}}{\mathrm{d}u}\left(uB(u)\right) + i\nu e^{-i\nu}e^{u}\mathrm{Ei}(-u+i\nu) = 0, \tag{4.85}$$

yet it is a difficult matter to solve this equation. The way around this difficulty is to first consider equation (4.81) in the limit $|\nu s| = |u| \ll 1$. Indeed, in this limit the terms enclosed in the square brackets can be neglected, and using the expansion $\mathrm{Ei}(z) \approx \ln(-z) + C$ (where C is the Euler constant), we directly obtain

$$\frac{\mathrm{d}B(s)}{\mathrm{d}s} \approx -i\nu\left\{\frac{C-1}{s+1} + \frac{\ln\left[(-i\nu)(s+1)\right]}{s+1} + \frac{\ln(s+1)}{s(s+1)}\right\} \text{ for } |\nu s| \ll 1. \tag{4.86}$$

An expansion of equation (4.86) for large s leads to

$$\frac{1}{-i\nu}\frac{\mathrm{d}B(s)}{\mathrm{d}s} \approx \frac{C-1+\ln(s)}{s} + \frac{\mathrm{d}}{\mathrm{d}s}\left[\frac{\ln(s)+C-1}{s}\right] + \frac{\ln(s)}{s^2} + \ldots \text{ for } |\nu s| \ll 1. \tag{4.87}$$

Going back to $u = -i\nu s$, we find

$$\frac{\mathrm{d}B(u)}{\mathrm{d}u} = -i\nu\left\{\frac{\ln(u)+C-1}{u}\right\} + (i\nu)^2\left\{\frac{\mathrm{d}}{\mathrm{d}u}\left[\frac{\ln(u)+C-1}{u}\right] + \frac{1}{u^2}\ln\left(\frac{u}{-i\nu}\right)\right\} + \ldots \tag{4.88}$$

From this last equation, it is clear that $B(u)$ as a ν expansion of the form

$$B(u) = i\nu B_1(u) + (i\nu)^2\ln(-i\nu)\hat{B}(u) + (i\nu)^2 B_2(u) + \ldots, \tag{4.89}$$

with the asymptotic forms as $u \to 0$

$$\frac{\mathrm{d}B_1(u)}{\mathrm{d}u} \to -\left(\frac{\ln(u)+C-1}{u}\right), \ \frac{\mathrm{d}\hat{B}(u)}{\mathrm{d}u} \to -\frac{1}{u^2}, \ \frac{\mathrm{d}B_2(u)}{\mathrm{d}u} \to \frac{2-C}{u^2}. \tag{4.90}$$

It is difficult to fully determine $B_1(u)$ and $B_2(u)$. $\hat{B}(u)$ is however quite simple to obtain. From the expansion of the nonhomogeneous term of equation (4.84):

$$\begin{aligned}&\frac{\mathrm{d}}{\mathrm{d}u}\left(u^2\frac{\mathrm{d}B(u)}{\mathrm{d}u}\right) - u\frac{\mathrm{d}}{\mathrm{d}u}\left(uB(u)\right) + i\nu\left\{-\frac{\mathrm{d}}{\mathrm{d}u}\left(uB(u)\right) + u\frac{\mathrm{d}B(u)}{\mathrm{d}u} + \frac{B(u)}{2}\right\}\\ &i\nu e^{u}\mathrm{Ei}(-u) - (i\nu)^2\left(e^{u}\mathrm{Ei}(-u) + \frac{1}{u}\right) + O\left(\nu^3\right) = 0,\end{aligned} \tag{4.91}$$

we identify the equation obeyed by $\hat{B}(u)$,

$$\frac{\mathrm{d}}{\mathrm{d}u}\left(u^2\frac{\mathrm{d}\hat{B}(u)}{\mathrm{d}u}\right) - u\frac{\mathrm{d}}{\mathrm{d}u}\left(u\hat{B}(u)\right) = 0, \tag{4.92}$$

whose solution, consistent with equation (4.90), is simply given by $\hat{B}(u) = 1/u$.

In the integral of equation (4.83), the contribution of the small u part is not very clear and requires some care (divergences appear due to the above expansion for large s, which clearly does not extend to $u = 0$). To handle it, we split the integral over two regions: $[0, s_0]$ and $[s_0, \infty]$, where

$s_0 \gg 1$, but $|\nu| s_0 \ll 1$. We start with the region $s < s_0$, where we can approximate $e^{i\nu s} - 1$ by $i\nu s$ and use equation (4.86), the integral is then not difficult to evaluate explicitly:

$$\begin{aligned}\frac{1}{-i\nu}\int_0^{s_0} s\frac{\mathrm{d}B(s)}{\mathrm{d}s}\mathrm{d}s &\approx \int_0^{s_0} s\left\{\frac{C-1}{s+1} + \frac{\ln\left[(-i\nu)(s+1)\right]}{s+1} + \frac{\ln(s+1)}{s(s+1)}\right\}\mathrm{d}s \\ &= (C-2)s_0 + (s_0+2-C)\ln(s_0+1) + \ln(-i\nu)(s_0 - \ln(s_0+1)).\end{aligned} \tag{4.93}$$

A large s_0 expansion provides

$$\frac{1}{-i\nu}\int_0^{s_0} s\frac{\mathrm{d}B(s)}{\mathrm{d}s}\mathrm{d}s \approx (C-2)s_0 + (s_0+2-C)\ln(s_0) - \ln(-i\nu)\ln(s_0) + \dots. \tag{4.94}$$

Expressing this last result in terms of $u_0 = -i\nu s_0$, we find the following contribution to $\langle x\rangle$:

$$\frac{4}{i\omega\gamma}\left[i\nu u_0(\ln(u_0) + C - 2) - (i\nu)^2\ln(-i\nu)(C - 2 - \ln(u_0)) + (i\nu)^2(C-2)\ln(u_0) + \nu^2\ln^2(-i\nu) + \dots\right]. \tag{4.95}$$

As for the remaining contribution, from the region $s > s_0$, we go from s to $u = -i\nu s$ and use equation (4.89), and consider only the contribution from $\hat{B}$, relevant for the center of mass. $\hat{B}$ being equal to $1/u$, in the limit $u_0 \to 0$, we are free to move the integration back to the reals, such that its contribution to $\langle x\rangle$ is

$$-\frac{4}{i\omega\gamma}(i\nu)^2\ln(-i\nu)\int_{u_0}^{\infty}\frac{e^{-u}-1}{u^2} = -\frac{4}{i\omega\gamma}(i\nu)^2\ln(-i\nu)(\ln(u_0) + C - 1) + O(u_0). \tag{4.96}$$

The limit $u_0 \to 0$ is now well defined (with the contributions from B_1 and B_2 at small u, the $\ln(u_0)$ cancel each other). Summing equations (4.95) and (4.96), we finally obtain

$$\langle x\rangle = \pi\alpha + \frac{16i\nu}{\gamma^2}\left(\ln^2(-i\nu) + (2C-3)\ln(-i\nu)\right) + O(\nu), \tag{4.97}$$

where α is a numerical constant which is difficult to determine using the above method (it comes from B_1) and irrelevant for the center of mass. It is given in [13] as $\alpha = 32(\pi^2 - C^3)/\gamma^2$. B_2 only contributes to $O(\nu)$.

The result for the center of mass obtained by Fourier transforming (4.97) is

$$\langle x\rangle = 64\ell\left[\frac{\ln(t/4\tau)\tau^2}{t^2} + \frac{\tau^2}{2t^2}\right] + \dots \tag{4.98}$$

Appendix 4.B Solution of Berezinskii equations from short times

To be consistent with the notations used in our submitted paper reproduced in section 4.9, we reintroduce $\hbar$, k_0 and m in this appendix.

To go beyond the long-time limit treated in appendix 4.A, we propose to solve the equations for the center of mass at any time. The solution takes the form of a short time expansion,

$$\langle x\rangle = \ell\sum_{n=0}^{\infty}\chi_n\left(\frac{t}{\tau}\right)^n, \tag{4.99}$$

rearranged under the form of a Padé approximant,

$$\langle x\rangle = \ell\frac{\ln(1+t/4\tau)\tau^2}{t^2}\lim_{N\to\infty}\frac{\sum_{n=0}^{N} a_n\left(t/\tau\right)^n}{\sum_{n=0}^{N} b_n\left(t/\tau\right)^n}. \tag{4.100}$$

Indeed, it is possible to work out the χ_n of equation (4.99) up to arbitrary order, but the resulting series has a finite convergence radius, estimated at 4τ from the first 100 terms[6]. Once rearranged under the form of a Padé approximant, as done in equation (4.100), we observe numerical convergence and the resulting $\langle x\rangle$ is in excellent agreement with our numerical simulations (figure 4.9a). It is the knowledge of the long-time limit [equation (4.98)] that suggests the form (4.100). In practice, (4.100) converges quite rapidly, the results for $N = 7$ demonstrate no visible difference with the results for $N = 14$ for times up to 120τ.

Let us find the χ_n then. We recall the expression of the center of mass [equation (4.65)]:

$$\langle x\rangle = -\frac{2\ell}{i\omega}\left[\sum_{m=0}^{\infty} P_m^1 Q_m^1\right], \tag{4.101}$$

where $P_m^1 = s\Gamma(m+1)[\Psi(m+1,2;-s) - (m+1)\Psi(m+2,2;-s)]$, with $s = 4i\omega\tau$, Γ the Gamma function and Ψ the confluent hypergeometric function of the second kind. The Q_m^1 are solutions of

$$[4i\omega\tau(m+1/2) - (m+1)^2 - m^2]Q_m^1 + (m+1)^2 Q_{m+1}^1 + m^2 Q_{m-1}^1 + P_m^1 = 0. \tag{4.102}$$

The difficulty lies in the calculation of the Q_m^1. Following the route outlined above, we write them under the form of a large frequency expansion

$$Q_m^1(\nu) \simeq \sum_{n=0}^{+\infty} \frac{q_{n,m}}{(i\nu)^n}. \tag{4.103}$$

And introduce this decomposition in equation (4.102), with P_m^1 reduced to its asymptotic form,

$$\begin{aligned} &O\left(\frac{1}{(i\nu)^m}\right) + \left(m+\frac{1}{2}\right)\sum_{n=0}^{+\infty}\frac{q_{n,m}}{(i\nu)^{n-1}} \\ &+ (m+1)^2\left(\sum_{n=0}^{+\infty}\frac{q_{n,m+1}}{(i\nu)^n} - \sum_{n=0}^{+\infty}\frac{q_{n,m}}{(i\nu)^n}\right) - m^2\left(\sum_{n=0}^{+\infty}\frac{q_{n,m}}{(i\nu)^n} - \sum_{n=0}^{+\infty}\frac{q_{n,m-1}}{(i\nu)^n}\right) = 0. \end{aligned} \tag{4.104}$$

For $m = 0$, we see that $q_{0,0} = 0$. Then, for $m = 1$, we see that $q_{0,1}$ and $q_{1,1}$ are vanishing. This pattern leads to

$$q_{n,m} = 0 \text{ if } n \leq m \Leftrightarrow Q_m^1(\nu) = \sum_{n>m}\frac{q_{n,m}}{(i\nu)^n}. \tag{4.105}$$

We can now turn to the non-vanishing terms. To that end, let us move to an "algorithmic point of view", and in this respect recast equation (4.102) to the general form

$$(\alpha_m\nu + \beta_m)Q_m^1 + \gamma_m Q_{m+1}^1 + m^2 Q_{m-1}^1 + \delta_m^0(\nu) = 0, \tag{4.106}$$

where $\alpha_m, \beta_m, \gamma_m$ and $\delta_m^0(\nu)$ are known. Plugging in equation (4.105), we find our basic equation

$$(\alpha_m\nu+\beta_m)\left(\sum_{n>m}\frac{q_{n,m}}{(i\nu)^n}\right) + \gamma_m\left(\sum_{n>m+1}\frac{q_{n,m+1}}{(i\nu)^n}\right) + m^2\left(\sum_{n>m-1}\frac{q_{n,m-1}}{(i\nu)^n}\right) + \delta_m^0(\nu) = 0. \tag{4.107}$$

To start with, one can scan m and consider the resulting equations from (4.107) at lowest order in $1/\nu$. Only $\alpha_m\nu Q_m^1$ and $m^2 Q_{m-1}^1$ contribute, they are thus straightforward to solve, to find all the

[6] More work is needed to identify the origin of this finite convergence radius.

$q_{n=m+1,m}$. One can then absorb the known $q_{n=m+1,m}$ and $\delta_m^0(\nu)$ in a new quantity, $\delta_m^1(\nu)$, to find an equation similar to (4.107):

$$(\alpha_m\nu+\beta_m)\left(\sum_{n>m+1}\frac{q_{n,m}}{(i\nu)^n}\right)+\gamma_m\left(\sum_{n>m+2}\frac{q_{n,m+1}}{(i\nu)^n}\right)+m^2\left(\sum_{n>m}\frac{q_{n,m-1}}{(i\nu)^n}\right)+\delta_m^1(\nu)=0. \quad (4.108)$$

We have highlighted in red the important differences between equations (4.107) and (4.108). Repeating the above procedure, one finds the $q_{n=m+2,m}$, in turn absorbed in a new $\delta_m^*(\nu)$, and so on and so forth. It is then immediate to deduce the χ_n of equation (4.99).

For practical purposes, we have included a copy of the Mathematica [100] notebook used to generate the results presented in figure 4.9 in Mathematica [100] notebook 4.1.

Note that an alternative numerical solution of Berezinskii equations exists [136].

```
nbterms = 15; (* Number of \chi_n computed. Should be greater than 1 *)
tmax = 120; (* Maximum time for which <x> is computed, in units of the scattering mean
free time *)
tstep = 0.01; (* Sample the time with a time step tstep. Should be smaller than tmax *)

fctr[m_, s_] := s*Gamma[m + 1]*HypergeometricU[m + 1, 2, -s]
fctp[m_, s_] := fctr[m, s] - fctr[m + 1, s] (* P_m^1 *)

SeriesCoefficient[fctp[m, s], {s, Infinity, n}];
p = Table[%, {m, 0, nbterms - 1}, {n, 0, nbterms - 1}];
(* Store P_m^1 large large \nu expansion for all m in a matrix *)
savp = p;

q = Table[ 0, {x, nbterms}, {y, nbterms}];
(* Store Q_m^1 large large \nu expansion for all m in a matrix *)
Do[ q[[1, 1 + i]] = -2*p[[1, i]];
 Do[q[[m, m + i]] = (-1/(m - 1/2))*((m - 1)^2*q[[m - 1, m - 1 + i]] +
       p[[m, m + i - 1]]), {m, 2, nbterms - i, 1}] /; (nbterms - i) > 1;
 Do[p[[m, m + i]] -= (m^2 + (m - 1)^2)* q[[m, m + i]],
       {m, nbterms - i}] /; (nbterms - i) > 0;
 Do[p[[m, m + i + 1]] += m^2* q[[m + 1, m + 1 + i]],
       {m, nbterms - i - 1}] /; (nbterms - i - 1) > 0; , {i, nbterms - 1}]

p = savp;

xomega = Table[ Sum[p[[m, i]]*q[[m, j]]*KroneckerDelta[n, i + j], {m, nbterms}, {i,
                    nbterms}, {j, nbterms}], {n, 3, nbterms + 2}];
       (* Sum over m P_m^1 Q_m^1, gives the series in frequency *)

xtime = Table[ 1/2*xomega[[n]]*(-1)^(n)/(Gamma[n + 1]*4^(n - 1)), {n, nbterms}];
(* = \chi_n *)

x[t_] := Sum[xtime[[n]]*t^n, {n, nbterms - 1}];

xpade = PadeApproximant[ t^2/Log[1 + t/4]*x[t], {t, 0, Floor[(nbterms - 1)/2]}];
tabxpade = Table[{t, xpade*Log[1 + t/4]/t^2}, {t, tstep, tmax, tstep}];
filename = "mean_x_pade_order" <> ToString[Floor[(nbterms - 1)/2]] <> ".dat";
Export[filename, tabxpade];
```

Mathematica [100] notebook 4.1 – Computes $\langle x \rangle$ under the form of a Padé approximant. The script outputs a two column file, the first column is the time in units of τ, and the second column is the corresponding $\langle x \rangle$ in units of ℓ. The parameter "nbterms" fixes the number of χ_n computed. The maximum time can be fixed with the parameter "tmax", and the time sampling with the parameter "tstep".

Chapter 5

Weakly interacting wave packets

So far, we have neglected atom-atom interactions and discussed only single-particle physics. Interactions are, however, often present in experiments, it is thus important to characterize their effects. In the present thesis, we restrict ourselves to dilute condensed bosonic gases, which are used in the Palaiseau [38] and Florence [40] groups.

The limitation to weakly interacting condensed bosonic gases allows us to approximate the full quantum many-body dynamics by a nonlinear equation for a classical field. Section 5.1 recalls some details on this approximation. We present a method to propagate numerically wave packets in the presence of a nonlinearity in section 5.2. As an illustration, we apply this method to an extensively studied scenario: the spreading of an initially narrow wave packet in a disordered potential. It is the opportunity to discuss the interplay between Anderson localization and interactions. Section 5.3 is devoted to the effect of the nonlinearity on the quantum boomerang effect of chapter 4. In sections 5.4 and 5.5, we trade the 1D initially narrow wave packet for 3D plane waves, with section 5.4 focusing on the dynamics of the energy distribution and section 5.5 examining the effect of interactions on the coherent back scattering peak. The subject of weakly interacting wave packets evolving in random potentials is vast, the present chapter is only concerned with some aspects and is not intended to cover it exhaustively.

Subsection 5.2.1 and sections 5.3, 5.4 and 5.5 present original results obtained during the present thesis. Sections 5.4 and 5.5 present on-going work.

5.1 Bose-Einstein condensates in random potentials

5.1.1 Many-body Hamiltonian

A common experimental scenario for probing localization consists in preparing a spatially narrow atomic wave packet in a trap, then opening the trap to release the atoms in a disordered potential and recording the time evolution of the gas [41, 42]. After it has been released, its dynamics is encoded in the many-body Hamiltonian, written in second quantization,

$$\widehat{H} = \int \mathrm{d}\boldsymbol{r}\widehat{\Psi}^\dagger(\boldsymbol{r})\left[-\frac{\hbar^2\Delta}{2m} + V_{\mathrm{ext}}(\boldsymbol{r})\right]\widehat{\Psi}(\boldsymbol{r}) + \frac{1}{2}\int \mathrm{d}\boldsymbol{r}\mathrm{d}\boldsymbol{r}' V_{\mathrm{int}}(\boldsymbol{r}-\boldsymbol{r}')\widehat{\Psi}^\dagger(\boldsymbol{r})\widehat{\Psi}^\dagger(\boldsymbol{r}')\widehat{\Psi}(\boldsymbol{r}')\widehat{\Psi}(\boldsymbol{r}), \quad (5.1)$$

where V_{ext} is the external (here disordered) potential and V_{int} is the two-body interaction potential. The field operator $\widehat{\Psi}$ obeys the non-trivial commutation relation (assuming a bosonic atomic cloud)

$$\left[\widehat{\Psi}(\boldsymbol{r}), \widehat{\Psi}^\dagger(\boldsymbol{r}')\right] = \delta(\boldsymbol{r}-\boldsymbol{r}'). \quad (5.2)$$

In the Heisenberg picture, the field operator evolves according to

$$i\hbar\partial_t\widehat{\Psi}(\boldsymbol{r},t)=\left[\widehat{\Psi}(\boldsymbol{r},t),\widehat{H}\right]=\left[-\frac{\hbar^2\Delta}{2m}+V_{\rm ext}(\boldsymbol{r})+\int \mathrm{d}\boldsymbol{r}' V_{\rm int}(\boldsymbol{r}-\boldsymbol{r}')\widehat{\Psi}^\dagger(\boldsymbol{r}',t)\widehat{\Psi}(\boldsymbol{r}',t)\right]\widehat{\Psi}(\boldsymbol{r},t). \quad (5.3)$$

5.1.2 Bogoliubov approximation

Equation (5.3) is fully general, but rather complicated, it is a nonlinear equation for a quantum field. In the limit of a weakly interacting Bose-Einstein condensate (BEC), we can proceed with the Bogoliubov approximation. The first step consists in singling out the condensate mode in the field $\widehat{\Psi}$:

$$\widehat{\Psi}(\boldsymbol{r},t)=\phi(\boldsymbol{r},t)\widehat{a}_0+\delta\widehat{\Psi}(\boldsymbol{r},t). \quad (5.4)$$

Here $\widehat{a}_0$ annihilates a particle in the condensate mode, described by the wave function $\phi(\boldsymbol{r},t)$. $\delta\widehat{\Psi}(\boldsymbol{r},t)$ accounts for non-condensed atoms. Then, since the initial state is a BEC, we expect $\widehat{\Psi}(\boldsymbol{r},t)$ to be dominated by $\phi(\boldsymbol{r},t)\widehat{a}_0$ and we thus neglect $\delta\widehat{\Psi}(\boldsymbol{r},t)$. Finally, the BEC containing many atoms, the operator $\widehat{a}_0$ is well approximated by a scalar ($\widehat{a}_0$ and $\widehat{a}_0^\dagger$ are approximately equal to the square root of the number of atoms in the condensate, N). Replacing $\widehat{\Psi}(\boldsymbol{r},t)$ by $\phi(\boldsymbol{r},t)\sqrt{N}$ in equation (5.3), we find

$$i\hbar\partial_t\phi(\boldsymbol{r},t)=\left[-\frac{\hbar^2\Delta}{2m}+V_{\rm ext}(\boldsymbol{r})+N\int \mathrm{d}\boldsymbol{r}' V_{\rm int}(\boldsymbol{r}-\boldsymbol{r}')|\phi(\boldsymbol{r}',t)|^2\right]\phi(\boldsymbol{r},t). \quad (5.5)$$

The dynamics of the BEC is described by the classical field $\phi(\boldsymbol{r},t)$, the wave function of the condensate, obeying the nonlinear equation (5.5). Note that $\phi(\boldsymbol{r},t)$ is normalized to unity.

5.1.3 Two-body low energy collisions and scattering potential

To simplify the problem even further, we can use the fact that, at the very low energies we are considering, the scattering properties of the atoms through the full interaction potential $V_{\rm int}(\boldsymbol{r}-\boldsymbol{r}')$ are encoded in a single length scale, the scattering length a [137]. In the dilute limit, it is thus sufficient to model the interaction potential by a potential reproducing the appropriate scattering length. The simplest choice is

$$V_{\rm int}(\boldsymbol{r}-\boldsymbol{r}')=\frac{4\pi a\hbar^2}{m}\delta(\boldsymbol{r}-\boldsymbol{r}')=\frac{g}{N}\delta(\boldsymbol{r}-\boldsymbol{r}'). \quad (5.6)$$

Substituting equation (5.6) into equation (5.5), we obtain the fundamental equation of the present chapter, the Gross-Pitaevskii equation, describing the evolution of the condensate wave function:

$$i\hbar\partial_t\phi(\boldsymbol{r},t)=\left[-\frac{\hbar^2\Delta}{2m}+V_{\rm ext}(\boldsymbol{r})+g|\phi(\boldsymbol{r},t)|^2\right]\phi(\boldsymbol{r},t). \quad (5.7)$$

The many-body evolution [equation (5.3)] is thus recast under the form of a single-particle Schrödinger equation [equation (5.7)] with an additional nonlinear potential, $g|\phi(\boldsymbol{r},t)|^2$, describing a kind of self interaction. The latter approximates the interaction of an atom with the other atoms in the condensate in a mean-field way. As we will see later on, the nonlinear nature of the Gross-Pitaevskii equation makes the associated physics very rich, as the nonlinearity can have widely different effects depending on the initial conditions.

5.1.4 Comments on the Gross-Pitaevskii equation

Before exploring the consequences of the nonlinearity, two comments are in order. First, even though we gave here a somewhat simplistic derivation of the Gross-Pitaevskii equation (5.7), one should not conclude that this chapter is on thin ice. Indeed, the Gross-Pitaevskii equation can be derived rigorously [138] and turns out to explain very well many experiments involving weakly interacting cold bosons (see [139] for a review). Nevertheless, the Gross-Pitaevskii equation accurately describes the evolution of the condensate wave function only, and in practice some atoms are inevitably not condensed. It is possible to take them into account approximately, for instance within Bogoliubov theory [70–76, 140]. We will however stay at the Gross-Pitaevskii level in this thesis.

Note that the non-condensed fraction may increase in time through the depletion of the condensate. To the best of our knowledge, this issue was only addressed in contexts that differ slightly from the ones considered in this chapter. To be more specific, as opposed to [75, 76, 140] where the atoms are condensed in the lowest energy state, we consider the evolution of atoms condensed in arbitrary wave functions. Another example is the study of transport of condensed atoms through disordered waveguides, in atom-laser-like configurations [72]. In these contexts, for weak enough potentials and interactions, the depletion of the condensate remains small.

Still, even though the Gross-Pitaevskii equation (5.7) represents a formidable simplification of the full many-body dynamics [equation (5.3)], reliable results remain generally difficult to obtain analytically. Numerical simulations of the Gross-Pitaevskii equation in the weakly interacting limit therefore turn out quite valuable.

5.2 Numerical integration of the Gross-Pitaevskii equation

This section being devoted to a numerical technique, we set $\hbar$ to 1 to lighten the notations.

We have seen in section 4.3 that the Schrödinger equation can efficiently be solved numerically by means of a Chebyshev polynomial expansion. The Gross-Pitaevskii equation (5.7) is *a priori* not well adapted to this method because of the time-dependent term $g|\phi(\boldsymbol{r},t)|^2$. In this thesis, however, interactions are always considered as a weak perturbation of the disordered Hamiltonian, such that it is tempting to integrate equation (5.7) similarly to the usual Schrödinger equation, with only a small modification accounting for the nonlinearity.

5.2.1 Numerical scheme and error estimate

To integrate the Gross-Pitaevskii equation numerically, we show in the present subsection that the evolution operator over a small time step can be conveniently separated into a linear operator and two simple nonlinear terms. To this end, we start from the formal solution

$$|\phi(t)\rangle = \widehat{U}(t)\,|\phi(t=0)\rangle = T\exp\left(-i\int_0^t \mathrm{d}t'\,\widehat{H}_{\mathrm{GP}}(t')\right)|\phi(t=0)\rangle\,, \tag{5.8}$$

where

$$\widehat{H}_{\mathrm{GP}}(t) = \frac{\boldsymbol{p}^2}{2m} + V_{\mathrm{ext}}(\boldsymbol{r}) + g|\phi(\boldsymbol{r},t)|^2 = \widehat{H}_{g=0} + g|\phi(\boldsymbol{r},t)|^2, \tag{5.9}$$

and T is the time-ordering operator. We proceed with a Taylor expansion of the time-dependent term

$$g|\phi(\boldsymbol{r},t')|^2 = g\left(|\phi(\boldsymbol{r},t=0)|^2 + \left[\partial_{t'}|\phi(\boldsymbol{r},t')|^2\right]_{t'=0} t'\right) + O(t'^2). \tag{5.10}$$

The key point is to notice that the term linear in t' in equation (5.10) can be taken out of the exponential in equation (5.8), with only an $O(t^3)$ error:

$$T\exp\left(-i\int_0^t \mathrm{d}t'\widehat{H}_{\mathrm{GP}}(t')\right) = \exp\left(-ig\left[\partial_t|\phi(\boldsymbol{r},t)|^2\right]_{t=0}\frac{t^2}{2}\right)\exp\left(-i\widehat{H}_{\mathrm{GP}}(t=0)t\right)+O(t^3). \quad (5.11)$$

Indeed, terms arising from the non-commutativity of $\left[\partial_t|\phi(\boldsymbol{r},t)|^2\right]_{t=0}t$ and the kinetic term are $O(t^3)$ (a t^2 comes from the two integrals over time and a t from the time dependence of the nonlinear part). To further simplify (5.11), we use the symmetrized Trotter formula [141]:

$$\begin{aligned}&\exp\left(-i\left[\widehat{H}_{g=0}+g|\phi(\boldsymbol{r},t=0)|^2\right]t\right)\\ =&\exp\left(-i\frac{g|\phi(\boldsymbol{r},t=0)|^2}{2}t\right)\exp\left(-i\widehat{H}_{g=0}t\right)\exp\left(-i\frac{g|\phi(\boldsymbol{r},t=0)|^2}{2}t\right)+O(t^3),\end{aligned} \quad (5.12)$$

as well as

$$\begin{aligned}\left[|\phi(\boldsymbol{r},t=0)|^2+\left[\partial_t|\phi(\boldsymbol{r},t)|^2\right]_{t=0}t\right]t &= \left[|\phi(\boldsymbol{r},t=0)|^2+|\phi(\boldsymbol{r},t)|^2-|\phi(\boldsymbol{r},t=0)|^2+O(t^2)\right]t\\ &= |\phi(\boldsymbol{r},t)|^2t+O(t^3),\end{aligned} \quad (5.13)$$

to finally obtain

$$\begin{aligned}&T\exp\left(-i\int_0^t \mathrm{d}t'\widehat{H}_{\mathrm{GP}}(t')\right)\\ =&\exp\left(-i\frac{g|\phi(\boldsymbol{r},t)|^2}{2}t\right)\exp\left(-i\widehat{H}_{g=0}t\right)\exp\left(-i\frac{g|\phi(\boldsymbol{r},t=0)|^2}{2}t\right)+O(t^3).\end{aligned} \quad (5.14)$$

To guarantee a small error, we split the total evolution in N time steps: $t=N\delta t$. The wave function at time t is then obtained by iterating N times the equation

$$|\phi(\delta t)\rangle = \exp\left(-i\frac{g|\phi(\boldsymbol{r},\delta t)|^2}{2}\delta t\right)\exp\left(-i\widehat{H}_{g=0}\delta t\right)\exp\left(-i\frac{g|\phi(\boldsymbol{r},t=0)|^2}{2}\delta t\right)|\phi(t=0)\rangle\,. \quad (5.15)$$

The error at time t scales as $1/N^2$. Equation (5.15) embodies our numerical technique to integrate the Gross-Pitaevskii equation. Note that $|\phi(\boldsymbol{r},\delta t)|^2$ in equation (5.15) follows from

$$\left|\phi(\boldsymbol{r},\delta t)\right|^2 = \left|\langle\boldsymbol{r}|\exp\left(-i\widehat{H}_{g=0}\delta t\right)\exp\left(-i\frac{g|\phi(\boldsymbol{r},t=0)|^2}{2}\delta t\right)|\phi(t=0)\rangle\right|^2, \quad (5.16)$$

such that our numerical integration scheme is explicit. For small g, the linear part can efficiently be implemented as a sum of Chebyshev polynomials, as done in section 4.3. The nonlinear part is simply accounted for through multiplication by phases before and after applying the Chebyshev polynomial expansion.

5.2.2 In practice

Keeping a weak interaction while having a weak disorder makes the numerical simulations quite demanding. Indeed, it imposes the hierarchy $\tau_k \ll \tau_{\mathrm{dis}} \ll \tau_g$ where the time scales are respectively associated to the kinetic, disorder and interaction terms. Practically, we want to reach long times

($t \gg \tau_g$) to see the effects of the nonlinearity, while the numerical simulations are constrained to describe correctly the kinetic dynamics ($t \simeq \tau_k$). To make the problem more tractable, we have chosen to release the constraint of describing the continuous situation as faithfully as possible and simply consider the lattice situation in subsection 5.2.3 and section 5.3. The corresponding 1D Hamiltonian writes

$$H_a = \sum_i \left[-\frac{\phi_{i+1} + \phi_{i-1} - 2\phi_i}{2ma^2} + V_i + g|\phi_i|^2 \right], \tag{5.17}$$

where a is the lattice spacing, $\phi_i = \phi(ai)$, and the sum runs over the lattice sites. Note that throughout the thesis, a lattice is used in the numerical simulations. However, in the rest of the thesis, we always choose a lattice spacing much smaller than the smallest length scale of the problem. It is this condition that is relaxed in subsection 5.2.3 and section 5.3, we expect the results presented there to describe the continuous situation at a qualitative level only. Note that in the non-interacting limit, there is little difference between a continuous and a discrete system, as far as localization on large spatial scales is concerned [108].

Throughout this chapter, we use an uncorrelated Gaussian potential of strength set by γ (in dimension d):

$$\overline{V_i V_j} = \gamma \delta_{i,j}/a^d, \tag{5.18}$$

with $\delta_{i,j}$ the Kronecker delta.

The rest of this chapter is devoted to the application of the present numerical approach to the Gross-Pitaevskii equation in various situations. Whenever possible, we will underline the qualitative physical picture at play. Sections 5.2.3, 5.3 and 5.4.1 discuss the interplay between localization and nonlinearity in the 1D case. From subsection 5.4.2 onward, on the other hand, we focus on the 3D geometry in the diffusive regime.

5.2.3 Nonlinearity and spreading

To illustrate the above numerical method, we propose to consider the common experimental scenario for probing localization in cold-atom experiments. It consists in releasing in a random potential an initially narrow atomic wave packet. Anderson localization is tracked in the evolution of the mean square displacement $\langle x^2 \rangle$ of the wave packet. Indeed, as opposed to diffusion, for which $\langle x^2 \rangle$ grows linearly in time, Anderson localization bounds $\langle x^2 \rangle$ to roughly the square of the localization length. In this section, we address the question of how the nonlinearity modifies this behavior. Note that this question has already been extensively studied numerically and theoretically [142–148].

Numerical experiment

Following [142], we propagate numerically a wave packet initially placed at $x = 0$ ($\phi^2(x, t = 0) = \delta_{x,0}/a$, with $\delta_{x,0}$ the Kronecker delta) in a strong random potential. The resulting mean square displacement $\langle x^2 \rangle$ as a function of time is shown in figure 5.3, and unambiguously displays subdiffusion at long times:

$$\langle x^2 \rangle \propto t^\alpha \quad \text{with } 0 < \alpha < 1. \tag{5.19}$$

The subdiffusive exponent (the slope of the dashed line in the figure) is approximately equal to 0.29, in agreement with [142]. This subdiffusive behavior was also observed numerically in [143–148] and experimentally in [50].

Subdiffusion is however predicted to breakdown at extremely long times, replaced by a slower spreading (if any) (see [51, 52] for rigorous proofs and [53, 54] for possible physical mechanisms). We however never reach this regime in the present thesis (with possibly the exception of the results presented in figure 5.3a).

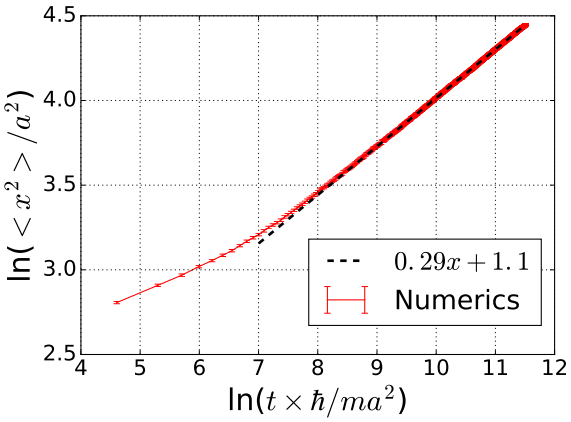

Figure 5.1 – Mean square displacement as a function of time. In log-log scale, the long time limit is well fitted by a straight line, hence demonstrating subdiffusion. The associated subdiffusive exponent (α in (5.19), i.e. the slope of the dashed line in the figure) is approximately equal to 0.29. For these simulations, we have used a nonlinear strength $g = 0.5\ \hbar^2/ma$ and a disorder strength $\gamma = 0.5625\ \hbar^4/m^2a$. A time step $\delta t = 0.04\ ma^2/\hbar$ was found sufficient. The results are averaged over 15000 disorder realizations.

Discussion

The nonlinearity thus affects Anderson localization, without destroying it completely (which would result in the restoration of a pure diffusive spreading). The reason for this mixed behavior lies in a trade-off between destruction of localization by the time-dependent nonlinearity on one hand, and dilution of the nonlinearity itself by a diffusive behavior on the other hand. In the literature, one finds two approaches attempting at quantifying this trade-off. One trend is to treat the nonlinearity as mixing the linear localized modes and hence restoring transport by allowing the atoms to jump from one localized mode to another (see [48, 49] for recent reviews). The mixing depending on the strength of the nonlinearity, it would disappear at long times if diffusion prevailed. Another approach that has been proposed consists in generalizing the self-consistent theory of localization (see section 1.1 for more details) to the nonlinear case [149]. Here as well localization would not be destroyed by the nonlinearity if diffusive transport were restored.

Both approaches predict that subdiffusion is the condition to balance destruction of localization and dilution of the nonlinearity. Although the numerical value of the subdiffusive exponent [α in (5.19)] is still debated. On the one hand, the generalized self-consistent theory of localization predicts $\alpha = 1/2$. On the other hand, the mixing of linear localized modes appear to be dependent on the chaotic properties of the Gross-Pitaevskii chain (5.17) [144]. These chaotic properties are only partially understood [49,57,150], resulting in different predictions for the subdiffusive exponent, e.g. $\alpha = 1/2$ [144, 151], $\alpha = 2/5$ [145, 147] or $\alpha = 1/3$ [143, 144, 152, 153].

5.3 Nonlinear quantum boomerang

5.3.1 Numerical experiment

The nonlinearity affecting Anderson localization, a natural question to ask is whether it prevents the quantum boomerang effect of chapter 4. Let us perform the numerical simulation then, and propagate the initial wave function

$$\phi(x) \propto e^{-x^2/2\sigma} e^{ik_0 x}. \tag{5.20}$$

We show in figure 5.2a the resulting center of mass $\langle x \rangle_g$ as a function of time, for two values of $g \neq 0$. We observe that $\langle x \rangle_g$ decreases more slowly than in the non-interacting limit and seems to saturate at a finite value at long times. The center-of-mass retroreflection is thus interrupted by the nonlinearity, the nonlinear quantum boomerang does not come back to the origin. For these simulations, we used a system of size $7500\pi/k_0$ discretized into 23562 grid points, and propagate a wave packet of width $\sigma = 10/k_0$ in a random potential of strength $\gamma = 0.0196\ \hbar^4 k_0^3/m^2$ ($k_0\ell \simeq 18.1$). The results are averaged over 600000 (8.85 millions) disorder realizations when $g \neq 0$ (respectively $g = 0$). A time step between 1.47 $m/(\hbar k_0^2)$ (for the largest g) and 2.27 $m/(\hbar k_0^2)$ (for the smallest g) was found sufficient.

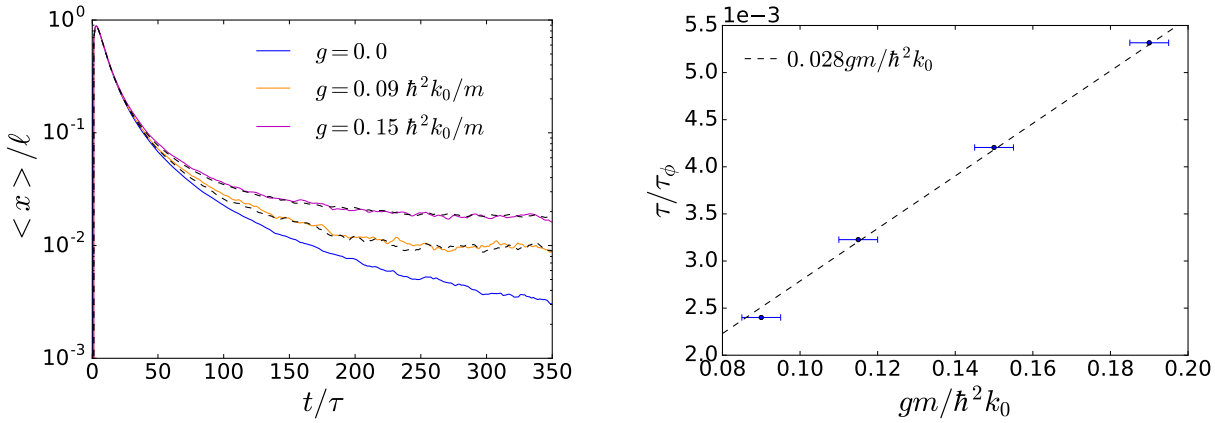

(a) (b)

Figure 5.2 – Figure a): center of mass $\langle x \rangle_g$ as a function of time, for $g = 0$ (solid lower blue curve), $g = 0.09\ \hbar^2 k_0/m$ (solid middle orange curve) and $g = 0.15\ \hbar^2 k_0/m$ (solid upper magenta curve). Two dashed curves show the center of mass $\langle x \rangle_\phi$ obtained with the model of decoherence, for $A_f = 0.02$ and 0.03 (from bottom to top). The scattering mean free path (ℓ) and time (τ) are calculated at the Born approximation, using the formula given in the caption of figure 4.9. Figure b): $\tau/\tau_\phi(g)$, well fitted by a linear regression. The effective decoherence time $\tau_\phi(g)$ associated with the nonlinearity thus behaves like $\hbar/\tau_\phi(g) \sim g/\ell$. The parameters used in the numerical simulations are given in the main text.

5.3.2 Comparison with decoherence

To better understand the role of the nonlinearity, we have also studied how the center of mass is affected by *decoherence*, modeled by the Hamiltonian

$$H = -\frac{\hbar^2 \Delta}{2m} + V(x) + V_\phi(x,t). \tag{5.21}$$

Here $V(x)$ is the usual random potential and

$$V_\phi(x,t) = h(x) f(t), \tag{5.22}$$

where $h(x)$ has the same statistical properties as $V(x)$ and $f(t)$ is a random, Gaussian distributed function of time with zero average. $f(t)$ is fully characterized by its time-time correlation function which we choose Gaussian,

$$\overline{f(t) f(t')} = A_f^2 \exp[-(t-t')^2/2\sigma_t^2], \tag{5.23}$$

with $A_f \ll 1$ to ensure that the temporally fluctuating potential is weaker than the static one. For this model, we use the same numerical scheme as for the Gross-Pitaevskii equation [with $g|\phi(x,t)|^2$ replaced by $V_\phi(x,t)$] and take $\sigma_t = 4\ m/(\hbar k_0^2)$ and a time step $\delta t = 0.735\ m/(\hbar k_0^2)$.

We have checked that the potential $V_\phi(x,t)$ does induce decoherence: at long times, it restores classical diffusion with $\langle x^2\rangle = 2D_\phi t$, where $D_\phi = \xi^2/\tau_\phi = 4\ell^2/\tau_\phi$ is the diffusion coefficient and τ_ϕ the decoherence time [14]. Because $V_\phi(x,t)$ preserves time-reversal and translational invariance after disorder averaging, equation (4.75) still holds for this model:

$$\langle x\rangle = \frac{\partial_t \langle x^2\rangle}{2v_0}. \tag{5.24}$$

Since $\langle x^2\rangle = 2D_\phi t$ at long times, $\langle x\rangle_\phi$ converges to the finite value $4\ell\tau/\tau_\phi$ (we have used $\ell = v_0\tau$). $\langle x\rangle_\phi$ is displayed in figure 5.2a (dashed curves), for two values of A_f. The two values of g chosen in the Gross-Pitaevskii model were adjusted so that $\langle x\rangle_g$ coincides with these two curves $\langle x\rangle_\phi$ in the long-time limit[1]. Surprisingly, the obtained curves $\langle x\rangle_\phi$ match extremely well the nonlinear curves $\langle x\rangle_g$ *in the whole time window*. This suggests that at least regarding $\langle x\rangle$, the nonlinearity acts similarly to a decoherence process. From this observation, we associate to the nonlinearity an effective decoherence time $\tau_\phi(g)$. To find this quantity, we first determine D_ϕ from the evolution of $\langle x^2\rangle$ with time in the model of decoherence, and then find the associated g by matching the curves $\langle x\rangle_\phi$ and $\langle x\rangle_g$ at long time. The results, shown in figure 5.2b, demonstrate that $\hbar/\tau_\phi(g) \propto g/\xi$, which can be interpreted as the average interaction energy within a localization volume $\xi = 2\ell$. A similar time scale for the dynamical alteration of localization by interactions was found in [147, 149]. Note that the subdiffusion regime ensuing the dynamical alteration of localization (see subsection 5.2.3) is only visible for times much longer than $\tau_\phi(g)$ [147,149], whereas figure 5.2a present times of order $\tau_\phi(g)$ (e.g. for $g = 0.15\hbar^2 k_0 m$ – magenta curve in figure 5.2a – $\tau_\phi(g) \approx 250\tau$).

5.4 Nonlinearity and energy distribution

We have seen in section 3.2 that in the linear case, it is quite natural to express the dynamics of a given wave packet as a sum over its energy components. For example, the density at time t is conveniently written as

$$\overline{|\psi(\boldsymbol{r},t)|^2} = \int \mathrm{d}\epsilon P(\epsilon)\Phi_\epsilon(\boldsymbol{r},t), \tag{5.25}$$

where $P(\epsilon)$ is the average wave packet energy distribution and $\Phi_\epsilon(\boldsymbol{r},t)$ describes the dynamics of the energy component ϵ. In the nonlinear case, the energy distribution may vary in time, due to the time-dependence of the nonlinear term. This section aims at studying the evolution of its average. We define the average energy distribution at time t as

$$P(\epsilon,t) = \overline{\langle\phi(t)|\delta(\epsilon - H)|\phi(t)\rangle}, \tag{5.26}$$

where H is the Gross-Pitaevskii Hamiltonian at time t and $\phi(t)$ the wave function at time t. Before studying the evolution of the energy distribution, let us provide some motivation through a second look at the spreading scenario of subsection 5.2.3.

5.4.1 Motivations: a second look at spreading

Numerical experiment

In subsection 5.2.3, we have used an initial wave packet of the form $\phi^2(x) = \delta_{x,0}/a$ and a strong random potential. We propose to consider now a wave packet of the form

$$\phi(x) \propto \cos(k_0 x)e^{-x^2/2\sigma^2}, \tag{5.27}$$

[1] Practically, a least-square fit method has been used for center-of-mass data corresponding to $t > 150\tau$.

evolving in a weak random potential. These conditions offer more control over the initial energy distribution, since at weak disorder the kinetic energy dominates and the momentum distribution of (5.27) can be tuned. In particular, in the limit $k_0\sigma \gg 1$, the momentum distribution [and thus the energy distribution – see subsection 3.1.4 for more details] of (5.27) is sharply peaked around $\hbar k_0$ [$\hbar^2 k_0^2/2m$].

The resulting mean square displacement $\langle x^2 \rangle$ is shown in figure 5.3 as a function of time for two values of k_0. On the one hand, the results for $k_0 = \pi/4a$ (figure 5.3b) unambiguously display subdiffusion at long times, $\langle x^2 \rangle \propto t^\alpha$, with a subdiffusive exponent (the slope of the dashed line in the figure) $\alpha \simeq 0.3$. On the other hand, the case $k_0 = \pi/2a$ (figure 5.3a) appears clearly different, with a much smaller subdiffusive exponent ($\alpha \simeq 0.19$) and a possible deviation from subdiffusion at long times. More work is however needed to fully characterize this possible deviation from subdiffusion.

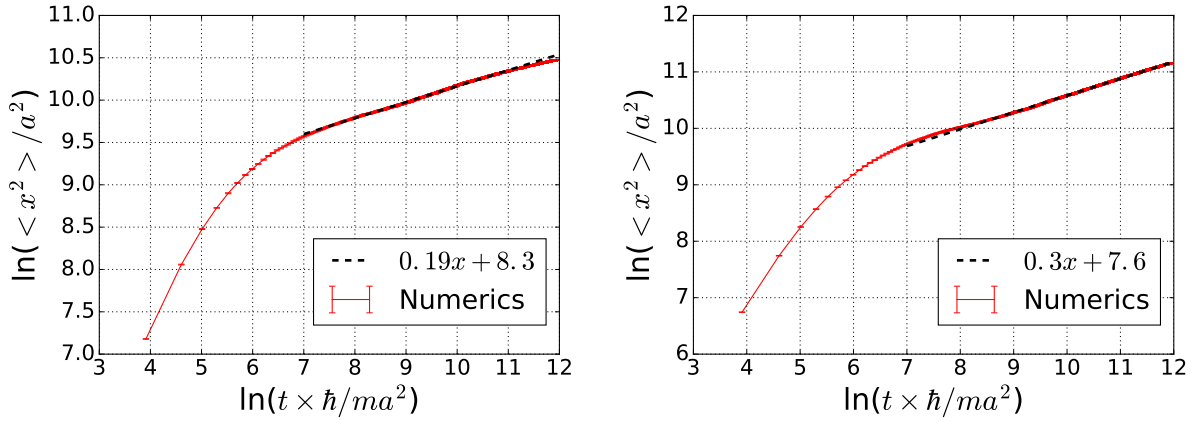

(a) $k_0 = \pi/2a$ (b) $k_0 = \pi/4a$

Figure 5.3 – Mean square displacement as a function of time, for two values of $k_0 a$. In log-log scale, the long time limit is well fitted by a straight line, hence demonstrating subdiffusion. Note however the possible deviation from subdiffusion at long times in figure a), although more work is needed to be conclusive. The associated subdiffusive exponent (α in (5.19) and slope of the line here) differs for the two values of k_0. For a) (respectively b), we have used a disorder strength $\gamma = 0.0225\ \hbar^4/m^2a^3$ (respectively $\gamma = 0.01\ \hbar^4/m^2a^3$), so that $\ell = 25a$ for both k_0 at the Born approximation (formula in caption of figure 4.9). In both cases, we have used a nonlinear strength $g = 0.5\ \hbar^2/ma$ and an initial wave packet of size $\sigma = 10a$. A time step $\delta t = 0.05\ ma^2/\hbar$ was found sufficient for both figures. The results are averaged over 3000 (1500) disorder realizations for figure a) (respectively b).

Possible interpretation

We propose to interpret the difference between the two results of figures 5.3a and 5.3b from the perspective of a wave packet exploring the energy landscape. At weak disorder, the localization length is maximal at energy $\hbar^2 k_m^2/2m$ with $k_m = \pi/2a$ [134], thus a wave packet starting with a wave vector $k_0 = \pi/2a = k_m$ can only explore energy regions where the localization length is smaller than the one at $\epsilon = \hbar^2 k_0^2/2m$ while the wave packet starting with a wave vector $k_0 = \pi/4a \neq k_m$ will expand to energy region of large localization length compared to the one at $\epsilon = \hbar^2 k_0^2/2m$. As a result, the wave packet starting with a wave vector $k_0 = \pi/4a$ spreads more rapidly than the one starting with $k_0 = \pi/2a$.

Note that in the context of many-body localization, a somewhat similar reasoning led Gornyi, Mirlin, Müeller and Polyakov to question the very possibility of many-body localization in the

continuum limit [154], for which the localization grows without bounds as the energy increases.

5.4.2 Numerical study of the energy distribution dynamics

We now come back to the primary object of this section: the dynamics of the energy distribution.

Definition

To simplify the discussion, we consider the evolution of an initial plane-wave,

$$\phi(x, y, z, t = 0) \propto e^{ik_0 x}, \tag{5.28}$$

evolving in a weak 3D Gaussian delta-correlated potential,

$$\overline{V_{\boldsymbol{r}} V_{\boldsymbol{r}'}} = \gamma \delta_{\boldsymbol{r},\boldsymbol{r}'}/a^3, \tag{5.29}$$

with $\delta_{\boldsymbol{r},\boldsymbol{r}'}$ the Kronecker delta. The motivation for considering the weakly disordered 3D case is twofold. On the one hand, we aim at describing the effect of the nonlinearity on the coherent back scattering peak in section 5.5, the latter is difficult to see in 1D, as it does not stand out from the background (see subsection 5.5.1 for more details). On the other hand, it offers a conceptual simplification by placing us on the diffusive side of Anderson transition.

Results at intermediate times

In the numerical simulations, we compute the average energy distribution using

$$P(\epsilon, t) = \overline{\langle \phi(t) | \delta(\epsilon - H) | \phi(t) \rangle} = \int_{-\infty}^{\infty} \frac{\mathrm{d}t'}{2\pi\hbar} \overline{\langle \phi(t) | e^{i(\epsilon - H)t'/\hbar} | \phi(t) \rangle}, \tag{5.30}$$

where $|\phi(t)\rangle$ is the wave function at time t and H is the full Hamiltonian (including the nonlinearity) at time t. The evolution is performed with the usual Chebyshev method (presented in section 4.3). The resulting average energy distribution at different times is shown in figure 5.4 as blue curves. The energy distribution visibly explores the energy landscape.

Note that $\epsilon = \langle \phi(t) | H | \phi(t) \rangle$ is not conserved during the nonlinear evolution. The conserved quantity is

$$E = \langle \phi(t) | \left[p^2/2 + V + g|\phi(t)|^2/2 \right] |\phi(t)\rangle = \epsilon(t) - \frac{g}{2} \int \mathrm{d}\boldsymbol{r} |\phi(\boldsymbol{r}, t)|^4. \tag{5.31}$$

However, the nonlinearity being very small, the distributions of ϵ and E are not expected to differ much. Our goal of describing the effect of the nonlinearity on the coherent back scattering peak (see subsection 5.5.1 for more details about it) led us to choose ϵ over E. We are however not quite certain that E is not more suited to the task.

Results at short times ($t \approx \tau$)

Naively, one expects the initial energy distribution to be set by the spectral function $A_{k_0}(\epsilon)$ with a given self-energy[2]:

$$P(\epsilon, t = 0^+) = A_{k_0}(\epsilon) = \frac{\left|\Im\left(\Sigma\right)\right|}{\pi} \frac{1}{\left(\epsilon - \epsilon(k_0) - \Re\left(\Sigma\right)\right)^2 + \left(\Im(\Sigma)\right)^2}, \tag{5.32}$$

[2] At short times, the momentum and energy distributions are sharply peaked, the self-energy Σ corresponds to $\Sigma(\epsilon = \hbar^2 k_0^2/2m, \boldsymbol{k} = \boldsymbol{k}_0)$. The reader not familiar with the concepts of spectral function or self-energy can find some details in section 3.1.

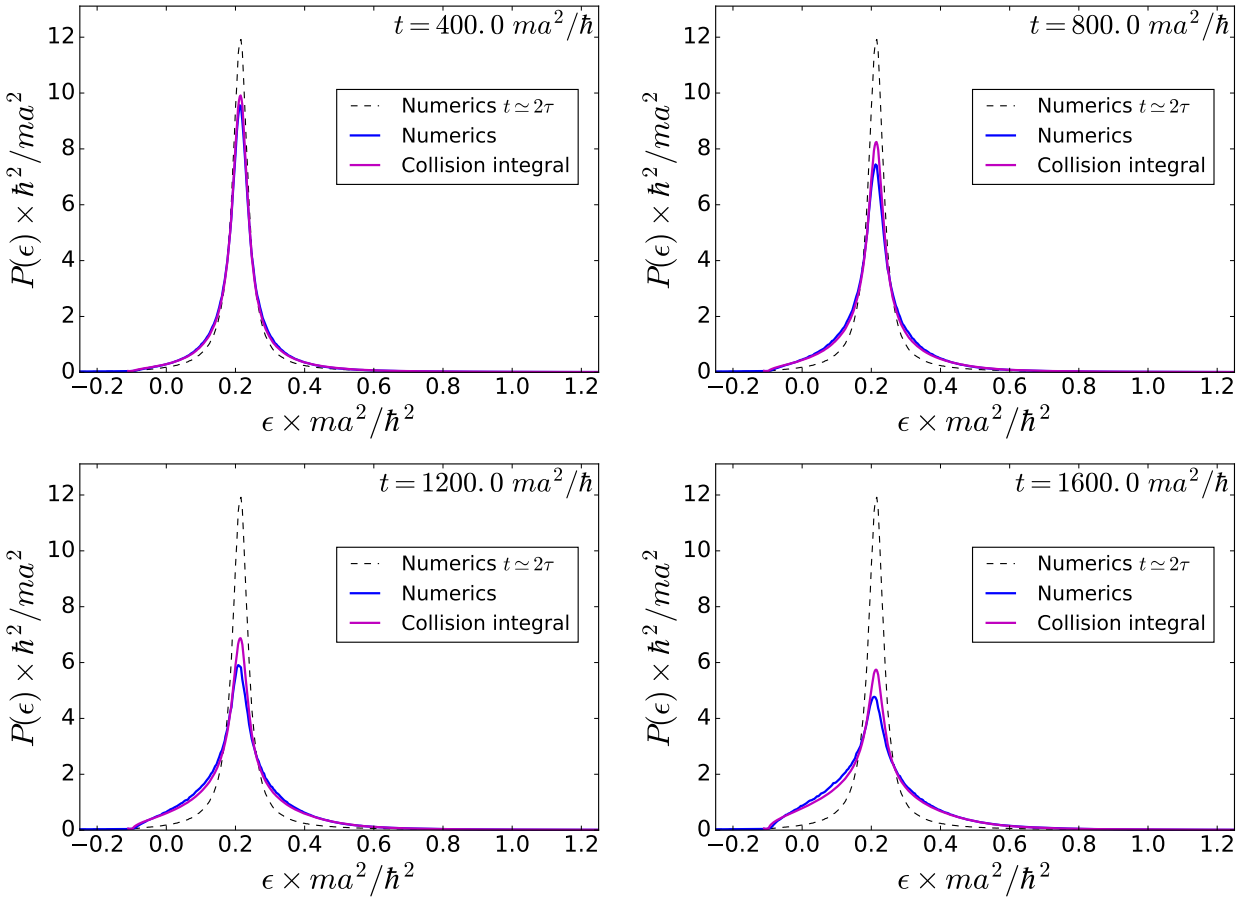

Figure 5.4 – Energy distribution at different times. The solution of the kinetic equation (5.37), is shown as magenta curves and is compared to numerical simulations shown as blue curves. The initial energy distribution (computed at time $t = 36\ ma^2/\hbar \simeq 2\tau$ as prescribed by subsection 5.4.4) is shown for comparison as a black dashed line. The parameters used in the numerical simulations can be found in the caption of table 5.1.

and to then slowly evolve through inelastic collisions on the nonlinear term of the Gross-Pitaevskii equation, not much happening at short times. Surprisingly, the numerical results present a very short-time dynamics ($t \approx \tau$) of the average energy distribution. We have characterized this short-time dynamics by fitting the average energy distribution with a time-dependent self-energy Σ_t:

$$P(\epsilon, t) = \frac{\left|\Im\left(\Sigma_t\right)\right|}{\pi} \frac{1}{\left(\epsilon - \epsilon(k_0) - \Re\left(\Sigma_t\right)\right)^2 + \left(\Im(\Sigma_t)\right)^2}. \tag{5.33}$$

The results are reported in table 5.1.

5.4.3 Short-time ($t \approx \tau$) picture: shifting and screening

In fact, at early times one needs to account for the rapid randomization of ϕ. Indeed, initially ϕ is a plane wave, thus $|\phi|^2$ does not fluctuate and $\overline{|\phi|^4} = \overline{|\phi|^2}^2$, but as ϕ gets randomized by the disorder, we expect $\overline{|\phi|^4}$ to include a fluctuating part, in addition to $\overline{|\phi|^2}^2$:

$$\overline{|\phi|^4} = \overline{|\phi|^2}^2 + \left[\overline{|\phi|^4} - \overline{|\phi|^2}^2\right] = \overline{|\phi|^2}^2 + \mathrm{var}\left(|\phi|^2\right). \tag{5.34}$$

Time ($ma^2/\hbar$)	τ ($ma^2/\hbar$)	$\Re(\Sigma)$ ($\hbar^2/ma^2$)
0	17.44 $\pm$ 0.04	$(-8.863 \pm 0.005) \times 10^{-2}$
6	18.28 $\pm$ 0.04	$(-8.475 \pm 0.005) \times 10^{-2}$
12	18.56 $\pm$ 0.04	$(-8.280 \pm 0.005) \times 10^{-2}$
18	18.68 $\pm$ 0.04	$(-8.135 \pm 0.005) \times 10^{-2}$
24	18.76 $\pm$ 0.04	$(-8.040 \pm 0.005) \times 10^{-2}$
30	18.76 $\pm$ 0.04	$(-7.975 \pm 0.008) \times 10^{-2}$
36	18.76 $\pm$ 0.08	$(-7.938 \pm 0.008) \times 10^{-2}$

Table 5.1 – Scattering mean free time $\tau = -\hbar/2\Im(\Sigma)$ and real part of the self-energy obtained numerically for various times. The simulations were performed on a 3D lattice made of 600×96^2 sites (the long direction is the one associated to $\boldsymbol{k}_0$), with a disorder strength $\gamma = 0.18\ \hbar^4/m^2a$, a nonlinearity $g/\mathrm{Vol} = 0.0075\ \hbar^2/ma^2$ and an initial wave vector $k_0 = \pi/4a$. The results are averaged over 15 disorder realizations. A time step $\delta t = 0.4\ ma^2/\hbar$ was found sufficient. The error estimates come from the fitting procedure.

The effect of this randomization corresponds to a shift of the real part of the self-energy accounting for the increase of $\overline{|\phi|^4}$ and the conserved quantity E [equation (5.31)][3]:

$$\int \mathrm{d}\epsilon P(\epsilon,t)\epsilon - \frac{g}{2}\int \mathrm{d}\boldsymbol{r}\overline{|\phi(\boldsymbol{r},t)|^4} = \epsilon(k_0) + \Re\left(\Sigma_t\right) - \frac{g}{2}\int \mathrm{d}\boldsymbol{r}\overline{|\phi(\boldsymbol{r},t)|^4} = \overline{E}. \tag{5.35}$$

Another effect takes place at short times, the screening of the random potential by the nonlinearity ensuing from the atoms preferring low potential regions to high potential ones. Effectively, the screening of the random potential reduces the self-energy (in absolute value).

Initially absent, both these effects build up rapidly, over roughly one scattering mean free time, in agreement with the results reported in table 5.1. To be a bit more quantitative, we propose to estimate the shift of the real part of the self-energy $\Re(\Sigma)$ associated to the randomization of the wave packet. Assuming that $\phi(\boldsymbol{r}, t > \tau)$ is a complex Gaussian random variable, $\mathrm{var}\left(|\phi|^2\right) = \overline{|\phi|^2}$, such that the randomization of the wave packet shifts $\Re(\Sigma)$ by approximately $0.5g/\mathrm{Vol} \simeq 4\times10^{-3}\ \hbar^2/ma^2$, i.e. roughly half of the observed shift of $\Re(\Sigma)$. In conclusion, both effects (the screening and the randomization) have a comparable effect on $\Re(\Sigma)$.

5.4.4 Intermediate-time picture: kinetic equation

We now turn to times longer than the scattering mean free time, at which the energy distribution evolves through inelastic collisions on the nonlinear potential $(g|\psi|^2)$. In the diffusive regime, it is possible to account for these inelastic collisions within a kinetic equation, via a collision integral. The latter can be derived using diagrammatic theory [56,58]. In this context, it is more convenient to use a variant of the energy distribution, f_ϵ, related to $P(\epsilon)$ [equation (5.26)], through $f_\epsilon = P(\epsilon)/\nu(\epsilon)$ with $\nu(\epsilon)$ the density of states per unit volume (DoS). The corresponding energy distribution is then normalized according to

$$\int f_\epsilon \nu(\epsilon)\mathrm{d}\epsilon = 1. \tag{5.36}$$

[3]Note that we define the real part of the self-energy with respect to the energy $\epsilon = \langle\phi(t)|H|\phi(t)\rangle$. One could work with E [equation (5.31)] instead, and the self-energy would then not be shifted by the randomization of ϕ. At this stage, this choice is arbitrary.

Surprisingly, in the case of an initial plane wave, the evolution equation for the energy distribution, f_ϵ, is closed [59, 155]:

$$\partial_t f_\epsilon = \int_{-\infty}^{\infty} \mathrm{d}\epsilon_1 \int_{-\infty}^{\infty} \mathrm{d}\epsilon_2 \; W(\epsilon;\epsilon_1,\epsilon_2)\Big[(f_\epsilon + f_{\epsilon_1+\epsilon_2-\epsilon})f_{\epsilon_1}f_{\epsilon_2} - f_\epsilon f_{\epsilon_1+\epsilon_2-\epsilon}(f_{\epsilon_1}+f_{\epsilon_2})\Big], \tag{5.37}$$

where

$$W(\epsilon;\epsilon_1,\epsilon_2) = \frac{m^3 g^2}{8\pi^3\hbar^7\nu_\epsilon}\left(2\nu_1 + |\nu_1+\nu_2+\nu_3-\nu_4| - |\nu_1-\nu_2-\nu_3+\nu_4|\right), \tag{5.38}$$

with $(\nu_1,\nu_2,\nu_3,\nu_4)$ being a permutation of $(\nu_{\epsilon_1},\nu_{\epsilon_2},\nu_\epsilon,\nu_{\epsilon_1+\epsilon_2-\epsilon})$ such that $\nu_1 \le \nu_2 \le \nu_3 \le \nu_4$. In fact, the energy distribution contains all the necessary information to describe the inelastic collisions. This is somewhat reminiscent of the spectral function, the energy distribution of a plane wave, containing all information about the elastic collisions (mean free path and time), as we have seen in subsection 3.1.4. The disorder enters in equation (5.37) through the DoS, and, more importantly, in the initial condition which is set by the spectral function [equation (5.32)].

The short-time effects discussed in subsection 5.4.3 are not included in equation (5.37), which describes the evolution of the energy distribution at times $t \gtrsim \tau$. In fact, they only affect the initial energy distribution to be fed into equation (5.37). The initial energy distribution is set by the self-energy, through the spectral function [equation (5.32)]. We thus take the short-time effects into account by simply using a corrected self-energy in (5.32), that corresponds to the self-energy at $t \simeq 2\tau$.

5.4.5 Density of states

To integrate equation (5.37) and compute the average energy distribution at time t, one needs the DoS. To compute it, we assume that is not affected by the nonlinearity, which should be the case as long as the latter is small [156]. The potential being delta-correlated [equation (5.29)], various approximate strategies can be employed, ranging from the Born approximation introduced in section 3.1 to more sophisticated methods, the self-consistent Born approximation (SCBA) and the coherent potential approximation (CPA) [109, 157, 158]. The corresponding formulas are given in appendix 5.A. To attest the accuracy of these approximate methods, we compare them to the numerically obtained DoS in figure 5.5, we also show in green the DoS of the disorder-free lattice for comparison. The numerical DoS follows from [159]

$$\nu(\epsilon) = \langle \mathbf{r}=0|\,\overline{\delta\left(\epsilon - H\right)}\,|\mathbf{r}=0\rangle = \int_{-\infty}^{\infty} \frac{\mathrm{d}t}{2\pi\hbar} e^{i\epsilon t/\hbar}\overline{\langle \mathbf{r}=0|\,e^{-iHt/\hbar}\,|\mathbf{r}=0\rangle}, \tag{5.39}$$

with the convention

$$|\mathbf{r}=0\rangle = \frac{\delta_{\mathbf{r},0}}{a^{3/2}}, \tag{5.40}$$

where a is the lattice spacing and $\delta_{\mathbf{r},0}$ is the Kronecker delta. The evolution is performed with the usual Chebyshev method (see section 4.3 for more details). As visible in figure 5.5, the CPA approximation describes very well the numerical DoS. It will thus be our choice for the integration of equation (5.37).

5.4.6 Comparison with numerics

To estimate the accuracy of equation (5.37), we solve it numerically, using the CPA DoS and taking into account the short-time effects as prescribed in subsection 5.4.4, and compare the solution to numerical simulations in figure 5.4. At this stage, we had to divide W [equation (5.38)] by 2 for the solution of (5.37) to match our numerical simulations. We presume that a factor 2 is missing in

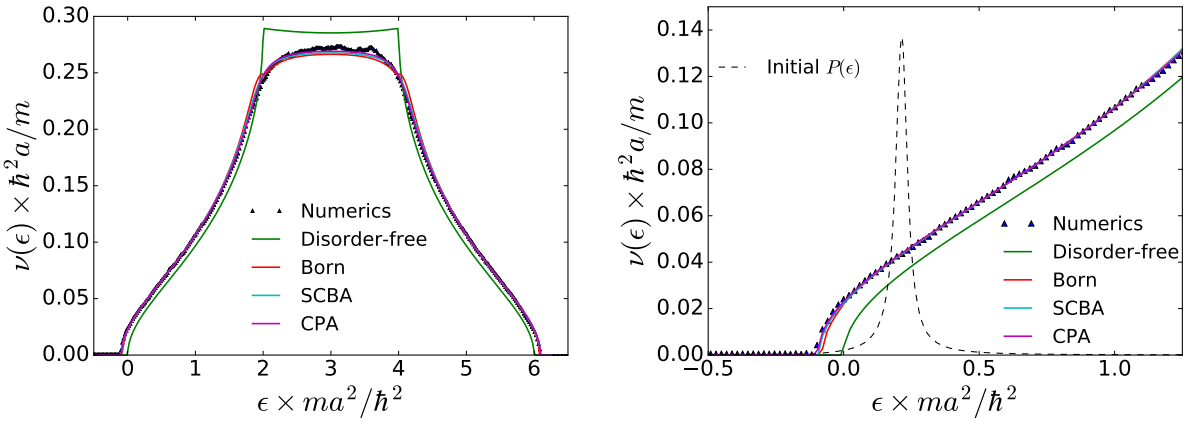

(a) (b)

Figure 5.5 – Density of states as a function of energy. Different approximate methods for the density of states are compared to numerical results. Figure a) presents the full energy range, while figure b) focus is on the small energy part. In figure (b), the initial energy distribution is also shown, with an arbitrary scale along the y-axis. The numerical simulations were performed on a 3D lattice made of 120^3 sites, with a disorder strength $\gamma = 0.18\ \hbar^4/m^2a$ and averaged over 1000 disorder realizations.

equation (5.38). Figure 5.4 shows what the evolution of the energy distribution is well described by the collision integral [equation (5.37)].

The energy distribution tends to explore the energy landscape on a time scale $\tau_g = \hbar^3/mg^2$. This time scale differs from the time scale found in section 5.3 for the alteration of the quantum boomerang effect, which is proportional to $1/g$. The quantum boomerang effect appears more sensitive to interactions than the energy distribution, we postulate that it is affected by processes leaving the energy distribution unchanged. This difference can be understood in the framework of decoherence and dissipation (see [160] and references therein), decoherence processes affect only the quantum boomerang effect, and dissipation is responsible for the slower dynamics in energy.

5.4.7 Infinite-time equilibrium

At infinite time, we expect the system to reach an equilibrium state, with a thermal Rayleigh-Jeans distribution maximizing entropy [161,162]:

$$f_\epsilon^{\mathrm{eq}} = \frac{1}{\Omega}\frac{T}{\epsilon - \mu}, \tag{5.41}$$

where Ω is the volume of the system, T and $\mu(\leq 0)$ are analogues of the usual temperature and chemical potential respectively. Plugging (5.41) into the collision integral (5.4.4), one indeed finds $\partial_t f_\epsilon^{\mathrm{eq}} = 0$ [60]. Distribution (5.41) is generally assumed to hold up to some cutoff, e.g. $\epsilon_{\max} = T + \mu$ [60, 163] (beyond which (5.41) starts to deviate from the Bose-Einstein distribution [78]). Unfortunately, this long time regime is beyond the reach of our numerical simulations.

Note that the entropy whose maximization leads to (5.41) is defined with plane-wave states [161], this is a good approximation since we are on the diffusive side of Anderson transition. This choice is consistent with the collision integral (5.37), which is derived neglecting localization effects. The case of strongly localized 1D chains was considered in [57, 164], where they assume a Boltzmann distribution.

5.5 Nonlinearity and the coherent back scattering peak

5.5.1 Coherent back scattering peak

In section 5.4, we have studied how the energy distribution of an initial plane wave evolves in a 3D random potential through the nonlinear term of the Gross-Pitaevskii equation [equation (5.4)]. The energy distribution is not easily measurable in cold-atom experiments, one often prefers to measure the related momentum distribution [40]. At times longer than the scattering mean free time, one naively expects no preferred direction for the momentum, and thus an isotropic momentum distribution given by the projection of the energy distribution on the momentum space:

$$\overline{|\phi(\boldsymbol{p},t)|^2} = \int \mathrm{d}\epsilon A_p(\epsilon) f_\epsilon(t), \tag{5.42}$$

where the spectral function $A_p(\epsilon)$ connects energy and momentum in the random potential (see subsection 3.1.4 for more details).

Equation (5.42) relies on a classical point of view and neglects an important contribution to the momentum distribution, the coherent back scattering (CBS) peak. To exhibit it, let us expand on the discussion of the weak localization phenomenon in subsection 1.1.1. It was argued there that two classes of paths contributing to the real space density survive the disorder averaging. The momentum distribution can be similarly decomposed as a sum of paths, with however different initial and final points for the wave function and its conjugate, according to

$$\overline{|\phi(\boldsymbol{p},t)|^2} = \frac{1}{\hbar^2}\int \mathrm{d}\boldsymbol{r}_3\mathrm{d}\boldsymbol{r}_4 e^{-i\boldsymbol{p}.(\boldsymbol{r}_3-\boldsymbol{r}_4)/\hbar}\overline{\phi(\boldsymbol{r}_3,t)\phi^*(\boldsymbol{r}_4,t)}. \tag{5.43}$$

Figure 5.6 adapts figure 1.1 to the present case by showing the two main paths that contribute to $\overline{\phi(\boldsymbol{r}_3,t)\phi^*(\boldsymbol{r}_4,t)}$. Assuming an initial plane wave with wave vector $\boldsymbol{k}_0$ and performing the Fourier transform, the Diffuson brings an isotropic contribution, described by equation (5.42) whereas the Cooperon contribution is strongly anisotropic and peaked around $-\hbar\boldsymbol{k}_0$ [165], as visible in figure 5.7. If phase coherence is fully preserved, the peak reaches twice the background height [165].

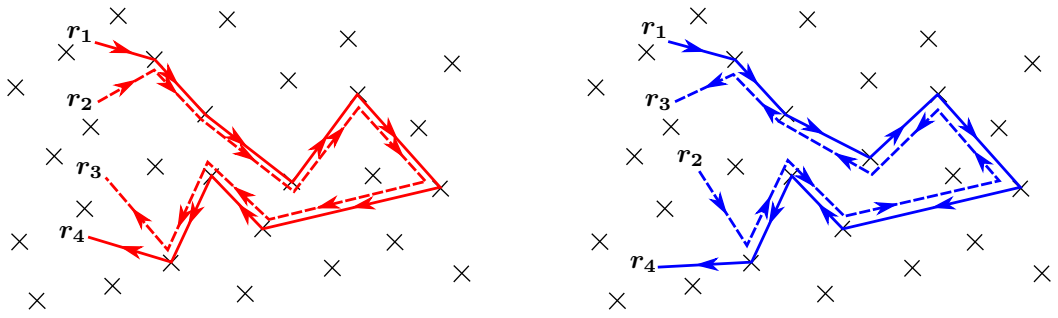

(a) Diffuson (b) Cooperon

Figure 5.6 – Two kinds of pair of scattering paths contributing to $\phi(\boldsymbol{r}_3,t)\phi^*(\boldsymbol{r}_4,t)$. Between the first and last scattering events, both paths follow the same sequence of scattering events by either propagating (a) in the same direction or (b) in opposite directions.

The present section is devoted to the effect of interactions on the CBS peak.

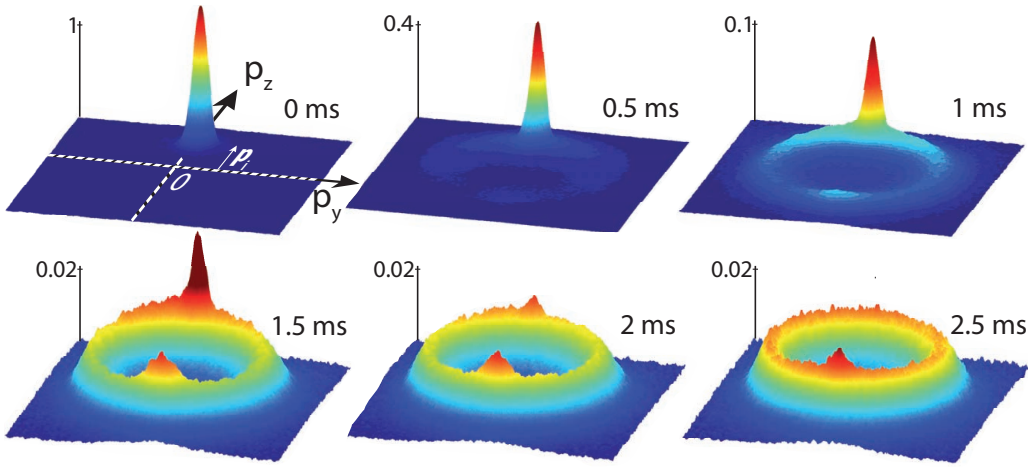

Figure 5.7 – Figure from [7] showing the experimentally measured momentum distribution after different propagation times in a 2D disordered potential. The initial momentum distribution (first image) is sharply peaked around $\hbar \boldsymbol{k}_0$. After few scattering mean free times (last image), the momentum distribution presents an isotropic part (associated to the Diffuson) and the coherent back scattering (CBS) peak around $-\hbar \boldsymbol{k}_0$ (associated to the Cooperon). It should be mentioned that another peak, the coherent forward scattering peak, is expected at longer times, when the localization regime is reached [43, 166]. Note that the situation is similar in three dimensions, with a spherical isotropic shell and a peak at $-\hbar \boldsymbol{k}_0$.

5.5.2 Numerics

To study the effects of interactions on the CBS peak, we propagate an initial plane wave exactly as we did in section 5.4, but keep track of the momentum distribution

$$|\phi(\boldsymbol{p}, t)|^2 = \left| \frac{1}{\hbar} \int \mathrm{d}\boldsymbol{r} e^{-i\boldsymbol{p}.\boldsymbol{r}/\hbar} \phi(\boldsymbol{r}, t) \right|^2 , \tag{5.44}$$

instead of the energy distribution. We define the CBS peak contrast as the height of the distribution at the top of the peak (located at $\boldsymbol{p} = -\hbar \boldsymbol{k}_0$) divided by the background amplitude, measured at a momentum $\hbar k_0$ in a direction orthogonal to $\hbar \boldsymbol{k}_0$. We show in figure 5.8 the numerically obtained CBS peak contrast. In the non interacting limit ($g = 0$), the CBS peak builds up rapidly (over few scattering mean free times) and saturates at twice the background as expected. In the nonlinear case ($g \neq 0$), the CBS does not build up completely at short times and saturates well below twice the background before decreasing on a much longer time scale.

5.5.3 Physical picture

The Cooperon diagrams of figure 5.6b are built by letting the dashed path follow the same trajectory as the continuous path but in the opposite direction, in order to guarantee that the phase accumulated along the continuous path is canceled by the one accumulated along the dashed path. In doing so, we implicitly assumed that on each segment the quasi-particles are the same for the continuous and dashed paths (i.e. same energy and self-energy, see section 3.1 for more details). This assumption may be challenged by the nonlinear time-dependent term of the Gross-Pitaevskii equation (5.4).

To make it more clear, we reproduce the diagrams in figure 5.6b, displaying the time as a color (going from blue at short times to red at long times) in figure 5.9. It appears that the phase cancellation on each segment is hampered by the mechanisms introduced in subsections 5.4.4

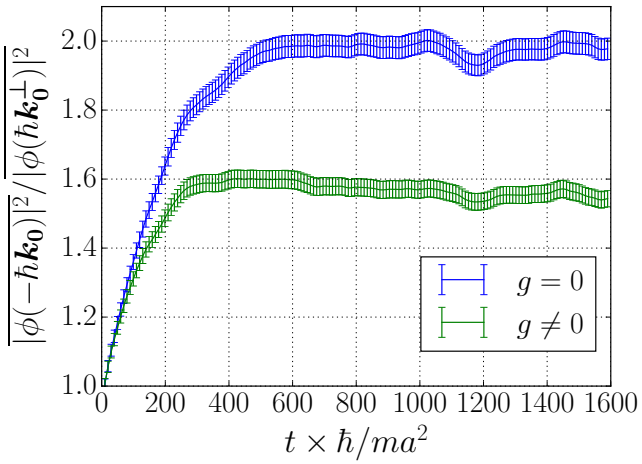

Figure 5.8 – Coherent back scattering (CBS) peak contrast as a function of time, with statistical error bars. We define the CBS peak contrast as the height of the distribution at the top of the peak ($\overline{|\phi(-\hbar\boldsymbol{k}_0)|^2}$) divided by the background amplitude ($\overline{|\phi(\hbar\boldsymbol{k}_0^\perp)|^2}$), where $\boldsymbol{k}_0^\perp.\boldsymbol{k}_0 = 0$ and $|\boldsymbol{k}_0^\perp| = k_0$. The nonlinear case ($g \neq 0$), shown in green, is compared to the linear one ($g = 0$), shown in blue. The simulations were performed on a 3D lattice made of 600×96^2 sites (the long direction is the one associated to $\boldsymbol{k}_0$), with a disorder strength $\gamma = 0.05\ \hbar^4/m^2a$ ($\tau \approx 71\ ma^2/\hbar$) and an initial wave vector $k_0 = \pi/4a$. The results are averaged over 5000 disorder realizations. In the nonlinear case, we have used a nonlinearity $g/\mathrm{Vol} = 0.004\ \hbar^2/ma^2$, and a time step $\delta t = 1.6\ ma^2/\hbar$.

and 5.4.3. On the one hand, as a result of the short-time effects of subsection 5.4.3, different quasi-particles are associated to the continuous and dashed paths in the vicinities of the starting and ending points. This affects all contributions to the Cooperon and results in the partial rise of the CBS peak at short times[4]. On the other hand, the energy redistribution of subsection 5.4.4 may change the energy after some time. This effect takes place on a much longer time scale: in the weak nonlinearity limit we are considering, many scattering events on the disordered potential are needed before the energy redistribution becomes effective. We expect this effect to eventually destroy the CBS peak as inelastic collisions add up. To summarize, the short-time effects are responsible for the CBS peak not rising to twice the background at short times ($t \approx \tau$), and the energy redistribution to the slow reduction of the CBS contrast on a much longer time scale.

5.6 Conclusion

In this chapter, we have touched upon the effect of weak interactions on the evolution of condensed bosonic gases in disordered potentials. This study consisted of three parts. We have first shown how the complex quantum many-body dynamics approximately reduces to a nonlinear equation on a classical field. We have then developed a numerical scheme to integrate said equation. In a third stage, we have applied the numerical method to various physical situations.

The main conclusions that we have drawn from this study follows. First, acting similarly to a decoherence process (with a decoherence time proportional to $\hbar\xi/g$), the nonlinearity seems to interrupt the quantum boomerang effect and prevent the full retroreflection of wave packets launched

[4]Continuing on the remark of footnote 3, we would like to stress that at the moment, it is not clear to us which definition of the couple energy/real part of the self-energy is relevant for the CBS peak. Nevertheless, both definitions lead to the same qualitative conclusion of a shift of the self-energy at short times, only the amplitude of the shift is in question.

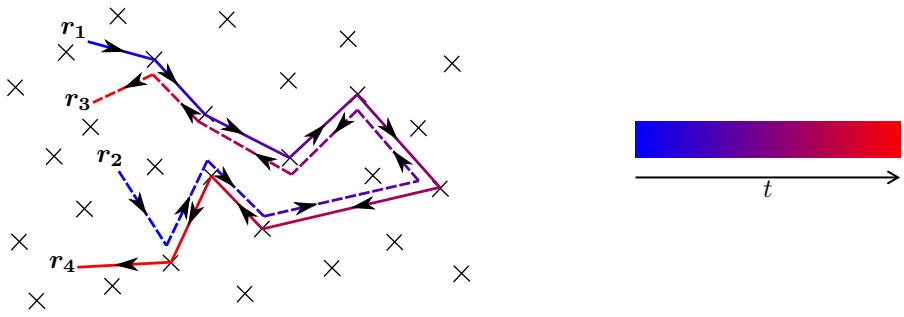

Figure 5.9 – Couple of scattering paths of Cooperon type, with time shown as a color (going from blue at short times to red at long times).

with finite velocity. Second, we have shown that the nonlinearity allows the wave packet to explore the energy landscape. Given an initial plane wave, the dynamics of the energy distribution obeys a closed equation and inelastic collisions happen on a time scale $\tau_g = \hbar^3/mg^2$. Third these inelastic collisions hit the CBS peak and are expected to eventually lead to its destruction. Fourth, the CBS peak is also affected by short-time effects, the screening of the disordered potential by the nonlinearity as well as the shift of the real part of the self-energy associated to the randomization of the wave packet[5]. As a result, the CBS peak does not rise to twice the background height at short times.

While we have underlined the physical picture behind these phenomena, our work was essentially numerical. Further analytical characterization of the effects introduced in this chapter should provide deeper insights and offer interesting perspectives for future work.

Appendix 5.A Approximations of the density of states

In this appendix, we give the formulas for the density of states (DoS) used in subsections 5.4.5 and 5.4.6. Four approximations of the DoS are presented, *a priori* in increasing order of accuracy (disorder-free, Born, SCBA and CPA). These formulas are taken from [109] and apply to delta-correlated potentials, for which the self-energy can be assumed to depend only on energy [$\Sigma(\boldsymbol{k}, \epsilon) = \Sigma(\epsilon)$].

5.A.1 Density of states in term of self-energy

The DoS is computed through the average Green function $\overline{G(\epsilon)}$ [section 3.1]:

$$\nu(\epsilon) = -\frac{1}{\pi}\Im\left[\overline{G(\epsilon)}\right], \tag{5.45}$$

which is in turn expressed in terms of the self-energy $\Sigma(\epsilon)$ [section 3.1]:

$$\overline{G(\epsilon)} = \int_{-\pi}^{\pi} \frac{\mathrm{d}^3k}{(2\pi)^3} \frac{1}{\epsilon - \epsilon(\mathbf{k}) - \Sigma(\epsilon)}, \tag{5.46}$$

where $\epsilon(\mathbf{k})$ is the lattice dispersion relation [$\epsilon(\mathbf{k}) = (3 - \cos(k_x a) - \cos(k_y a) - \cos(k_z a))\hbar^2/ma^2$]. The integral over $\boldsymbol{k}$ can be performed to express $\overline{G(\epsilon)}$ as [167]

$$\overline{G(\epsilon)} = \frac{P(6/E)}{E}, \text{ where } E = \frac{2ma^2}{\hbar^2}\left[\epsilon - \Sigma(\epsilon)\right] - 6 \text{ and } P(z) = \frac{1 - 9\xi^4}{(1-\xi)^3(1+3\xi)}\left[\frac{2}{\pi}K(k_1)\right]^2. \tag{5.47}$$

[5]The effect of the randomization of the wave packet on the CBS peak should be taken with a grain of salt, see footnote 4.

Here ξ and k_1 are functions of z defined as

$$\xi(z) = \left(\frac{1-\sqrt{1-z^2/9}}{1+\sqrt{1-z^2}}\right)^{1/2}, \qquad k_1(z)^2 = \frac{16\xi^3}{(1-\xi)^3(1+3\xi)}, \tag{5.48}$$

and K is the complete elliptic integral of the first kind.

5.A.2 Approximations of the self-energy

The simplest approximation is to ignore the disordered potential and set Σ to 0, hence recovering the disorder-free DoS:

$$\nu^{\text{free}}(\epsilon) = -\frac{1}{\pi}\Im\left[G_0(\epsilon)\right], \tag{5.49}$$

where $G_0(\epsilon)$ is the disorder-free Green function (which can be deduced from $\overline{G(\epsilon)}$ by setting Σ to 0).

Alternatively, one can compute the self-energy perturbatively in the disorder (see section 3.1 for more details). At lowest order (Born approximation), the self-energy writes

$$\Sigma(\epsilon) = V_0^2 G_0(\epsilon). \tag{5.50}$$

A slight, but simple, improvement is the self-consistent Born approximation (SCBA) where the disorder-free Green's function in equation (5.50) is modified self-consistently, leading to

$$\Sigma(\epsilon) = V_0^2 G_0(\epsilon - \Sigma(\epsilon)). \tag{5.51}$$

$\Sigma(\epsilon)$ can then be computed numerically, e.g. with a root-searching algorithm.

A supposably better approximation scheme is the coherent potential approximation (CPA) [157, 158], which leads to an equation involving the potential on-site distribution $P(V)$ [here $P(V) = \exp(-V^2/2V_0^2)/V_0\sqrt{2\pi}$]:

$$\int \mathrm{d}V \frac{V-\Sigma(\epsilon)}{1-(V-\Sigma(\epsilon))G_0(\epsilon-\Sigma(\epsilon))} P(V) \;=\; 0. \tag{5.52}$$

Again, a root-searching algorithm allows to compute $\Sigma(\epsilon)$ numerically.

Chapter 6

The kicked rotor, a paradigmatic simulator for Anderson localization

We have so far discussed Anderson localization and its manifestations in the dynamics of particles evolving in random potentials. Such systems do not have the exclusivity though, Anderson localization also appears in deterministic models. In this chapter, we consider an example of deterministic model displaying Anderson localization, the kicked rotor. This model has been of great experimental importance [168], in particular in the context of the early observations with cold-atoms of Anderson localization in one dimension [169], of the Anderson transition in three dimensions [36] and more recently of Anderson localization in two dimensions [39]. Besides these experimental successes, the kicked rotor has also constituted theoretical challenges, starting from the numerical observation of dynamical localization [170] and its connection to Anderson localization through a mapping onto a disorder model [171]. Later the connection was also established through a supersymmetric field theory [172]. More recently, the emergence of topological features in kicked-rotor models for particle with half-integer spins was reported [173–175].

The aim of this chapter is to show that many areas are still to be explored. We start by briefly introducing the kicked rotor and its connection with Anderson localization in section 6.1. Section 6.2 introduces the three simplest universality classes and some of their universal properties. From these notions, section 6.3 challenges common wisdom by exploring the possibility of a spinless kicked rotor in the symplectic class. In section 6.4, we start by introducing an important possibility offered by the kicked rotor, the simulation of high dimensions with specific 1D quasi-periodically modulated kicked rotors. This possibility is then applied to a kicked rotor belonging to the symplectic universality class. We conclude section 6.4 by investigating the properties of a new type of quasi-periodically modulated kicked rotor.

Note that this chapter presents works in progress.

6.1 From chaos to disorder

The kicked-rotor model describes the motion of a particle living on a circle of length 2π and periodically kicked. The corresponding Hamiltonian takes the form

$$H = \frac{p^2}{2} + V(\theta) \sum_n \delta(t - n), \tag{6.1}$$

with $p = -i\hbar\partial_\theta$. The single-valuedness of the wave function quantizes the momentum in units of $\hbar$ ($p = l\hbar$ with $l \in \mathbb{Z}$). A commonly studied kicked rotor has the simple form

$$H = \frac{p^2}{2} + K\cos(\theta)\sum_n \delta(t-n), \tag{6.2}$$

i.e. $V(\theta) = K\cos(\theta)$.

In cold-atomic realizations of model (6.1) [168], the particle does not strictly live on a circle, but rather in a virtually infinite 1D space parametrized by x, and is kicked with a periodic optical potential (of period $2\pi/k$). The Hamiltonian takes the form

$$H = \frac{p^2}{2m} + V(kx)\sum_n \delta(t-n\tau), \tag{6.3}$$

with V a periodic function of period 2π. The periodicity of the potential allows one to write the dynamics on a circle by application of the Bloch theorem. This procedure shifts the momentum, quantized in integer units of $\hbar k$ on the circle ($\theta \in [-\pi/k, \pi/k[$), by a quasi-momentum $\beta\hbar k$ ($\beta \in [0,1[$):

$$H = \frac{(k\hbar)^2(l+\beta)^2}{2m} + V(k\theta)\sum_n \delta(t-n\tau). \tag{6.4}$$

The quasi-momentum β is conversed during the evolution. The theoretician model (6.1) corresponds to using the units $m = \tau = k = 1$. In these units, $\hbar$ is proportional to $m/k^2\tau$. In practice, it can thus effectively be experimentally tuned via τ.

Throughout out this chapter, we work in units $m = \tau = k = 1$.

6.1.1 Classical chaotic dynamics

Let us start by recalling what is the classical dynamics associated to (6.2). From Hamilton equations, one can express the classical dynamics as Chirikov's standard map [176]:

$$p_{t+1} = p_t + K\sin(\theta_t), \tag{6.5}$$
$$\theta_{t+1} = \theta_t + p_{t+1}, \tag{6.6}$$

where θ_n (p_t) is the position (momentum) of the classical particle at time t (right before a kick). As it turns out, Chirikov's standard map is chaotic for large enough K [176]. The associated extreme sensitivity on the initial conditions results in a deterministic diffusion process in momentum space: for large enough K and at long enough times, the average of p^2 over the initial angle θ grows linearly in time [176]. With respect to Anderson localization, this diffusion process in momentum space plays the role of the classical real space diffusion of disorder models.

6.1.2 Quantum evolution: Floquet operator

At the quantum level, the dynamics is similarly obtained by applying repeatedly the Floquet operator

$$F = U_{\text{kinetic}}U_{\text{kick}}, \tag{6.7}$$

which governs the evolution over one period. Here, U_{kick} describes the kick [it is the quantum counterpart of (6.5)] and U_{kinetic} describes the free propagation between kicks [it corresponds to (6.6)]. For the kicked rotor (6.2), they are respectively given by

$$U_{\text{kick}} = \exp\left(-iK\cos(\theta)/\hbar\right) \quad \text{and} \quad U_{\text{kinetic}} = \exp\left(-ip^2/2\hbar\right). \tag{6.8}$$

6.1.3 Quantum evolution: pseudo-random kicked rotor

We now turn to the kicked rotor (6.4), relevant for cold-atom experiments. It is useful to express U_{kick} and U_{kinetic} in the momentum basis. The momentum being quantized in units of $\hbar$, we parametrize the momentum basis by integers l: $p\,|l\rangle = l\hbar\,|l\rangle$. On the one hand, the kick changes the momentum, and is thus non diagonal:

$$\langle l|U_{\text{kick}}|l'\rangle = \int_{-\pi}^{\pi} \mathrm{d}\theta e^{-iK\cos(\theta)/\hbar} e^{-i(l-l')\theta} = i^{l'-l} J_{l'-l}(K/\hbar), \tag{6.9}$$

where $J_{l'-l}$ denotes the $(l'-l)^{\text{th}}$ Bessel function of the first kind. On the other hand, U_{kinetic} is diagonal:

$$\langle l|U_{\text{kinetic}}|l'\rangle = \exp\left(-i\hbar(l+\beta)^2/2\right)\delta_{l',l}, \tag{6.10}$$

with $\delta_{l',l}$ the Kronecker delta.

Let us now consider the difference between two consecutive phases of (6.10):

$$\frac{\hbar}{2}\left[(l+1+\beta)^2 - (l+\beta)^2\right] = \hbar l + \hbar\beta + \hbar/2. \tag{6.11}$$

In the limit $K/\hbar \gg 1$, (6.9) populates large momenta, such that two consecutive phases typically differ by much more than 2π. Alternatively, the same holds true when $\hbar \gg 1$. In either one of the two limits, $\hbar(l+\beta)^2/2$ in (6.10) is essentially equivalent to a pseudo-random momentum-dependent phase:

$$\langle l|U_{\text{kinetic}}|l\rangle \approx \exp\left(-i\phi_l\right), \quad \phi_l \in [0, 2\pi[, \tag{6.12}$$

with different realizations of the phases depending on β [177, 178]. In experiments, many β components are initially populated such that the measurements can be viewed as averaged over β [179].

In the rest of the chapter, we approximate the ϕ_l of equation (6.12) by uniformly distributed random phases. Within this approximation, $\hbar$ only appears in the kick term and can thus be absorbed in the kick strength: we set it to 1 to lighten the notations. The reason for using this approximation is essentially conceptual, it is used to bring out the effects discussed and facilitate their understanding. The consistency of the results for a pseudo-random sequence is systematically checked numerically, with the exception of the results presented in figure 6.6. Note that this approximation is only valid for $\hbar$ values incommensurate with π (e.g. for $\hbar = 4\pi$, two consecutive phases differ only by $\hbar\beta$ $[2\pi]$, which can be very small) [180, 181].

6.1.4 From classical diffusion to localization

In the spirit of what we have done in section 1.1 for disordered systems, we write the quantum probability to go from momentum p_1 to momentum p_2 in a time span t as a sum over classical paths weighted by complex numbers A_i (averaging over the quasi-momentum β is implied):

$$P(p_1 \to p_2, t) = \left|\sum_{\text{path } i} A_i\right|^2 = \underbrace{\sum_{\text{paths i}} A_i A_i^*}_{\text{classical}} + \underbrace{\sum_{\text{paths i}\neq\text{j}} A_i A_j^*}_{\text{quantum}}. \tag{6.13}$$

With only the so-called "classical" contribution, the momentum space dynamics would be diffusive. Following the reasoning of section 1.1, to this contribution we should add the phaseless "quantum" contributions, among which the important Cooperon contribution, built from a path i and its time-reversed counterpart j. In a way, the chaotic properties of the classical dynamics select the classical paths, and thus play a role similar to disorder. In close analogy with disorder models (see section 1.1

for more details), the accumulation of Cooperon loops[1] leads to localization: the classical momentum space diffusion is stopped at long times and replaced by localization [182].

These perturbative similarities between the kicked rotor and disordered systems can be formalized through a mapping of the kicked rotor onto a 1D lattice with pseudo-random on-site potential [171]. The equivalence between the kicked rotor and disorder models can also be shown through a supersymmetric field theory [172]. The latter method connects the kicked rotor to quasi-1D disorder models, with thus an important difference with respect to the 1D disorder models of chapter 4, the presence of a diffusive regime at short times.

6.2 Universality classes and random matrix theory

6.2.1 From a perturbative perspective

As discussed in subsection 6.1.4, the Cooperon, formed by coupling a path and its time-reversed counterpart, plays an important role in the transport properties. It is based on time-reversal symmetry, thus suggesting that this symmetry plays a central role. In the particular case of the kicked rotor, for which the Cooperon is built in momentum space, the relevant time-reversal symmetries are combinations of spatial parities and conventional time-reversal symmetries [183]:

$$\begin{aligned} &t \to t_0 - t, \\ &p \to p, \\ &\theta \to \theta_0 - \theta, \end{aligned} \tag{6.14}$$

with arbitrary t_0 and θ_0. The kicked rotor (6.2) clearly has this symmetry (e.g. with $t_0 = \theta_0 = 0$), it thus belongs to the so-called orthogonal class and the Cooperon is nonzero. When all time-reversal symmetries of type (6.14) (i.e. for all t_0 and θ_0) are broken, the system belongs to the unitary class and the Cooperon is zero.

In the case of particles with half-integer spin, the situation is somewhat more subtle, with the time-reversal symmetry having different effects depending on the presence of additional geometrical symmetries. We come back to these subtleties in subsection 6.2.2. For now, we just note that when the only symmetry is of the form

$$\begin{aligned} &t \to t_0 - t, \\ &p \to p, \\ &\theta \to \theta_0 - \theta, \\ &\boldsymbol{S} \to -\boldsymbol{S}, \end{aligned} \tag{6.15}$$

where $\boldsymbol{S}$ is the spin, the associated kicked rotor belongs to the symplectic class [184] and the Cooperon is present, although it manifests itself as an *antilocalization* contribution (we come back to this point in subsection 6.3.1).

Based on the interplay between Cooperon and time-reversal symmetries, we distinguish three classes. First the orthogonal class, for spinless kicked rotors invariant under a time-reversal symmetry, featuring a Cooperon inhibiting transport. Second the unitary class, for spinless kicked rotors without any time reversal invariance, for which the Cooperon is irrelevant. Third the symplectic class, for spin-1/2 particle with time-reversal symmetry of type (6.15) as only symmetry, featuring a Cooperon enhancing transport.

[1] Note that other more complicated interferential contributions also play an important role for localization [22]. They also have analogues in disorder models [22].

6.2.2 Universal properties and random matrix theory

Generalities

The present subsection aims at pointing out universal properties associated with each class, based on the framework of random matrix theory. The idea behind random matrix theory is that local spectral properties of disordered or quantum chaotic Hamiltonians[2] are universal and depend only on specific symmetries of the Hamiltonian. As an example, given the ordered eigenvalues $(\lambda_1, \lambda_2, \ldots, \lambda_n)$ of an Hamiltonian, the distribution of the level spacings $(s_1 = \lambda_2 - \lambda_1, s_2 = \lambda_3 - \lambda_2, s_{n-1} = \lambda_n - \lambda_{n-1})$ is universal, provided the level spacings are expressed in units of the local mean level spacing $(\langle s_i \rangle)$. To find the corresponding universal properties, one uses ensembles of random matrices.

Random matrices were introduced by Wigner to model the nuclei of heavy atoms [185]. This fruitful idea then spread to many fields, from disordered and quantum chaotic systems to two-dimensional gravity and string theory [186]. Perhaps more surprisingly, it was also found useful in number theory, to study the distribution of zeros of the Riemann zeta function [187].

In this thesis, we consider only a particular class of random matrix ensembles, the so-called Dyson ensembles, which are ensembles of Hermitian matrices featuring statistically independent entries, with only one possible symmetry: time reversal. Note that in the context of disordered and quantum chaotic systems, other random matrix ensembles play an important role, they include the possibility of other symmetries [188, 189].

In the following two subsections, we discuss the different random matrix ensembles describing systems with and without time reversal symmetry. The discussion follows the book by Haake [123]. For the sake of brevity, we only gather here some important results for the upcoming section 6.3, and refer the reader to [123] for a more thorough discussion.

Hamiltonians not invariant under time reversal

Before exploring the consequences of time reversal symmetry on the local spectral properties of disordered or quantum chaotic Hamiltonians, let us consider the non-symmetric case. Concretely speaking, we want to define the random matrix ensemble that describes a given disordered or chaotic Hamiltonian featuring no time reversal symmetry. For simplicity, we assume that the random matrix ensemble has statistically independent entries.

To characterize this random matrix ensemble, we need to identify under which transformations it should be statistically invariant. A generic transformation changes the Hamiltonian H to $H' = AHA^{-1}$. Since no time reversal symmetry applies here, the only requirement is that the transformation should retain Hermiticity:

$$H'^{\dagger} = (AHA^{-1})^{\dagger} = AHA^{-1} \Leftrightarrow \left[H, AA^{\dagger}\right] = 0. \tag{6.16}$$

The general transformations for non-time-reversal invariant systems are thus unitary, up to an irrelevant global factor. For $N \times N$ matrices, they form the $U(N)$ group.

Only one random Hermitian matrix ensemble has statistically independent entries and is statistically independent under $U(N)$ transformations, the Gaussian unitary ensemble [190]. This ensemble of Hermitian matrices has real (resp. complex) statistically independent Gaussian (resp. non-)diagonal entries[3].

[2] By quantum chaotic Hamiltonian, we mean a quantum Hamiltonian whose classical counterpart displays a chaotic dynamics.

[3] Of course, strictly speaking, an Hermitian matrix cannot have statistically independent entries, since the upper and lower triangular part of the matrix are related by complex conjugation. Only the upper (lower) triangular part of the matrix has literally statistically independent entries.

Time reversal operator

To explore the consequences of time-reversal symmetries, we need to represent them by operators acting on wave functions. As it turns out, time-reversal operators T are antiunitary [123]:

$$\langle T\psi|\ T\phi\rangle = \langle\phi|\psi\rangle\,, \tag{6.17}$$

and can always be written [123]

$$T = UK, \tag{6.18}$$

where U is an arbitrary unitary matrix and K is the antiunitary complex conjugation operator in position representation. The case $U = 1$ is associated to conventional time-reversal symmetry:

$$\begin{aligned} &t \to -t, \\ &p \to -p, \\ &\theta \to \theta. \end{aligned} \tag{6.19}$$

It is reasonable to require that every time-reversal operators T acting twice on a wave function does not change it (up to a phase factor, i.e. $T^2\psi = e^{i\alpha}\psi$). It can be shown that $T^2 = 1$ ($\alpha = 0$) and $T^2 = -1$ ($\alpha = \pi$) are the only possibilities consistent with the antiunitarity of T [123].

Let us first consider the case $T^2 = 1$. Assuming an Hamiltonian invariant under T ($[H, T] = 0$), its local spectral properties should be described by a random matrix ensemble similarly invariant under T. To exhibit the constraint imposed by this invariance, we first show that a T-invariant basis exists. To that end, given an arbitrary vector ϕ_1 and a complex number a_1, we build the vector

$$\psi_1 = a_1\phi_1 + Ta_1\phi_1, \tag{6.20}$$

which is manifestly T-invariant. Repeating the same procedure with a vector ϕ_2 orthogonal to ψ_1, we get the T-invariant vector

$$\psi_2 = a_2\phi_2 + Ta_2\phi_2, \tag{6.21}$$

which turns out to be orthogonal to ψ_1:

$$\langle\psi_2|\psi_1\rangle = a_2^*\langle\phi_2|\psi_1\rangle + a_2\langle T\phi_2|\psi_1\rangle = a_2\langle T^2\phi_2|\psi_1\rangle^* = a_2\langle\phi_2|\psi_1\rangle^* = 0. \tag{6.22}$$

From this procedure, one can build a complete basis of orthogonal vectors.

With a T-invariant basis at hand, we consider an arbitrary matrix O invariant under T ($[O, T] = 0$). The matrix O is real in the T-invariant basis:

$$O_{\mu\nu} = \langle\psi_\mu|O\psi_\nu\rangle = \langle T\psi_\mu|TO\psi_\nu\rangle^* = \langle\psi_\mu|TOT^2\psi_\nu\rangle^* = \langle\psi_\mu|TOT\psi_\nu\rangle^* = O^*_{\mu\nu}. \tag{6.23}$$

The entries of the random matrices invariant under T can thus be described by real distributions. The ensemble of matrices that leave a $N \times N$ real matrix real is the $O(N)$ group, a subgroup of the $U(N)$ group. The random Hermitian matrix ensemble that has statistically independent entries and is statistically independent under $O(N)$ transformations is the Gaussian orthogonal ensemble [190]. This ensemble of symmetric matrices has statistically independent real Gaussian entries.

The case $T^2 = -1$ is somewhat richer, with different distributions depending on the presence of geometrical symmetries. Independently of the presence of geometrical symmetries, the $T^2 = -1$ case has a distinguishable feature, the presence of Kramers' degeneracy. Indeed, if ψ is an eigenstate of the Hamiltonian with energy E, so is $T\psi$ since $[H, T] = 0$, moreover ψ and $T\psi$ are orthogonal:

$$\langle\psi|T\psi\rangle = \langle T\psi|T^2\psi\rangle^* = -\langle T\psi|\psi\rangle^* = -\langle\psi|T\psi\rangle = 0, \tag{6.24}$$

all eigenvalues are thus doubly degenerate. An important consequence of this double degeneracy is that the Hilbert space dimension, if finite, must be even (we denote it $2N$). This result is consistent with the common wisdom that $T^2 = -1$ is only possible for half-integer spin particles.

In the absence of geometrical symmetries, one can use a basis organized in pairs ($|i\rangle$,$T|i\rangle$). In this basis, a matrix invariant under T can be decomposed in 2×2 blocks formed by the pairs ($|i\rangle$,$T|i\rangle$). Similarly to the real T-invariant matrices when $T^2 = 1$, when $T^2 = -1$ each block of a T-invariant matrix can be described by four real numbers giving the weights associated to the matrices $(1,-i\boldsymbol{\sigma})$ [with $\boldsymbol{\sigma}$ the Pauli matrices]. Further Hermiticity connects the blocks on each side of the diagonal and reduces the description of diagonal blocks to a single real number [123]. These matrices are thus formally equivalent to $N \times N$ Hermitian quaternionic matrices[4]. On the one hand, for off-diagonal elements, there is a one-to-one correspondence between the four real numbers composing a quaternion and the four real numbers describing a block[5]. On the other hand, the N real diagonal elements of the Hermitian quaternionic matrix describes the diagonal blocks. The ensemble of transformations leaving this structure unchanged is the symplectic $Sp(N)$ group. The random Hermitian matrix ensemble that has statistically independent entries and is statistically independent under $Sp(N)$ transformations forms the Gaussian symplectic ensemble [190]. This ensemble of $2N \times 2N$ Hermitian matrices can be described by $N \times N$ Hermitian matrices with real (resp. quaternionic) statistically independent Gaussian (resp. non-)diagonal entries.

The presence of an additional geometrical symmetry (e.g. parity) splits the matrices in two blocks transposed of one another:

$$H = \begin{pmatrix} H_+ & 0 \\ 0 & H_+^T \end{pmatrix}. \tag{6.25}$$

Kramers' degeneracy is a direct consequence of this structure. The associate random Hermitian matrix ensemble is then that of H_+, which is only constrained by Hermiticity, it is thus the Gaussian unitary ensemble. The presence of an additional geometric symmetry imposes real fluctuations for H_+ and the corresponding ensemble is thus the Gaussian orthogonal ensemble.

Level spacing distribution in the three Dyson random matrix ensembles

We have defined three ensembles of Hermitian random matrices, the Gaussian orthogonal ensemble (GOE), the Gaussian unitary ensemble (GUE), and the Gaussian symplectic ensemble (GSE). In each ensemble, one can work out local spectral properties that are expected to be universal. A commonly used quantity is the distribution of level spacings. Given the ordered eigenvalues $(\lambda_1, \lambda_2, \ldots, \lambda_N)$ of a given matrix, it is the distribution of s_i ($s_1 = \lambda_2 - \lambda_1$, $s_2 = \lambda_3 - \lambda_2$, ..., $s_{N-1} = \lambda_N - \lambda_{N-1}$). It is expressed in units of the local mean level spacing ($\langle s_i \rangle$).

For sufficiently large matrices, the approximate results are respectively for the orthogonal, unitary and symplectic ensembles [190]:

$$P_{\mathrm{GOE}}(s) = \frac{\pi}{2} s e^{-\frac{\pi}{4}s^2}, \tag{6.26}$$

$$P_{\mathrm{GUE}}(s) = \frac{32}{\pi^2} s^2 e^{-\frac{4}{\pi}s^2}, \tag{6.27}$$

$$P_{\mathrm{GSE}}(s) = \frac{2^{18}}{3^6\pi^3} s^4 e^{-\frac{64}{9\pi}s^2}. \tag{6.28}$$

A comparison between these three results and the Poisson distribution

$$P_{\mathrm{Poisson}}(s) = e^{-s}, \tag{6.29}$$

[4] An Hermitian quaternionic matrix is composed of real entries on the diagonal and off-diagonal quaternionic entries.
[5] In fact, the analogy between the structure of the 2×2 blocks and quaternions goes much deeper, see e.g. [191].

which would prevail if the eigenvalues were just uniformly and independently distributed over some interval, is shown in figure 6.1. The random matrix ensembles show different degrees of level-level repulsion, with a level spacing distribution starting as s for the orthogonal ensemble, s^2 for the unitary ensemble and s^4 for the symplectic ensemble.

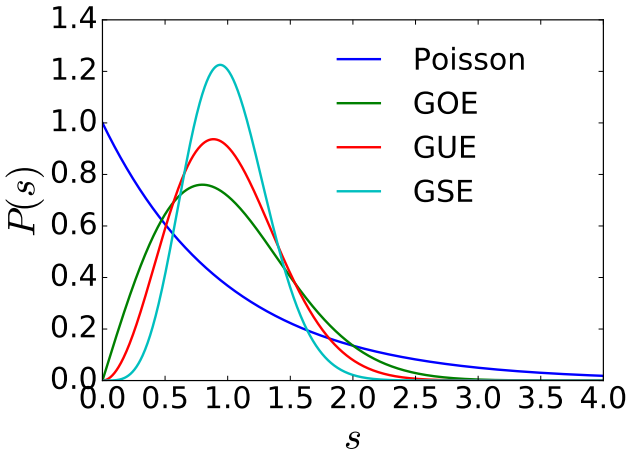

Figure 6.1 – Eigenvalue spacing distributions for different random matrix ensembles. The approximate results for the three Dyson ensembles are shown: equation (6.26) for the orthogonal ensemble in green, equation (6.27) for the unitary ensemble in red and equation (6.28) for the symplectic ensemble in light blue. For comparison, the Poisson distribution (6.29) (which would prevail if the eigenvalues were just uniformly and independently distributed over some interval) is shown in dark blue.

6.2.3 Time reversal symmetry for Floquet models

Going back to our initial model, equation (6.1), we see that it does not fit in the above framework. Indeed, (6.1) being time-dependent, it does not make much sense to look at its (time-dependent) eigenvalues. In fact, it is the Floquet operator (6.7), describing the evolution over a period, that plays the role of the Hamiltonian in this case. The universal local spectral properties are found in the eigenvalues of the Floquet operator. The Floquet operator being unitary, it is not described by the above Gaussian ensembles, but by very similar ensembles, the circular ensembles. The eigenvalues of unitary operators being complex numbers of modulus 1, the interesting spectral properties lie in their phase. In fact, for large enough matrices, defining the level spacing as the distance between two consecutive eigenphases, one finds the same distributions of level spacings than for the Gaussian ensembles.

The interplay with the time-reversal symmetry is slightly changed. Indeed, since the Floquet operator propagates a given state over a period, its time-reversed counterpart should propagate a state backward in time over a period, such that the time-reversed Floquet operator should be the inverse of the Floquet operator:

$$TFT^{-1} = F^{-1} = F^{\dagger}. \tag{6.30}$$

Equation (6.30) replaces $[H, T] = 0$ for Floquet operators.

A Floquet operator without property (6.30) has the universal properties of the circular unitary ensemble (CUE). A Floquet operator with property (6.30) and $T^2 = 1$ [respectively $T^2 = -1$] has the universal properties of the circular orthogonal (COE) [respectively symplectic (CSE)] ensemble.

To a good approximation, their level spacing distribution are respectively given by (6.27), (6.26) and (6.28).

6.2.4 Critical exponents

The above classification of Hamiltonians in terms of their local spectral properties may seem a bit unusual to the statistical physicist. Indeed, in statistical physics it is more common to group models in universality classes characterized by some critical exponents [192]. In the case of Anderson transitions, the same characterization applies and different universality class features different critical exponents. It is now clear that the above three classes (orthogonal, unitary and symplectic) define three different universality classes, each displaying a different universal divergence of the localization length near the critical point [189]. Concerning the critical properties, to the best of our knowledge, nothing is known for kicked rotors besides spinless time-reversal invariant ones that are known to belong to the orthogonal class, together with disorder models [36, 179].

6.3 A spinless kicked rotor in the symplectic class?

It is commonly accepted that the time-reversal operator can only square to -1 for particles with half-integer spin [123]. As a corollary, it is believed that the symplectic Anderson universality class can only be explored with half-integer spin particles. This section aims at challenging this restriction.

6.3.1 Weak antilocalization

Model

To start with, we look for a kicked-rotor model exhibiting weak antilocalization. This characteristic of the symplectic class corresponds to a Cooperon with a sign opposite to the Diffuson [3]. The Cooperon is built from a path and its time-reversed counterpart. A path itself is defined as a sequence of free propagations with momenta p_t, separated by kicks. The intuitive idea is to use a kicking potential $V(\theta)$ with the property

$$\langle p_1|e^{-iV(\theta)}|p_2\rangle = -\langle p_2|e^{-iV(\theta)}|p_1\rangle \text{ for all } (p_1,p_2), \tag{6.31}$$

such that, for each kick, the Cooperon accumulates a minus sign as compared to the usual time-reversal invariant situation, for which

$$\langle p_1|e^{-iV(\theta)}|p_2\rangle = \langle p_2|e^{-iV(\theta)}|p_1\rangle\,. \tag{6.32}$$

We need to go one step further and impose that the Cooperon only hosts an odd number of kicks, otherwise the accumulation of positive and negative signs would simply kill it. This can be easily achieved with an alternation of two different kicks. Figure 6.2 presents a pictorial view of these ideas.

To achieve property (6.31), we need a kicking term $e^{-iV(\theta)}$ whose Fourier transform

$$f(p) = \int \mathrm{d}\theta e^{-ip\theta} e^{-iV(\theta)}, \tag{6.33}$$

is odd [$f(p) = -f(-p)$]. From the properties of Fourier transforms, it is sufficient and necessary for $e^{-iV(\theta)}$ to be odd as well. An example of a potential with property (6.31) is

$$V(\theta) = K\cos(\theta) + \frac{\pi}{2}\mathrm{sgn}(\theta). \tag{6.34}$$

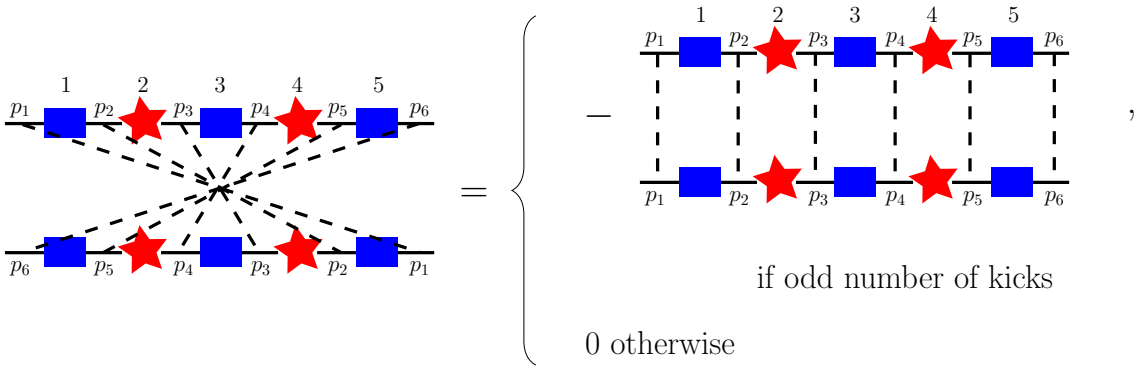

Figure 6.2 – Cooperon with alternation of two different kicks, respectively shown as blue squares and red stars, lines are free propagations. On the one hand, for odd number of kicks, we can use property (6.31) to express the Cooperon as minus its Diffuson counterpart. On the other hand, the alternation of two kicks make it impossible for a Cooperon to have an even number of kicks.

The potential (6.34) has however a serious issue with respect to Anderson localization: it is discontinuous. Indeed, one kick with potential (6.34) is sufficient to populate arbitrary high momenta, with only an algebraic decay of the momentum density, which is inconsistent with exponential Anderson localization [193].

In order to achieve the desired properties without destroying Anderson localization, we introduce an additional dimension, made of only two sites, and place the discontinuity along it. We end up with the following Hamiltonian (with only two sites along y, $y = \pm 1$):

$$H_{\mathrm{CSE}} = \frac{p_{\theta_x}^2}{2} + t_y + g_{\mathrm{CSE}}(\theta_x, y, \alpha) \sum_n \delta(t - 2n) + g_{\mathrm{CSE}}(\theta_x, y, -\alpha) \sum_n \delta(t - 2n + 1), \tag{6.35}$$

where

$$g_{\mathrm{CSE}}(\theta_x, y, \alpha) = K(1 + \alpha) \left[\cos(\theta_x) + y\epsilon \sin(2\theta_x)\right] + y\frac{\pi}{2}. \tag{6.36}$$

t_y accounts for the tunneling between the two sites along y. In practice, we treat it like $p_{\theta_x}^2/2$: in momentum space, we approximate it by a p_y-dependent random number uniformly distributed in $[0, 2\pi[$ (see subsection 6.1.3 for more details). Here, the term in $y\sin(2\theta_x)$ is introduced to couple the θ_x and y directions; if they were uncoupled the dynamics along the two directions would be separated. It is chosen invariant under $(\theta_x, y) \to (-\theta_x, -y)$, such that (6.31) holds.

We will also consider an orthogonal variant of (6.35) for comparison:

$$H_{\mathrm{COE}} = \frac{p_{\theta_x}^2}{2} + t_y + g_{\mathrm{COE}}(\theta_x, y, \alpha) \sum_n \delta(t - 2n) + g_{\mathrm{COE}}(\theta_x, y, -\alpha) \sum_n \delta(t - 2n + 1), \tag{6.37}$$

where

$$g_{\mathrm{COE}}(\theta_x, y, \alpha) = K(1 + \alpha) \left[\cos(\theta_x) + y\epsilon \sin(2\theta_x)\right]. \tag{6.38}$$

Signatures

In order to check that model (6.35) indeed features weak antilocalization, we perform two types of numerical simulations.

A first signature of weak antilocalization is visible in real space. In usual time-reversal invariant kicked rotors, starting from a wave packet placed at $(\theta_x, y) = (\theta_0, 1)$, the Cooperon of subsection 6.2 manifests itself as a peak in the density at $(\theta_x, y) = (-\theta_0, -1)$ (the Cooperon is built in momentum space, we are thus looking at an analogue of the coherent back scattering peak), on top of the uniform

background associated to the Diffuson [194]. Should its sign be reversed, the Cooperon manifests itself as a dip in the density at $(\theta_x, y) = (-\theta_0, -1)$. This is indeed what we observe numerically, as visible in figure 6.3.

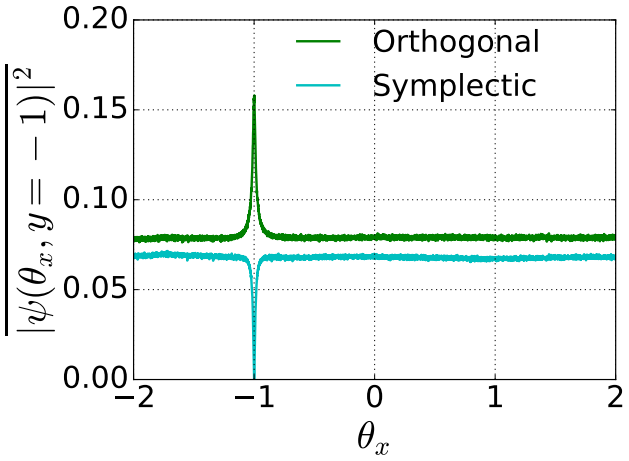

Figure 6.3 – Average densities as a function of θ_x, along $y = -1$, obtained by kicking 2000 times a wave packet initially placed at $(\theta_x = 1, y = 1)$. The numerical parameters are $K = 7.5$, $\epsilon = 0.2$ and $\alpha = 1/3$. The space $([-\pi, \pi[)$ is discretized in 12584 points. The results are averaged over 15000 random realizations of the kinetic operator. The results were respectively obtained with Hamiltonian (6.35) (blue) and Hamiltonian (6.37) (green). Note that the same wave function normalization is used in both cases; for some reason the density obtained with Hamiltonian (6.35) is slightly imbalanced between $y = -1$ and $y = 1$.

A second signature is visible in momentum space. In usual time-reversal invariant kicked rotors, starting from a plane wave, the weak localization correction slows down the short-time diffusion. Should the sign of the Cooperon be reversed, a weak antilocalization correction appears and enhances the short-time diffusion. These effects are most conveniently observed in a variant of the β function, defined as [21]

$$\beta(g) = \frac{\mathrm{d}\ \ln(g)}{\mathrm{d}\ \ln(L)}, \tag{6.39}$$

with $L = \sqrt{\langle p^2 \rangle}$ and $g = \sqrt{\langle p^2 \rangle}/t$. With these definitions, the β function writes

$$\beta(g) = 1 - \frac{2}{\frac{\mathrm{d}\ \ln(\langle p^2 \rangle)}{\mathrm{d}\ \ln(t)}}. \tag{6.40}$$

We calculate this function numerically by propagating a plane wave and recording $\langle p^2 \rangle$ versus time. Diffusion at short times manifests itself as a β function going to -1 at large g. Weak (anti) localization correction brings a (positive) negative correction to the β function at large g. This is clearly visible in figure 6.4.

We have thus found a spinless kicked rotor exhibiting features typical of the symplectic class. Note that in the numerical simulations, we use a finite grid chosen with care. Indeed for relation (6.31) to hold on a finite grid, each point $\theta_x \in [-\pi, \pi[$ must have a partner $-\theta_x$, in particular the grid should not include the point $\theta_x = 0$. Typically, $2N$ grid points are used, with a uniform sampling: $\{\pm 2\pi n/N \pm \pi/N \ / \ \ n \in \mathbb{N}\}$. Relation (6.31) is true in the continuous case since the point $\theta_x = 0$ is of measure zero.

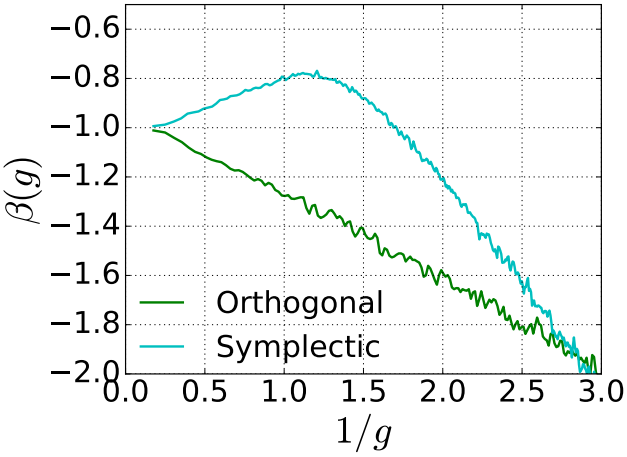

Figure 6.4 – $\beta(g)$ as a function of $1/g$. The numerical parameters are $K = 10$, $\alpha = 1/3$ and $\epsilon = 0.2$. The space $([-\pi, \pi[)$ is discretized in 6292 points. The results are averaged over 5000 random realizations of the kinetic operator. The results were respectively obtained with Hamiltonian (6.35) (blue) and Hamiltonian (6.37) (green). As there are strong fluctuations from one kick to the other, due to the structure of the Hamiltonian, we have only kept measurements done after an even number of kicks to compute β.

6.3.2 Eigenvalue statistics

To see how far the analogy with spin-1/2 particles goes, we now consider the eigenvalue statistics. In the limit of an infinite system, localized eigenstates do not overlap, such that their associated eigenvalue are independent. The Poisson distribution is thus expected, independently of the Hamiltonian symmetries. Of course, we can only simulate numerically finite systems. For kicked rotors, eigenstates are localized in momentum space, the system size is thus set by the spatial discretization: assuming that the spatial grid varies by step of Δ_x, momenta take values in $[-\hbar\pi/\Delta_x, \hbar\pi/\Delta_x[$. For the eigenvalues to obey the random matrix predictions of subsection 6.2.2, we must ensure that the localization length is much larger than $\hbar\pi/\Delta_x$ (this is generally achieved by using huge kicking strengths). Apart from that, the localization properties of the Hamiltonian are not especially important for the eigenvalue statistics. We thus consider directly the 1D model[6]

$$\begin{aligned} H_{\text{1D-CSE}} = \frac{p_\theta^2}{2} &+ \left[K(1+\alpha)\cos(\theta) + \frac{\pi}{2}\text{sgn}(\theta)\right] \sum_n \delta(t-2n) \\ &+ \left[K(1-\alpha)\cos(\theta) + \frac{\pi}{2}\text{sgn}(\theta)\right] \sum_n \delta(t-2n+1). \end{aligned} \tag{6.41}$$

As discussed in subsection 6.2.3, the relevant operator to be diagonalized is the associated Floquet operator. The Floquet operator being unitary, its eigenvalues are complex numbers of modulus 1. The statistical study is performed on the phases of the eigenvalues. To be more specific, given the ordered eigenphases of the eigenvalues $(\phi_1, \phi_2, \ldots, \phi_N)$, we consider the distribution of the level spacings s_i ($s_1 = \phi_2 - \phi_1$, $s_2 = \phi_3 - \phi_2$, $\ldots$, $s_{N-1} = \phi_N - \phi_{N-1}$). Level spacing distributions computed numerically for the Floquet operator of (6.41) with different parameters are shown in figure 6.5.

[6]While the conventional time-reversal symmetry ($t \to -t$, $p_\theta \to -p_\theta$, $\theta \to \theta$) plays no role for the kicked rotor, it could disturb the spectral analysis [183]. For the random kicked rotor, using independent random phases (as opposed to phases with parity properties, e.g. $\phi_l = \phi_{-l}$) in equation (6.12) allows to stay clear of this parasitic effect.

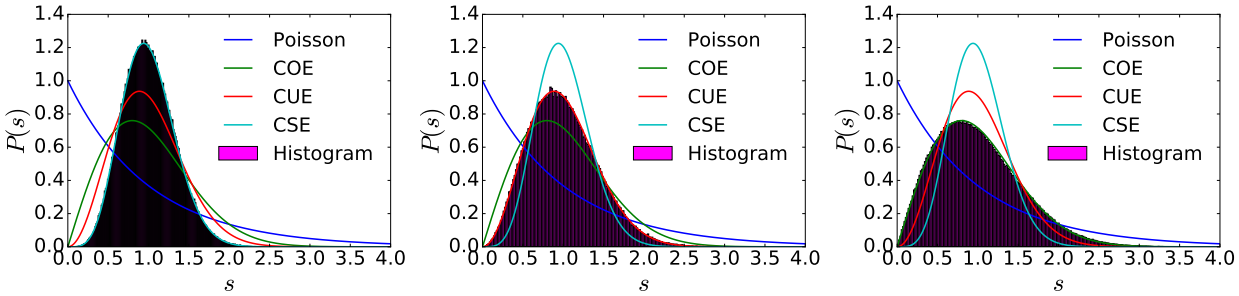

(a) Even grid size, $\alpha \neq 0$. (b) Even grid size, $\alpha = 0$. (c) Odd grid size, $\alpha \neq 0$.

Figure 6.5 – Distributions of level spacing for the Floquet operator of (6.41). For the three figures, we have used $K = 100$ and computed all the eigenvalues for 10000 random realizations of the Floquet operator. Figure (a) was obtained for $\alpha = 0.3$ and a spatial discretization made of 32 points in $]0, \pi[$ and their partner obtained by parity (the grid was of the form $\{\pm 2\pi n/N \pm \pi/N \ / \ n \in \mathbb{N}\}$). Figure (b) was obtained for $\alpha = 0$ and the same spatial grid as figure (a). Figure (c) was obtained for $\alpha = 0.3$ and a spatial grid including the point $\theta = 0$ (the grid was of the form $\{\pm 2\pi n/N \ / \ n \in \mathbb{N}\}$). Random matrix theory predictions, equation (6.26) (COE), equation (6.27) (CUE) and equation (6.28) (CSE), as well as the Poisson distribution, equation (6.29), are shown for comparison.

In addition, given the level spacings, one can define the quantity [195]

$$\tilde{r_i} = \frac{\min(s_i, s_{i-1})}{\max(s_i, s_{i-1})}. \tag{6.42}$$

Its average over both the spectrum and different realizations of the Floquet operator is denoted $\langle \tilde{r} \rangle$. We have compared the $\langle \tilde{r} \rangle$ found for the Floquet operator of (6.41) to the random matrix results of [195] in table 6.1. Table 6.1 also reports the presence of Kramers' degeneracy.

Parameters	Kramers' degeneracy	$\langle \tilde{r} \rangle$	$\langle \tilde{r} \rangle$ from [195]
Same as figure 6.5a	Present	0.6751 ± 0.0004	0.6744 ± 0.0001 (GSE)
Same as figure 6.5b	Present	0.6012 ± 0.0004	0.5996 ± 0.0001 (GUE)
Same as figure 6.5c	Absent	0.5313 ± 0.0004	0.5307 ± 0.0001 (GOE)

Table 6.1 – $\langle \tilde{r} \rangle$ as obtained for the Floquet operator of (6.41) and different parameters. The quantity $\langle \tilde{r} \rangle$ is defined in the main text. For comparison, we have reported the values found in [195] for random matrices in the Gaussian orthogonal (GOE), unitary (GUE) and symplectic (GSE) ensembles. We have also reported the presence of Kramers' degeneracy. As discussed in subsection 6.3.3, only the *square* of the Floquet operator associated to figure 6.5b exhibits Kramers' degeneracy. The Floquet operator itself exhibits pairs of opposite eigenvalues.

The results for the eigenvalue statistics reported in this section confirm the analogy with spin-1/2 particles. The results are indeed fully consistent with the symplectic class when the conditions of subsection 6.3.1 are met (figure 6.5a): i) $\alpha \neq 0$ (i.e. alternation of two different kicks), and ii) a spatial grid built in such a way that each point θ as a partner $-\theta$ [so as to guarantee (6.31)]. Interestingly, the case $\alpha = 0$ (figure 6.5b) seems to correspond to the case of a spin-1/2 particle in the presence of a geometrical symmetry (Kramers' degeneracy and unitary fluctuations). For the sake of completeness, we have also included the results obtained with a grid including $\theta = 0$, even

though it is not relevant to the continuous case since the point $\theta = 0$ should be of measure zero. Quite surprisingly, adding the point $\theta = 0$ (figure 6.5c) leads to eigenvalue statistics consistent with the orthogonal class.

6.3.3 Time-reversal invariance

The above results suggest to look for a time-reversal symmetry of the Floquet operator of (6.41) squaring to -1. To this end, we write the Floquet operator as

$$F = U_1 U_2, \tag{6.43}$$

with

$$U_1 = e^{-ip_\theta^2/2} e^{-i\left[K(1+\alpha)\cos(\theta)+\frac{\pi}{2}\mathrm{sgn}(\theta)\right]}, \tag{6.44}$$

$$U_2 = e^{-ip_\theta^2/2} e^{-i\left[K(1-\alpha)\cos(\theta)+\frac{\pi}{2}\mathrm{sgn}(\theta)\right]}. \tag{6.45}$$

As discussed in subsection 6.2.1, in the case of the kicked rotor, one usually considers the product of the parity (P) and the conventional time-reversal (T) operators[7] ($T_K = PT$). As such, it squares to 1 ($T_K^2 = 1$). Its associated symmetry writes

$$\begin{cases} t \to -t, \\ \theta \to -\theta, \\ p \to p. \end{cases} \tag{6.46}$$

Case of even number of sites, $\alpha \neq 0$ (figure 6.5a)

Clearly the Floquet operator of (6.41) is not invariant under T_K:

$$T_K^{-1} F T_K = U_1^\dagger U_2^\dagger \neq F^\dagger. \tag{6.47}$$

We can nevertheless consider the time-reversal operator

$$\tilde{T} = U_1 T_K. \tag{6.48}$$

One then finds (it is easy to check that $\tilde{T}^{-1} = T_K U_1^\dagger$)

$$\tilde{T}^{-1} F \tilde{T} = T_K U_1^\dagger F U_1 T_K = T_K^{-1} U_2 U_1 T_K = U_2^\dagger U_1^\dagger = F^\dagger. \tag{6.49}$$

For U_1 given by equation (6.44), one can use the important relation

$$T_K^{-1} U_1 T_K = -U_1^\dagger, \tag{6.50}$$

to compute $\tilde{T}^2$:

$$\tilde{T}^2 = U_1 T_K U_1 T_K = U_1 T_K^{-1} U_1 T_K = U_1(-U_1^\dagger) = -1. \tag{6.51}$$

In conclusion, the Floquet operator is invariant [in the sense of equation (6.30)] under the action of a time-reversal operator squaring to -1. This explains the symplectic statistics of eigenvalues observed in figure 6.5a and table 6.1, as well as the presence of Kramers' degeneracy.

[7] For the sake of clarity, we omit the factors $e^{\pm ip_\theta^2/2}$ that should enter the definitions of the time-reversal operators [123], they do not change anything to the reasoning. This remark applies to the whole subsection.

Case of even number of sites, $\alpha = 0$ (figure 6.5b)

In the case $\alpha = 0$, the Floquet operator reduces to $F_{\alpha=0} = U_1$ and we still have [equation (6.50)]

$$T_K^{-1} U_1 T_K = -U_1^\dagger \Leftrightarrow T_K^{-1} F_{\alpha=0} T_K = -F_{\alpha=0}^\dagger. \tag{6.52}$$

It has an important consequence on the spectrum. To exhibit it, we start from the eigenvalue equation

$$F_{\alpha=0} |\phi_v\rangle = e^{-i\phi_v} |\phi_v\rangle \Leftrightarrow F_{\alpha=0}^\dagger |\phi_v\rangle = e^{i\phi_v} |\phi_v\rangle . \tag{6.53}$$

We then apply T_K on both sides of the right equality and insert $T_K^2 = 1$ to find

$$T_K F_{\alpha=0}^\dagger T_K T_K |\phi_v\rangle = e^{-i\phi_v} T_K |\phi_v\rangle \Leftrightarrow F_{\alpha=0} T_K |\phi_v\rangle = -e^{-i\phi_v} T_K |\phi_v\rangle . \tag{6.54}$$

$T_K |\phi_v\rangle$ is an eigenstate of $F_{\alpha=0}$ with eigenvalue $-e^{-i\phi_v}$. Assuming a finite dimension $2N$, we finally use the basis $\{\phi_1, \ldots, \phi_N\}$, $\{T_K\phi_1, \ldots, T_K\phi_N\}$ to write $F_{\alpha=0}$ as

$$F_{\alpha=0} = \begin{pmatrix} F_+ & 0 \\ 0 & -F_+ \end{pmatrix}. \tag{6.55}$$

Figure 6.5b and table 6.1 show the eigenvalue statistics of

$$F_{\alpha=0}^2 = \begin{pmatrix} F_+^2 & 0 \\ 0 & F_+^2 \end{pmatrix}. \tag{6.56}$$

The structure of $F_{\alpha=0}^2$ explains the results of figure 6.5b and table 6.1, in the spirit of Kramers' degeneracy with one geometric symmetry [equation (6.25)].

Case of odd number of sites (figure 6.5c)

In the case of an odd number of sites, equation (6.50) does not hold due to the presence of the site $\theta = 0$ on which T_K has no effect. Equation (6.49) however does hold. The question is thus whether $\tilde{T}$ squares to plus or minus 1. The case -1 implying Kramers' degeneracy, it is possible only if the Hilbert space dimension is even. The number of sites is odd, so is the Hilbert space dimension, such that all time-reversal symmetries must square to 1. We conclude that the Floquet operator is invariant [in the sense of equation (6.30)] under the action of a time-reversal operator squaring to 1, explaining the orthogonal statistics of eigenvalues observed in figure 6.5c and table 6.1.

6.3.4 Conclusion

We have presented in this section a spinless kicked rotor consistent with the symplectic class. It shows clear signatures of weak antilocalization and the statistics of its eigenvalues unambiguously place it in the symplectic class. It is indeed invariant under the effect of a time-reversal operator squaring to -1. Yet, it is desirable to confirm these observations by an analysis of its critical properties in higher dimensions. Let us take that road.

6.4 From incommensurate frequencies to higher dimensions

6.4.1 Generalities

The kicked rotor offers a very powerful, yet intriguing, way to explore high dimensions experimentally or numerically. It consists in modulating quasi-periodically the kick sequence of a 1D kicked rotor. For example, one can use the kicked rotor

$$H = \frac{p_\theta^2}{2} + K(t)\cos(\theta) \sum_n \delta(t - n), \tag{6.57}$$

with

$$K(t) = K\left[1 + \eta\cos(\omega_1 t + \varphi_1)\cos(\omega_2 t + \varphi_2)\right], \tag{6.58}$$

to simulate a 3D disorder problem. (6.57) was shown to be equivalent to 3D disorder models, provided ω_1 and ω_2 are chosen incommensurate with each other and 2π [179, 196, 197] (we use $\omega_1 = 2\pi\sqrt{5}$ and $\omega_2 = 2\pi\sqrt{13}$ in the following).

The current understanding of this correspondence between 1D modulated kicked rotors and 3D problems is based on the equivalence between the dynamics generated by (6.57) and the dynamics generated by the 3D pseudo-rotor

$$H = \frac{p_\theta^2}{2} + \omega_1 p_1 + \omega_2 p_2 + K\left[1 + \eta\cos(\theta_1)\cos(\theta_2)\right]\cos(\theta)\sum_n \delta(t-n), \tag{6.59}$$

with initial conditions $\theta_1 = \varphi_1$ and $\theta_2 = \varphi_2$. The equivalence appears directly when writing down the evolution of a given wave packet with the two models [196]. Note that similarly to the 1D usual kicked rotor, the pseudo-rotor (6.59) can be mapped onto a 3D disorder model [179, 196] and can be shown to be equivalent to disorder models through a supersymmetric field theory [197].

6.4.2 Incommensurate frequencies in the symplectic class

To the best of our knowledge, the idea of using a quasi-periodic modulation to study higher dimensions has only been applied to kicked rotors in the orthogonal class. Before applying it to our spinless kicked rotor presumably belonging to the symplectic class, we propose to check the validity of the approach in the more familiar situation of a spin-1/2 kicked rotor [184, 198].

Model

We use the following kicked rotor

$$H = \frac{p^2}{2} + K(t)g^e_{\frac{1}{2}}(\theta)\sum_n \delta(t-2n) + K(t)g^o_{\frac{1}{2}}(\theta)\sum_n \delta(t-2n+1), \tag{6.60}$$

where

$$g^e_{\frac{1}{2}}(\theta) = (1+\alpha)\left[\cos(\theta) + \epsilon\sin(2\theta)\sigma_z\right] \text{ and } g^o_{\frac{1}{2}}(\theta) = (1-\alpha)\left[\cos(\theta) + \mu\sin(2\theta)\sigma_x\right]. \tag{6.61}$$

Here σ_x and σ_z are Pauli matrices. $K(t)$ is given by equation (6.58). (6.60) is invariant under (6.15) (with $\theta_0 = 0$ and half-integers t_0) and does not have any geometrical symmetry (this is ensured by the $\sin(2\theta)$ terms), it thus belongs to the symplectic class [183].

Finite time scaling

The kicked rotor (6.60) presents a phase transition. To extract the associated critical exponent, which governs the divergence of the localization length near the transition, we follow [179] and perform a finite time scaling analysis of $\langle p^2\rangle$. Practically, $\langle p^2\rangle$ is obtained by propagating an initial plane wave with the Hamiltonian (6.60) and averaging the result over random realizations of the kinetic term and the phases φ_1 and φ_2. Near the phase transition and at long enough times, $\langle p^2\rangle$ follows the universal scaling law

$$\langle p^2\rangle = t^{2/3}F\left[(K-K_c)t^{1/3\nu}\right], \tag{6.62}$$

where K_c is the critical point and ν is the critical exponent characterizing the transition. To extract the critical exponent, we define the quantity $\ln\Lambda = \ln(\langle p^2\rangle / t^{2/3})$ and fit it with a Taylor expansion of $\ln(F)$:

$$\ln(\Lambda) = \ln(\Lambda_c) + (K-K_c)t^{1/3\nu}\mathcal{F}_1 + \dots \tag{6.63}$$

The best fit $\ln \Lambda_{\text{fit}}(K,t)$ is obtained by minimizing

$$\chi^2 = \sum_{K,t} \left(\frac{\ln\left[\Lambda_{\text{data}}(K,t)\right] - \ln\left[\Lambda_{\text{fit}}(K,t)\right]}{\sigma(K,t)} \right)^2, \tag{6.64}$$

where $\sigma(K,t)$ is the numerical uncertainty of $\ln\left[\Lambda_{\text{data}}(K,t)\right]$. The numerical data $\ln\left[\Lambda_{\text{data}}(K,t)\right]$ for different times t are correlated. For the fitting procedure to be meaningful, we resample them with a bootstrap method. The error estimates on the position of the critical point K_c and the value of the critical exponent ν given below correspond to their respective standard deviation during the bootstrap process.

Results

We have performed numerical simulations of (6.60) with the numerical parameters $\alpha = 0.5$, $\epsilon = 0.5$, $\eta = 0.15$, $\mu = 0.5$ and for various values of K. The space $([-\pi, \pi[)$ was discretized in 6284 points. To avoid deviations from (6.62) due to finite time effects, we have carried out the finite time analysis with values of $\langle p^2 \rangle$ measured between 200000 and 1000000 kicks. Generically, the results are averaged over 120 random realizations. We have used more realizations near the critical point, with 480 realizations for $K \in [1.68, 1.695[$ and 1560 realizations for $K \in [1.695, 1.75]$.

The results are reported in figure 6.6 and exclude the possibility of (6.60) being in the same universality class as spin-1/2 disorder models, with a critical exponent more than 4σ away from the one found in spin-1/2 disorder models.

Our numerical simulations strongly suggests that the spin-1/2 quasi-periodically modulated kicked rotor is not in the symplectic universality class. This result is consonant with similar observations for unitary kicked rotors [200]. This issue forces us to postpone the characterization of the critical properties of the spinless kicked rotor presumably in the symplectic class.

6.4.3 Beyond the incommensurate frequencies

It is presently not clear why quasi-periodically modulated kicked rotors appear not to fall in the expected unitary and symplectic universality classes. The reason may be that the "quasi-periodic trick" is limited to the orthogonal universality class and is not suited to the unitary and symplectic universality classes. One may envision that the commonly used cosine quasi-periodic sequences reproduce the fluctuations of the orthogonal class, and should not be used in an attempt at exploring the unitary and symplectic universality classes.

In this line of thoughts, we propose to consider the possibility of other quasi-periodic sequences. Before targeting specifically the unitary and symplectic universality classes, we propose to explore the possibility of simulating Anderson localization on fractals with quasi-periodically modulated kicked rotors. Such kicked rotors may be useful to study the symplectic class, and in particular to identify the lower critical dimension, which is believed to be somewhere between 1 and 2 [201], with intriguing consequences [202]. Other possible applications include the validation of $d = 2 + \epsilon$ expansions [22, 203]. It is indeed a difficult task to simulate numerically (not to mention experimentally) such problems on actual fractals [201–205].

Casati *et al.* quasi-periodic sequences

Before exploring other quasi-periodic sequences, we need to develop some understanding of the commonly used quasi-periodic sequences [196]. These sequences are built by sampling trigonometric functions. More precisely, one studies 2D Anderson localization with a kick sequence

$$K_2(t) = K\left[1 + \eta \cos(\omega_1 t + \varphi_1)\right] \text{ for } t \in \mathbb{N}, \tag{6.65}$$

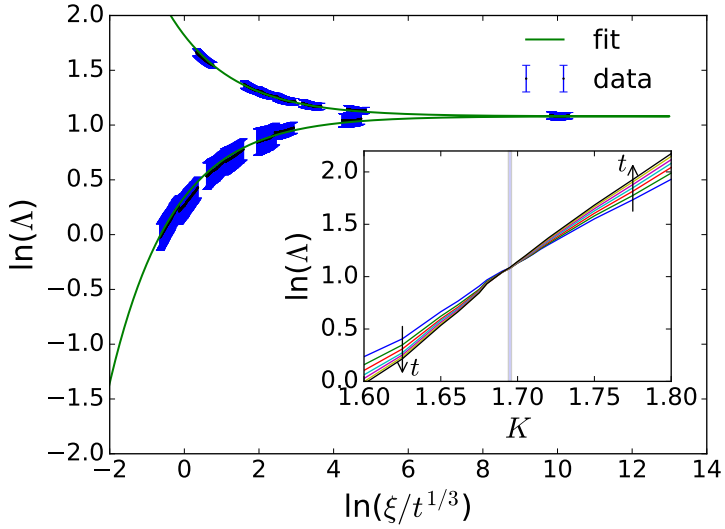

Figure 6.6 – Main plot: scaling quantity $\ln(\Lambda)$ as a function of $\ln(\xi/t^{1/3})$. ξ is proportional to $|K - K_c|^{-\nu}$. The numerical data in blue, with their statistical error bars, are well fitted by a function of the form (6.63), with the expansion stopped at $\mathcal{F}_1$. The χ^2 per degree of freedom associated to the fit, equal to 1.1, is indeed satisfactory (close to 1). The fit provides the following estimates for the critical point and critical exponent: $K_c = 1.695 \pm 0.001$ and $\nu = 1.68 \pm 0.07$. The value of the critical exponent is more than 4σ away from the one found in spin-1/2 disorder models, which lies in the range $[1.35, 1.39]$ [199]. Inset: $\ln(\Lambda)$ as a function of K at various times between 200000 and 1000000 kicks. For $K < K_c$ (on the localized side of the transition), $\ln(\Lambda)$ decreases in time, while for $K > K_c$ (on the diffusive side of the transition), $\ln(\Lambda)$ increases in time. Between these two limits, $\ln(\Lambda)$ is constant at the critical point $K = K_c$. A critical point $K_c \in [1.694, 1696]$ (represented as a blue rectangle) is fully consistent with the results. The numerical parameters used are given in the main text, in subsection 6.4.2 Results.

where ω_1 is incommensurate with 2π, and studies higher dimensions by adding incommensurate frequencies, e.g. three dimensions with

$$K_3(t) = K\left[1 + \eta\cos(\omega_1 t + \varphi_1)\cos(\omega_2 t + \varphi_2)\right] \text{ for } t \in \mathbb{N}. \tag{6.66}$$

To find other relevant quasi-periodic sequences, our angle is to retain two important properties of these sequences, namely the quasi-time-reversal-invariance and the quasi-periodicity. Indeed, it is with these properties that the diagrams responsible for Anderson localization can be built [22, 182, 206]. Quasi-time-reversal-invariance and quasi-periodicity correspond to approximations of $\omega_1/2\pi$ (or $\omega_1/2\pi$ and $\omega_2/2\pi$) by rationals.

In this vein, the important difference between K_2 and K_3 is the scaling of "how difficult it gets to achieve quasi-time-reversal-invariance (quasi-periodicity)" as "one becomes more and more demanding on the precision of the time-reversal (quasi-period)". In mathematical terms, this statement takes the following form: calling α the number of acceptable rational approximations to $\omega_1/2\pi$ (or $\omega_1/2\pi$ and $\omega_2/2\pi$) and β the maximal distance between $\omega_1/2\pi$ (or $\omega_1/2\pi$ and $\omega_2/2\pi$) and its rational approximations, we are interested in how α changes with β. For example, for K_2 one finds $\alpha \propto \beta$, while for K_3 one obtains $\alpha \propto \beta^2$. More generally, for K_d one gets $\alpha \propto \beta^{d-1}$. This reasoning neglects the properties of the rational approximations that may change with β.

Two theorems from number theory

Two theorems from number theory are of interest for the matter at hand. The first one is Hurwitz's theorem [207], it states that for every irrational number ξ there are infinitely many coprime integers m, n such that

$$\left|\xi - \frac{m}{n}\right| < \frac{1}{\sqrt{5}\,n^2}. \tag{6.67}$$

The second one is Roth's theorem [208], which states that every irrational algebraic number ξ has approximation exponent equal to 2, i.e., for any $\varepsilon > 0$, the inequality

$$\left|\xi - \frac{m}{n}\right| < \frac{1}{n^{2+\varepsilon}} \tag{6.68}$$

can have only finitely many solutions in coprime integers m and n.

From these two theorems, we conclude that the error in approximating $\omega/2\pi$ by a rational is inversely proportional to the square of the associated period.

Quasi-periodic sequences from series

From the above discussion, we want a function $f(t)$ that has approximate time reversals (periods), with the number of time reversals (periods) scaling as ϵ^{d-1}, where ϵ is the precision of the time-reversal (period). In addition, the lengths of the time-reversals (periods) should scale as $\sqrt{\epsilon}$. We propose the following function $f(t)$[8]:

$$f(t) = \cos\left(\frac{2\pi t}{4}\right) + 8\sum_{n>2}(-1)^{n+1} f_{2^n}(t), \tag{6.69}$$

where

$$f_m(t) = \left[\left(\frac{1}{2m}\right)^{\frac{1}{d-1}} + \left(\frac{1}{2m}\right)^{\frac{1}{d-1}} \frac{2t}{m}\right]^{d-1} \quad \text{for } t \in \left\{0, \frac{m}{2}\right\}, \tag{6.70}$$

with a time-reversal symmetry around $m/2$: $f_m(m/2+t) = f_m(m/2-t)$, and a period m. d supposably encodes the spatial dimension of the equivalent disorder model. In the following, we average over the origin of time to ensure statistical time-translational invariance.

Results

We have tested the sequence (6.69) numerically with the Hamiltonian

$$H = \frac{p^2}{2} + K\left[1 + \eta f(t)\right]\cos(\theta)\sum_n \delta(t-n), \tag{6.71}$$

the results are reported in figure 6.7. The results show that localization prevails at small K and turns into subdiffusion as K is increased. Surprisingly, subdiffusion does not concern only one value of K but a full range of values of K (η being fixed), with a subdiffusive exponent increasing with K. To go further, we have compared the results displaying a subdiffusive exponent of $2/3$ ($K = 1.64$ in figure 6.7b) with the known critical profile of the usual quasi-periodic kicked rotor [equation (6.57)] [209]:

$$\overline{|\psi(p)|^2} = \frac{3\alpha}{2}\mathrm{Ai}(\alpha|p|), \tag{6.72}$$

[8] As the functions $f_{m\gg1}(t)$ are slowly varying and positive, we have added the $(-1)^{n+1}$ to ensure some time-translational-invariance. The factor 8 is simply here for the sum not to be negligibly small.

where Ai is the Airy function. As visible in the main plot of figure 6.8c, the numerical results are very well fitted by (6.72) with $\alpha \simeq 0.0056$, thus suggesting that it corresponds to an Anderson-3D critical point. Note that equation (6.72) corresponds to a 3D diffusion process with a frequency dependent diffusion coefficient $D(\omega) = (-i\omega)^{1/3}$, integrated over two directions [209,210]. Deviations from (6.72) are expected at small p, due to the multifractal structure of the critical eigenfunctions [209–213], they are clearly visible in the inset of figure 6.8c. These deviations constitute a more specific signature of a critical point, although more work is needed to describe them in terms of the multifractal exponents of the critical eigenfunctions [214], which would provide an unambiguous correspondence with an Anderson-3D critical point.

Admittedly, these results are not consistent with (6.71) being equivalent to a d-dimensional disorder model (for which one expects subdiffusion for only one value of K – at fixed η), but we believe that they open the door to exciting perspectives. A theoretical framework is lacking to put these results into perspective. We can only notice a similarity with the power-law random banded matrix (PRBM) ensemble [193], which features a set of critical points. An important difference with this model resides in the localized regime (small K in the present context), where we observe exponential localization (figures 6.8a and 6.8b) as opposed to algebraic localization in the PRBM ensemble.

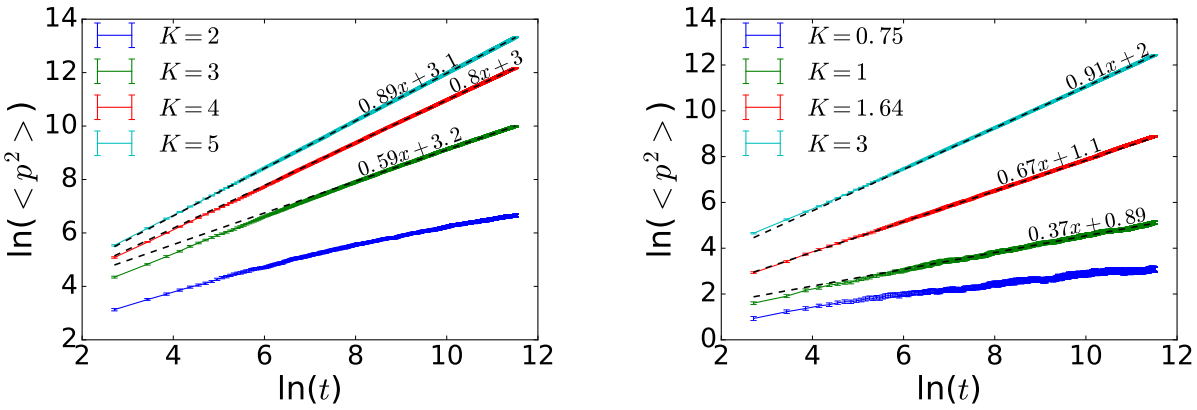

(a) $d = 2$. (b) $d = 3$.

Figure 6.7 – $\langle p^2 \rangle$ as a function of time for an initial plane wave evolving according to (6.71), with $\eta = 0.45$. The space ($[-\pi, \pi[$) is discretized in 25168 points and the results are averaged over 96 realizations of the kinetic term. The dashed lines are linear fits.

6.5 Conclusion

In this chapter, we have discussed various aspects of Anderson localization from the perspective of kicked-rotor models. The main conclusions of these studies is that many aspects of Anderson localization are still to be explored with the kicked rotor. We have put forward three main directions.

The first one concerns the possibility of exploring the symplectic class without the need of a spin. This has both theoretical and experimental motivations. On the theoretical side, it goes against common wisdom that a spinless model belongs to the symplectic class. From an experimental point of view, while it would open exciting possibilities [174], the introduction of a spin necessitates quite some efforts [168], avoiding it is desirable. We have presented strong evidences in favor of this possibility.

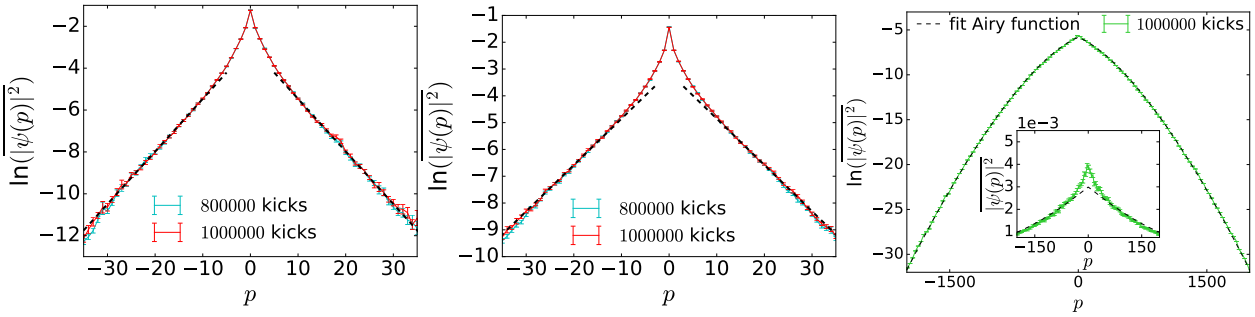

(a) $d = 2$, $K = 1.0$. (b) $d = 3$, $K = 0.75$. (c) $d = 3$, $K = 1.64$.

Figure 6.8 – Logarithms of the average momentum-density profiles for an initial plane wave evolving according to (6.71), with $\eta = 0.45$. In figures a) and b), the dashed lines are fits of the form $a|x| + b$. For figures a) and b), the space $([-\pi, \pi[)$ is discretized in 1260 points and the results are averaged over 10000 realizations of the kinetic term. For figure c), the space is discretized in 6292 points and the results are averaged over 2000 realizations of the kinetic term. Figure c) main plot: at large scales the numerical results in green are well fitted by (6.72) with $\alpha \simeq 0.0056$. Inset: average momentum-density profile, deviations from (6.72) with $\alpha \simeq 0.0056$ are clearly visible at small p, they could be a manifestation of the multifractal structure of the critical eigenfunctions [209–213].

The study of the symplectic class led us to a second direction, the apparent failure of the "quasi-periodic modulation trick" [196] in the unitary and symplectic classes. To begin addressing this issue, one could perform numerical simulations with actual 3D kicked rotors, as done in [215] for the orthogonal class, rather than through the introduction of incommensurate frequencies. Such a study would either point to the quasi-periodic modulation, or to a more fundamental difference between kicked rotors and disorder models in the unitary and symplectic classes.

A third aspect concerns the possibility of using new types of quasi-periodic kicking sequences, with different possible intentions. Although our attempt at exploring Anderson localization on fractals has not yet gone through, we believe that our preliminary study shows promising results and open exciting perspectives for future work.

Chapter 7

Conclusion

In this thesis, we theoretically investigated several interesting effects related to Anderson localization, focusing on the context of cold-atomic systems. We naturally started by characterizing the speckle potentials typically used in cold-atom experiments. In particular, we calculated statistical properties of intensity minima. In short, these minima typically lie at low energies and the distribution of their curvature is peaked around the average value.

With these results at hand, we embarked into the description of the spectral properties of atoms in speckle potentials. More precisely, we considered the spectral function and the density of states, in the strong disorder limit. Semiclassical methods turned out very powerful and allowed for a good description of the whole energy spectrum. Besides, our calculations provide a simple interpretation of intriguing features of the spectral function and density of states and of the difference between red- and blue-detuned speckles.

The study of spectral properties was also the opportunity to set the general framework for describing the dynamics of wave packets in random potentials. We applied it to a particular scenario, differing from the experiment performed in Palaiseau in 2008 [37] only in that atoms are given a finite velocity at $t = 0$. Remarkably, we found that after an initial ballistic motion, the packet center-of-mass experiences a retroreflection and slowly returns to its initial position, mimicking a boomerang. We associated this quantum boomerang effect to Anderson localization, and described it thoroughly in one dimension, both analytically and numerically.

We then considered the effects of weak interactions on the evolution in disordered potentials of condensed bosonic gases. To that end, we have developed a numerical integrate scheme of the Gross-Pitaevskii equation, which describes the evolution of an interacting gas at the mean-field level. This method was applied to various situations, with three main conclusions. First, nonlinear interactions tend to inhibit the quantum boomerang effect of wave packets launched with finite velocity. Second, because of inelastic collisions on the nonlinear potential, the wave packet explores the energy landscape. Third, the coherent back scattering (CBS) peak of matter waves prepared as plane wave states is strongly affected by the nonlinearity. We identified two kind of processes reducing the CBS contrast: short-time effects that break time-reversal invariance on the one hand, and inelastic collisions eventually leading to its destruction on a much longer time scale on the other hand.

These results point to interesting perspectives for future work. Concerning the spectral properties, we have not treated the three-dimensional case, involved in important questions related to Anderson localization [38, 40, 44, 109, 115, 128]. Its description would be of great interest. For example, the spectral function could be used to estimate the position of the mobility edge, through a generalized Ioffe-Regel criterion [109, 216–218].

As far as the quantum boomerang effect is concerned, while we have given a thorough description of the one-dimensional case, more work is needed in higher dimensions. For example, in light of recent

work on the coherent backward and forward scattering peaks across Anderson transition [44,128], it would be very interesting to perform a fine numerical analysis of the quantum boomerang effect in three dimensions. Another interesting possibility is to look for similar phenomena in other symmetry classes (e.g. in the unitary class where the qualitative understanding of retroreflection in terms of localized *real* modes does not apply).

Our study of the effects of weak interactions on the evolution of condensed bosonic gases was essentially numerical. While we underlined the physical picture explaining our observations, much remains to be done to describe them analytically. For example, we pointed out strong similarities, regarding the quantum boomerang effect, between the nonlinearity and a simple decoherence process. Exhibiting the microscopic origin of these similarities would probably be very enlightening. On a more fundamental level, we treated the interactions through a mean-field approximation, thus possibility missing coherent many-body effects. Their inclusions may lead to qualitatively different conclusions (e.g. a many-body coherent backscattering peak [86,219,220]).

Finally, we have shown that the kicked rotor constitutes a good platform to characterize various aspects of Anderson localization, and have identified three interesting directions of research for future work. First, going against common wisdom, we have presented strong evidence that the symplectic class can be explored with spinless particles. Second, we have observed that the "quasi-periodic modulation trick" of Casati *et al.* [196] seems to fail in the unitary and symplectic classes. Third, we have explored the possibility of using new types of quasi-periodic kicking sequences. We believe that our preliminary study in this direction shows promising results and opens exciting perspectives for future work.

Bibliography

[1] P. W. Anderson, Phys. Rev. **109**, 1492 (1958).

[2] G. Stolz, Contemporary Mathematics **552**, 71 (2011).

[3] E. Akkermans and G. Montambaux, *Mesoscopic Physics of Electrons and Photons* (Cambridge University Press, 2007).

[4] G. Bergmann, Phys. Rep. **107**, 1 (1984).

[5] F. Pierre, A. B. Gougam, A. Anthore, H. Pothier, D. Esteve, and N. O. Birge, Phys. Rev. B **68**, 085413 (2003).

[6] C. Hainaut, I. Manai, R. Chicireanu, J. F. Clément, S. Zemmouri, J. C. Garreau, P. Szriftgiser, G. Lemarié, N. Cherroret, and D. Delande, Phys. Rev. Lett. **118**, 184101 (2017).

[7] F. Jendrzejewski, K. Müller, J. Richard, A. Date, T. Plisson, P. Bouyer, A. Aspect, and V. Josse, Phys. Rev. Lett. **109**, 195302 (2012).

[8] G. Labeyrie, T. Karpiuk, J. F. Schaff, B. Grémaud, C. Miniatura, and D. Delande, Euro Phys. Lett. **100**, 66001 (2012).

[9] D. Vollhardt and P. Wölfle, Phys. Rev. B **22**, 4666 (1980).

[10] P. Wölfle and D. Vollhardt, Int. J. Mod. Phys. B **24**, 1526 (2010).

[11] F. Evers and A. D. Mirlin, Rev. Mod. Phys. **80**, 1355 (2008).

[12] O. I. Lobkis and R. L. Weaver, Phys. Rev. E **71**, 011112 (2005).

[13] V. L. Berezinskii, Zh. Eksp. Teor. Fiz. **65**, 1251 (1973) [Sov. Phys. JETP **38**, 620 (1974)].

[14] A. A. Gogolin, Physics Reports **86**, 1 (1982).

[15] C. W. J. Beenakker, Rev. Mod. Phys. **69**, 731 (1997).

[16] R. L. Weaver and J. Burkhardt, J. Acoust. Soc. Am. **96**, 3186 (1994).

[17] R. L. Weaver and O. I. Lobkis, Phys. Rev. Lett. **84**, 4942 (2000).

[18] E. Abrahams, P. W. Anderson, D. C. Licciardello, and T. V. Ramakrishnan, Phys. Rev. Lett. **42**, 673 (1979).

[19] H. G. Schuster, Z. Phys. B **31**, 99 (1978).

[20] D. Vollhardt and P. Wölfle, Phys. Rev. Lett. **48**, 699 (1982).

[21] P. Ostrovsky, T. Nakayama, K. A. Muttalib, and P. Wölfle, New J. Phys **15**, 055010 (2013).

[22] K. Efetov, *Supersymmetry in Disorder and Chaos* (Cambridge University Press, 1999).

[23] G. Feher, Phys. Rev. **114**, 1219 (1959).

[24] G. Feher and E. A. Gere, Phys. Rev. **114**, 1245 (1959).

[25] B. Kramer and A. MacKinnon, Rep. Prog. Phys. **56**, 1469 (1993).

[26] P. A. Lee and T. V. Ramakrishnan, Rev. Mod. Phys. **57**, 287 (1985).

[27] K. Byczuk, W. Hofstetter, and D. Vollhardt, Chapter 20 in *50 Years of Anderson Localization*, ed. E. Abrahams (World Scientific, Singapore, 2010); reprinted in Int. J. Mod. Phys. B **24**, 1727 (2010).

[28] B. A. van Tiggelen, Chapter 1 in *Diffuse Waves in Complex Media*, ed. J. P. Fouque (Springer Netherlands, 1999).

[29] R. Dalichaouch, J. P. Armstrong, S. Schultz, P. M. Platzman, and S. L. McCall, Nature **354**, 53 (1991).

[30] L. Ye, G. Cody, M. Zhou, P. Sheng, and A. N. Norris, Phys. Rev. Lett. **69**, 3080 (1992).

[31] A. A. Chabanov, M. Stoytchev, and A. Z. Genack, Nature **404**, 850 (2000).

[32] T. Schwartz, G. Bartal, S. Fishman, and M. Segev, Nature **446**, 52 (2007).

[33] M. Störzer, P. Gross, C. M. Aegerter, and G. Maret, Phys. Rev. Lett. **96**, 063904 (2006).

[34] T. Sperling, L. Schertel, M. Ackermann, G. J. Aubry, C. M. Aegerter, and G. Maret, New J. Phys. **18**, 013039 (2016).

[35] H. Hu, A. Strybulevych, J. H. Page, S. E. Skipetrov, and B. A. van Tiggelen, Nature Phys. **4**, 945 (2008).

[36] J. Chabé, G. Lemarié, B. Grémaud, D. Delande, P. Szriftgiser, and J. C. Garreau, Phys. Rev. Lett. **101**, 255702 (2008).

[37] J. Billy, V. Josse, Z. Zuo, A. Bernard, B. Hambrecht, P. Lugan, D. Clément, L. Sanchez-Palencia, P. Bouyer, and A. Aspect, Nature **453**, 891 (2008).

[38] F. Jendrzejewski, A. Bernard, K. Müller, P. Cheinet, V. Josse, M. Piraud, L. Pezzé, L. Sanchez-Palencia, A. Aspect, and P. Bouyer, Nature Phys. **8**, 398 (2012).

[39] I. Manai, J. F. Clément, R. Chicireanu, C. Hainaut, J. C. Garreau, P. Szriftgiser, and D. Delande, Phys. Rev. Lett. **115**, 240603 (2015).

[40] G. Semeghini, M. Landini, P. Castilho, S. Roy, G. Spagnolli, A. Trenkwalder, M. Fattori, M. Inguscio, and G. Modugno, Nature Phys. **11**, 554 (2015).

[41] G. Modugno, Rep. Prog. Phys. **73**, 102401 (2010).

[42] B. Shapiro, J. Phys. A: Math. Theor. **45**, 143001 (2012).

[43] T. Karpiuk, N. Cherroret, K. L. Lee, B. Grémaud, C. A. Müller, and C. Miniatura, Phys. Rev. Lett. **109**, 190601 (2012).

[44] S. Ghosh, C. Miniatura, N. Cherroret, and D. Delande, Phys. Rev. A **95**, 041602(R) (2017).

[45] S. S. Kondov, W. R. McGehee, J. J. Zirbel, and B. DeMarco, Science **334**, 66 (2011).

[46] W. R. McGehee, S. S. Kondov, W. Xu, J. J. Zirbel, and B. DeMarco, Phys. Rev. Lett. **111**, 145303 (2013).

[47] P. Lugan, A. Aspect, L. Sanchez-Palencia, D. Delande, B. Grémaud, C. A. Müller, and C. Miniatura, Phys. Rev. A **80**, 023605 (2009); Erratum Phys. Rev. A **84**, 019902 (2011).

[48] S. Flach, chapter 1 in *Nonlinear Optical and Atomic Systems: At the Interface of Physics and Mathematics*, ed. C. Besse and J. C. Garreau (Springer, Cham 2015).

[49] A. Iomin, Comp. Math. Appl. **73**, 914 (2017).

[50] E. Lucioni, B. Deissler, L. Tanzi, G. Roati, M. Zaccanti, M. Modugno, M. Larcher, F. Dalfovo, M. Inguscio, and G. Modugno, Phys. Rev. Lett. 106, 230403 (2011).

[51] G. Benettin, J. Fröhlich, and A. Giorgilli, Commun. Math. Phys. **119**, 95 (1988).

[52] W. M. Wang and Z. Zhang, J. Stat. Phys. **134**, 953 (2009).

[53] E. Michaely and S. Fishman, Phys. Rev. E **85**, 046218 (2012).

[54] M. Mulansky, Chaos **24**, 024401 (2014).

[55] G. Schwiete and A. M. Finkel'stei, Phys. Rev. Lett. **104**, 103904 (2010).

[56] N. Cherroret and T. Wellens, Phys. Rev. E **84**, 0211141 (2011).

[57] D. M. Basko, Ann. Phys **326**, 1577 (2011).

[58] G. Schwiete and A. M. Finkel'stein, Phys. Rev. A **87**, 043636 (2013).

[59] G. Schwiete and A. M. Finkel'stein, Phys. Rev. A **88**, 053611 (2013).

[60] N. Cherroret, T. Karpiuk, B. Grémaud, and C. Miniatura, Phys. Rev. A **92**, 063614 (2015).

[61] M. Hartung, T. Wellens, C. A. Müller, K. Richter, and P. Schlagheck, Phys. Rev. Lett. **101**, 020603 (2008).

[62] T. Hartmann, J. Michl, C. Petitjean, T. Wellens, J. D. Urbina, K. Richter, and P. Schlagheck, Ann. Phys **327**, 1998 (2012).

[63] V. M. Agranovich and V. E. Kravtsov, Phys. Rev. B **43**, 13691(R) (1991).

[64] A. Heiderich, R. Maynard, and B. A. van Tiggelen, Optics Comm. **115**, 392 (1995).

[65] T. Wellens and B. Grémaud, J. Phys. B: At. Mol. Opt. Phys. **39**, 4719 (2006).

[66] B. Grémaud, T. Wellens, D. Delande, and C. Miniatura, Phys. Rev. A **74**, 033808 (2006).

[67] S. A. Gredeskul and Y. S. Kivshar, Phys. Rep. **216**, 1 (1992).

[68] T. Paul, P. Leboeuf, N. Pavloff, K. Richter, and P. Schlagheck, Phys. Rev. A **72**, 063621 (2005).

[69] T. Paul, P. Schlagheck, P. Leboeuf, and N. Pavloff, Phys. Rev. Lett. **98**, 210602 (2007).

[70] N. Bilas and N. Pavloff, Eur. Phys. J. D **40**, 387 (2006).

[71] P. Lugan, D. Clement, P. Bouyer, A. Aspect, and L. Sanchez-Palencia, Phys. Rev. Lett. **99**, 180402 (2007); Erratum Phys. Rev. Lett. **99**, 219902 (2007).

[72] T. Ernst, T. Paul, and P. Schlagheck, Phys. Rev. A **81**, 013631 (2010).

[73] P. Lugan and L. Sanchez-Palencia, Phys. Rev. A **84**, 013612 (2011).

[74] C. Gaul and C. A. Müller, Phys. Rev. A **83**, 063629 (2011); Erratum Phys. Rev. A **84**, 029901 (2011).

[75] C. A. Müller and C. Gaul, New J. Phys **14**, 075025 (2012).

[76] C. Gaul and C. A. Müller, Eur. Phys. J. Special Topics **217**, 69 (2013).

[77] J. Dujardin, T. Engl, and P. Schlagheck, Phys. Rev. A **93**, 013612 (2016).

[78] T. Geiger, T. Wellens, and A. Buchleitner, Phys. Rev. Lett. **109**, 030601 (2012).

[79] T. Geiger, A. Buchleitner, and T. Wellens, New J. Phys **15**, 115015 (2013).

[80] D. M. Basko, I. L. Aleiner, and B. L. Altshuler, Ann. Phys. **321**, 1126 (2006).

[81] R. Nandkishore and D. A. Huse, Annu. Rev. Condens. Matter Phys. **6**, 15 (2015).

[82] E. Altman and R. Vosk, Annu. Rev. Condens. Matter Phys. **6**, 383 (2015).

[83] J. H. Bardarson, F. Pollmann, and J. E. Moore, Phys. Rev. Lett. **109**, 017202 (2012).

[84] M. Schreiber, S. S. Hodgman, P. Bordia, H. P. Lüschen, M. H. Fischer, R. Vosk, E. Altman, U. Schneider, and I. Bloch, Science **349**, 842 (2015).

[85] J. Choi, S. Hild, J. Zeiher, P. Schauß, A. Rubio-Abadal, T. Yefsah, V. Khemani, D. A. Huse, I. Bloch, and C. Gross, Science **352**, 1547 (2015).

[86] T. Engl, J. Dujardin, A. Argüelles, P. Schlagheck, K. Richter, and J. D. Urbina, Phys. Rev. Lett. **112**, 140403 (2014).

[87] M. Brenes, M. Dalmonte, M. Heyl, and A. Scardicchio, arXiv:1706.05878.

[88] M. Mierzejewski, K. Giergiel, and K. Sacha, arXiv:1706.05878.

[89] V. Chulaevsky and Y. Suhov, Math Phys Anal Geom **12**, 117 (2009).

[90] M. Fauser and S. Warzel, Rev. Math. Phys. **27**, 1550010 (2015).

[91] J. Z. Imbrie, Jour. Stat. Phys. **163**, 998 (2016).

[92] J. W. Goodman, *Statistical Properties of Laser Speckle Patterns* (Springer, 2008).

[93] J. Dalibard, *Cours au Collège de France* (2013).

[94] J. Dalibard and C. Cohen-Tannoudji, Foreword: Laser Cooling and Trapping of Neutral Atoms. In Springer Berlin Heidelberg, *Atomic and Molecular Beams* (2001).

[95] N. Goldman, G. Juzeliūnas, P. Öhberg, and I. B. Spielman, Rep. Prog. Phys **77**, 126401 (2014).

[96] C. Chin, R. Grimm, P. Julienne, and E. Tiesinga, Rev. Mod. Phys. **82**, 1225 (2010).

[97] Annual Review of Cold Atoms and Molecules (World Scientific, 2013-2014-2015).

[98] I. Bloch, J. Dalibard, and W. Zwerger, Rev. Mod. Phys. **80**, 885 (2008).

[99] I. Bloch, J. Dalibard, and S. Nascimbène, Nature Phys. **8**, 267 (2012).

[100] Wolfram Research, Inc., Mathematica, Version 10.3, Champaign, IL (2015).

[101] G. N. Watson, *A treatise on the theory of Bessel functions* (Cambridge University Press, 1966).

[102] A. Weinrib, Phys. Rev. B **26**, 1352 (1982).

[103] A. Weinrib and B. I. Halperin, Phys. Rev. B **26**, 1362 (1982).

[104] I. L. Aleiner, B. L. Altshuler, and G. V. Shlyapnikov, Nature Phys. **6**, 900 (2010).

[105] M. I. Trappe, D. Delande, and C. A. Müller, J. Phys. A: Math. Theor. **48**, 245102 (2015).

[106] G. D. Mahan, *Many-Particle Physics* (Springer New York, 2000).

[107] R. C. Kuhn, O. Sigwarth, C. Miniatura, D. Delande, and C. A. Müller, New J. Phys. **9**, 161 (2007).

[108] D. Delande and C. A. Müller, chapter 9 in *Les Houches 2009 - Session XCI: Ultracold Gases and Quantum Information*, ed. C. Miniatura, L. C. Kwek, M. Ducloy, B. Grémaud, B. G. Englert, L. Cugliandolo, A. Ekert, and K. K. Phua (Oxford University Press, 2011).

[109] M. Pasek, Z. Zhao, D. Delande, and G. Orso, Phys. Rev. A **92**, 053618 (2015).

[110] V. V. Volchkov, M. Pasek, V. Denechaud, M. Mukhtar, A. Aspect, D. Delande, and V. Josse, arXiv:1707.07577.

[111] J. P. Ramírez Valdes and T. Wellens, Phys. Rev. A **93**, 063634 (2016).

[112] M. Piraud, P. Lugan, P. Bouyer, A. Aspect, and L. Sanchez-Palencia, Phys. Rev. A **83**, 031603(R) (2011).

[113] C. A. Müller and B. Shapiro, Phys. Rev. Lett. **113**, 099601 (2014).

[114] C. A. Müller, D. Delande, and B. Shapiro, Phys. Rev. A **94**, 033615 (2016).

[115] M. Pasek, G. Orso, and D. Delande, Phys. Rev. Lett. **118**, 170403 (2017).

[116] G. M. Falco, A. A. Fedorenko, J. Giacomelli, and M. Modugno, Phys. Rev. A **82**, 053405 (2010).

[117] B. Grammaticos and A. Voros, Ann. Phys. **123**, 359 (1979).

[118] W. Magnus, Comm. Pure Appl. Math. **7**, 649 (1954).

[119] D. R. Brillinger, *Time series data analysis and theory* (Siam, 2001).

[120] V. P. Leonov and A. N. Shiryaev, Theor. probab. appl. **4**, 319 (1959). Note that "semi-invariant" is another word for joint cumulant.

[121] M. C. Gutzwiller, *Chaos in classical and Quantum mechanics* (Springer, 1990).

[122] M. Tabor, Physica **6D**, 195 (1983).

[123] F. Haake, *Quantum Signatures of Chaos* (Springer, 2010).

[124] I. M. Lifshitz, Adv. Phys. **13**, 483 (1964).

[125] G. M. Falco and A. A. Fedorenko, Phys. Rev. A **92**, 023412 (2015).

[126] A. Altland and B. Simons, *Condensed Matter Field Theory* (Cambridge University Press, 2010).

[127] M. C. Gutzwiller, Physica D **5**, 183 (1982).

[128] S. Ghosh, D. Delande, C. Miniatura, and N. Cherroret, Phys. Rev. Lett. **115**, 200602 (2015).

[129] S. Roche and D. Mayou, Phys. Rev. Lett. **79**, 2518 (1997).

[130] H. Fehske, J. Schleede, G. Schubert, G. Wellein, V. S. Filinov, and A. R. Bishop, Phys. Lett. A **373**, 2182 (2009).

[131] M. Abramowitz and I.A. Stegun, *Handbook of Mathematical Functions: with Formulas, Graphs, and Mathematical Tables* (Dover Publications, 1965).

[132] D. J. Thouless, J. Phys C.:Solid State Phys **6**, L49 (1973).

[133] E. P. Nakhmedov, V. N. Prigodin, and Y. A. Firsov, Zh. Eksp. Teor. Fiz. **92**, 2133 (1987) [Sov. Phys. JETP **65**, 1202 (1987)].

[134] E. N. Economou, *Green's Functions in Quantum Physics* (Springer-Verlag Berlin Heidelberg, 2006).

[135] T. Plisson, T. Bourdel, and C. A. Müller, Eur. Phys. J. Spec. Top. **217**, 79 (2013).

[136] A. A. Gogolin and V. I. Mel'nikov, Phys. Stat. Sol. (b) **88**, 377 (1978).

[137] L. D. Landau and E. M. Lifshitz, *Quantum Mechanics (Non-relativistic theory)* (Pergamon, 1977).

[138] L. Erdős, B. Schlein, and H. T. Yau, Phys. Rev. Lett. **98**, 040404 (2007).

[139] F. Dalfovo, S. Giorgini, L. P. Pitaevskii, and S. Stringari, Rev. Mod. Phys. **71**, 463 (1999).

[140] K. G. Singh and D. S. Rokhsar, Phys. Rev. B **49**, 9013 (1994).

[141] M. Suzuki, J. Math. Phys. **26**, 601 (1985).

[142] A. S. Pikovsky and D. L. Shepelyansky, Phys. Rev. Lett. **100**, 094101 (2008).

[143] S. Flach, D. O. Krimer, and C. Skokos, Phys. Rev. Lett. **102**, 024101 (2009); Erratum Phys. Rev. Lett. **102**, 209903 (2009).

[144] T. V. Laptyeva, J. D. Bodyfelt, D. O. Krimer, C. Skokos and S. Flach, Europhys. Lett. **91**, 30001 (2010).

[145] D. L. Shepelyansky, Phys. Rev. Lett. **70**, 1787 (1993).

[146] G. Kopidakis, S. Komineas, S. Flach, and S. Aubry, Phys. Rev. Lett. **100**, 084103 (2008).

[147] A. Iomin, Phys. Rev. E **81**, 017601 (2010).

[148] B. Min, T. Li, M. Rosenkranz, and W. Bao, Phys. Rev. A **86**, 053612 (2012).

[149] N. Cherroret, J. Phys.: Cond. Matt. **29**, 024002 (2017).

[150] D. M. Basko, Phys. Rev. E **86**, 036202 (2012).

[151] D. M. Basko, Phys. Rev. E **89**, 022921 (2014).

[152] A. V. Milovanov and A. Iomin, Europhys. Lett. **100**, 10006 (2012).

[153] A. V. Milovanov and A. Iomin, Phys. Rev. E **89**, 062921 (2014).

[154] I. V. Gornyi, A. D. Mirlin, M. Müller, and D. G. Polyakov, Ann. Phys. (Berlin) **529**, 1600365 (2017).

[155] T. Wellens, private communication.

[156] B. Spivak and A. Zyuzin, Phys. Rev. Lett. **84**, 1970 (2000).

[157] R. J. Elliott, J. A. Krumhansl, and P. L. Leath, Rev. Mod. Phys. **46**, 465 (1974).

[158] G. Rickayzen, *Green's Functions and Condensed Matter* (Dover Publications, 2013).

[159] T. Prat, N. Cherroret, and D. Delande, Phys. Rev. A **94**, 022114 (2016).

[160] W. H. Zurek, Phys. Today **44**, 36 (1991), see also the updated version, arXiv:quant-ph/0306072.

[161] C. Connaughton, C. Josserand, A. Picozzi, Y. Pomeau, and S. Rica, Phys. Rev. Lett. **95**, 263901 (2005).

[162] C. Sun, S. Jia, C. Barsi, S. Rica, A. Picozzi, and J. W. Fleischer, Nature Phys. **8**, 470 (2012).

[163] S. V. Nazarenko, *Wave Turbulence* (Springer-Verlag, Berlin Heidelberg 2011).

[164] M. Mulansky, K. Ahnert, A. Pikovsky, and D. L. Shepelyansky, Phys. Rev. E **80**, 056212 (2012).

[165] N. Cherroret, T. Karpiuk, C. A. Müller, B. Grémaud, and C. Miniatura, Phys. Rev. A **85**, 011604(R) (2011).

[166] S. Ghosh, N. Cherroret, B. Grémaud, C. Miniatura, and D. Delande, Phys. Rev. A **90**, 063602 (2014).

[167] G. S. Joyce, J. Phys. A **31**, 5105 (1998).

[168] J. C. Garreau, Comptes Rendus Physique (in english) **18**, 31 (2017).

[169] F. L. Moore, J. C. Robinson, C. F. Bharucha, B. Sundaram, and M. G. Raizen, Phys. Rev. Lett. **75**, 4598 (1995).

[170] G. Casati, B. V. Chirikov, J. Ford, and F. M. Izrailev, *Stochastic Behavior of A Quantum Pendulum Under Periodic Perturbation* (Springer-Verlag Berlin, 1979).

[171] D. R. Grempel, R. E. Prange, and S. Fishman, Phys. Rev. A **29**, 1639 (1984).

[172] A. Altland and M. R. Zirnbauer, Phys. Rev. Lett. **77**, 4536 (1996).

[173] J. P. Dahlhaus, J. M. Edge, J. Tworzydło, and C. W. J. Beenakker, Phys. Rev. B **84**, 115133 (2011).

[174] Y. Chen and C. Tian, Phys. Rev. Lett. **113**, 216802 (2014).

[175] C. Tian, Y. Chen, and J. Wang, Phys. Rev. B **93**, 075403 (2016).

[176] B. V. Chirikov, Phys. Rep. **52**, 263 (1979).

[177] M. Griniasty and S. Fishman, Phys. Rev. Lett. **60**, 1334 (1988).

[178] N. Brenner and S. Fishman, Nonlinearity **4**, 211 (1992).

[179] G. Lemarié, J. Chabé, P. Szriftgiser, J. C. Garreau, B. Grémaud, and D. Delande, Phys. Rev. A **80**, 043626 (2009).

[180] F. M. Izrailev, Phys. Rep. **196**, 299 (1990).

[181] C. Tian and A. Altland, New J. Phys **12**, 043043 (2010).

[182] A. Altland, Phys. Rev. Lett. **71**, 69 (1993).

[183] R. Blümel and U. Smilansky, Phys. Rev. Lett. **69**, 217 (1992).

[184] M. Thaha, R. Blümel, and U. Smilansky, Phys. Rev. E **48**, 1764 (1993).

[185] E. P. Wigner, Ann. Math. **62**, 548 (1955).

[186] *Applications of Random Matrices in Physics*, ed. E. Brezin,V. Kazakov, D. Serban, P. Wiegmann, and A. Zabrodin (Springer Netherlands, 2006).

[187] J. Keating, *The Riemann Zeta-Function and Quantum Chaology* (Enrico Fermi International School of Physics, 1993).

[188] A. Altland and M. R. Zirnbauer, Phys. Rev. B **55**, 1142 (1997).

[189] F. Evers and A. D. Mirlin, Rev. Mod. Phys. **80**, 1355 (2008).

[190] M. L. Mehta, *Random Matrices* (Academic Press, 2004).

[191] J. H. Conway and D. Smith, *On Quaternions and Octonions* (A K Peters/CRC Press, 2003).

[192] J. Cardy, *Scaling and Renormalization in Statistical Physics* (Cambridge University Press, 1996).

[193] A. D. Mirlin, Y. V. Fyodorov, F. M. Dittes, J. Quezada, and T. H. Seligman, Phys. Rev. E **54**, 3221 (1996).

[194] G. Lemarié, C. A. Müller, D. Guéry-Odelin, and C. Miniatura, Phys. Rev. A **95**, 043626 (2017).

[195] Y. Y. Atas, E. Bogomolny, O. Giraud, and G. Roux, Phys. Rev. Lett. **110**, 084101 (2013).

[196] G. Casati, I. Guarneri, and D. L. Shepelyansky, Phys. Rev. Lett. **62**, 345 (1989).

[197] C. Tian, A. Altland, and M. Garst, Phys. Rev. Lett. **107**, 074101 (2011).

[198] R. Scharf, J. Phys. A **22**, 4223 (1989).

[199] Y. Asada, K. Slevin, and T. Ohtsuki, J. Phys. Soc. Jpn. **74**, 238 (2005).

[200] D. Delande, private communication.

[201] Y. Asada, K. Slevin, and T. Ohtsuki, Phys. Rev. B **73**, 041102(R) (2006).

[202] D. Sticlet and A. Akhmerov, Phys. Rev. B **94**, 161115(R) (2016).

[203] M. Schreiber and H. Grussbach, Phys. Rev. Lett. **76**, 1687 (1996).

[204] I. Travěnec and P. Markoš, Phys. Rev. B **65**, 113109 (2002).

[205] A. Kosior and K. Sacha, Phys. Rev. B **95**, 104206 (2017).

[206] T. Micklitz, C. A. Müller, and A. Altland, Phys. Rev. B **91**, 064203 (2015).

[207] A. Hurwitz, Mathematische Annalen (in german) **39**, 279 (1891), see also (in english) G. H. Hardy, E. M. Wright, R. Heath-Brown, J. Silverman and A. Wiles, *An introduction to the Theory of Numbers* (Oxford University Press, 2008).

[208] K. F. Roth, Mathematika **2**, 1 (1955).

[209] G. Lemarié, H. Lignier, D. Delande, P. Szriftgiser, and J. C. Garreau, Phys. Rev. Lett. **105**, 090601 (2010).

[210] G. Lemarié, Ph.D. thesis, Université P. et M. Curie, Paris (2009).

[211] J. T. Chalker and G. J. Daniell, Phys. Rev. Lett. **61**, 593 (1988).

[212] J. T. Chalker, Physica A **167**, 253 (1990).

[213] R. Ketzmerick, K. Kruse, S. Kraut, and T. Geisel, Phys. Rev. Lett. **79**, 1959 (1997).

[214] P. Akridas and D. Delande, to be published.

[215] J. Wang and A. M. García-García, Phys. Rev. E **79**, 036206 (2009).

[216] E. N. Economou, C. M. Soukoulis, and A. D. Zdetsis, Phys. Rev. B **30**, 1686 (1984).

[217] A. Yedjour and B. A. Van Tiggelen, Eur. Phys. J. D **59**, 249 (2010).

[218] M. Piraud, L. Pezzé, and L. Sanchez-Palencia, New J. Phys. **15**, 075007 (2013).

[219] T. Engl, J. D. Urbina, and K. Richter, Phil. Trans. R. Soc. A **374**, 20150159 (2016).

[220] P. Schlagheck and J. Dujardin, Ann. Phys. (Berlin) **529**, 1600311 (2017).

Abstract

This thesis theoretically investigates several effects related to Anderson localization, focusing on the context of disordered and chaotic cold-atomic systems.

In cold-atomic systems, optical speckle patterns are often used to create the disorder. The resulting potentials felt by the atoms differ from Gaussian random potentials, commonly assumed in the description of condensed-matter systems. In the first part of the thesis, we discuss their specificities, with an emphasis on the spectral properties of atoms in such potentials. In particular, we derive several approximations for the spectral function.

Atom-optics experiments offer interesting possibilities, such as the possibility to directly probe the atoms inside the disordered potential. In view of these possibilities, we consider in the second part of the thesis the spreading of matter wave packets initially launched with a non-zero velocity. We find that after an initial ballistic motion, the packet center-of-mass experiences a retroreflection and slowly returns to its initial position, mimicking a boomerang. We show that this unexpected quantum boomerang effect is a consequence of Anderson localization, and describe it both numerically and analytically in dimension 1.

Atom-atom interactions are then introduced in a third part. We consider dilute condensed bosonic gases, and treat the interactions at the mean-field (Gross-Pitaevskii) level. Various situations are studied numerically, in particular the quantum boomerang scenario, and the dynamical spreading – both in momentum and energy – of matter waves prepared as plane waves.

In the last part, we show that chaotic models offer interesting prospects for the study of Anderson localization. On the one hand, going against common wisdom, we present strong evidences in favor of a spinless kicked rotor in the sympletic ensemble. On the other hand, a second look at a commonly studied quasi-periodically modulated kicked rotor reveals intriguing results.